SMART BUILDINGS:

SYNERGY IN STRUCTURAL CONTROL, STRUCTURAL HEALTH MONITORING AND ENVIRONMENTAL SYSTEMS

by

Tat S. Fu

A Thesis Presented to the
FACULTY OF THE GRADUATE SCHOOL
UNIVERSITY OF SOUTHERN CALIFORNIA
In Partial Fulfillment of the
Requirements for the Degree
DOCTOR OF PHILOSOPHY
(CIVIL AND ENVIRONMENTAL ENGINEERING)

May 2009

Dedication

To everyone who has supported me year after year

Acknowledgements

I am indebted to my co-advisers Prof. Erik A. Johnson and Prof. Sami F. Masri for their wisdom, guidance and supports. My dissertation and training would not be possible if not for Prof. Johnson's wholehearted support on my desire to study in a multi-disciplinary setting. He has given me countless opportunities to grow professionally and see the world. I will cherish the friendship we have developed. I am grateful for the advice from my other committee members: Prof. Roger Ghanem and Prof. Marc Schiler, especially to Prof. Schiler who chaired my Architecture (M.B.S) thesis. I would also like to thank many of the Civil Engineering faculty and staff whom I got to know, particularly Dr. Hung L. Wong (Doc) and Dr. Vincent W. Lee.

I appreciated the collaboration with faculty and (former and current) graduate students from different programs: Prof. G. Goetz Schierle, Prof. Thomas Spiegelhalter and Prof. Doug Noble from Architecture; Prof. Ramesh Govindan, Dr. Krishna K. Chintalapudi and Jeongyeup Paek from Computer Science; and Prof. Bhaskar Krishnamachari and Amitabha Ghosh from Electrical Engineering. I am thankful to the support from my former and current labmates, particularly Dr. Mohamed Ihab Sherif Mohamed Elmasr, Dr. Baris Erkus, Dr. Vicrom Panichacarn, Ali Asghari and Dongyu Zhang.

To my family, I do not know how to thank you enough, especially to my parents who are always encouraging. To my life partner, who has been by my side since our first year in undergraduate, I wish that I will be as supportive to your doctoral study as you have been to mine.

I gratefully acknowledge the partial support by the National Science Foundation under CAREER Award 00-94030 and through grant 03-25875, and the Doctoral Fellowship from USC Engineering.

Table of Contents

List of Figures

List of Tables

Abstract

Smart buildings are different from traditional buildings in their ability to react to external and internal building conditions and provide building functions that concern safety, comfort and energy efficiency. The capability to monitor and control different building systems makes a building smart. Efficient cooperation among various building systems is also crucial because of the increasing complexity in buildings. This dissertation focuses on structural control and health monitoring as well as integrating the structural system with an environmental system to create safe, energy efficient and smart buildings.

Structural health monitoring (SHM) aims to assess the health of structures in a systematic and automatic manner. Cost and reliability are the biggest challenges for SHM. A SHM system with a wireless sensor network is studied to reduce cost by avoiding expensive wiring in installation. The bandwidth and power concerns of wireless sensors are addressed using a distributed algorithm for damage detection and optimizing sensor placements. Reliability in damage detection is also examined for both global and local excitations. With the measured responses from exciting the structure globally, an SHM algorithm is expanded to conduct a multi-directional analysis, providing more information and accuracy on damage detection. By exciting a structural member locally and studying the wave propagation within this member, damage is successfully detected and the effect of sensor placements on damage detection accuracy is analyzed.

Synergy of integrating structural and environmental systems is explored with a proposed Shading Fin Mass Damper (SFMD) system. Movable and heavier shading fins are used instead of typical static fins to function as mass dampers. The added mobility allows the fins to change positions for greater sunlight control, thus minimizing energy consumption on cooling and heating loads. Since the shading fins are placed along the height of the building, the dampers are distributed rather than concentrated in a few locations as in typical tuned mass damper systems. Passive, active and semiactive control strategies are analyzed for the distributed mass damper (DMD) system; results show that the DMD system can reduce structural vibration significantly. Additionally, the actuators controlling the movements of the SFMDs are studied to excite the structure for SHM. It is observed that by using combinations of the multiple actuators, damaged detection can be greatly improved for the DMD system.

Chapter 1 – Introduction

A smart structure is defined as a structure that alters its structural behavior to improve safety under external forces and/or has the ability to monitor its own integrity. Smart structures have been an active research area that consists of structural control and health monitoring. This dissertation builds on smart structures and proposes a smart building that reacts to external and internal building conditions to provide building functions that concern safety, comfort and energy efficiency. Monitoring and control are the foci of smart buildings because smart technologies rely on the abilities to collect, process and react effectively to information about the building conditions. Additionally, since buildings comprise various building systems that serve different functions, such complexity calls for efficient cooperation among these systems is essential for smart buildings.

As buildings become larger and taller, building technologies have been evolving and becoming more complex. Buildings today have to be maintained and controlled for safety and comfort of the occupants and efficiency of building operations. For example, tall buildings adopt computer algorithms to control the movements of elevators and optimize people flow. Large buildings require layers of control systems to work together for smooth operations. These operations rely on accurate and current information about building conditions for decision making and performance evaluations. More sophisticated sensing/monitoring networks, more capable building control systems, and system integration are vital in creating efficient, sustainable and smarter buildings. This dissertation focuses on several building systems — structural health monitoring, and structural and environmental controls — and explores synergy among them to improve efficiency.

1.1 Smart Building / Smart Structure

In the field of structural engineering, the term "building" often refers to the structure of a building because structural engineers primarily deal with the structural aspect of buildings. However, for architects, "building" and "structure" have different meanings because they consider structure to be an element of a building. Although the majority of this dissertation focuses on structural engineering, some architectural aspects of buildings are also discussed. Therefore, the terms, "building" and "structure," must be well defined: a *building* is a closed form that houses people and/or goods, consisting of multiple components (*e.g.*, windows, roof, etc.); a *structure*, consisting of columns, beams, etc., is the part of a building that supports the weight of the building and ensures that it will stand upright.

Building operations enable buildings to function properly and involve many components. For large buildings, there are:

- Architectural design (*e.g.*, appearance, form)
- Structures
- Heating units
- Air Conditioning (A/C) units
- Air supply
- Water supply
- Elevator systems
- Lighting units

- Fire warning / sprinkler systems
- Waste management
- Electronic wiring (*e.g.*, power, internet, phone)

Many of these components are very technologically advanced and constantly under research. In fact, some components are becoming "smart" — they are starting to think and react. For example, advanced elevator systems for high rise buildings have algorithms to determine the most efficient path to transport occupants. The elevator may stop selectively (instead of making all possible stops) depending on the destinations of occupants inside of the elevator and the number of occupants waiting for elevator.

Another example of smart building technologies is a smart structure, which is a focus of this dissertation. Smart structures have been an ongoing research topic since the 1960s. It has two major components: structural control (SC) and structural health monitoring (SHM). SC tries to control structural behavior, and to prevent or minimize structural damage under external forces (*e.g.*, strong winds and earthquakes). SHM, on the other hand, checks the integrity of the structure throughout its life cycle and after major events (*e.g.*, wind storms, earthquakes and fire). Other than identify unsafe structures, SHM systems can also locate structural damage and call for further investigations and repairs.

However, having smart building components alone does not make a building smart. A smart building also needs to efficiently integrate these smart components because some of them may have competing objectives. Another focus of the dissertation is to discuss current developments of smart structures and propose an example of smart buildings by integrating smart structures with another building system.

1.1.1 Structure Health Monitoring (SHM)

Structural health monitoring (SHM) aims to assess the health of structures in a systematic and automatic manner. The collapse of the Minnesota I35W bridge in 2007 showed engineers yet again the importance of detecting structural damage/deterioration accurately, promptly, and effectively. Given the countless structures that require periodic assessments, the current practice and reliance on human inspections are inefficient and error-prone. Moreover, most structural damage is hidden in building elements such as damaged beams above ceilings and damaged columns behind walls. Removing building elements to expose the hidden damage can be costly and wasteful since not all removals yield damage detection. In addition to continuous structural assessments, an automatic SHM system can respond to emergencies when the safety of the structure must be assessed immediately for an evacuation decision.

The biggest challenges of SHM are the accuracy of structural assessments and cost of installation. No building developers would invest in SHM if it cannot accurately detect and localize damage, especially when such systems require hundreds or thousands of sensors that are costly to install. Damage assessment can be affected by many factors such as measurement noise, modeling error, uncertainty in the structure, and environmental changes (*e.g.*, temperature). This dissertation looks to improve SHM qualities and reduce the installation cost of SHM using wireless sensor networks.

1.1.2 Structure Control

Structural control (SC), which first emerged in the 1970s, aims to prevent structural damage by reacting to external forces the structure experiences. Dampers and base isolators are two major examples of SC to reduce structural vibration. A structure system is the most important building component that supports the entire building and thus ensures the safety of the occupants. There are two key design considerations in structural designs — vertical and lateral loads. Vertical loads are mostly caused by gravity and, therefore, remain generally constant during the life cycle of buildings. In contrast, lateral loads can be caused by winds, ground motions, etc. These events are constantly changing and sometimes unpredictable. Ground motions of different characteristics can have quite different effects on the same structure. Moreover, winds and ground motions often are better buffered by structures with different structural characteristics. Structural control offers a good solution to this problem, controlling the behavior of structures in response to the external forces.

From the Northridge Earthquake in 1994 to the collapse of the World Trade Center in 2001, the effect of structural failure can be widespread and deadly. Although natural and man-made disasters happen rarely, their consequences cannot be ignored. The cost of repairing/rebuilding and the immeasurable cost of human lives are two very valid reasons that structural designs must account for these disasters.

Similar to SHM, SC also lacks investments from building developers. Although there has been increasing interest in the technology of building designs, SC systems exist in a very small percentage of the buildings constructed. Soong and Spencer (2002) stated that there were only 41 full-scale implementations of "active" SC systems with 40 of them in Asia (mostly Japan) and one in America (active SC systems exclude traditional passive SC systems such as the John Hancock Tower in Boston — the first building with tuned mass dampers). There are two key reasons behind the lack of buildings with SC: unfamiliarity and cost. Most structural engineers are aware of such technology but few are knowledgeable enough to incorporate it into their designs; even fewer developers and architects are familiar with SC to invest in the technology. SC can also be costly and its benefits are not fully appreciated due to the unfamiliarity. There are many little known benefits of SC such as smaller and less costly structural systems/elements because SC reduces the forces that a structural system has to withstand and prevents the loss of productivity when a building is under repair.

1.2 Environmental Control

If structural systems are comparable to the backbones of buildings, environmental control (EC) systems are analogous to the vital organs that regulate the homeostasis of the buildings. The productivity of the buildings' occupancy is directly related to the ability of EC systems to maintain a comfort zone for the occupants. For example, EC systems must maintain comfortable temperatures and humidity while providing sufficient lighting, clean and hot water, and fresh air. Sufficiency is the basic requirement for EC systems; performance of the system is mostly measured by building integration, energy efficiency and ease of maintenance. If the EC system can fit seamlessly into the rest of the building, compromises or changes can be minimal in the building designs. An energy efficient EC system saves building operation cost, making the building sustainable. This dissertation focuses on the building integration and energy efficiency aspects of EC systems.

In comparison to SHM and SC, EC is a more mature building technology. All large buildings require elaborate systems to control lighting and human comfort while conserving energy cost. Cost is also a major concern for EC, originating from two sources: initial (installation) cost and annual energy cost. Initial cost is based on the system design and is a part of the construction cost. Annual energy cost is directly related to the performance of the designed system and is a part of the building operation cost. Since the construction cost is much higher than the annual building operation cost, a less effective and cheaper EC system is often chosen to cut the construction cost. However, this practice is shortsighted because the long term savings of a better performing system can surpass the extra initial cost after years of operations. Although this logic is simple, budgeting politics and the fact that different groups may handle the two costs make it difficult to build a more expensive EC system with better performance.

1.3 Integrated Systems

SHM, SC and EC all suffer from a lack of investment during building design and construction phases. This dissertation attempts to address this problem by creating synergy through integrating the three systems in buildings. By attaching the less known technologies of SHM and SC to EC, builders (developers, architects, engineers, etc.) will not dismiss the combined technology as easily. Additionally, the combined structural and environmental benefits can attract interests from both researchers and builders, while the cost can be reduced by sharing the synergy between the two control systems. The initial cost is now owed to both the structural and environmental aspects of the building. And since structural safety directly affects occupants' safety, builders cannot easily sacrifice the performance of the combined control system to cut the construction cost. Nonetheless, this thesis does not focus on cost analysis of the combined SC and EC system. Instead, it explores the possible synergy of the combined systems to make such integration worthwhile.

A system that integrates SHM, SC and EC is proposed in this dissertation — the shading fin mass damper system[1]. The proposed system combines both SC and EC by using shading fins as mass dampers. The fins block sunlight and reduce excessive heat gain while they dissipate energy from large building vibrations. In addition to SC and EC, the actuators controlling the fin movements can be used to excite the structure and the resulting structural responses are useful for SHM. More explanation of the synergy system will be discussed in Chapter 4.

Chapter 2 discusses the background of SHM, structural, environmental and integrated controls. Chapter 3 discusses new research in SHM on topics such as global and local vibration techniques and algorithms, wireless sensor networks, and wave propagation. Chapter 4 addresses the synergy of SHM, SC and EC though a proposed integrated system of shading fin mass dampers. Lastly, Chapter 5 summarizes the findings and impact of this dissertation and suggests future work.

[1] A part of this dissertation is a continuation of the author's thesis from the Master of Building Science program in USC School of Architecture and therefore the dissertation contains materials from the master thesis.

Chapter 2 – Background of Structural Health Monitoring, Structural Control and Environmental Control

This chapter gives a brief background of structural health monitoring (SHM), structural control (SC) and environmental control (EC). SHM and SC are components of smart structures while EC is an architectural system intended to integrate with smart structures to move toward creating smart buildings. In SHM, focuses are on vibration and wave propagation damage detection techniques. For SC, there are base isolation systems, passive energy dissipation systems and active/semiactive systems. EC systems are categorized into passive and active systems.

2.1 Structural Health Monitoring (SHM)

The goal of SHM is to identify damage through measurements from healthy and damaged structures. Changes in these measurements can be caused by many factors such as measurement noise, changes of environment (*e.g.*, temperature), structural damage, etc. From these changes, SHM hopes to detect damage in the structures. This is essentially a pattern recognition problem between two classes of the system: healthy and damaged structures. There are many different SHM techniques under research, but this dissertation focuses on two types: damage detection through global vibration measurements and through wave propagation. For details on other SHM techniques and SHM generally, the reader is referred to literature reviews by Doebling et al. (1998a, 1998b) and Sohn et al. (2003).

2.1.1 Global Vibration Damage Detection

Vibration testing usually involves two types — forced and ambient vibrations. In forced vibration, actuators apply forces on the building to cause vibration. Sensors then measure the building movements to identify damage. Shakers and impact hammers are typically used for harmonic and impact excitations, respectively. In ambient vibration, building movement is caused by surrounding activities such as wind, nearby traffic, mechanical operation within the building, etc. All buildings experience ambient vibration constantly. The advantage of ambient vibration over forced vibration is that the former does not artificially affect any building operation; forced vibration causes larger movements that may interference with building operations. However, because of the small movements by ambient vibration, sensors need to be more sensitive to measurement noise.

2.1.2 Wave Propagation Damage Detection

Wave propagation damage detection uses the propagation and reflection of high frequency (ultrasonic) waves in a medium. The disturbances in the wave field can help detect damage or flaws in the medium. This damage detection technique is highly localized since the signal of the wave weakens as it moves away from the wave source. Wave propagation or ultrasonic damage detection is well established especially in the aerospace and mechanical engineering communities and has begun to attract attention for civil structures. For more details on the technology, the reader is referred to the review paper by Giurgiutiu and Cuc (2005).

2.1.3 Wireless SHM

A large civil structure may require thousands or ten of thousands of sensors for SHM purposes to detect and localize structural damage. Existing wired data acquisition systems of such scale are likely too costly for many developers to consider (Straser and Kiremidjian, 1998). Recent work has demonstrated the feasibility of continuous structural data collection using an inexpensive wireless sensor network (Lynch and Loh, 2006). Although a wireless sensor network is able to cut the wiring cost, it comes with two major side effects — energy and bandwidth constraints. Unlike wired sensors, wireless sensors are subject to energy limitation because they rely on an onboard battery as an energy source. Bandwidth is the capacity of data transmittable in the communication channel, and it is a main concern for all types of communication channels. However, wireless channels typically have lower bandwidth compared to wired channels because wireless communication lacks a dedicated medium where transfer rate and data delivery are more reliable. Therefore, bandwidth becomes a larger concern for wireless sensor networks. A simple analogy of energy and bandwidth constraints between wired and wireless sensors is the comparison of landline telephones and early generations of cellular phones (low battery and bad signal).

2.2 Structural Control (SC)

SC prevents structural damage by reducing building vibration induced by natural and man-made hazards. There are three key SC systems: base isolation systems, passive energy dissipation systems and active/semiactive systems. The following sections explain briefly and offer some examples of these systems. For more details regarding SC systems, the reader is referred to the review papers by Soong and Spencer (2002) and by Housner *et al.* (1997).

2.2.1 Base Isolation System

A base isolation system is considered to be the most mature system of the three SC types. There are more buildings constructed with base isolators than other SC systems. The system isolates the building from its foundation during strong motions such that most of the relative motion is in the base, instead of the superstructure (Figure 2.1). The superstructure of the building experiences less motion and, therefore, a decreased likelihood of damage. The challenge of the base isolation system is the special connection between the foundation and the structure above. The connection must allow lateral movements while transferring the weight vertically from the structure to the foundation. Moreover, the lateral movements must be restricted and damped out in such a way that the building is not "sliding off" the foundation. Additionally, while connections across the isolation layer (e.g., utility lines, plumbing, etc.) use flexible components, the isolator motion is limited by these connections. There are several types of base isolators such as elastomeric bearings, lead rubber bearings, and sliding friction pendulum bearings.

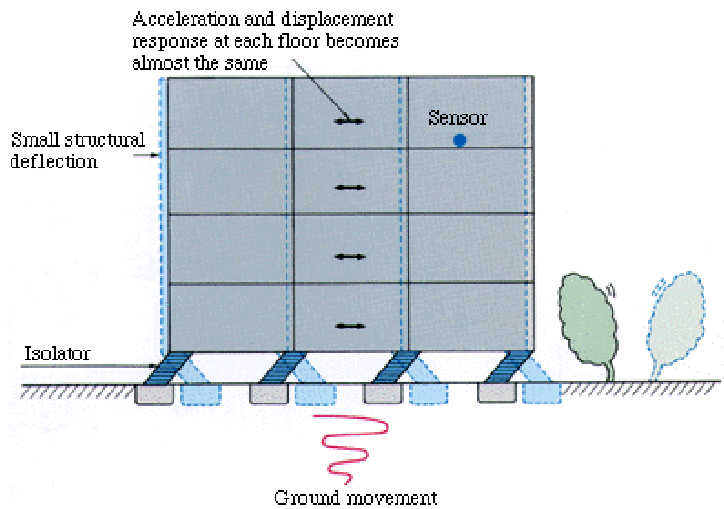

Figure 2.1: Base isolator diagram (Takenaka Corp. 2001)

2.2.2 Passive Energy Dissipation

In general, passive energy dissipation (PED) systems use dampers to dissipate energy from excited structures to reduce vibrations. These dampers mostly operate on the dissipating nature of friction, metal yielding, phase transformation in metals, viscoelastic (VE) solids or fluid, and fluid orificing. The following are some of the well known examples:

- Metallic dampers

- Friction dampers
- VE dampers
- Viscous fluid dampers
- Tuned mass dampers
- Tuned liquid dampers

Of all the PED systems mentioned, mass dampers are most utilized, with the first application in the John Hancock Tower (1976) at Boston. A mass damper is a secondary mass, attached to a (usually much larger) primary mass, to affect the dynamic response of the primary mass. The tuned mass damper (TMD) was first suggested by Frahm in 1909 (Den Hartog, 1956) and later studied by Lin (1967), Wirsching and Campbell (1974) and many others to reduce vibration of the primary system by tuning the TMD stiffness and damping coefficients to specific natural frequencies of the primary system. The greatest challenge of PED systems is that their passive nature limits their applicability to different types of external forces that excite the structures. For example, TMDs are ineffective at frequencies other than the design range.

2.2.2.1 Multiple Mass Damper System

Since the proposed shading fin mass damper (SFMD) system employs a type of a multiple tuned mass damper (MTMD) system, this section briefly introduces the MTMD. The MTMD was first proposed by Igusa and Xu (1994) in the early 1990s to compensate for the sensitivity of a single TMD to the uncertain natural frequencies of the building system. The MTMD was later extensively studied by Yamaguchi and Harnpornchai (1993), Abe and Fujino (1994), and Kareem and Kline (1995). However, the MTMD in these 1990s studies concentrates the multiple dampers in one floor in contrast with the SFMD herein which has dampers on every floor. The shading fin function would require the dampers to be distributed along the height of the building (dampers on all floors). Figure 2.2 illustrates the difference between the single TMD and the two types of MTMDs. Recently, Chen and Wu (2001, 2003) studied a MTMD system with TMDs placed in multiple floors on a 6 story simulation model and a 3 story, 1/4 scaled experimental building model. They showed that MTMDs can effectively reduce seismic responses.

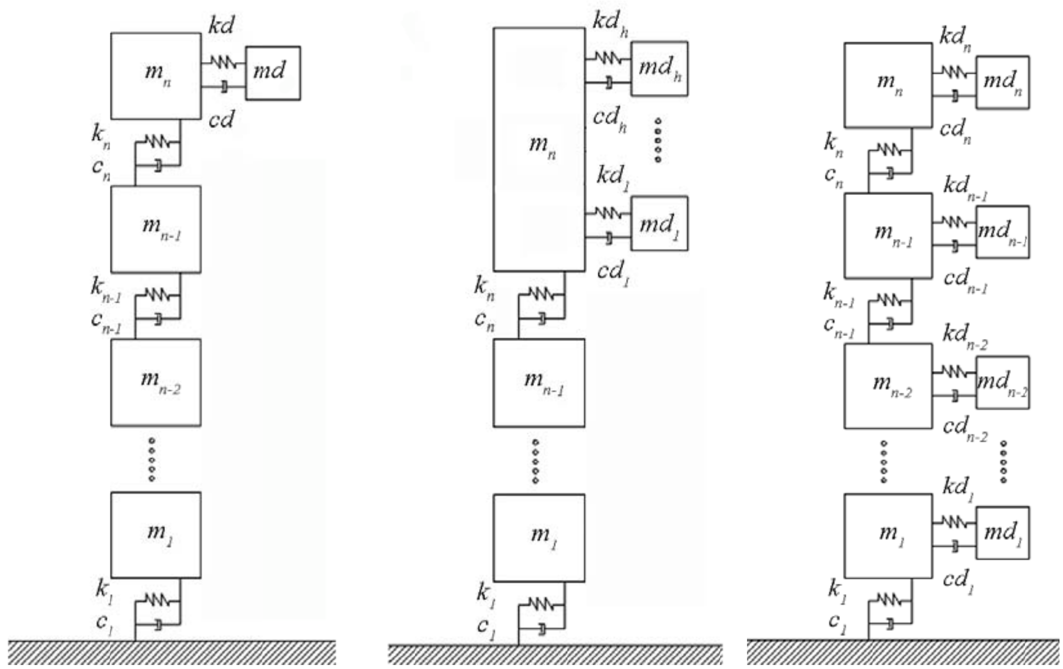

Figure 2.2: Single TMD, MTMD, and MTMD distributed along the building height

2.2.3 Active and Semiactive Control

Unlike passive systems, active and semiactive systems are designed to adapt to various kinds of excitations. Active control uses actuators to apply forces on the structure to counteract external forces. Examples include active bracing systems and active mass drivers. Theoretically, active control can counter all excitation and keep the structural vibration to a minimum. However, to achieve such an ideal result, the system often would require energy too great to be practical, and perfect actuators and noiseless sensors throughout the structure. Semiactive control addresses such impracticalities by uniting active and passive control systems. Semiactive systems are essentially PED systems with controllable parameters, such as stiffness and damping. By controlling PED system parameters according to structural conditions, semiactive systems can adapt to various kinds of excitations. Additionally, since semiactive control does not directly use energy to restrict structural motion, it works with limited energy requirements. Some examples of semiactive systems are variable stiffness or damping systems, and magnetorheological (MR) dampers. Greater details of the active and semiactive systems will be discussed in Chapter 4 for the proposed Shading Fin Mass Damper system.

2.3 Environmental Control (EC)

Besides the structure, the environmental control (EC) system is also an important component in a building. EC maintains the productivity of the building occupants by providing sufficient human comfort in areas such as lighting, humidity and temperature. Well-designed EC systems also aim to provide services under minimal energy cost. The following sections briefly describe some examples of EC systems by separating them into passive and active systems.

2.3.1 Passive Systems

Passive EC systems require little or no input energy from man-made sources. Some examples include:

- *Natural ventilation* – aided by natural air flow, ventilation cools and brings fresh air into spaces. Openings such as windows, doors and vents allow air movement between exterior and interior spaces. There are two types of natural circulation techniques — wind-induced cross ventilation and gravity or convection ventilation. Cross ventilation places openings carefully to exploit local wind patterns while gravity ventilation draws cool air from lower inlets by letting the warm air out through higher outlets when the outside air is cooler than the upper vent inside air.
- *Thermal mass* – large masses such as masonry walls trap heat during day-time and release heat slowly throughout the rest of the day. One advantage of a thermal mass is that the space can be heated for a prolonged period of time (*e.g.*, after sunset). Also, the temperature increase is less intense with thermal masses, preventing overheating from direct sunlight. The main disadvantage

is the uncontrollability of the heat stored. It takes a long time to heat up spaces and it is difficult to stop heat gain even when the spaces are warm enough. In addition to temperature increase, thermal masses can also be used for cooling when the masses are colder than the surrounding temperature.

- *Sunspace* – attached space that is heated directly by the sun and transfers the heat to connecting rooms. Unlike the thermal mass, sunspace can quickly increase the temperature in the attached space but it also cause large temperature fluctuations. Another disadvantage is that sunspace does not store heat to prolong temperature increase.
- *Shading devices* – overhangs and fins that block portions of direct sunlight. Not only can solar heat gain be blocked, glazing can also be controlled with shading devices. Nonetheless, a compromise must be made when only one of solar heat gain or daylighting is needed and the other is undesired. Site condition and orientation also play major roles in designing shading devices. Overhangs are typically placed in the south façade while vertical fins are typically placed in the east and west façades to deal with sunlight coming in from different angles throughout the day. Shading fins are discussed further in Chapter 4 for the Shading Fin Mass Damper system.
- *Insulation* – separation between interior and exterior of the building that prevents quick heat gain and loss. A well insulated space can decrease the amount of heat gain in hot weather and heat loss in cold weather.

2.3.2 Active Systems

Active EC systems, on the other hand, usually require constant energy input such as electricity and natural gas. Some examples include:

- *Refrigeration* – a vapor-compression cycle that transfers heat between locations. Many air-conditioning units use refrigeration to cool or heat air for buildings. The process involves compressing a refrigerant (gas or liquid depending on the temperature and pressure) such that it becomes warmer than outside air. The compressed/heated refrigerant then loses heat to the cooler outside air though a heat exchanger. After being cooled, the refrigerant is "decompressed" through an expansion valve, causing (typically) a change of phase from liquid to vapor due to the pressure drop, which results in dramatic drop in temperature. The resulting refrigerant is much colder than the refrigerant before compression and can be used to cool other mediums (air, water, etc.) before going through the compression refrigeration cycle again.
- *Chiller* – water chiller that cools water to supply other cooling units throughout the building. It uses a large amount of electricity and a compression refrigeration cycle to chill water. Water chillers are more suitable for large buildings because of the large capacity. They can be categorized as reciprocating, centrifugal, rotary and absorption chillers ranging from 60 to 400 tons, where a "ton" is 12,000 Btu-hr.

- *Movable shading devices* – overhangs and fins that can adjust to block targeted portions of direct sunlight. This increases the effectiveness of the shading devices by balancing the need for solar heat gain and lighting according to the weather/sun orientation. More about movable shading fins is discussed in Chapter 4 for the proposed Shading Fin Mass Damper system.
- *Heating units* – use electricity, gas or other fuels to heat the building by warming a medium (air, water, etc.). The medium is then supplied to various parts of the building. A furnace is a typical type of heating unit that warms air using an electric or combustion heating chamber. Boilers are closed vessels that produce hot water or even steam. Heat pumps are very efficient heating units for mild climates since they, instead of producing heat, transfer heat by compression refrigeration cycles. They are also easily scalable, ideal for buildings unsuitable for central systems. Heating coils are one of easiest ways to heat air. Transferred through air ducts, air is heated before it is supplied to building areas.
- *Ice storage* – cools or freezes water (or other media) at off-peak hours (nights) to be used to cool the building throughout the day. By cooling water at night, energy cost is decreased while the colder temperature can help cooling more efficiently. A storage system is needed and its size is proportional to the building size.

- *Air system* – air-handling system that transports air throughout the building to complement existing heating/cooling, humidifying/dehumidifying, and filtering units. Fresh air is drawn into the building by inlets and, after conditioning, is supplied to the building. Return air from the building is then either reconditioned or exhausted through outlets, usually in some percentage ratio. Fans and ducts are key components of air systems.

For more details and other EC systems, readers are referred to the many text books published on this subject, such as Bradshaw's (2006) *The Building Environment: Active and Passive Control Systems.*

Chapter 3 – Structural Health Monitoring

Structural health monitoring (SHM) tries to identify damage through measurements from healthy and damaged structures in an automatic manner. Using algorithms, SHM converts measurements into an assessment of the structural integrity. This chapter discusses approaches and issues of collecting measurements with sensors and the algorithms and techniques in estimating damage in the structure.

3.1 Introduction

There are several SHM issues covered in the rest of this chapter. For vibration based SHM, there are global and local excitations that aim to assess the state of the structure globally and locally respectively. In global excitations, the entire structure undergoes motion while measurements from various parts of the structure are used to assess the health of the structure. In local excitations, the vibrations are smaller and typically localized to a small region of the structure where damage is suspected. Using the combination of global and local excitations, engineers can detect damage in susceptible regions of the structure and further closely examine these regions. Several concerns of the global excitation method are addressed in this chapter, such as system identification in multiple directions and using wireless sensor networks for SHM purposes. The last part of the chapter discusses detecting damage on a plate with local excitation and wave propagation.

Many existing algorithms of structural stiffness estimation under the global excitation are derived and tested for systems in single direction (*e.g.*, *x*-direction) and then adopted or expanded to multiple directions (*i.e.*, *x*, *y* directions and rotations). By assuming a structure and its damage is symmetric in the *x* and *y* directions, the structural motions are kept in the same direction the structure is excited. This type of structure and motions allows decoupling of the *x* and *y* directions, making system identification relatively simple. Nonetheless, structures are rarely symmetric (due to design and/or construction considerations) and damage is unexpected and most certainly non-symmetric to the structure. The coupling effect of multiple directions can throw off the accuracy of some system identification algorithms or techniques. One of the following sections attempts to improve an existing method of stiffness estimation that is fairly accurate in a single direction but inaccurate in multiple directions.

Another section in this chapter addresses the emerging technology of wireless sensor networks (WSN) in SHM. Wireless sensors can reduce the installation cost of an extensive sensor network by eliminating the need of wiring. They are also more suitable for deploying sensor networks on existing building without substantially altering the existing wiring systems. However, without dedicated media (wires) for transmitting power and data, wireless sensors are constrained by the amount of power and the bandwidth they can sustain. This section of the chapter deals with these drawbacks by (1) reducing the amount of data transmitted by processing SHM data locally at the sensors and (2) avoiding unnecessary sensor energy consumption with an optimal sensor placements suitable for SHM and WSN. These approaches can prolong the life of a WSN, increasing the usability of such a network for SHM that provides service throughout the long life cycle of a building.

The last section of this chapter studies damage detection by observing wave propagation in a plate with local excitations. Ultrasonic waves are typically used as the excitation and damage can be detected by comparing the waves propagating in the undamaged and damaged plates. This section explains and shows the details how damage can be identified using sensors that can apply forces and measure the wave propagation on the plate. The effect of sensor placement on damage detection is also analyzed.

3.2 Global Excitation on Shear Structures

Many existing damage detection techniques detect changes in the stiffness in structural members based on the structural responses collected from various locations in the structure. This section focuses on using modal parameters of the structure computed from structural responses to estimate the stiffness of the structure. Building on the one-directional analysis of the stiffness estimations, a three-directional analysis is studied to further localize damage for a simple shear type structure. A comparison between the one-directional and the three-directional analysis shows that the one-directional method is more reliable. A modification is then proposed to improve the three-directional stiffness estimation.

3.2.1 Modal Parameters and Eigensystem Realization Algorithm (ERA)

From the measured vibration of a structure, engineers can detect damage through first estimating the modal parameters of the structure based on the measurements. There exists a significant breadth of literature for damage detection techniques based on modal parameter extraction. Additionally, there are many methods for modal parameter extraction. For example, the Eigensystem Realization Algorithm (ERA) constructs a state-space representation for an entire structure using impulse response measurements, which can then be used to estimate its modes. Garibaldi *et al.* (1999) used canonical variate analysis (CVA) to extract mode shapes of the structures. The following section explains briefly the concept behind ERA.

ERA was developed by Juang and Pappa (1985) and uses the singular value decomposition of the Hankel matrix,

$$\mathbf{H}(k-1)=\begin{bmatrix} \mathbf{Y}(k) & \mathbf{Y}(k+1) & \cdots & \mathbf{Y}(k+p) \\ \mathbf{Y}(k+1) & \mathbf{Y}(k+2) & \cdots & \mathbf{Y}(k+p+1) \\ \vdots & \vdots & \ddots & \vdots \\ \mathbf{Y}(k+r) & \mathbf{Y}(k+r+1) & \cdots & \mathbf{Y}(k+p+r) \end{bmatrix} \tag{3.1}$$

where $\mathbf{Y}(k)$ is the pulse response matrix such that $Y_{ij}(k)$ is the impulse response at the k^{th} time instant collected at the i^{th} location due to an impulsive excitation at the j^{th} location in the structure. The singular value decomposition of $\mathbf{H}(0)$ is denoted by

$$\mathbf{H}(0) = \mathbf{PDQ}^{\mathbf{T}}\ . \tag{3.2}$$

Here, **P** and $\mathbf{Q}^{\mathrm{T}}$ are unitary matrices formed by the left and right singular vectors respectively and **D** is the diagonal matrix formed by the singular values. Singular vectors corresponding to "small" singular values are attributed to noise and the reduced order matrices $\mathbf{P}_n$, $\mathbf{Q}_n$ and $\mathbf{D}_n$, are generated by using only the singular vectors corresponding to the "large" singular values. The linear system parameters corresponding to the reduced order system can now be estimated using the equations:

$$\mathbf{A} = \mathbf{D}_n^{-1/2}\ \mathbf{P}_n^{\mathrm{T}}\ \mathbf{H}(1)\ \mathbf{Q}_n\ \mathbf{D}_n^{-1/2} \tag{3.3}$$

$$\mathbf{B} = \mathbf{D}_n^{-1/2}\ \mathbf{Q}_n^{\mathrm{T}}\ \mathbf{E}_m \tag{3.4}$$

$$\mathbf{C} = \mathbf{E}_n^{\mathrm{T}}\ \mathbf{P}_n\ \mathbf{D}_n^{-1/2} \tag{3.5}$$

where $\mathbf{E}_p^{\mathrm{T}} = [\ \mathbf{I}_p\ \ \mathbf{0}\ ]$ with $\mathbf{I}_p$ being the identity matrix of order p. The mode shapes of the structure correspond to the columns in the matrix $\mathbf{V} = \mathbf{C}\ \mathbf{\Phi}$, where $\mathbf{\Phi}$ contains the eigenvectors of **A**. The modal frequencies of the structure correspond to the eigenvalues of **A**.

3.2.2 Least Squares Estimate (One-Directional)

After finding the modal parameters of the structure, the structural stiffness can be estimated using a least squares estimate (Caicedo *et al.*, 2001) that is summarized as follows. A one-directional N-story shear structure has mass and stiffness matrices

$$\mathbf{M} = \begin{bmatrix} m_1 & 0 & \cdots & 0 \\ 0 & m_2 & \ddots & \vdots \\ \vdots & \ddots & \ddots & 0 \\ 0 & \cdots & 0 & m_n \end{bmatrix}, \quad \mathbf{K} = \begin{bmatrix} k_1+k_2 & -k_2 & 0 & \cdots & 0 \\ -k_2 & k_2+k_3 & -k_3 & & \\ \vdots & \ddots & \ddots & \ddots & \vdots \\ & & -k_{n-1} & k_{n-1}+k_n & -k_n \\ 0 & \cdots & 0 & -k_n & k_n \end{bmatrix} \tag{3.6}$$

By rearranging the eigenvalue problem (Chopra, 1995),

$$(\mathbf{K} - \lambda_j \mathbf{M})\,\mathbf{\Phi}_j = 0 \quad \text{or} \quad \mathbf{K}\,\mathbf{\Phi}_j = \lambda_j \mathbf{M}\,\mathbf{\Phi}_j \tag{3.7}$$

with λ_j and $\mathbf{\Phi}_j$ being the j^{th} eigenvalue and eigenvector of the structure, respectively, (3.7) becomes

$$\begin{bmatrix} \phi_{1,j} & \phi_{1,j}-\phi_{2,j} & 0 & \cdots & 0 \\ 0 & \phi_{2,j}-\phi_{1,j} & \phi_{2,j}-\phi_{3,j} & & \\ \vdots & \ddots & \ddots & \ddots & \vdots \\ & & & \phi_{n-1,j}-\phi_{n-2,j} & \phi_{n-1,j}-\phi_{n,j} \\ 0 & & \cdots & 0 & \phi_{n,j}-\phi_{n-1,j} \end{bmatrix} \begin{bmatrix} k_1 \\ k_2 \\ \vdots \\ k_{n-1} \\ k_n \end{bmatrix} = \begin{bmatrix} \phi_{1,j}\lambda_j m_1 \\ \phi_{2,j}\lambda_j m_2 \\ \vdots \\ \phi_{n-1,j}\lambda_j m_{n-1} \\ \phi_{n,j}\lambda_j m_n \end{bmatrix} \tag{3.8}$$

where $\phi_{i,j}$ is the i^{th} element of $\mathbf{\Phi}_j$. Knowing the mass matrix $\mathbf{M}$ (or m_i's) of the structure, the stiffness can be solved in a least squares sense, for any particular eigenvalue and eigenvector by pre-multiply both sides of (3.8) with the pseudo inverse of the matrix of ϕ values.

Using this least squares approach, the overall structural stiffness can be estimated from the eigenvalues and corresponding eigenvectors computed by ERA or other modal parameter extraction techniques.

3.2.2.1 Least Squares Stiffness Estimate (Three-Directional)

The previous section deals with one-directional analysis; this section expands the least square estimates to three-directional (x, y and θ). Consider the following diagram

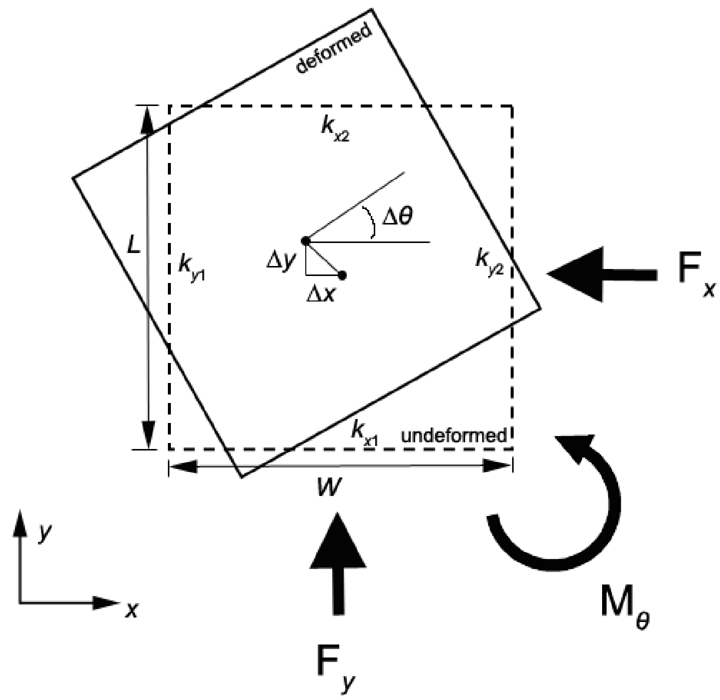

Figure 3.1: Floor Diagram

where W and L are the width and length of a floor respectively with k_{x1}, k_{x2}, k_{y1} and k_{y2} are stiffness in x and y directions for different faces of the floor. F_x, F_y and M_θ are external forces and moment in x, y and θ directions, respectively while Δx, Δy and $\Delta\theta$ are displacements in the indicated directions due to F_x, F_y and M_θ. The static equations can be formed as

$$\begin{bmatrix} F_x \\ F_y \\ M_\theta \end{bmatrix} = \begin{bmatrix} k_{x1}+k_{x2} & 0 & (k_{x1}-k_{x2})\dfrac{W}{2} \\ 0 & k_{y1}+k_{y2} & (k_{y1}-k_{y2})\dfrac{L}{2} \\ (k_{x1}-k_{x2})\dfrac{W}{2} & (k_{y1}-k_{y2})\dfrac{L}{2} & 0 \end{bmatrix} \begin{bmatrix} \Delta x \\ \Delta y \\ \Delta\theta \end{bmatrix} \tag{3.9}$$

or $$\mathbf{F}_i = \mathbf{K}_i\,\Delta_i$$

where i indicates the floor number. The individual stiffness can be estimated following similar analysis from the one-directional study by using (3.8) with the stiffness matrix of the i^{th} floor in (3.9) and the following mass matrix of the i^{th} floor,

$$\mathbf{M}_i = \begin{bmatrix} m_i & 0 & 0 \\ 0 & m_i & 0 \\ 0 & 0 & I_i \end{bmatrix} \tag{3.10}$$

where I_i is the rotational inertia for the i^{th} floor. This three-directional approach can detect stiffness loss not only in which story but also which face of the story. Such information is useful to further localize damage for structures.

3.2.3 Simulation Comparison

A simulated 4-story structure is studied to test the three-directional stiffness estimate (details of the structure are explained in Section 3.3.2.1 and shown in Figure 3.5). Asymmetric damage (*i.e.*, different stiffness loss in the four faces of the stories) is introduced, which causes some rotation in the structure. Noise is also applied to the simulated measurements to reflect realistic conditions (Figure 3.2).

Table 3.1 shows the result from two one-directional analyses in the x and y directions with separate impulse forces in the corresponding direction. The stiffness is computed with ERA and the least squares estimation. Table 3.2 is from a three-directional analysis with three concurrent impulses in x, y and θ directions. ERA is also performed once on the responses for this analysis. The least squares estimation is then used with the estimated model parameters from ERA. The error is significantly smaller in Table 3.1 compared to Table 3.2, implying the damage detection technique is more robust in one-directional analysis.

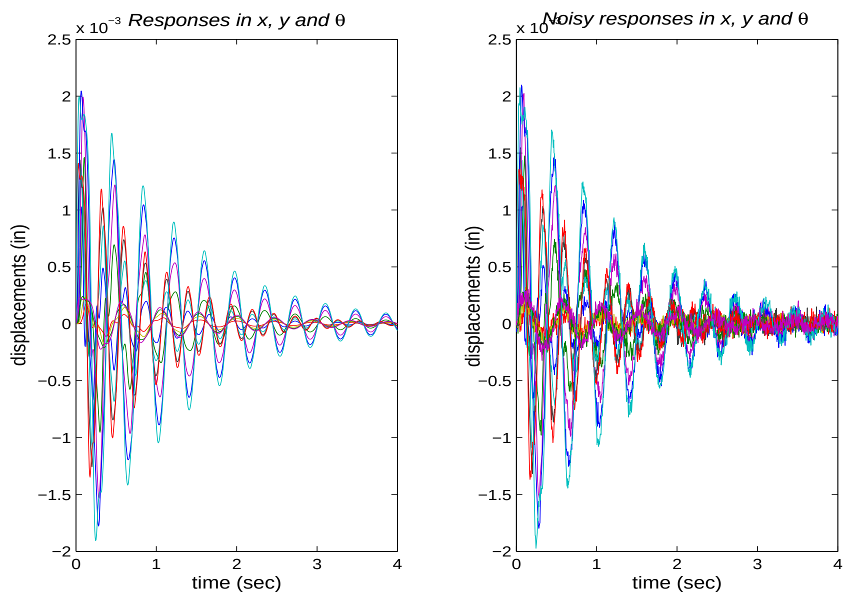

Figure 3.2: Comparison between responses with and without noise.

3.2.4 Improving Stiffness Estimation

As can be observed from Table 3.1 and 3.2, the stiffness estimation is more accurate in the one-directional analysis. Moreover, the stiffness estimation disagrees between the one-directional and three-directional analysis. For the actual stiffness of the i^{th} story, the following equation should hold:

$$k_x(i) = k_x(i,1) + k_x(i,2). \tag{3.11}$$

where $k_x(i)$ is the overall stiffness in the x-direction in the i^{th} story, and $k_x(i,1)$ and $k_x(i,2)$ are stiffnesses in the x-direction for face 1 and 2, respectively. The y-direction equation is similar to (3.11). However, for most stories, the stiffness estimation for face 1 and face 2 (from the three-directional analysis) do not add up to be the corresponding overall estimated stiffness (from the one-directional analysis). Despite the inaccuracies, the three-direction analysis is able to identify the weaker faces for most stories, providing valuable information to localize damage within the stories. Additionally, by assuming (3.11) holds true even for estimated stiffness and using the results from the one-directional analysis, the three-directional analysis can be improved in the following way:

$$\widetilde{k}_x(i,j) = k_x(i,j)\frac{k_x(i)}{k_x(i,1) + k_x(i,2)} \tag{3.12}$$

where $\widetilde{k}_x(i,j)$ is the modified stiffness in the x-direction for face j (j = 1, 2) of story i. The y-direction stiffness can be modified in the similar manner. (3.12) essentially combines the one-directional and the three-directional analyses by normalizing the values of $k_x(i,j)$, for j = 1, 2, such that they would add up to $k_x(i)$.

Table 3.3 shows the modified results using (3.12) with improvement in error compared to Table 3.2. Damage now can be detected and localized using information from Tables 3.1 and 3.3. The result in Table 3.1 accurately identifies damaged stories in the *x* and *y* directions. Then, for each damaged story, Table 3.3 can further localize the damage to the particular face(s) of the story.

one-directional estimate				
floor	direction	stiffness remain	actual	**error (diff)**
1	x	92.39%	92.50%	**0.11%**
2	x	92.56%	92.50%	**0.06%**
3	x	92.73%	92.50%	**0.23%**
4	x	98.80%	100.00%	**1.20%**
1	y	85.76%	86.12%	**0.36%**
2	y	97.43%	100.00%	**2.57%**
3	y	94.28%	92.50%	**1.78%**
4	y	100.40%	100.00%	**0.40%**

Table 3.1: One-directional analysis

three-directional estimate				
floor	direction	stiffness remain	actual	**error (diff)**
1	x (face 1)	70.58%	85.00%	**14.42%**
	x (face 2)	81.05%	100.00%	**18.95%**
	y (face 1)	114.10%	100.00%	**14.10%**
	y (face 2)	64.93%	72.25%	**7.32%**
2	x (face 1)	70.85%	85.00%	**14.15%**
	x (face 2)	58.84%	100.00%	**41.16%**
	y (face 1)	85.35%	100.00%	**14.65%**
	y (face 2)	65.70%	100.00%	**34.31%**
3	x (face 1)	59.54%	85.00%	**25.46%**
	x (face 2)	91.33%	100.00%	**8.67%**
	y (face 1)	78.84%	100.00%	**21.16%**
	y (face 2)	70.66%	85.00%	**14.34%**
4	x (face 1)	90.63%	100.00%	**9.37%**
	x (face 2)	76.27%	100.00%	**23.73%**
	y (face 1)	90.91%	100.00%	**9.09%**
	y (face 2)	82.49%	100.00%	**17.51%**

Table 3.2: Three-directional analysis

three-directional estimate (modified)				
floor	direction	stiffness remain	actual	**error (diff)**
1	x (face 1)	86.52%	85.00%	**1.52%**
	x (face 2)	99.35%	100.00%	**0.65%**
	y (face 1)	114.46%	100.00%	**14.46%**
	y (face 2)	65.13%	72.25%	**7.12%**
2	x (face 1)	100.78%	85.00%	**15.78%**
	x (face 2)	83.69%	100.00%	**16.31%**
	y (face 1)	112.22%	100.00%	**12.22%**
	y (face 2)	86.38%	100.00%	**13.63%**
3	x (face 1)	75.10%	85.00%	**9.90%**
	x (face 2)	115.19%	100.00%	**15.19%**
	y (face 1)	98.32%	100.00%	**1.68%**
	y (face 2)	88.12%	85.00%	**3.12%**
4	x (face 1)	106.85%	100.00%	**6.85%**
	x (face 2)	89.93%	100.00%	**10.07%**
	y (face 1)	105.44%	100.00%	**5.44%**
	y (face 2)	95.67%	100.00%	**4.33%**

Table 3.3: Modified three-directional analysis

3.2.4.1 SHM Benchmark 120 DOF Example

To further test the stiffness estimate improvement using (3.12), the analytical model of the SHM Benchmark structure (Johnson *et al.*, 2000) is used (Figure 3.3). The finite element model has 120 degrees of freedom (DOF) while the three-directional least squares stiffness estimation uses a 12 DOF model (three directions × four floors). The goal of this study is to see if the improvement using (3.12) would remain even with modeling error. For testing, the fully braced structure is said to be the undamaged structure. Two damage patterns are tested with noise: Damage

Pattern 1 (all braces removed in floor 1 in both x and y directions) and Damage Pattern 3 (one brace removed in floor 1 in the y direction).

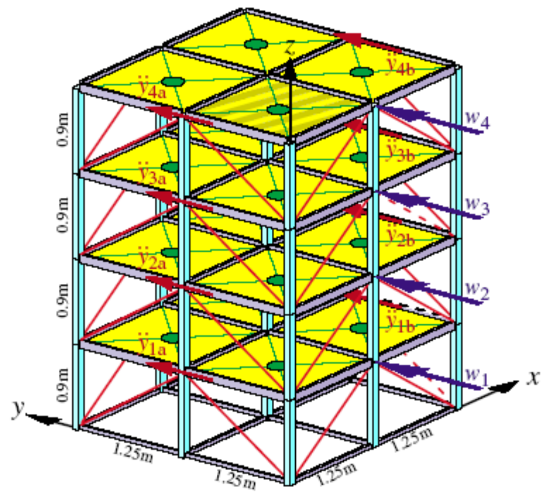

Figure 2. Diagram of analytical model. The w_i are excitations. The $\ddot{y}_{ij}$ are accelerometer measurements (the $\ddot{y}_{ic}$ and $\ddot{y}_{id}$ in the x-direction are omitted for clarity). The braces and floor beam drawn with dashed lines are ones damaged in damage patterns (*iii*)–(*v*).

Figure 3.3: SHM Benchmark (Johnson *et al.*, 2000)

Tables 3.4 and 3.5 show the results from the least squares stiffness estimation without and with modification (3.12) for Damage Patterns 1 and 3, respectively. In both damage patterns, the errors in stiffness estimation decrease, implying the improvement technique performs well even when modeling error is present.

one-directional estimate				
floor	direction	actual stiffness remain	estimate	**error (diff)**
1	x	54.78%	51.62%	**3.16%**
2	x	100.00%	99.90%	**0.10%**
3	x	100.00%	95.96%	**4.04%**
4	x	100.00%	100.33%	**0.33%**
1	y	29.01%	27.15%	**1.86%**
2	y	100.00%	101.15%	**1.15%**
3	y	100.00%	100.59%	**0.59%**
4	y	100.00%	98.15%	**1.85%**

			three-directional estimate		***modified three-directional estimate***	
floor	direction	actual stiffness remain	estimate	**error (diff)**	estimate	**error (diff)**
	x (face 1)	54.78%	43.58%	**11.20%**	52.04%	**2.74%**
	x (face 2)	54.78%	42.91%	**11.87%**	51.24%	**3.54%**
	y (face 1)	29.01%	17.47%	**11.54%**	27.55%	**1.46%**
1	y (face 2)	29.01%	16.96%	**12.05%**	26.74%	**2.27%**
	x (face 1)	100.00%	101.67%	**1.67%**	99.27%	**0.73%**
	x (face 2)	100.00%	102.99%	**2.99%**	100.56%	**0.56%**
	y (face 1)	100.00%	98.18%	**1.82%**	102.24%	**2.24%**
2	y (face 2)	100.00%	96.17%	**3.83%**	100.14%	**0.14%**
	x (face 1)	100.00%	95.85%	**4.15%**	96.09%	**3.91%**
	x (face 2)	100.00%	95.62%	**4.38%**	95.87%	**4.13%**
	y (face 1)	100.00%	104.22%	**4.22%**	99.65%	**0.35%**
3	y (face 2)	100.00%	106.18%	**6.18%**	101.53%	**1.53%**
	x (face 1)	100.00%	99.40%	**0.60%**	100.26%	**0.26%**
	x (face 2)	100.00%	99.59%	**0.41%**	100.45%	**0.45%**
	y (face 1)	100.00%	100.23%	**0.23%**	97.47%	**2.53%**
4	y (face 2)	100.00%	101.64%	**1.64%**	98.84%	**1.16%**

Table 3.4: Damage Pattern 1 (all braces removed in floor 1)

one-directional estimate				
floor	direction	actual stiffness remain	estimate	**error (diff)**
1	x	100.00%	99.99%	**0.01%**
2	x	100.00%	100.00%	**0.00%**
3	x	100.00%	100.00%	**0.00%**
4	x	100.00%	99.99%	**0.01%**
1	y	82.25%	79.62%	**2.63%**
2	y	100.00%	99.91%	**0.09%**
3	y	100.00%	99.92%	**0.08%**
4	y	100.00%	99.64%	**0.36%**

			three-directional estimate		***modified three-directional estimate***	
floor	direction	actual stiffness remain	estimate	**error (diff)**	estimate	**error (diff)**
	x (face 1)	100.00%	97.03%	**2.97%**	99.47%	**0.53%**
	x (face 2)	100.00%	98.08%	**1.92%**	100.55%	**0.55%**
	y (face 1)	64.51%	60.86%	**3.66%**	59.27%	**5.24%**
1	y (face 2)	100.00%	102.39%	**2.39%**	99.73%	**0.27%**
	x (face 1)	100.00%	106.01%	**6.01%**	100.07%	**0.07%**
	x (face 2)	100.00%	105.85%	**5.85%**	99.91%	**0.09%**
	y (face 1)	100.00%	91.03%	**8.97%**	99.90%	**0.10%**
2	y (face 2)	100.00%	91.04%	**8.96%**	99.91%	**0.09%**
	x (face 1)	100.00%	105.69%	**5.69%**	100.32%	**0.32%**
	x (face 2)	100.00%	105.01%	**5.01%**	99.68%	**0.32%**
	y (face 1)	100.00%	93.82%	**6.18%**	101.12%	**1.12%**
3	y (face 2)	100.00%	91.58%	**8.42%**	98.71%	**1.29%**
	x (face 1)	100.00%	102.07%	**2.07%**	99.87%	**0.13%**
	x (face 2)	100.00%	102.34%	**2.34%**	100.13%	**0.13%**
	y (face 1)	100.00%	96.34%	**3.67%**	99.23%	**0.77%**
4	y (face 2)	100.00%	97.14%	**2.86%**	100.05%	**0.05%**

Table 3.5: Damage Pattern 2 (one brace removed in floor 1 in the *y* direction)

3.3 Wireless SHM[2]

Wireless SHM networks are a new area in SHM research. This section examines the innovation behind wireless SHM and the challenges it faces. SHM of civil structures requires a large number of sensors throughout the structure to detect and localize structural damage. Wireless sensor networks (WNS) can help reduce installation cost by eliminating wiring expenditures, but they come with energy and bandwidth constraints. Relying on batteries and radio communication, WSNs are less capable compared to their wired counterparts in terms of energy consumption and data transmission. To successfully implement wireless SHM, a distributed algorithm recently developed by the USC SHM/ITR group is discussed in this section. The distributed algorithm can distribute processing requirement locally at the wireless sensor nodes to reduce the amount of data that must be sent over radio communication. Sensor placement is also studied to optimize the tradeoffs of the accuracy in SHM and the energy consumption in wireless sensors.

3.3.1 Wireless Sensor Constraints

The energy and bandwidth constraints of wireless sensor networks impose limitations on SHM. Many existing damage localization techniques detect changes in the stiffness in structural members based on the structural responses collected

---

[2] This work is in cooperation with Prof. Ramesh Govindan, Dr. Krishna K. Chintalapudi and Jeongyeup Paek, currently or formerly from the Embedded Networks Laboratory in the USC Computer Science Department.

from various locations in the structure. One approach to accommodate the energy and bandwidth constraints is distributed local processing. Instead of transmitting the raw data collected at the sensors, sensor nodes locally process the data and compute the necessary characteristics that can sufficiently describe the data collected for the specific application. Energy and bandwidth are conserved by transmitting only these characteristics (that are more compact than the raw data), whereas traditional SHM techniques would transmit all the structural responses (raw data) from sensors to a central node.

Straser and Kiremidjain (1998) first proposed a distributed algorithm for wireless SHM. Using the normalized Arias intensity, they estimated energy dissipated by the structure due to damage, using an algorithm that would run on the microcontrollers of wireless sensors. Lynch *et al.* (2003a) successfully embedded the Cooley-Tukey implementation of the fast Fourier transform (FFT) in a wireless sensing unit's computational core. The embedded FFT was to calculate the frequency response functions (FRFs) of the structure. The AR-ARX time series model was also proposed for embedding in wireless sensors for damage detection because of the model's decentralized nature and low computational resource requirement (Lynch *et al.,* 2003b). The AR-ARX model first fits an autoregressive (AR) time series model to the structural response data, and then fit a second autoregressive with exogenous input (ARX) time series model to the residual error of the AR model. The coefficients of the AR-ARX models are utilized as features for pattern recognition between damaged and undamaged structures. In other words, AR-ARX models of the undamaged structure serve as comparisons to AR-ARX models of the unknown (damaged or undamaged) structure (Sohn and Farrar, 2001). Recently, Gao *et al.* (2006) proposed a distributing strategy that divides sensors into "communities" that detect damage using locally measured information within each sensor community. The damage results are then communicated among the neighboring sensor communities and sent to a central station. Yuan *et al.* (2006) presented a parallel distributed SHM system using a multi-agent system that separates components of the overall system into agents with specific duties such as sensing, processing, fusion, coordinating, etc. Each agent processes local information while making the processed results available to other agents for cooperation. Lynch and Loh (2006) recently reviewed the state of the technology of wireless SHM and more details can be found in the review paper.

This following section discusses a recently developed SHM distributed algorithm that allows sensors to locally estimate the modal parameters (characteristics) of the structural responses such as phase, amplitude and frequency. The estimated modal parameters are then transmitted to the central node to help detect and localize damage. For long-lived SHM systems based on wireless sensor networks, scheduled forced excitation and distributed local processing are two desirable approaches to conserve energy and bandwidth. Figure 3.4 illustrates the difference between traditional SHM schemes that gather all structural responses before estimating the stiffness and the proposed SHM scheme that utilizes distributed local processing to cut radio communication for long-lived wireless sensor networks.

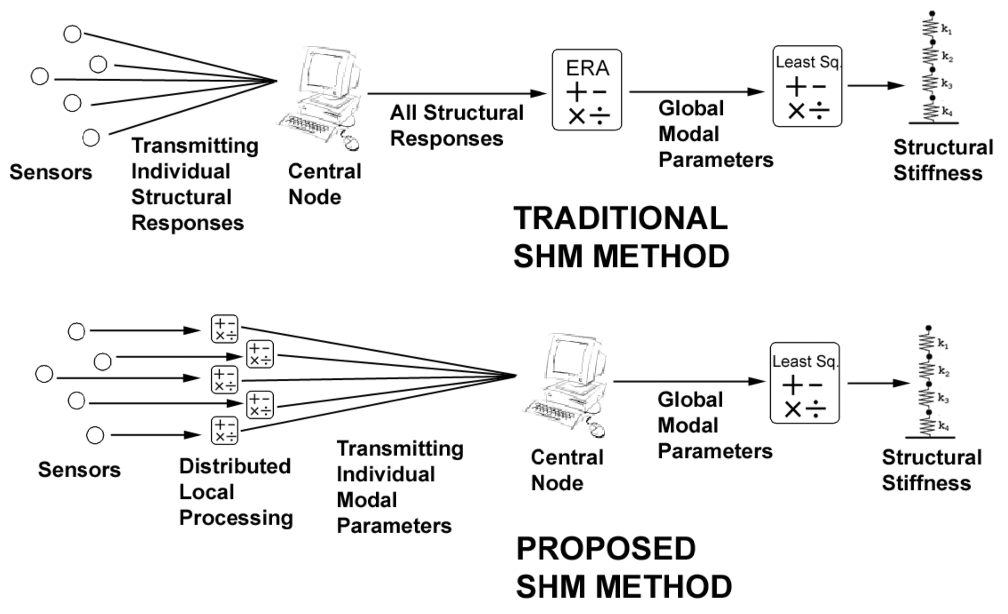

Figure 3.4: SHM methods comparison

3.3.2 Data Reduction via Distributed Algorithm

The singular value decomposition of the Hankel matrix **H** in ERA cannot be decentralized as it requires responses from all sensors to be collected at a single location. This section discusses a distributed algorithm for mode shape estimation developed by the USC SHM/ITR group and led by Chintalapudi (2006); the same least squares method can then be used to estimate structural stiffness. In general, the response of a structure at a location l can be expressed as,

$$y^l(k,\Delta t) = \sum_m a_m^l \exp\left(-\eta_m k\Delta t\right)\cos\left(\omega_m k\Delta t + \phi_m^l\right)$$
$$= \frac{a_m^l}{2}\sum_m \exp\left(-(\eta_m + i\omega_m)k\Delta t - i\phi_m^l\right) + \exp\left(-(\eta_m - i\omega_m)k\Delta t + i\phi_m^l\right) \quad . \tag{3.13}$$

Here, a_m^l and ϕ_m^l are the amplitude and phase of the m^{th} mode at the l^{th} location, while ω_m and η_m are the (damped) frequency and attenuation of the m^{th} mode. The m^{th} mode shape can then be expressed as,

$$\mathbf{v}_m = \left[a_m^1 \exp\left(i\phi_m^1\right) \quad \cdots \quad a_m^L \exp\left(i\phi_m^L\right)\right]^{\mathrm{T}} \Big/ \left\|\mathbf{a}_m\right\| \tag{3.14}$$

In the distributed algorithm, every sensor locally estimates the values of a_m^l, ϕ_m^l, ω_m and η_m from the collected structural response and transmits only these modal characteristics to a central computer instead of transmitting the entire structural response data. The modes shapes are then estimated using (3.14) centrally.

It can be shown that the discrete Laplace transform, $L\{y^l(k)\}(s)$, where $s = \lambda + i\,\omega$, is given by,

$$\lim_{\Delta t \to 0} \Delta t \sum_{k=0}^{\infty} y^l(k)\exp\left[-(\lambda + i\omega)k\Delta t\right]$$
$$= \sum_m a_m^l \frac{(\eta_m+\lambda)\cos\phi_m^l\left[(\eta_m+\lambda)^2 + (\omega^2+\omega_m^2)\right] - \omega_m \sin\phi_m^l\left[(\eta_m+\lambda)^2 + (\omega_m^2-\omega^2)\right]}{\left[(\eta_m+\lambda)^2 + (\omega^2+\omega_m^2)\right]\left[(\eta_m+\lambda)^2 + (\omega_m^2-\omega^2)\right]}$$
$$+ \; i\sum_m a_l \omega \frac{\cos\phi_m^l\left[(\eta_m+\lambda)^2 + (\omega_m^2-\omega^2)\right] + 2\omega_m \sin\phi_m^l(\eta_m+\lambda)}{\left[(\eta_m+\lambda)^2 + (\omega^2+\omega_m^2)\right]\left[(\eta_m+\lambda)^2 + (\omega_m^2-\omega^2)\right]} \quad . \tag{3.15}$$

Knowing, the modal frequencies, the amplitude, phase and attenuation can be estimated approximately using the following equations (the detailed derivation can be found in Chintalapudi, 2006)

$$\phi_m^l \approx \text{phase}\left[L\{y^l(k)\}(\lambda_1 + i\omega_m) - L\{y^l(k)\}(\lambda_2 + i\omega_m)\right] \tag{3.16}$$

$$\eta_m \approx \frac{-\omega_m}{(n_1 - n_2)\pi}\log\left(\left\|L\left\{y^l(k + \frac{n_1\pi\omega_m}{\Delta t})\right\}(i\omega_m)\right\| \Big/ \left\|L\left\{y^l(k + \frac{n_2\pi\omega_m}{\Delta t})\right\}(i\omega_m)\right\|\right) \tag{3.17}$$

$$a_m^l \approx 2\left\|L\{y^l(k)\}(i\omega_m)\right\| \Big/ \sqrt{1 + \frac{1}{\eta^2} + \frac{2\cos 2\phi_m^l}{\eta_m^2 + 4\omega_m^w} + \frac{4\omega_m \sin 2\phi_m^l}{\eta_m(\eta_m^2 + 4\omega_m^w)}} \tag{3.18}$$

where integers, n_1 and n_2, are used to create two time shifts that are multiples of the time period of the mode for estimating η_m. A least squares fit for ten different values of n_2 is used while n_1 was fixed at 1. Finally, the distributed algorithm for mode shape estimation has the following steps:

1. Each sensor approximately estimates its dominant modal frequencies by detecting peaks in the power spectral density of the received signal. All spectral peaks with energy less than 1% of the total signal energy are ignored.
2. Each sensor transmits the list of its estimated modal frequencies to a central computer. The central computer then creates a comprehensive set of modal frequencies of the structure and sends this list back to each sensor node.
3. Knowing the modal frequencies, the sensors estimate the modal parameters (phase, amplitude and attenuation) for each of the modal frequencies in the list using (3.16) through (3.18).

4. The estimates of the modal parameters are refined using a greedy local search to minimize the root mean square (RMS) error between the spectrum of the signal and that using the estimated modal parameters in using (3.17) for $\lambda = 0$.
5. The modal parameters are then transmitted back to the central computer that estimates the mode shapes using (3.14).

The algorithm completely avoids transmitting the full sensor measurement data over the radio and, hence, dramatically reduces the radio communication overhead.

3.3.2.1 Experiment

Both ERA and the distributed algorithms are tested on a 48-inch scale model of a 4-story building. The structure responses under forced excitation are collected using wireless sensors to get a sense of its performance under realistic wireless conditions. This section describes the experiments and results. A wireless sensor network, NetSHM, developed at USC Embedded Network Lab is used for this experiment.

The scale building model (Figure 3.5) is 48 inches high, with 1/2x12x18-inch aluminum plates which serve as floors. The model is supported by 1/2x1/8-inch steel columns with columns' strong axis in the direction of the plates' longer sides. Removable 5.5 lb/inch springs serve as braces between the floors of the structure in the weak direction. Damage is "induced" by removing these springs from the structure. The building has four wirelessly controlled shakers built using off-the-shelf components. These can be tasked via an attached Mica-Z mote (wireless sensor) to deliver impulses to the top floor of the structure in the weak direction (Crossbow Inc., 2005). Upon receiving signal, the four shakers simultaneously apply forces by extending their "arms" rapidly and hitting the structure (Figure 3.6 shows the impact of the forces at around t = 2 seconds). After the impact, the arms of the shakers will be retracted to the original positions.

Figure 3.5: The 4-story model with sensors and actuators

The NetSHM prototype runs on a hierarchical network of PCs, Stargates and Mica-Z motes. Mica-Z motes are the embedded wireless sensors with power and bandwidth constraints. The Stragets are gateway nodes that are more endowed in terms of power and bandwidth; their main objectives are to manage the aggregate data rates generated by the motes and communicate with the end users (PCs). Attached to the Mica-Z motes is a *vibration card* specially designed for high-quality vibration sensing. The vibration card can be programmed to sample at frequencies from 5 Hz to 20 kHz at 16 bits per sample and has a programmable anti-aliasing filter to accommodate different sampling rates. The 16-bit ADC (Analog-to-Digital Conversion) of the vibration card is controlled by an onboard microprocessor, which in turn can be commanded by the attached Mica-Z mote via a serial port. The stored samples can be retrieved in one shot from the on-card 64KB SRAM by issuing commands over the serial port. The card firmware is modified to support retrieval of blocks of samples from the card's RAM. This enabled conservation of memory on the Mica-Z. Finally, sensitive tri-axial accelerometers (dynamic range of $\pm 2.5g$, sensitivity $1\mathrm{V}/g$) are attached to the vibration card for each floor of the building model.

3.3.2.2 Results

Various damage patterns are tested on the scale model. Figure 3.6 shows the responses of the structure for one of the patterns. The responses are then used to estimate the modal parameters, such as the mode shapes shown in Figure 3.7, using both the ERA and the distributed algorithm. The Least Square solution is then applied to compute the structural stiffness from the modal parameters for all tested patterns.

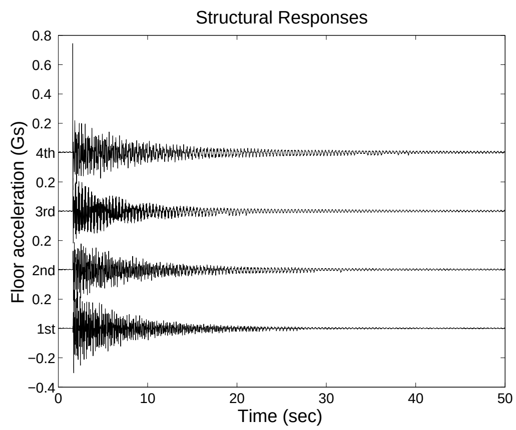

Figure 3.6: Floor Responses

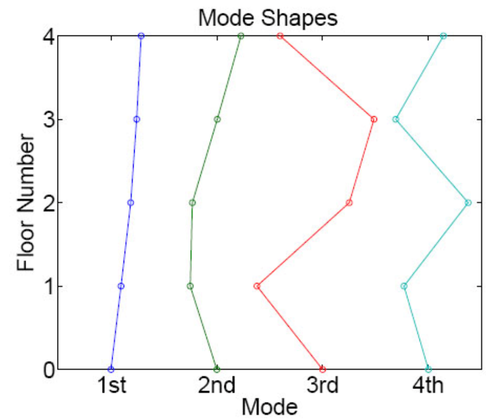

Figure 3.7: Mode shapes

Each damage pattern is then compared with the undamaged case to detect and localize the stiffness loss defined as

$$\text{Stiffness loss (\%)} = 100 \times \left(1 - \frac{\text{damaged stiffness}}{\text{undamaged stiffness}} \right) \tag{3.19}$$

Table 3.6 lists all of the damage patterns with stiffness losses computed using the centralized ERA scheme and the distributed approach; bold face denotes where there is actual damage. The distributed scheme is able to successfully detect the loss of story stiffness. The amount of data transmitted for the ERA-based scheme for each sensor over the radio is about 160Kbits, since each sensor transmitted 10,000 16-bit samples. With the distributed scheme, each node transmits only 640 bits of data per sensor — four 32-bit modal frequencies in step 2 followed by the estimated amplitude, a_m^l, phase ϕ_m^l, attenuation η_m and frequency ω_m for four modes. This is a reduction in communication cost by a factor of 250.

Damage Pattern	stiffness loss in corresponding stories							
	Δk_1 (%)		Δk_2 (%)		Δk_3 (%)		Δk_4 (%)	
	ERA	*Distrib.*	ERA	*Distrib.*	ERA	*Distrib.*	ERA	*Distrib.*
1 (50% springs in 4th story)	0.1	*0.243*	0.073	*0.045*	–0.251	*–3.220*	**4.371**	***6.69***
2 (no springs in 4th story)	0.24	*1.087*	0.126	*–0.529*	–0.179	*–0.316*	**8.814**	***9.415***
3 (50% springs in 3rd story)	–0.234	*0.851*	–0.054	*–1.510*	**4.486**	***5.129***	–0.150	*0.164*
4 (no springs in 3rd story)	0.997	*2.258*	–0.22	*0.338*	**8.741**	***7.004***	–0.318	*–0.566*
5 (50% springs in 2nd story)	0.683	*0.335*	**4.734**	***5.078***	–0.100	*–0.811*	–0.298	*–0.041*
6 (no springs in 2nd story)	0.708	*–0.927*	**9.539**	***10.137***	–0.282	*–0.181*	–0.373	*–0.525*
7 (50% springs in 1st story)	**5.846**	***4.908***	0.044	*–0.094*	–0.563	*–0.005*	–0.139	*–0.013*
8 (no springs in 1st story)	**10.394**	***9.62***	–0.054	*0.903*	–0.675	*–0.979*	–0.137	*–0.443*
9 (no springs in 3rd & 4th stories)	1.128	*3.727*	–0.285	*–1.296*	**11.515**	***9.715***	**6.867**	***8.281***
10 (no springs in 1st & 4th stories)	**14.919**	***10.71***	–0.457	*–0.457*	–0.784	*0.933*	**9.208**	***8.8***

Table 3.6: Computed stiffness loss values (numbers in bold indicate the expected damage)

3.3.3 Energy Conservation via Sensor Placement[3]

The previous section discusses adopting SHM for WSNs using a distributed algorithm to locally process SHM data; this section of the chapter discusses adopting WSNs for SHM by placing the sensors suitable for SHM. For any sensor network, determining the placement of sensors is a crucial problem that depends on two related issues — the number of sensors and where the sensors are placed.

[3] This work is in cooperation with Prof. Bhaskar Krishnamachari and Amitabha Ghosh from the Autonomous Networks Research Group in the USC Electrical Engineering Department.

Sensors in a WSN have to be connected; thus, no sensor should be out of the wireless communication range of other sensors. In this section, wireless SHM is applied to a simple shear n-story structure with identical floors (*i.e.*, identical masses, stiffness and damping coefficients). Each floor is equipped with the same number of sensors to record structural responses. A large number of sensors amounts to redundancy or a lower signal-to-noise ratio (SNR) and a large amount of data or high communication cost, while a small number of sensors implies a larger SNR and lower communication cost. To understand the relationship between WSNs and SHM in terms of sensor placement, two most natural heuristic deployments — random and grid placements — are considered. The sensor placements are simulated based on modal analysis using the Eigensystem realization algorithm (ERA) and network energy consumption. Using ERA, modal characteristics of the structure can be estimated from structural response and then used for damage detection and localization (see section 3.2.1 and 3.2.2 for more details). An energy-balanced routing tree is constructed for the WSN to realistically estimate the energy consumption due to sensor placements.

3.3.3.1 Related Work

There are many studies on optimum sensor placements for identification and control of dynamic structures. Udwadia and Sharma (1978), and Udwadia (1994) proposed to optimally locate sensors by maximizing the trace or determinant of the

Fisher information matrix which is expressed as a function of selected parameters corresponding to the objective function. Heredia-Zavoni and Esteva (1998) extended this approach to large model uncertainties in model updating by minimizing the expected Bayesian loss function with the Fisher information matrix. Kammer (1991) evaluated the sensor locations by their contribution to the linear independence of the identified model. Hemez and Farhat (1994) extend this independence method in terms of strain energy contribution of the structure. Papadimitriou *et al.* (2000) used information entropy as a unique measure of model parameter uncertainty and a Bayesian statistical methodology to find optimum sensor placements. Recently, the genetic algorithms (GA) have been used for finding the optimum sensor placements (Papadimitriou *et al.,* 2000, Abdullah *et al.*, 2001, and Guo *et al.*, 2004).

Early studies had been mostly concerned with the observability and controllability of dynamic structures while recent studies have started to tie sensor placements with the quality of damage detection. Cobb and Liebst (1997) studied the relationship between the sensor placement, measured modes, and the extent of damage localization on flexible structures using modal analysis. Shi *et al.* (2000) proposed to optimize sensor placements according to damage detection based on the eigenvector sensitivity method. These studies focused on placing sensors optimally for the structural analysis and the sensor network is not considered. The typical objective is to determine where to place m sensors in an n degree-of-freedom (DOF) system usually where $m \leq n$ and at most one sensor is located at each DOF. This section assumes there are multiple sensors per floor since wireless sensors are designed for large sensor deployment. The sensor placement in this dissertation concerns both the quality of damage detection and the sensor network limitation.

3.3.3.2 Structure Model

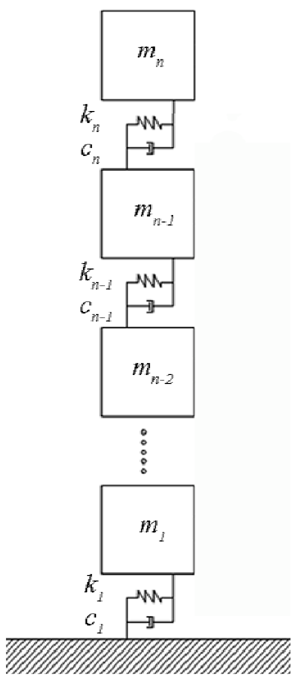

Figure 3.8: Shear structure (showing one direction only)

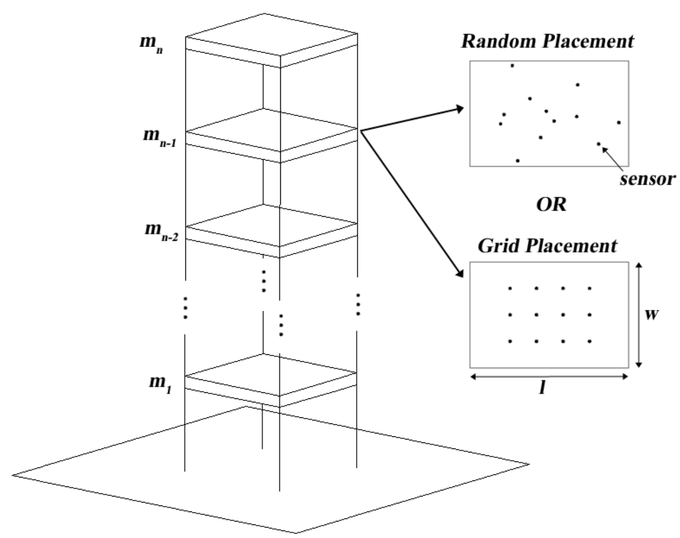

Figure 3.9: An *n*-story structure with sensors on each floor

An *n*-story shear structure is assumed for the study (Figure 3.8). Two types of sensor placements are studied — random and grid placements (Figure 3.9). In the random placement, sensors are placed randomly on each floor with uniformly distributions in both *x* and *y* directions. Different numbers of sensors per floor, *m*, and different noise levels, *p*, are also studied to see their effects. For a given *m*, one thousand realizations of the random sensor placements are simulated and analyzed for different p. In the grid placement, sensors are placed in identical rectangular grids for all floors. On top of different sensor numbers and noise levels, the distances between sensors are also studied for the grid placement.

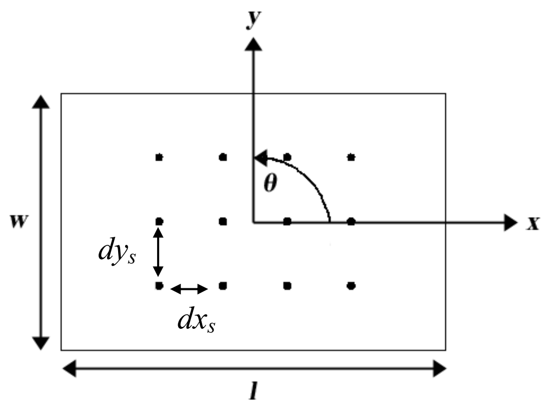

Figure 3.10: Floor diagram

For a particular floor, let s_{ij} be the j^{th} sensor (j =1,2,…, m) on the i^{th} floor (i =1, 2, …, n) and let x_{sij} and y_{sij} be the measurements recorded by sensor s_{ij} in the x and y directions respectively. From Figure 3.10, dx_{sij} and dy_{sij} are the distances between the center of the i^{th} floor and sensor s_{ij}. The relationship between (x_{sij} , y_{sij}) and the i^{th} floor's movements, (x_i , y_i , θ_i), is

$$\begin{bmatrix} x_{sij} \\ y_{sij} \end{bmatrix} = \begin{bmatrix} 1 & 0 & dx_{sij} \\ 0 & 1 & dy_{sij} \end{bmatrix} \begin{bmatrix} x_i \\ y_i \\ \theta_i \end{bmatrix} \tag{3.20}$$

assuming θ_i is small and, thus, $\theta_i \approx \sin(\theta_i)$. For m sensors, (3.20) can be expanded as

$$\begin{bmatrix} x_{si1} \\ y_{si1} \\ x_{si2} \\ y_{si2} \\ \vdots \\ x_{sim} \\ y_{sim} \end{bmatrix} = \begin{bmatrix} 1 & 0 & dx_{si1} \\ 0 & 1 & dy_{si1} \\ 1 & 0 & dx_{si2} \\ 0 & 1 & dy_{si2} \\ & \vdots & \\ 1 & 0 & dx_{sim} \\ 0 & 1 & dy_{sim} \end{bmatrix} \begin{bmatrix} x_i \\ y_i \\ \theta_i \end{bmatrix} \tag{3.21}$$

or $$\mathbf{X_{si}} = \mathbf{QX_i} .$$

Let $\mathbf{Q}^+$ be the pseudo-inverse of $\mathbf{Q}$, and the floor movement estimation can be found from sensor measurements by

$$\mathbf{\hat{X}_i} = \mathbf{Q}^+\mathbf{X_{si}} . \tag{3.22}$$

This is a least squares estimate of the floor movements with lateral movements (x_i and y_i) heavily affected by the accuracy of the sensor measurements and the rotation (θ_i) more affected by the location of the sensors (*i.e.*, dx_{sij} and dy_{sij}). Large dx_{sij} and dy_{sij} are expected to improve accuracy of rotation estimates since sensors further away from the rotating axis (center of the floor) can better record the effects of the rotations. Since there are noises in sensor measurements, (3.22) is more realistically represented as

$$\mathbf{\hat{X}_i} = \mathbf{Q}^+\left(\mathbf{X_{si}} + \mathbf{W}\right) \tag{3.23}$$

where $\mathbf{W}$ is a vector of measurement noises, assumed to be independently to be normally distributed with zero-mean and p variance, or N(0, p).

The results of the following sections are based on simulations of the 4-story scale structure discussed in Section 3.3.2.1. The floor are said to be 8ft×12ft, but the dimensions are scalable (*e.g.*, the simulation results can be scaled to dimensions 80ft×120ft). The networking capability of the wireless sensors, such as radio range, is scaled to the said dimensions.

3.3.3.2.1 Identification and Error Measure

Using measurements from the sensors, the structural characteristics can be identified by estimating modal parameters (*i.e.*, frequencies and mode shapes — see Figure 3.7). To check the accuracy of the system identification using the sensor placements, comparisons are made between mode shapes estimated using ERA from measured responses with and without noises. The noise-free estimated mode shapes are used as the baseline case against which other estimated mode shapes (with different noise levels) are compared. Since mode shapes, similar to eigenvectors, are scalable vectors for specific frequencies, the Modal Amplitude Coherence (MAC) is used to differentiate between different sets of mode shapes (Juang and Pappa, 1985). The MAC between two vectors is defined as

$$MAC(\mathbf{\Phi}_i, \mathbf{\Phi}_j) = \frac{\left|\mathbf{\Phi}_i * \mathbf{\Phi}_j\right|}{\sqrt{(\mathbf{\Phi}_i * \mathbf{\Phi}_i)(\mathbf{\Phi}_j * \mathbf{\Phi}_j)}} \tag{3.24}$$

with values ranging from 0 to 1. When two vectors are parallel, their MAC value is 1, whereas two perpendicular vectors have a MAC value of 0. Thus, by finding

MAC values of the mode shapes from the base case and from cases with different sensor placements and noise levels, accuracy can be measured. Error is measured as the Frobenius norm of $\lfloor MAC(\hat{\mathbf{\Phi}},\mathbf{\Phi})-\mathbf{I}\rfloor$ or

$$\text{error} = \sqrt{trace\left(\left[MAC(\hat{\mathbf{\Phi}},\mathbf{\Phi})-\mathbf{I}\right]^{\mathrm{T}}\left[MAC(\hat{\mathbf{\Phi}},\mathbf{\Phi})-\mathbf{I}\right]\right)}, \tag{3.25}$$

where $\hat{\mathbf{\Phi}}$ is the estimated mode shape from measured responses of the structure and $\mathbf{I}$ is the identity matrix. When $\hat{\mathbf{\Phi}}=\mathbf{\Phi}$, $MAC(\hat{\mathbf{\Phi}},\mathbf{\Phi})=\mathbf{I}$ and error = 0.

3.3.3.2.2 Random Deployment

In random deployment, the sensors are uniformly distributed on each floor. In other words, dx_{sij} and dy_{sij} are random variables characterized by uniform distributions of U(-*l*/2,*l*/2) and U(-*w*/2,*w*/2) respectively. This random sensor deployment may not be a good placement for the sensors in both SHM accuracy and network connectivity, but it facilitates looking at a wide range of different deployment configurations. Figure 3.11 shows errors in mode shape estimations of 1000 realizations simulated for combinations of a given number of sensors per floor (m = 2, 3, …, 10) and a given noise level (p = 2%, 4%, …, 10% of the maximum response). Obviously, as p increases, so do the errors. Meanwhile, increasing m overall lowers the errors since more sensors can improve measurements. Typically, the errors converge to a single band as m increases, but for some cases the errors converge into two bands such as p = 8% and p = 10%. To understand the relationship between sensor deployments and errors, the realizations with the five best and worst errors are further examined.

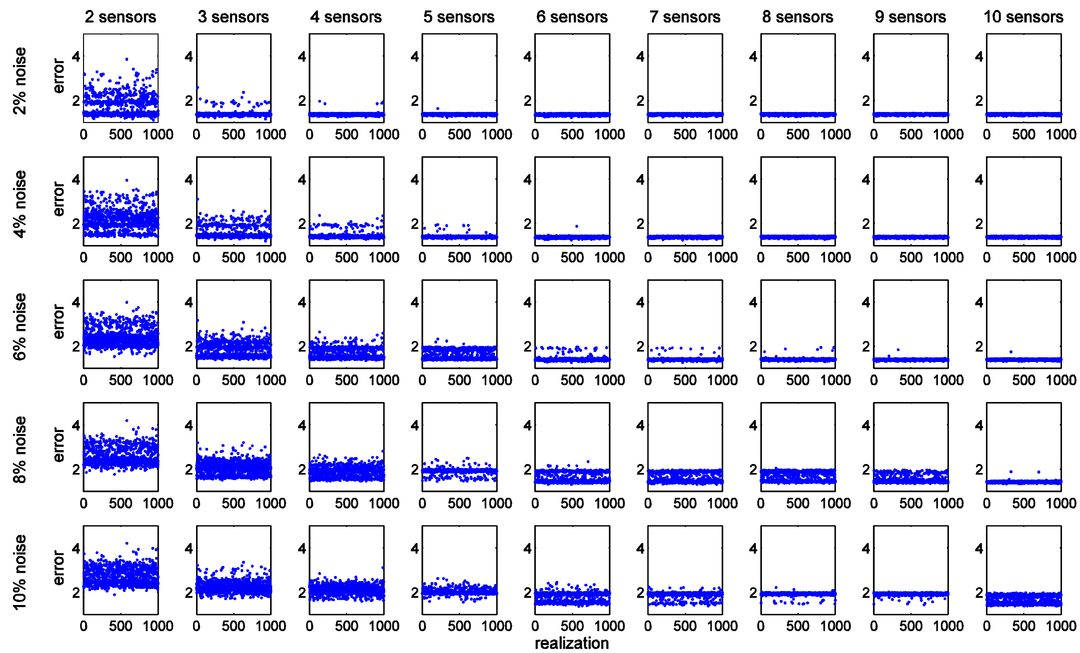

Figure 3.11: Effect of sensor numbers and measurement noise in mode shape estimations over 1000 realizations (lower values = more accurate)

Figure 3.12 and 3.13 show the location plots of sensors of the five cases with the lowest and highest errors, respectively, from the 1000 random sensor location realizations for m=3 (sensors per floor) and p=8% (noise level). Comparing the two figures, it can be seen that the sensors of the low error cases are less clustered than the sensors of the high error cases. This observation falls in line with the mathematical interpretation from (3.23) that the accuracy of rotation estimates increases as distances between sensors increases. Figure 3.14 and 3.15 show the sensor location plots of the five cases with the lowest and highest errors, respectively, for m=7 and p=8%. However, unlike the cases with m=3, there is no significant increase in sensor clusters between Figure 3.14 and 3.15, or any observations for confident conclusions. For simple cases (a small number of sensor) of random deployment, accuracy in system identification increases when sensors are placed far apart; when a larger of sensors are involved in random deployment, the separation between sensors is less influential on accuracy in identifying the system.

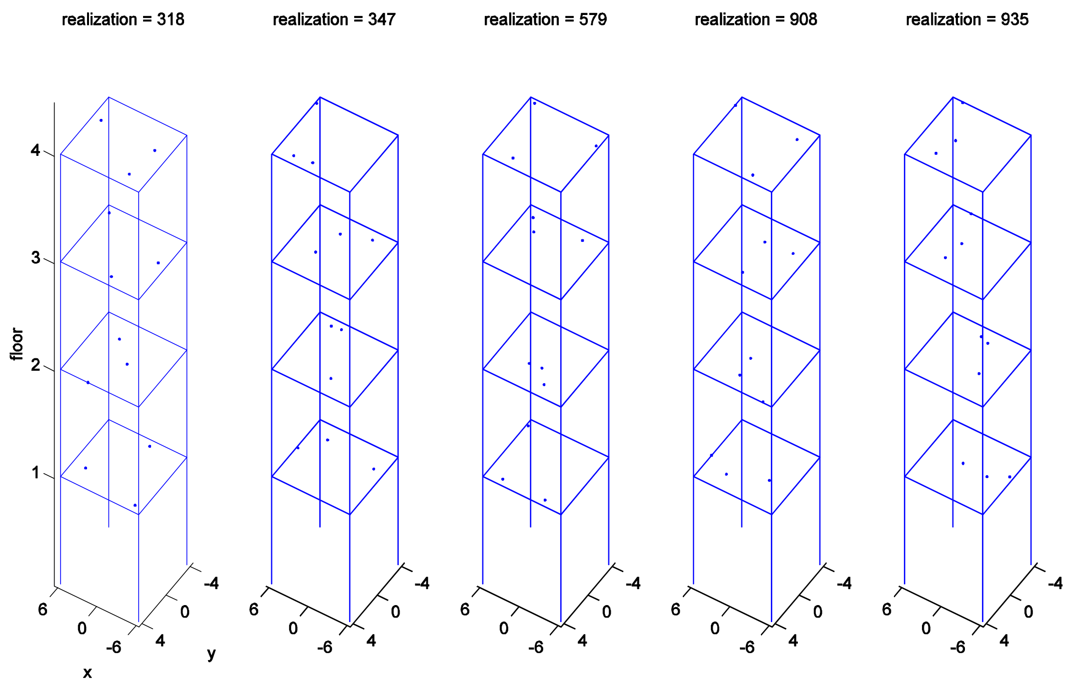

Figure 3.12: Location plots of the 5 best cases (lowest error in estimating mode shapes) with 3 sensors per floor (units are in ft in the *x* and *y* directions).

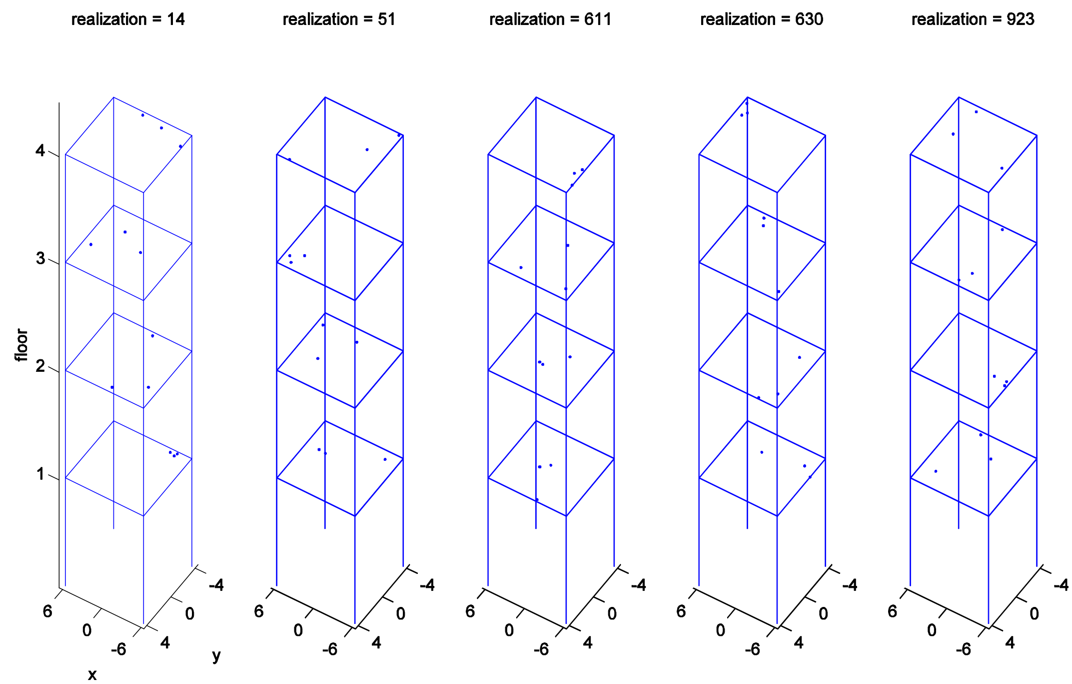

Figure 3.13: Location plots of the 5 worst cases (highest error) with 3 sensors per floor.

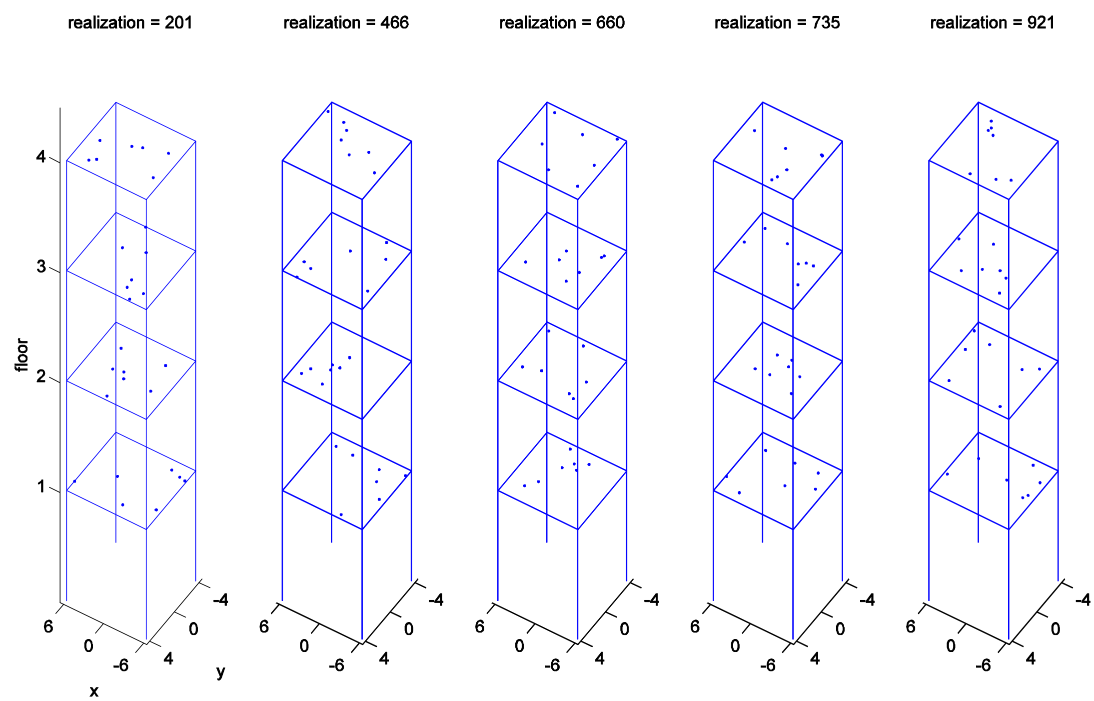

Figure 3.14: Location plots of the 5 best cases (lowest error) with 7 sensors per floor.

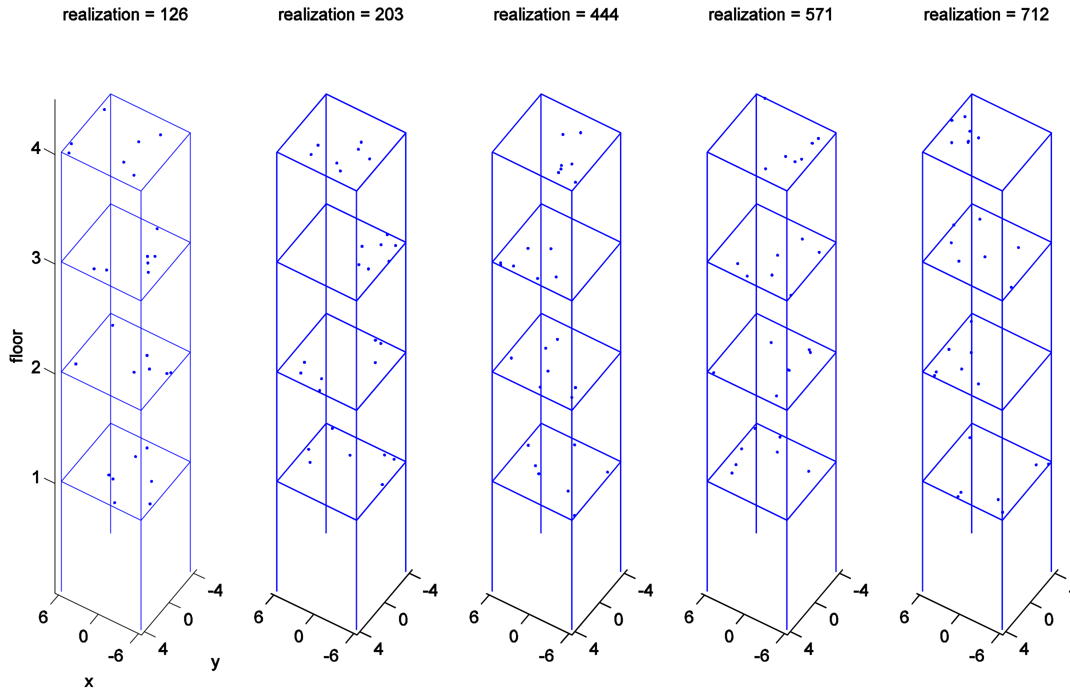

Figure 3.15: Location plots of the 5 worst cases (highest error) with 7 sensors per floor.

3.3.3.2.3 Grid Deployment

Under grid deployment, for a given number of sensors per floor, $m = m_1 \times m_2$ grids are formed with different inter-node separations and one sensor is placed at each grid point. To maintain connectivity on each floor, the maximum inter-node separation is kept smaller than the communication range of a node. The objective here is to find the optimal inter-node separation that minimizes the mode shape error for given floor dimensions.

In Figure 3.16, 24 different configurations are shown for 16 sensors placed on a floor of dimension 12ft by 8ft. Figure 3.17 illustrates that the corresponding mode shape errors for each of these configurations decrease sharply as the nodes are placed further apart from each other. However, after a certain point approximately when the separation reaches around 0.7ft, the rate of decrease flattens out. A similar trend is observed when the number of sensors per floor is increased keeping the noise level fixed at 4%, as shown in Figure 3.17. These results indicate that a larger number of sensors with longer distances between sensors reduces the mode shape errors, though, with diminishing returns.

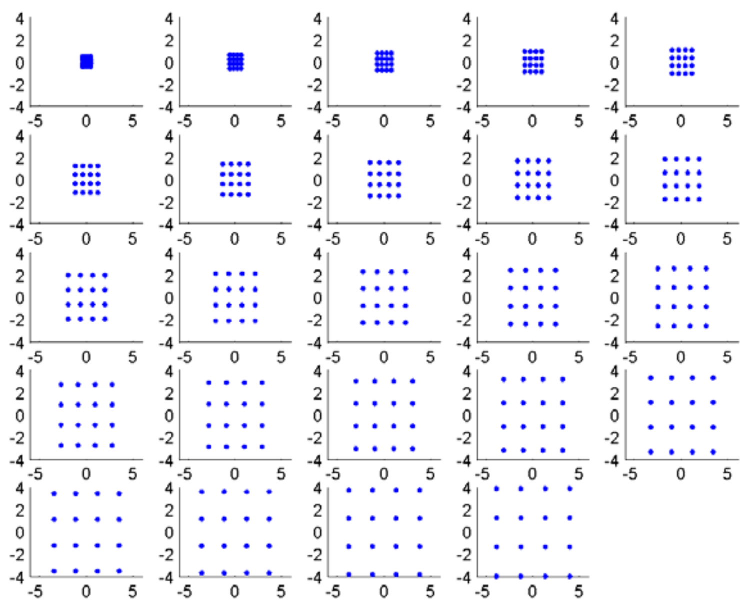

Figure 3.16: Sensor grid layouts (units: ft).

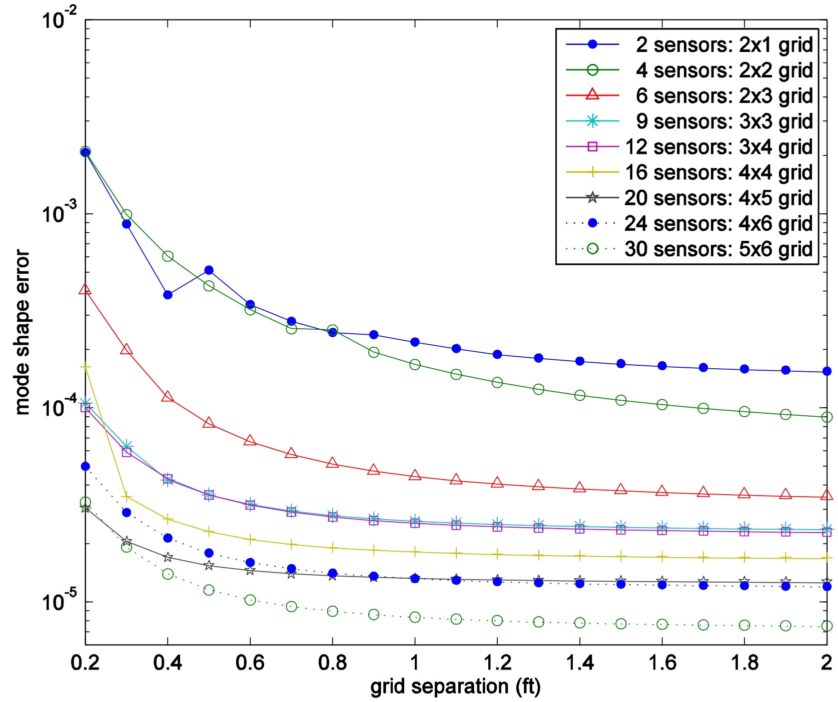

Figure 3.17: Effect of sensor number and distances on mode shape error with 4% noise level

3.3.3.3 Network and Energy Model

In the network connectivity model, it is assumed that the nodes can adjust their transmission power levels and, thereby, adjust their transmission ranges. It is possible for every node in the network to have a different transmission range depending on the placement of the node and the layout of the structure. However, there is a maximum transmission range $R_{\max}$ corresponding to a maximum power level $P_{\max}$ for all the nodes. In the simulations described herein, $R_{\max}$ is taken as 3ft (for the scaled structure model). Two nodes are able to communicate with each other if the distance between them is less than or equal to the maximum of their transmission ranges. This model, more commonly known as the binary disk model, is idealistic and does not incorporate interference, capture effects, and the anisotropic nature of radio propagation. Each floor is also assumed to be equipped with a high powered node (local sink) located at the center of the floor that connects adjacent floors to exchange measurements. Thus, all the nodes in a given floor are only required to send their measurements to their local sinks.

A wireless SHM system, once deployed, is expected to be functional for months or years, depending on how often an inspection or diagnosis is performed on the structure. Since the battery powered wireless nodes are limited in energy, an important aspect of designing a wireless SHM system is to minimize energy consumption. In these systems, high sampling rate and high sampling resolution results in high power consumption; however, the power consumption by the radio module of the sensor node is orders of magnitude higher than the CPU. While various radios differ in their absolute power values, a common feature among them is that the sleep mode generally consumes three orders of magnitude less power than the transmission or reception mode. The power costs for: 1) keeping the node in receive mode without actively receiving packets, 2) keeping the node in receive mode while receiving packets, and 3) keeping the node in receive mode while overhearing packets intended for other nodes, are often very similar (within about 20−30%). These observations suggest that it is best to keep the radio in the sleep mode as much as possible to cut down on idle receive mode costs. For short range transmission on a 2.4GHz carrier frequency the power usage is dominated by radio electronics (frequency synthesizer, mixer, etc.), which is of the order of 100mW (Wang *et al.*, 2001). Meanwhile, the output transmit power is about 52mW and the receive power is about 59mW for bit error rate as low as 10^{-5} at 250Kbps for CC2420 radios (Texas Instruments, 2006). Moreover, the power consumption of the transceiver does not vary much with the data rate to the first order. Thus, it makes sense to send packets in burst at high data rates to minimize transmission time and shut off the transmitter during idle period. Min and Chandrakasan (2003) observed that, since the startup energy of the transceiver exceeds the energy of transmission short-range radios with small packet sizes, energy costs may not be reduced significantly (if at all) by traveling multiple shorter hops with reduced output power.

Unfortunately, transmitters require a significant overhead in terms of time and energy dissipation to go from the sleep state to the active state. Typical start-up time for CC2420 radios is about 0.6ms or more, while transmit on-time is less than that. This means that the transient energy during the start-up can be higher than the energy required for actual transmission, implying that it is advisable to keep the radio on for long duration each time to minimize switching costs. In this dissertation, the following model is considered for energy expenditure per bit for communication over a link of length d,

$$E(d) = E_{tx} + E_{rx} = \alpha + \beta\, d^{\eta} \quad , \qquad (3.26)$$

where α is a distance-independent term and represents the energy cost of transmitter and receiver electronics with typical values about 100mW for GHz radios, β

represents a transmit amplifier constant with a typical value of 1.5, η is the path-loss exponent with typical values between 2 and 6 depending on the environment, and d^{η} captures the amplification required to ensure constant power reception at the receiver. In the simulations, α =100, β =1.5, and η = 2.

3.3.3.3.1 Energy Consumption

The results presented in the previous section show that the mode shape error decreases with increasing inter-node separation and the number of sensors per floor, albeit with diminishing returns. However, as the separation increases a node needs to transmit at a higher power level to send its measurements to its neighbors, thus spending more energy. Similarly, a large number of sensors also results in higher energy consumption. The goal of this section is to study these trade-offs and find an optimal on the grid separation and the number of sensors per floor to minimize the amount of energy consumed in communicating the measurements. Based on the network connectivity model described in the last section, an energy efficient routing tree is first constructed, assuming that all nodes on a given floor must send their measurements to a local sink located at the center of that floor. Then, from (3.26) and the energy model from the last section, the total energy spent for gathering all measurements over the routing tree to the local sink is estimated for a given inter-node separation. Finally, simulations are carried out to examine the trends in energy consumption with varying node separations and the numbers of sensors per floor.

3.3.3.4 Locations and Number of Sensors

The simulation results presented so far indicate that, with increasing grid separations and a larger number of nodes, the mode shape error decreases. In contrast, the network energy consumption increases with larger sensor separations (see (3.26)) and with a larger number of nodes due to increased data and, thus, increased energy transmission cost. These two opposing trends lead to a joint optimization problem of finding the right grid separation and the number of nodes that optimally balances the mode shape errors and the energy consumption. In this section, a numerical technique is presented to achieve that goal. For ease of presentation and understanding, the numerical method is first illustrated through an example for finding the optimal grid separation and then extended to incorporate the optimality on the number of nodes.

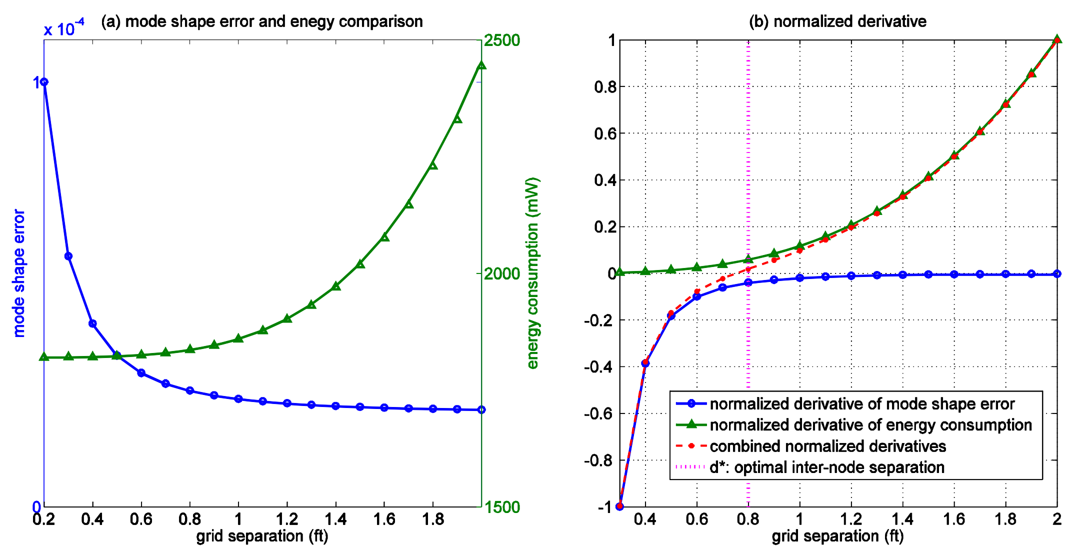

Figure 3.18: Comparison of mode shape error and energy consumption

In Figure 3.18(a), the mode shape errors and the energy consumption per floor with increasing grid separation is plotted for the 12-node configurations. The growth rates of the curves depend on the grid separation. At smaller separations, the rate of decrease in mode shape error is much higher than the rate of increase in energy consumption compared to that at larger separations. In particular, denoting the mode shape error as $M(d_j)$ and the energy consumption per floor as $E(d_j)$ at separation d_j, the optimal separation d^* is defined such that $\forall\ d_j \in (0, d^*]$, $M(d_j)$ is increasing at a much faster rate than $E(d_j)$ is decreasing as d_j decreases, and $\forall\ d_j \in [d^*, d_{max})$, $E(d_j)$ is increasing at a much faster rate than $M(d_j)$ is decreasing as d_j increases. This would imply that away from d^*, the improvement in the mode shape error is outweighted by the decline in energy efficiency, and vice versa. Thus the optimality conditions are:

$$\left|\alpha_M \frac{d}{dd_j} M(d_j)\right| > \left|\alpha_E \frac{d}{dd_j} E(d_j)\right|, \qquad \text{if } 0 < d_j \le d^*$$

$$< \left|\alpha_E \frac{d}{dd_j} E(d_j)\right|, \qquad \text{if } d^* < d_j \le d_{\max}$$

where α_M and α_E are normalizing constants with the following forms:

$$\alpha_M = 1 \Big/ \max_{d_j} \left|\frac{d}{dd_j} M(d_j)\right| \quad \text{and} \quad \alpha_E = 1 \Big/ \max_{d_j} \left|\frac{d}{dd_j} E(d_j)\right|.$$

This is equivalent to the following:

$$d^* = \arg\min_{0<d_j \le d_{\max}} \left| \frac{d^{nor}}{dd_j} M(d_j) + \frac{d^{nor}}{dd_j} E(d_j) \right| \tag{3.27}$$

where $\frac{d^{nor}}{dd_j} M(d_j) = \alpha_M \frac{d}{dd_j} M(d_j)$ and $\frac{d^{nor}}{dd_j} E(d_j) = \alpha_E \frac{d}{dd_j} E(d_j)$ are the normalized derivatives of the mode shape error curve and the energy curve, respectively. (3.27) is solved numerically for the configuration shown in Figure 3.18(b). Figure 3.18(b) shows the plot of the two normalized derivatives, their difference, and the numerical solution for d^*, which comes out to be 0.8ft.

The constants, α_M and α_E, are used to normalize the derivatives such that $M(d_j)$ and $E(d_j)$ are equally weighted in optimizing d_j. In practice, α_M and α_E can also take other values depending the weightings on SHM accuracy and energy consumption. The optimized grid separation, d^* in (3.27), would change according to the values of α_M and α_E. For the example shown in Figure 3.18(b), d^* increases for a larger α_M (with the same α_E) and decreases for a larger α_E (with the same α_M). This follows the logic that an increasing grid separation improves SHM accuracy while a decreasing separation improves energy consumption.

Extending this numerical method to jointly optimize the grid separation and the number of nodes, the sum of the normalized gradients $\nabla^{\text{nor}}M$ of $M(d_j, m)$ and $\nabla^{\text{nor}}E$ of $E(d_j, m)$ with respect to d_j and m is calculated. Here $M(d_j, m)$ and $E(d_j, m)$ represent the mode shape error and the energy consumption per floor for a given grid separation d_j and number of sensors m. Similar to (3.27) the optimal d^* and m^* are found by minimizing the square of the sum of $\nabla^{\text{nor}}M$ and $\nabla^{\text{nor}}E$, such as

$$(d^*, m^*) = \underset{\substack{0<d_j\le d_{\max} \\ 0<m\le m_{\max}}}{\arg\min}\left[\left(\nabla^{\text{nor}} M + \nabla^{\text{nor}} E\right)^2\right] \tag{3.28}$$

$$= \underset{\substack{0<d_j\le d_{\max} \\ 0<m\le m_{\max}}}{\arg\min}\left[\left(\alpha_M\left(\frac{\partial M}{\partial d_j} + \frac{\partial M}{\partial m}\right) + \alpha_E\left(\frac{\partial E}{\partial d_j} + \frac{\partial E}{\partial m}\right)\right)^2\right],$$

where the normalizing constants, α_M and α_E, here can be expressed as

$$\alpha_M = 1\Big/\max_{d_j,m}\left|\frac{\partial M}{\partial d_j} + \frac{\partial M}{\partial m}\right| \qquad \text{and} \qquad \alpha_E = 1\Big/\max_{d_j,m}\left|\frac{\partial E}{\partial d_j} + \frac{\partial E}{\partial m}\right|.$$

Solving (3.28) gives d^* and m^* such that moving away from (d^*, m^*) will result in no improvement in the mode shape error or energy consumption that will not be outweighed by the decline in the other measure. Figure 3.19(a) and 3.19(b) show the variation of mode shape error and its gradients with respect to both the grid separation and the number of sensors per floor, respectively. Likewise, Figure 3.19(c) and 3.19(d) show the variation of energy consumption and its gradients with respect to both the grid separation and the number of sensors per floor. Figure 3.19(e) illustrates $(\nabla^{\text{nor}} M + \nabla^{\text{nor}} E)^2$ with the optimal pair of values at (d^*=1.8ft, m^*=4) in this particular example. As seen in this figure, the local minima are not robust since there are sharp increases in values in the neighboring nodes.

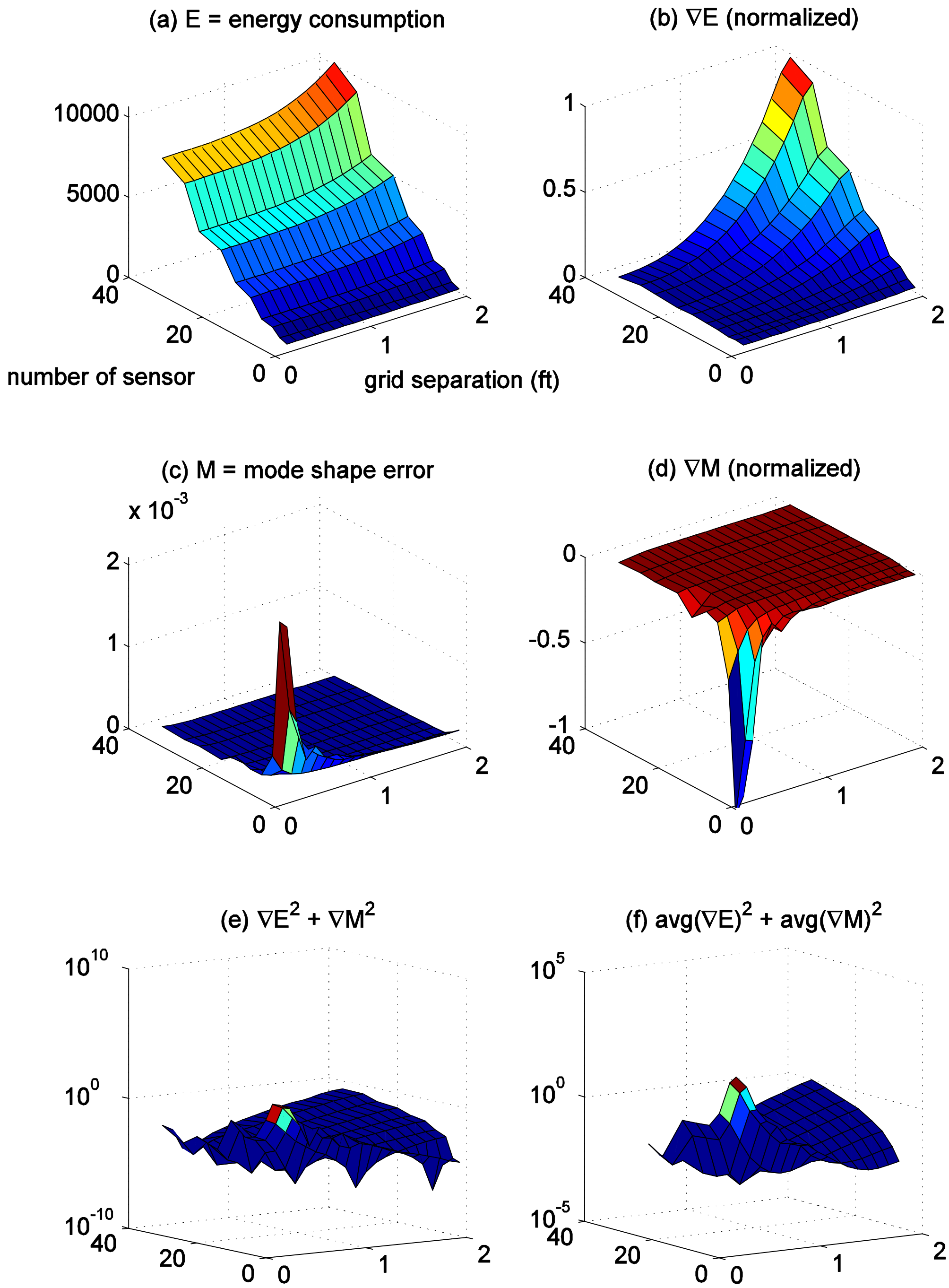

Figure 3.19: Effect of sensor numbers and distances on energy consumption and mode shape error

A modification of (3.28) is presented in Figure 3.19(f) that would increase the robustness of the optimized grid separation and number of sensors. Each node value of Figure 3.19(f) is assigned by averaging the values of the corresponding node and its eight surrounding nodes (in a rectangular grid) from Figure 3.19(e); the boundary nodes in Figure 3.19(e) are ignored for simplification since the boundary nodes have fewer than eight surrounding nodes. The global minimum is (d*=0.6ft, m*=20) in Figure 3.19(f) instead of (d*=1.8ft, m*=4) in Figure 3.19(e). Although this minimum set of averaging values may not produce the absolute minimum combination of the mode shape error and energy consumption, it can be more robust compared the optimal values from (3.28).

3.3.3.5 Result

Wireless sensor networks (WSNs) are promising for structural health monitoring (SHM) due to the ease of installation, inexpensive costs, and the scalability. However WSN comes with its constraints of power and bandwidth. This dissertation provides the first study on optimizing wireless sensors placements for SHM in terms of the quality of system identification and the sensor energy cost. The two contradicting metrics would prefer a tight placement of a few sensors to decrease sensor energy cost and a separated placement of many to increase the accuracy in estimating structural modal parameters for SHM. A compromise is suggested in this dissertation by computing the gradients of sensor energy cost and modal parameter estimation error with respect to the number of sensors and the distances between the sensors. Using the computed gradients, an optimal sensor placement is found using (3.28). A modification of (3.28) is also given for a robust sensor placement optimized for WSN and SHM.

Future work will look at the optimal wireless sensor placements for more complex structures in terms of floor layouts, non-shear structures, sensor failures, realistic wireless signal inferences such as walls, and etc. An existing building is suitable for future investigation where practical difficulties in deploying the sensors, real world noises, movements in the building and factors affecting the quality of system identification cannot be foreseen in simulation models.

3.4 Local Excitation via Wave propagation

A Wave propagation SHM approach detects damage by propagating ultrasonic waves in a medium such as a metal plate. The difference in wave propagation between undamaged and damage cases is used to assess damage. The wave propagation SHM approach can serve as a complement to global vibration-based technique (Figure 3.20) by further refining the types and locations of the damage in the structural members. However, due to the large number of members in a structure, it might not be feasible to scan all members to detect damage via wave propagation. Thus, starting with a global vibration-based approach can provide coarse information that can be improved using local approaches. The following section talks about how waves propagate in a plate and gives examples how damage can be detected using ultrasonic wave propagation.

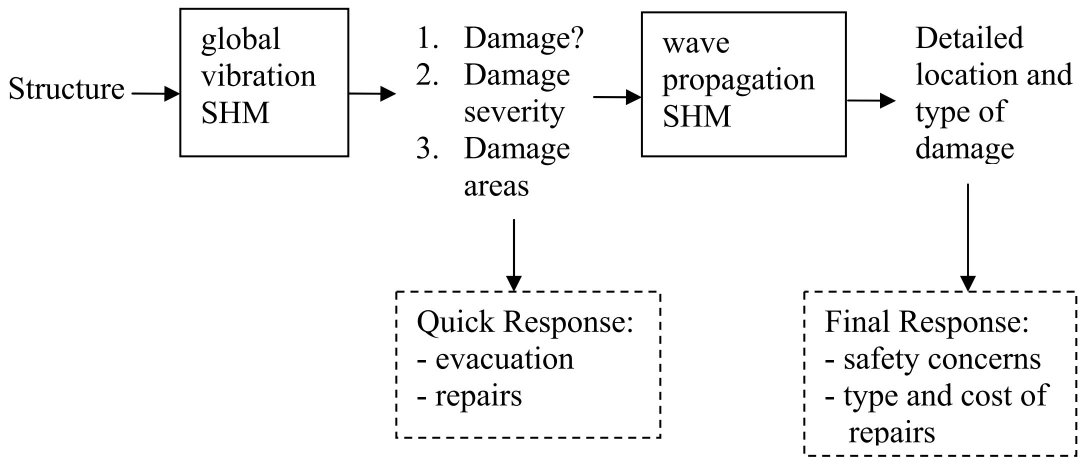

Figure 3.20: SHM flow chart between damage detection via global vibration to wave propagation

3.4.1 Wave Propagation in Plates

Confined by the boundary of a plate, waves propagated in plates are called guided waves. Ultrasonic guided waves travel as Lamb waves and shear horizontal (SH) waves in flat plates and they can reach large distances while repeatedly being reflected at the boundary. The waves can be symmetric and antisymmetric with respect to the mid-plane of the plate. The following presents a brief analysis of guided wave equations studied by Meeker and Meitzler (1964) and later by Graff (1975).

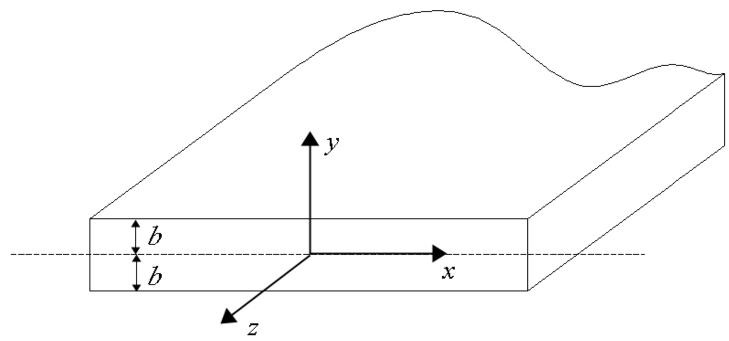

Figure 3.21: A plate with thickness 2*b* and infinite lengths in the *x* and *z* directions

Considering straight-crested waves propagating in the x-direction of a plate with stress-free upper and lower surfaces (Figure 3.21), the governing equations are

$$\mathbf{u} = \nabla\Phi + \nabla \times \mathbf{H}, \qquad \nabla \bullet \mathbf{H} = 0,$$

$$\nabla^2\Phi = \frac{1}{c_\mathrm{p}^2}\frac{\partial^2\Phi}{\partial t^2}, \qquad \text{and} \qquad \nabla^2\mathbf{H} = \frac{1}{c_\mathrm{s}^2}\frac{\partial^2\mathbf{H}}{\partial t^2} \tag{3.29}$$

where $\mathbf{u}$ is the displacement vector. Φ and $\mathbf{H}$ are the potential functions with general forms as

$$\Phi = f(y)\exp\{i(\xi x - \omega t)\}, \qquad H_x = h_x(y)\exp\{i(\xi x - \omega t)\},$$

$$H_y = h_y(y)\exp\{i(\xi x - \omega t)\}, \text{ and } \qquad H_z = h_z(y)\exp\{i(\xi x - \omega t)\} \tag{3.30}$$

where ω is the circular frequency, and ξ is the wave number. c_p and c_s are pressure (longitudinal) and shear (transverse) waves speeds, respectively, defined as

$$c_\mathrm{p}^2 = (\lambda + 2\mu)/\rho \qquad \text{and} \qquad c_\mathrm{s}^2 = \mu/\rho \tag{3.31}$$

where λ and μ are the Lamé constants and ρ is the mass density of the plate material. Substituting potential function (3.30) into the differential equations (3.29) gives

$$\Phi = (A\cos\alpha y + B\sin\alpha y)\exp\{i(\xi x - \omega t)\}$$

$$H_x = (C\cos\beta y + D\sin\beta y)\exp\{i(\xi x - \omega t)\}$$

$$H_y = (E\cos\beta y + F\sin\beta y)\exp\{i(\xi x - \omega t)\}$$

$$H_z = (G\cos\beta y + H\sin\beta y)\exp\{i(\xi x - \omega t)\} \tag{3.32}$$

where $\alpha^2 = (\omega^2 / c_p^2) - \xi^2$ and $\beta^2 = (\omega^2 / c_s^2) - \xi^2$.

Applying the boundary conditions ($\tau_{yy} = \tau_{yx} = \tau_{yz} = 0$ at $y = \pm b$) and the divergence condition on $\mathbf{H}$ ($\nabla \bullet \mathbf{H} = 0$), the constants $A, B, \ldots, H$ can be rearranged into the following matrix representation

$$\begin{bmatrix} g\cos\beta b & d\cos\alpha b & 0 & 0 & 0 & 0 & 0 & 0 \\ f\sin\beta b & c\sin\alpha b & 0 & 0 & 0 & 0 & 0 & 0 \\ 0 & 0 & -\beta\sin\beta b & i\xi\sin\beta b & 0 & 0 & 0 & 0 \\ 0 & 0 & h\sin\beta b & \beta^2\sin\beta b & 0 & 0 & 0 & 0 \\ 0 & 0 & 0 & 0 & c\cos\alpha b & f\cos\beta b & 0 & 0 \\ 0 & 0 & 0 & 0 & -d\sin\alpha b & g\sin\beta b & 0 & 0 \\ 0 & 0 & 0 & 0 & 0 & 0 & i\xi\cos\beta b & \beta\cos\beta b \\ 0 & 0 & 0 & 0 & 0 & 0 & \beta^2\cos\beta b & h\cos\beta b \end{bmatrix} \begin{bmatrix} B \\ G \\ E \\ D \\ A \\ H \\ C \\ F \end{bmatrix} = \mathbf{0} \tag{3.33}$$

where $c = (\lambda + 2\mu)\alpha^2 + \lambda\,\xi^2$, $d = 2\mathrm{i}\,\xi\,\alpha$, $f = 2\mathrm{i}\,\mu\,\xi\,\alpha$, $g = \xi^2 - \beta^2$, and $h = \mathrm{i}\,\xi\,\beta$. Solutions of (3.33) exist when the determinant of the coefficient matrix is zero. The following presents the solutions for Lamb (Rayleigh-Lamb equations) and SH waves:

- Symmetric Lamb wave (*B, C, D, E, F, G* = 0, and *A, H* ≠ 0):

$$u_x = (iA\xi\cos\alpha y + \beta H\cos\beta y)\exp\{i(\xi x - \omega t)\},$$

$$u_y = -(A\alpha\sin\alpha y + \xi H\sin\beta y)\exp\{i(\xi x - \omega t)\},$$

$$u_z = 0. \tag{3.34}$$

- Antisymmetric Lamb wave (*A, C, D, E, F, H* = 0, and *B, G* ≠ 0):

$$u_x = (iB\xi\sin\alpha y - \beta G\sin\beta y)\exp\{i(\xi x - \omega t)\},$$

$$u_y = (B\alpha\cos\alpha y - i\xi G\cos\beta y)\exp\{i(\xi x - \omega t)\},$$

$$u_z = 0. \tag{3.35}$$

- Symmetric SH wave (*A, B, C, F, G, H* = 0, and *D, E* ≠ 0):

$$u_x = u_y = 0, \qquad u_z = (-D\beta + iE\xi)\cos\beta y\exp\{i(\xi x - \omega t)\}. \tag{3.36}$$

- Antisymmetric SH wave (*A, B, D, E, G, H* = 0, and *C, F* ≠ 0):

$$u_x = u_y = 0, \qquad u_z = (C\beta + iF\xi)\sin\beta y\exp\{i(\xi x - \omega t)\}. \tag{3.37}$$

The constant *A, B, ..., H* in (3.34) to (3.37) can be solved using (3.33).

3.4.1.1 Damage Detection Example

Figure 3.22 shows how cracks can be detected using ultrasonic wave propagation. This example is from a paper by Giurgiutiu *et al.* (2003). Lamb waves (symmetric: S_0 and antisymmetric: A_0) pass a sensor between 0 and 0.05 ms. Then the waves pass by a crack 8mm away from the sensor and an echo or reflection from the crack travels back to the sensor (around 0.25 ms for S_0 and around 0.45 ms for A_0). Finally the waves reach the boundary and reflect back to the sensor. By detecting the reflection of waves from the crack, the crack can be identified.

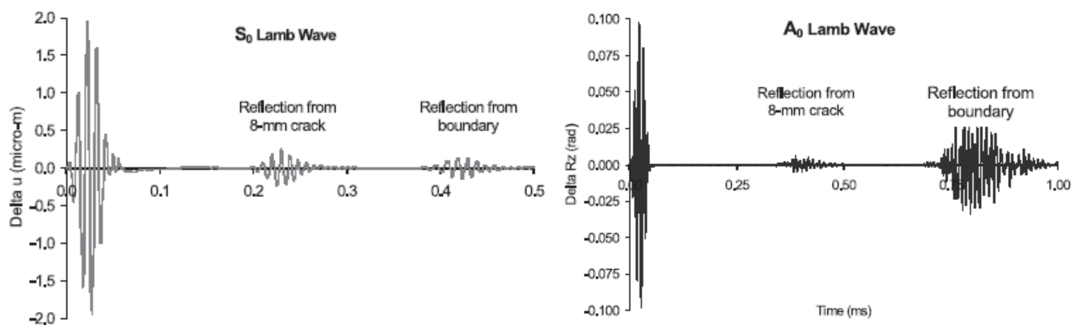

Figure 3.22: Finite element simulation of Lamb waves on damage detection in a plate (Giurgiutiu *et al.*, 2003)

3.4.2 Finite Element Model

To start research on the wave propagation SHM approach, damage detection on a metal plate will serve as an initial study. The research goal is to test the approach on small scales where it is difficult to detect damage using the vibration SHM approach. A finite element model (FEM) of the metal plate can be used to simulate wave propagation. Damage should be detected by modeling damage (*i.e.*, cracks) in the finite element model. Consider a plate with width w, length l and height h; a FEM of the plate is presented in Figure 3.23. Table 3.7 lists the dimensions and modeling of the steel plate; its material proprieties are listed in Table 3.8. Sensors capable of applying forces and measuring motions are placed on the plate to induce and capture motions.

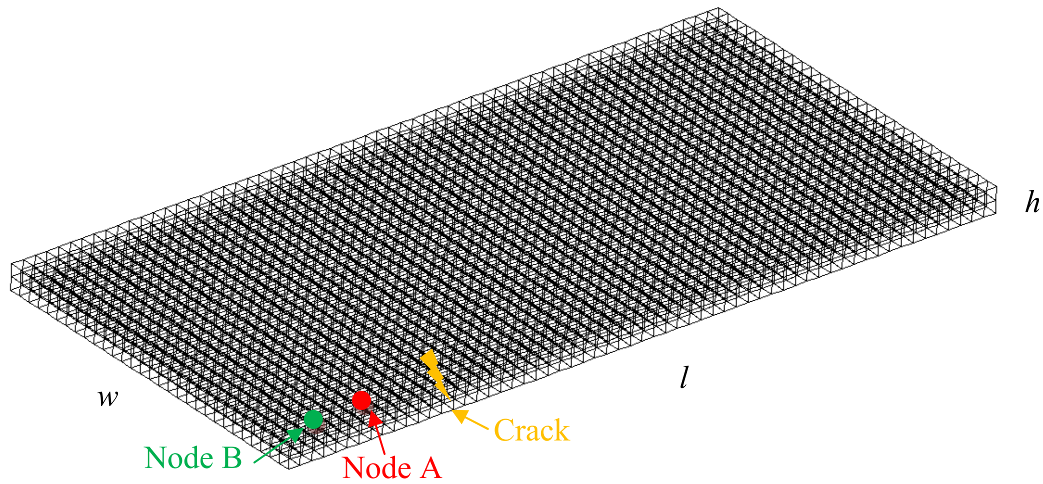

Figure 3.23: Finite element model of a plate (sensor Nodes A and B and the damage/crack will be discussed in a later section)

	directions		
	x (length)	y (width)	z (height)
number of elements	60	30	2
dimensions	60 in	30 in	2 in

Table 3.7: FEM plate dimensions and elements

steel material properties		
weight density	0.28	lb/in^3
Young's modules (E)	2.90E+07	lb/in^2
Poisson’s ratio (V)	0.29	
shear modules (G)	11.5	lb-in^2
wave speed	2.00E+05	in/sec

Table 3.8: FEM plate material properties

3.4.2.1 Simulations and Result

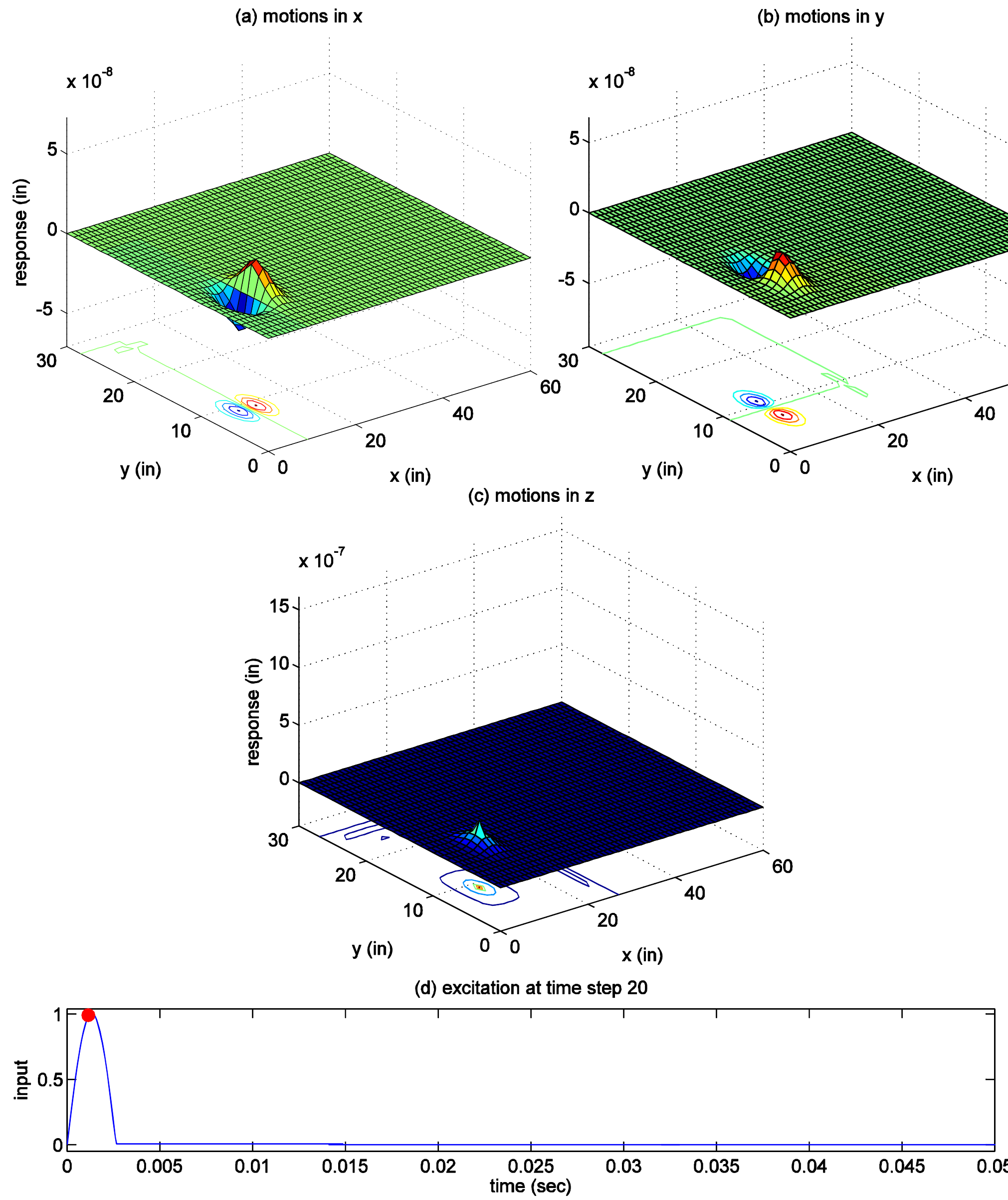

Figure 3.24: Motions of the FEM plate in x, y and z direction undergoing excitation (at time step 20)

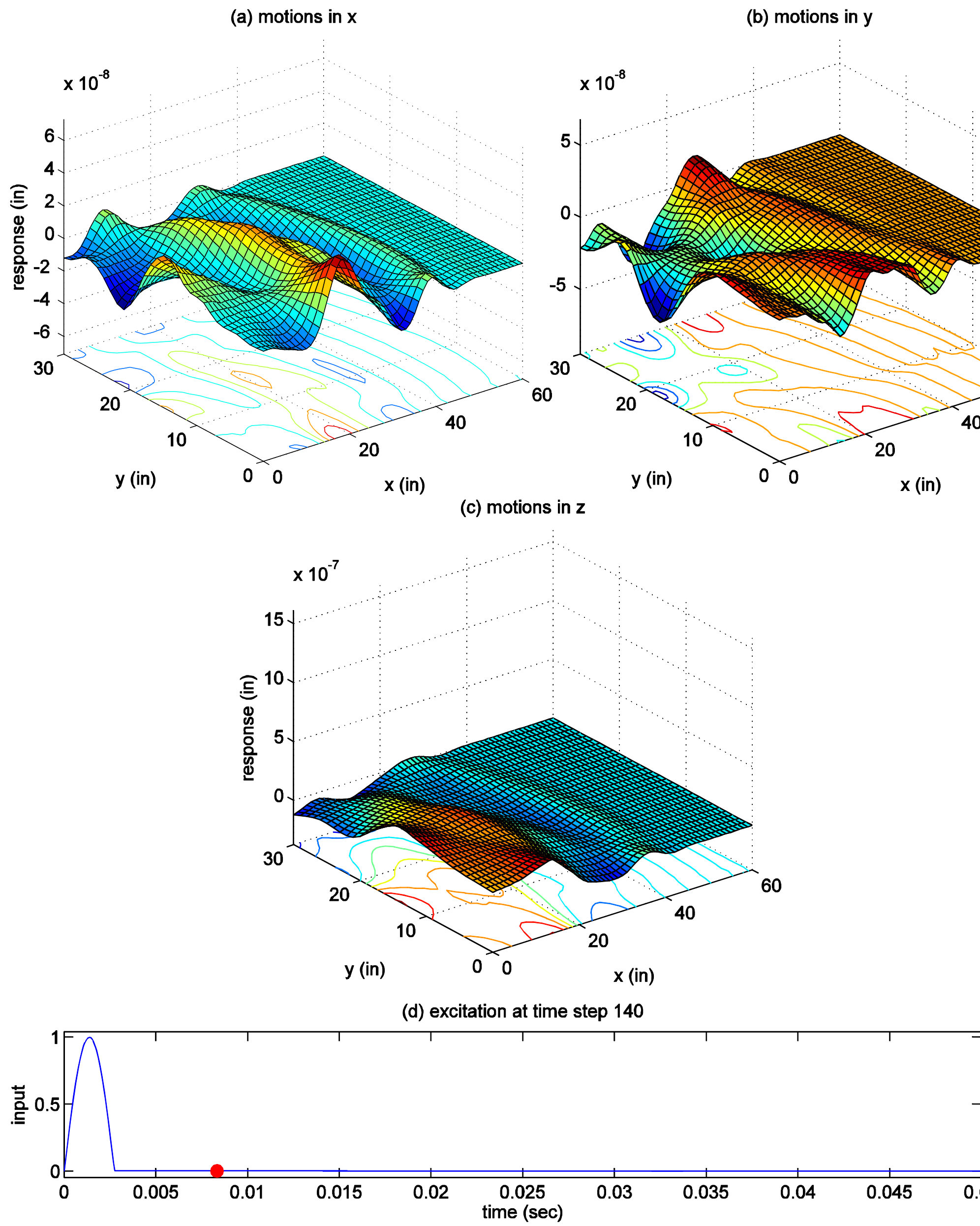

Figure 3.25: Motions of the FEM plate in x, y and z directions undergoing excitation (at time step 140)

Figure 3.24 and 3.25 illustrate the wave propagating motions in the FEM plate in three directions (x, y, and z) caused by the input force shown in Figure 3.24(d) and 3.25(d). Since the excitation is caused by a sensor located at (x = 10in (length direction), y = 10in (width direction)), the motions start at the region close to (x = 10in, y = 10in) and propagate to the rest of the plate. By comparing the motions of an undamaged plate and a damaged plate, Figure 3.26 and 3.27 shows the distortion effect of the crack propagating in the damage plate. The distortion starts at the location of the crack and spreads to the rest of the plate as time passes. By detecting distortions and measuring the spread patterns of the distortions, cracks or defects that form during the service cycle of the plate can identified and localized.

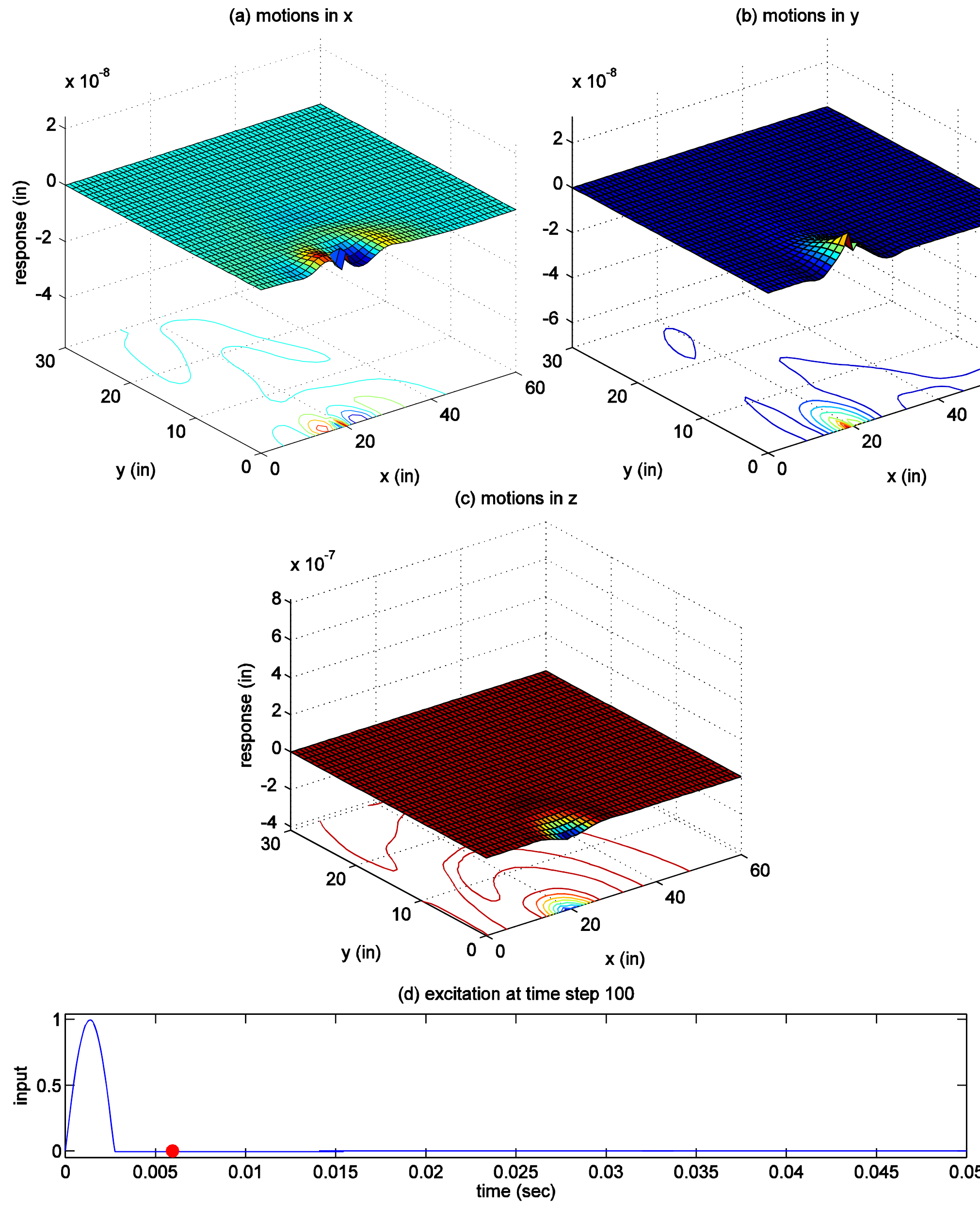

Figure 3.26: Distortion of the FEM plate in x, y and z directions undergoing excitation (at time step 100)

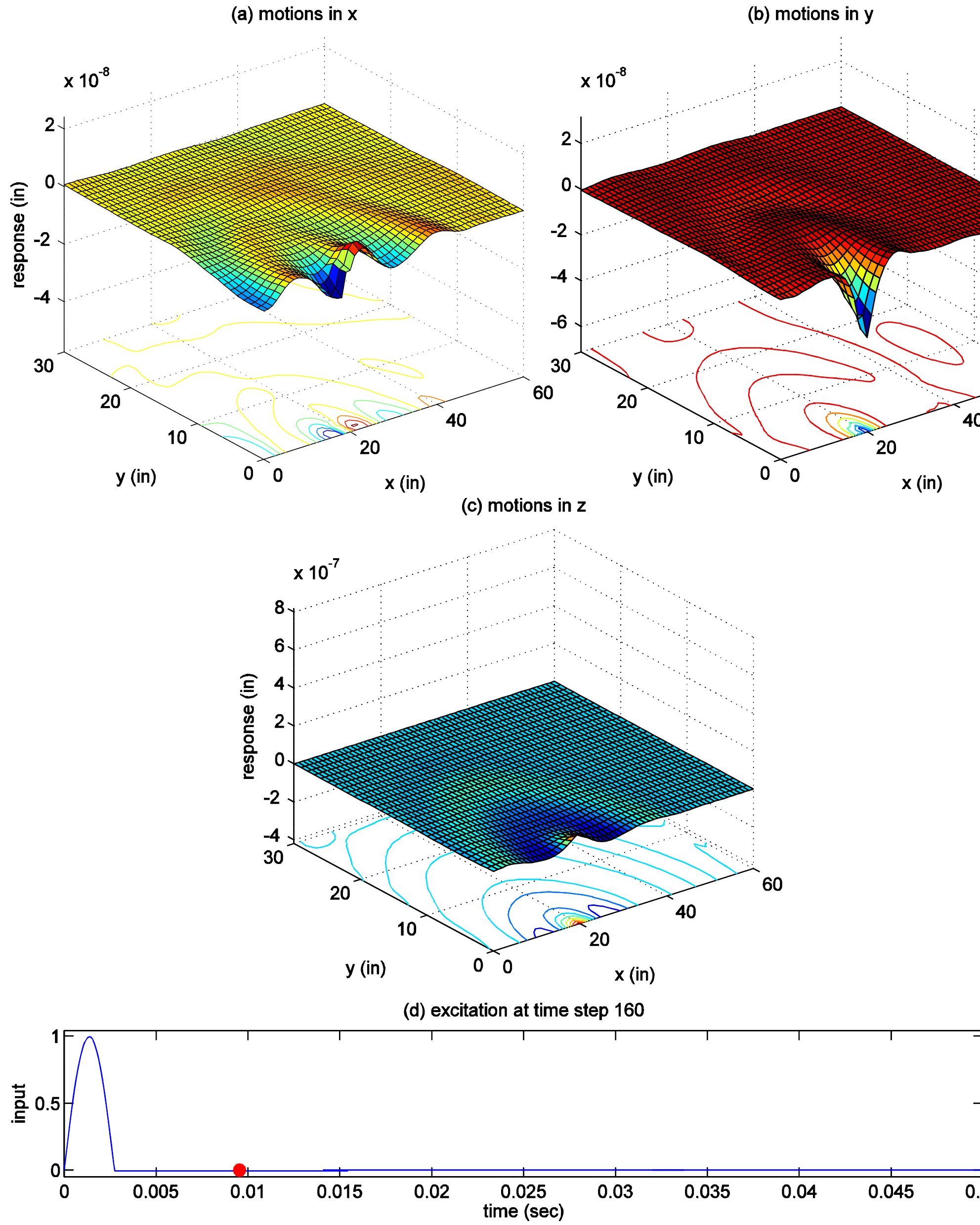

Figure 3.27: Distortion of the FEM plate in x, y and z directions undergoing excitation (at time step 160)

Figure 3.28 illustrates the responses of two nodes in the FEM simulation. Node A is closer to the crack than Node B in this example (see Figure 3.23) and therefore the crack should affect Node A earlier (and possibly with a greater impact) than Node B. Consider the responses measured by Nodes A and B in simulating the undamaged plate, $y_0^A(t)$ and $y_0^B(t)$, respectively, and in the damaged plate (with a crack), $y_c^A(t)$ and $y_c^B(t)$, respectively. Figures 3.28(a) and 3.28(b) show these responses over time with and without the presence of noise.

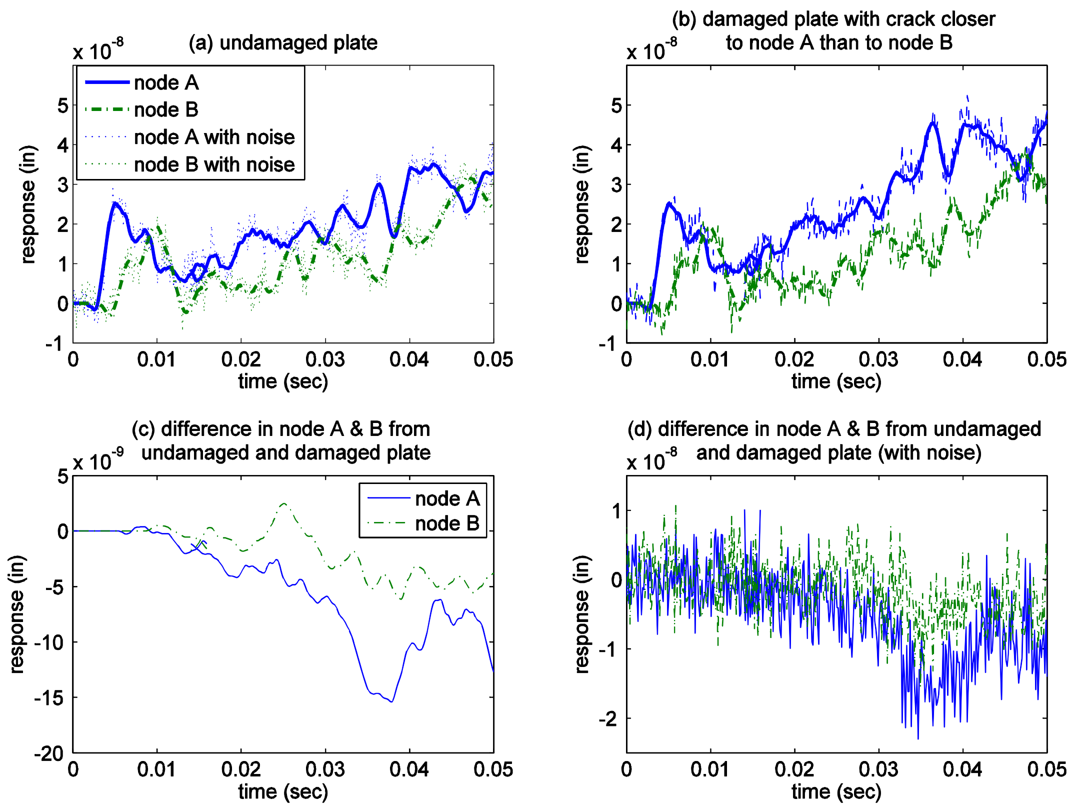

Figure 3.28: Reponses of two nodes on the FEM plate (Node A is located closer to the damage than Node B)

Damage can be detected by studying the distortions between the responses of undamaged and damage plates, given by:

$$y_*^{\mathrm{A}}(t) = y_0^{\mathrm{A}}(t) - y_c^{\mathrm{A}}(t) \qquad \text{or} \qquad \hat{y}_*^{\mathrm{A}}(t) = y_*^{\mathrm{A}}(t) + \mathbf{N}_{\mathrm{A}}(t) \qquad (3.38)$$

and
$$y_*^{\mathrm{B}}(t) = y_0^{\mathrm{B}}(t) - y_c^{\mathrm{B}}(t) \qquad \text{or} \qquad \hat{y}_*^{\mathrm{B}}(t) = y_*^{\mathrm{B}}(t) + \mathbf{N}_{\mathrm{B}}(t)$$

where $\mathbf{N}_{\mathrm{A}}(t)$ and $\mathbf{N}_{\mathrm{B}}(t)$ is noise in the measurement from senor Nodes A and B, respectively. Figure 3.28(c) illustrates that distortions without noise (*i.e.*, $\mathbf{N}_{\mathrm{A}}(t)=\mathbf{N}_{\mathrm{B}}(t)=0$) appear sooner at nodes closer (Node A) to the damage/crack. However, noise in the measurement can severely challenge detecting which node's distortions appear sooner (Figure 3.28(d)). To account for noises in the measurements, integrating the distortions over time is used to determine which nodes are closer to damage. Integrating the squares of (3.38) results in

$$\int \left(\hat{y}_*^{\mathrm{A}}(t)\right)^2 dt = \int [y_*^{\mathrm{A}}(t) + \mathbf{N}_{\mathrm{A}}(t)]^2 dt$$

$$= \int \left(y_*^{\mathrm{A}}(t)\right)^2 dt + 2\int y_*^{\mathrm{A}}(t)\mathbf{N}_{\mathrm{A}}(t)dt + \int \mathbf{N}_{\mathrm{A}}^2(t)dt \qquad (3.39)$$

And
$$\int\left(\hat{y}_*^{\mathrm{B}}(t)\right)^2 dt = \int\left(y_*^{\mathrm{B}}(t)\right)^2 dt + 2\int y_*^{\mathrm{B}}(t)\mathbf{N}_{\mathrm{B}}(t)dt + \int \mathbf{N}_{\mathrm{B}}^2(t)dt. \qquad (3.40)$$

Assuming the noise to be a zero-mean Gaussian random process that is statistically independent among the sensor nodes, $\int \mathbf{N}_{\mathrm{A}}^2(t)dt = \int \mathbf{N}_{\mathrm{B}}^2(t)dt$, as $t\rightarrow\infty$. Moreover, since $y_*^{\mathrm{A}}(t)$ is independent from $\mathbf{N}_{\mathrm{A}}(t)$ and $\mathbf{N}_{\mathrm{A}}(t)$ is assumed to be zero-mean Gaussian, $\int y_*^{\mathrm{A}}(t)\mathbf{N}_{\mathrm{A}}(t)dt = 0$, (likewise for $\int y_*^{\mathrm{B}}(t)\mathbf{N}_{\mathrm{B}}(t)dt$), as $t\rightarrow\infty$. Thus, from (3.39) and (3.40),

$$\int\left(\hat{y}_*^{\mathrm{A}}(t)\right)^2 dt > \int\left(\hat{y}_*^{\mathrm{B}}(t)\right)^2 dt \quad \leftrightarrow \quad \int\left(y_*^{\mathrm{A}}(t)\right)^2 dt > \int\left(y_*^{\mathrm{B}}(t)\right)^2 dt \tag{3.41}$$

Assuming that nodes closer to the crack should experience more distortions over time, (3.41) will hold true when Node A is located closer to the damage/crack than Node B. Thus, comparing the integrals of the squared distortions (*i.e.*, (3.39) and (3.40)) can determine which sensor node is closer to the damage. Figure 3.29(b) shows the cumulative integration of the distortions in Node A and B which clearly indicates that Node A has a higher value and therefore more likely the node closer to the crack; it is more difficult to compare the nodes using their distortions in Figure 3.29(a). There is also the issue of motions reflected from the edges of plate that increase the motions on nodes/sensors close to the edges, affecting the assumption of larger distortions on nodes/sensors close to the damage. This reflection issue will be further discussed in the following sections.

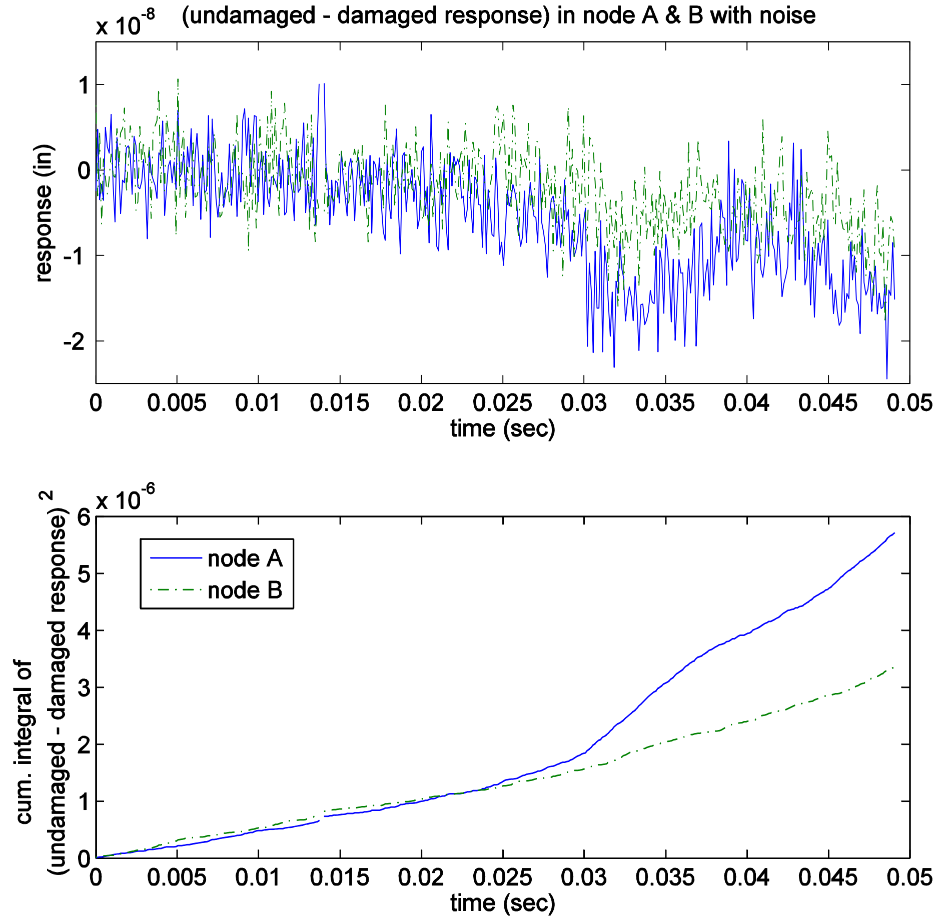

Figure 3.29: Noisy measurements on two nodes and their cumulative integrals over time

3.4.2 Effect of Sensor Placement

The sensor placement has a significant effect on the small scale damage detection via wave propagation. The damage is detected by comparing measurements of the undamaged and damaged structural element where the sensors serve two functions — inducing and capturing motions. Since the distortions from damage in the propagating motions of the plate are used to identify and localize damage, the closer the sensor is located to the damage, the sooner and larger effect the distortions the sensor can measure. However, since wave propagation reflects from edges of the plate, sensor nodes close to the edges and corners are likely to experience larger motions compared to the inner-nodes. This poses a challenge to identify sensors with larger distortions from a nearby crack but not from additional reflections from edges of the plate.

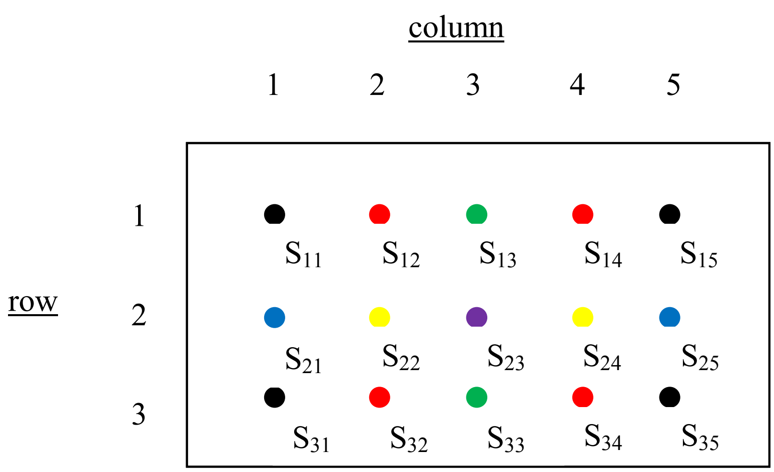

Figure 3.30: Senor layout and grouping illustration

Consider a rectangular plate with $n \times m$ sensors placed in a $n \times m$ (n rows and m columns) grid (*i.e.*, 15 sensors in 3×5 grid in Figure 3.30). The sensors are grouped in the following way such that the sensors within a group have similar separations from the corners and edges of the plate:

- Group: $S_{i,j}$, $S_{i,(m\text{-}j+1)}$, $S_{(n\text{-}i+1),j}$ and $S_{(n\text{-}i+1),(m\text{-}j+1)}$ for $i = 1, 2, \ldots, n$ and $j = 1, 2, \ldots, m$.
- For n or m odd, there are groups of two sensors instead of four.

This effectively creates sensor groups by matching rows and columns that have similar separations from the edges of the plate. For example in Figure 3.30,

1. Corner sensors are grouped (S_{11}, S_{15}, S_{31} and S_{35}, black sensors) by grouping sensors of the first and last rows and the first and last columns.
2. The sensors of the next inter-columns are grouped for the same first and last rows (S_{12}, S_{14}, S_{32} and S_{34}, red sensors).
3. Since $m = 5$ (odd), there are only two sensors remaining in the first and last rows to be grouped (S_{13} and S_{33}, green sensors).
4. Row 2 (the remaining unmatched row) is grouped following the previous steps except there are groups of two sensors (S_{21} and S_{25}, blue sensors, and S_{22} and S_{24}, yellow sensors) since $n = 3$ (odd).
5. Since both m and n are odd, there is an unmatched sensor (S_{23}, purple sensors).

By the described grouping approach, the sensors within the group have similar separations from the four edges of the plate such that the grouped sensors should experience similar reflections from the edges. For each sensor group, the location of the damage can be estimated by the amount of distortions (between responses of undamaged and damaged plates) at the sensors assuming the reflections from the edges can be accounted for using this grouping method. The amount of distortions is assumed to be proportional to the distances between the sensors and the damage (sensors closer to the damage experience larger distortions). For example, S_{31} in

Figure 3.31 should experience the largest distortions since d_{31} is the shortest, and the levels of distortions detected by S_{11}, S_{15}, S_{31} and S_{35} should be proportional to d_{11}, d_{15}, d_{31} and d_{35}, respectively. Thus, the scalar relationships between d_{11}, d_{15}, d_{31} and d_{35} can be estimated by observing the distortion levels in S_{11}, S_{15}, S_{31} and S_{35}.

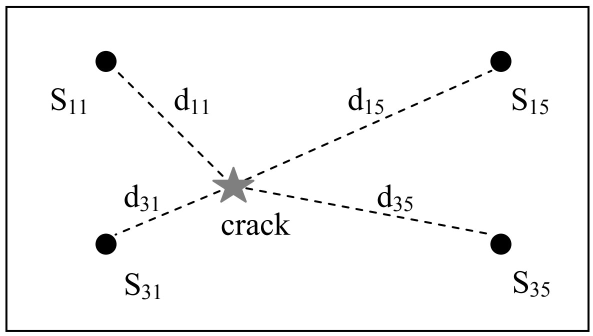

Figure 3.31: Distances between sensors and the damage

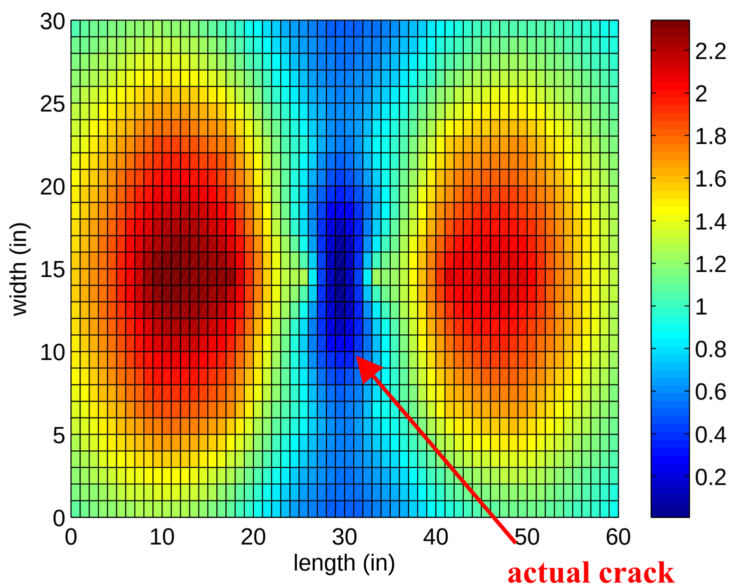

Figure 3.32: Plot of the damage location likelihood for damage pattern 1 (lower value = more likely)

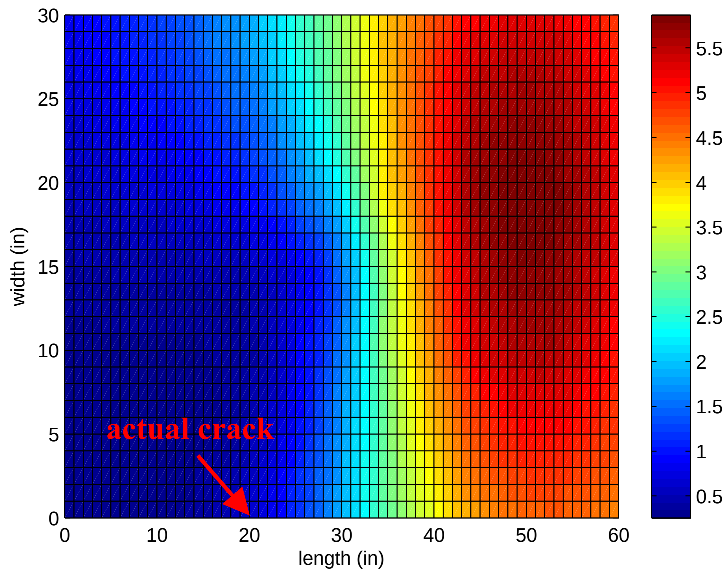

Figure 3.33: Plot of the damage location likelihood for damage pattern 2 (lower value = more likely)

To estimate the location of the damage, the plate is first divided into grid nodes such as Figure 3.32. Each node is assumed to be the damage origin and an error value is computed by comparing the distances between the node and a group of sensors and the distortion levels of the sensors. If the distance lengths match proportionally to the distortion levels, the error value is low; otherwise, the error value is high. The sum of the error values for all groups of sensors creates error maps shown in Figure 3.32 and 3.33. In both figures, the lowest error value regions are the most likely locations of damage and the actual crack locations are close to these regions.

3.4.2.1 Layout and Number of Sensors

The previous section details an approach to estimate the damage locations in plates from comparing the responses of undamaged and damaged plates. Such estimation is heavily influenced by the sensor placements that, in fact, are controlled by the numbers of sensors, the layouts and distances between sensors. Since the damage is detected by estimating the distances between the sensors and the damage, ideally at least some of the sensors should be placed close to where the damage is. If cost and practicality are not concerns, a larger number of sensors is desirable to cover the plate extensively. For a certain number of sensors, the sensors should be spread throughout the plate such that each sensor covers similar size of area on the plate (Figure 3.34). This can minimize the distance between the unknown location of the damage and its closest sensor. This study compares how different sensor placements (the number and the layout of sensors) affect the quality of damage detection in the plate.

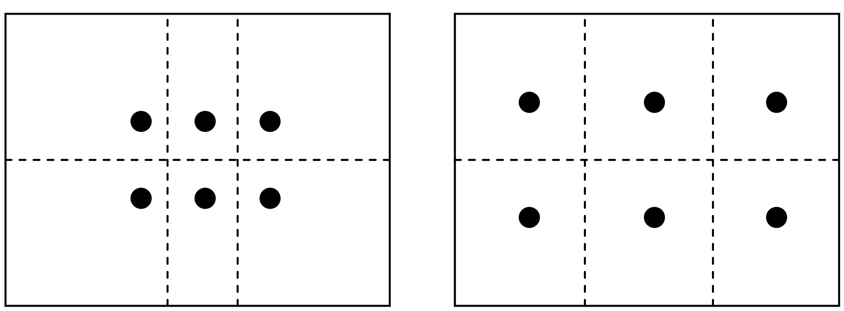

Figure 3.34: Cluster sensor layout and spread sensor layout

Using a grid layout, the number of sensors is directly related to the sensor layout. Nine grids with different numbers of sensors are presented in Table 3.9 for the damage study on the plate. Different distances between neighboring sensors are also considered to study the effect of sensor placements. Figure 3.16 (in section 3.3.3.3.2.3) shows some sensor placements for a rectangular region similar to the plate in this study.

number of sensor	6	8	9	10	12	15	18	20	24
layout grid	2×3	2×4	3×3	2×5	3×4	3×5	3×6	4×5	4×6

Table 3.9: Sensor numbers and layouts

3.4.2.2 Result

Figure 3.35 demonstrates the effect of different sensor placements on estimating the location of the damage shown in Figure 3.33. For all sensor grid layouts, the estimation errors generally decrease with increasing distances between sensors. Increasing distances between sensors spreads out the sensors on the plate and evens out the area of the plate each sensor is associated with (Figure 3.34). The lower errors in larger distances between sensors suggest that a spread out sensor placement is more favorable for damage detection. Figure 3.35 also shows that increase numbers of sensors lower damage estimation errors. With more sensors, each sensor is responsible for a smaller region of the plate and the probability of the damage being close by a sensor increases. The large number of sensor can also helps dealing with the noises in measurements.

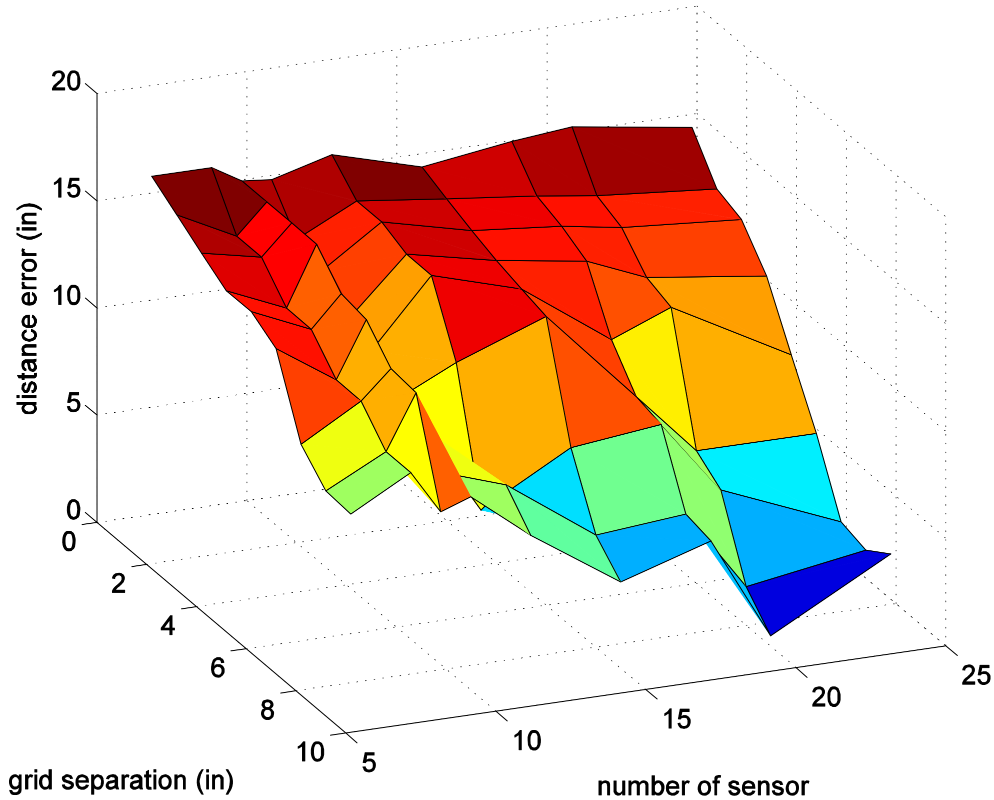

Figure 3.35: Effect of sensor numbers and distances on damage estimation

The number of sensors is directly related to the grid layout (Table 3.9). To understand the effect of sensor numbers and grid layout, Figure 3.36 separates Figure 3.35 by the numbers of rows in the sensor grid layouts. For the sensor layouts with the same rows of sensors (*e.g.*, the grids of 3×3, 3×4, 3×5, and 3×6), as the number of sensors or the number of columns in the grid increases, the estimate errors generally decrease. Additionally the slopes in Figure 3.36 appear to be sharper for large numbers of sensors, implying that sensor distances lead greater improvement rates in damage estimations with a larger number of sensors.

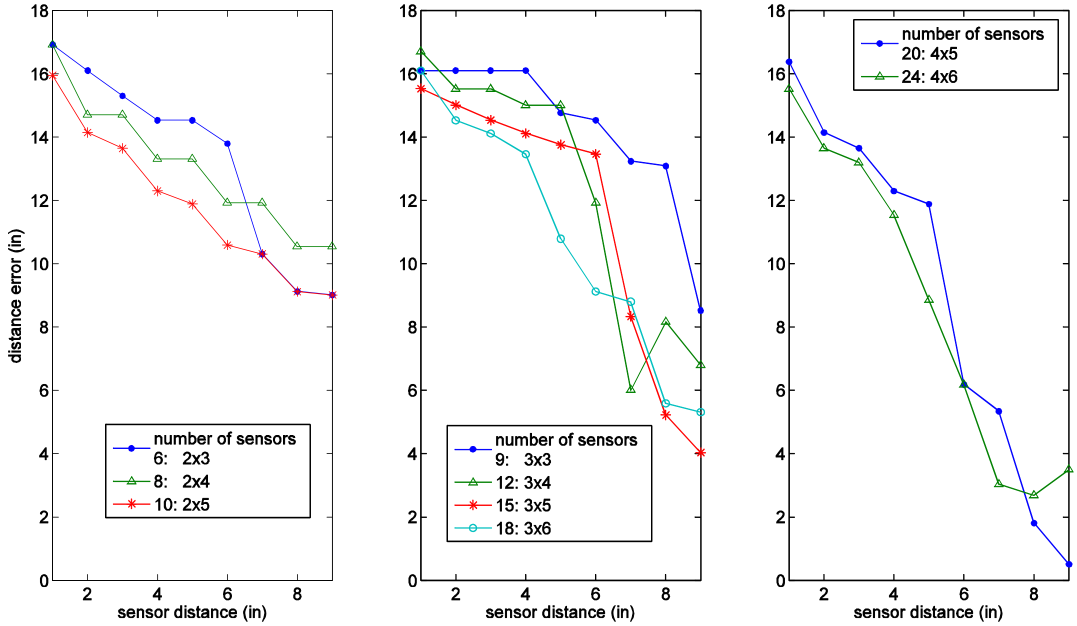

Figure 3.36: Effect of sensor distances on damage estimation

3.5 Summary

By exciting structures globally, SHM algorithms can detect damage by analyzing the resulting structural responses. This chapter improves a SHM algorithm by expanding from one directional (single lateral motions) analysis to three directional (two lateral motions and rotations). The three directional analysis can apply to more realistic structures when damage and the structures are not perfectly symmetric, while revealing more information on structural stiffness estimates. The standard three directional analysis is less accurate compared to the one directional analysis. A proposed method is shown to significantly increase accuracy by combining the structural stiffness estimates from both the one- and three-directional analyses.

Using wireless sensor networks (WSNs) for SHM can reduce installation cost by eliminating the wiring cost at the expenses of energy and bandwidth constraints. By processing data locally at the sensors and transmit only the processed and reduced data, the energy and bandwidth constraints can be addressed for WSNs. A recently developed distributed algorithm is shown effective for SHM by processing local data to estimate modal parameters of the structure. The analysis of the distributed algorithm is comparable to a more traditional SHM algorithm (ERA) that requires transmitting unprocessed data to a central node. The distributed algorithm accurately detects damage while reducing data transmission and energy consumption caused by radio communication.

The placement of wireless sensors also has significant impact on energy consumption of WSNs. Energy spent on radio communication increases rapidly to the distances between sensors, encouraging dense sensor placements. However, structural measurements are more accurate with sensors placed far from each other. By studying the conflicting effect of the number of sensor and their separations on SHM and WSNs, an optimization method for sensor placement is derived to balance the accuracy in SHM and energy efficiency in WSNs.

Global excitations are effective in identifying damaged regions for structures, but only local excitations are suitable for localizing damage in structural elements. By measuring wave propagation induced by local excitations, damage can be detected when the responses differ significantly from those of the undamaged elements. Damage in a finite element model of a structural plate is successfully detected using local excitation. The effect of sensor placement on the plate is also studied in terms of the numbers, layouts and distances between the sensors. Accuracy in damage detection increases sharply with more sensors and larger distances between sensors.

Chapter 4 – Shading Fin Mass Damper System

This chapter introduces a shading fin mass damper (SFMD) system integrating a smart structure with an environmental control system. By exploring the synergy between structural and environmental control systems, the integrated system can be more efficient, better utilized, and cost saving, while creating smarter buildings. Figure 4.1 shows a plan view of the system, while Figure 4.2 shows the perspective, front and section views of the SFMD system. The movable shading fins can adjust positions to allow or block sunlight into the building. Moreover, the fins also serve as mass dampers (see Figure 4.3) which move and damp energy out of the structure to reduce vibration. The shading fins may also affect the aerodynamics of the building but this is a subject beyond the scope of the dissertation.

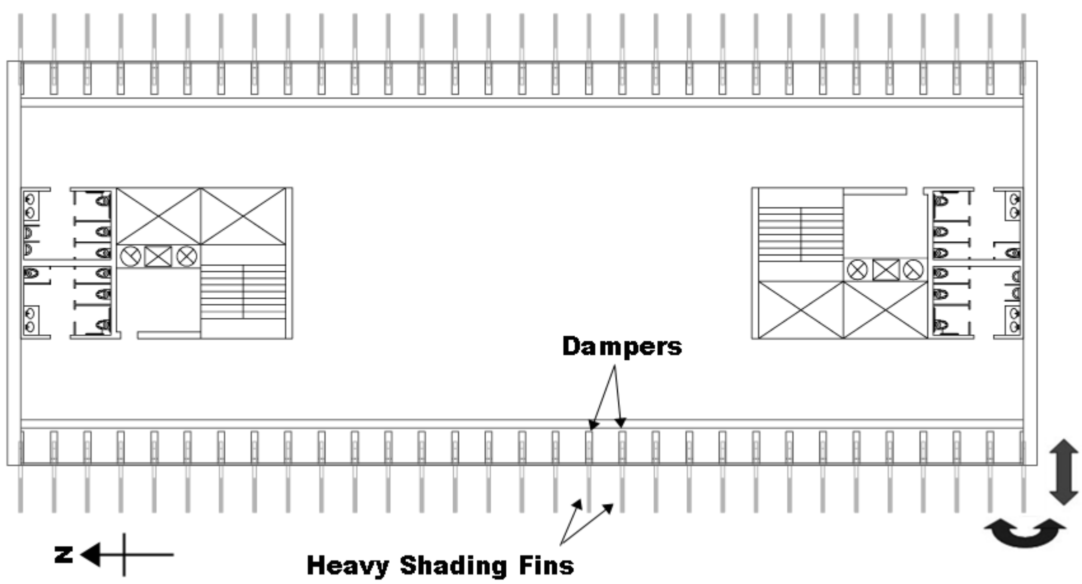

Figure 4.1: Plan view of the Shading Fin Mass Damper system

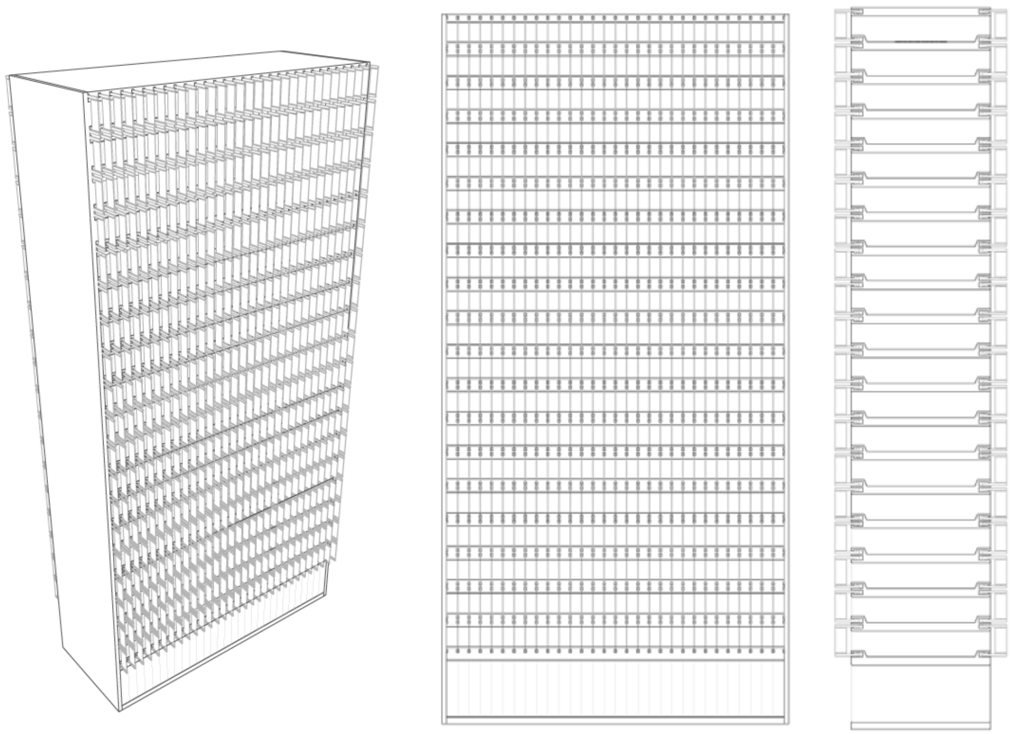

Figure 4.2: Shading Fin Mass Damper system: perspective, front, section views

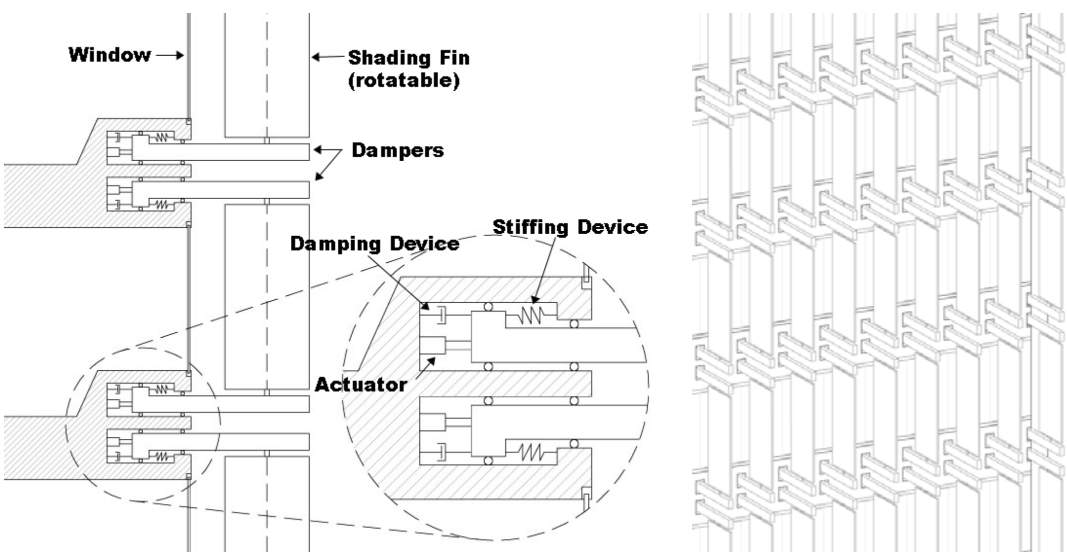

Figure 4.3: Shading Fin Mass Damper system: (left) details; (right) outside details

4.1 Introduction

There are two fundamental tasks to show the effectiveness of the SFMD system: 1) how to use the mass dampers to reduce structural vibration and 2) how to use the shading fins to reduce building energy consumption. Since the structural and environmental control systems are joined, the two fundamental problems face an additional challenge of providing sufficient capacity of the joined functions without significantly compromising the individual functions. Additionally, since the SFMDs are designed to be controlled by actuators to adjust the fin positions, the actuators can also be used to excite the structure for SHM purposes. This chapter addresses this new challenge of using the SFMD system for damage detection, along with the aforementioned challenges of reducing structural vibration and energy consumption concurrently.

The mass dampers of the SFMD system are unique because they are placed throughout the structure to shade the entire building. Traditional mass dampers are concentrated in a few locations in the structure (typically in the upper floors). Another contrast is the larger number of individual mass dampers for the SFMD system, making each of them less massive compared to the traditional mass dampers. This non-traditional damper system presents the challenge of designing many dampers in various locations of the structure to reduce vibration. This chapter first analyzes the SFMD system for passive, active and semiactive structural control.

Another challenge of the SFMD system is shading the building to reduce solar and heat gain for energy efficiency. Traditionally shading devices (*e.g.*, overhangs, fins) are stationary and can only shade the building for specific periods of time. The stationary shades are usually designed for the hottest periods of the year, around noon and afternoon in the summer time. This inflexibility can result in poor performance in time periods other than those for which the shades are designed, such as winter time when the heating is needed and shading is, thus, undesirable. Some stationary shading designs (*e.g.*., overhangs) can remedy some of the inflexibility. This chapter studies movable shading fins that are completely flexible by adjusting continuously to the conditions of the building and weather. The derived movements of the SFMDs are determined for minimizing the annual energy consumption of the building.

SHM using the SFMDs is also studied in this chapter. The SFMDs present a unique opportunity to SHM where the structure can be excited in many locations within the structure. By exciting the structure at different combinations of locations instead of single location, the structure can undergo a wider range of response behaviors such that more key structural characteristics can possibly be exposed. The difficulty in exciting the structure with SFMDs is that the excitations can only induce small structural motions. The actuators controlling movements of the SFMDs are designed to accommodate the slow changing building environmental and weather conditions. Such actuators are, most likely, incapable of inducing large excitations on the structure. The last part of this chapter discuses the challenge of exciting the structure with multiple SFMDs to detect structural damage with small excitation forces. Although only one-directional structural motion is studied for SHM in this dissertation, the many SFMDs on each floor allows study of three-directional motions (such as torsions) for SHM on more complex and realistic structures.

4.1.1 Synergy

Identifying and exploring synergy is very important to efficiently integrate distinct systems. Synergy is defined as a joint venture that is mutually advantageous to the involved partners (Merriam-Webster, 2008). To clarify mutual advantages, one can consider the following equation:

$$\text{Mutual Measure} = M = (B_j - \sum B_i) - (C_j - \sum C_i) \tag{4.1}$$

where the B_j are the benefits of the joint venture, the B_i are the benefits of the individual partners in separate settings, and the C_j and C_i are the costs of the joint venture and individual partners, respectively. Clearly, the joint venture is only profitable or meaningful when $M > 0$ and only then can the joint venture be called synergy.

Most of the time, M is positively related to the compatibility of the different partners. If the partners are highly compatible, they are more likely to increase their joint benefits while decreasing their joint costs. Therefore, partner compatibility is a major consideration when selecting partners to form synergy. A compatible example of synergy is gasoline and electricity in hybrid automobiles. In conventional automobiles, gasoline is used to accelerate the vehicles and electricity is used to power the electronics of the vehicles. Hybrid technology draws energy from both gasoline and electricity for acceleration. Since more electricity is needed, a battery of larger capacity stores more electricity converted from the energy created during braking. Clearly, the joint venture of gasoline and electricity in automobiles is a synergy since they yield better mileage compared to conventional automobiles. The success of hybrid automobiles lies in their compatibilities in the following ways:

- They have compatible objectives. In fact, their objective is the same – to increase mileage efficiency.
- They are physically compatible; both gas and electricity are used in the engine to accelerate the vehicles.

As shown in the example, objective and physical compatibilities play important roles in creating synergy.

There is an additional benefit of the hybrid automobiles: sustainability. In a macro scale, the improved mileage reduces the gasoline consumption and, thus, conserving natural resources for future generations. The positive effect by the hybrid technology on the environment is obvious and yet hard to quantify in a macro scale. However, consumers are paying attention and investing into this increasing popular "green" technology. The SFMD system is very similar in the following aspect. The structural improvement and energy saving can be measured accurately, assessing the cost and returns of the system. Although the sustainability and the environmental effect can be difficult to be gauged for the SFMD system, they would only present as positive incentives to building developers and the general public who are increasing environmentally conscious.

4.1.2 Compatibilities between Structural Control and Environmental Control

Although Structural Control (SC) and Environmental Control (EC) have generally different objectives, their objectives are indeed compatible. The goal of SC is to prevent structural damage in large structural motions as well as to reduce smaller motions that are unlikely to cause damage but likely to cause occupant discomfort. The goal of EC is to provide human comfort for the occupants of the building under a reasonable cost. The compatibility lies in the scheduling and urgency of the objectives.

EC is, essentially, operating continuously for large buildings since there are always occupants within the building. The number of occupants may differ from time to time (for example, there are more people during office hours for office buildings while there are still maintenance and security crews during off-peak hours), but EC still provides service regardless of occupancy level. Moreover, EC of a large building often has different duties during off-peak hours, such as ice storage that chills water at night when electricity is cheaper.

SC, on the other hand, is not continuously operating. Since buildings undergo violent vibrations only during wind storms, earthquakes or other rare events, SC may not be needed daily. Even when these events occur, they typically last for a short time and common building operations can resume quickly. Strong wind may occur more frequently and last longer in windy area such as Chicago, but their severity and occurrence are somewhat predictable with weather forecasts. Such information can be used in sharing service times between SC and EC in a structural and environmental control synergy system.

Since the objectives of SC and EC do not overlap much in scheduling, they seldom get in each other's way. However, under rare circumstances when their objectives are needed concurrently, there is another fundamental factor of the objectives that makes SC and EC compatible: the urgency of the objectives. When different objectives need to be addressed concurrently and they cannot be addressed separately with full resources, then a compromise must be made between them based on the importance of the objectives under the current situation. It is difficult to argue whether SC or EC is more important overall since their importance is measured in different time frames. Although the failure of SC may be more devastating than the failure of EC (structural safety compared with human comfort), the frequency of a building using SC is relative small compared to EC. Over time, EC may even have greater effects on building cost because it is utilized more frequently. Nonetheless, structural safety is definitely a more urgent concern than human comfort when both concerns are present. Moreover, controlling building vibration typically takes a short period of time and EC can be resumed quickly afterward. Thus, the objectives of SC and EC are still compatible when both objectives are to be addressed.

Other than scheduling, the physical compatibility between SC and EC is another key factor for creating structural and environmental control synergy. However, Chapter 2 shows that there are many different types of SC and EC and each type can have its distinct physical characteristic. Therefore, it is impractical to discuss the physical compatibility in a general sense. The following section proposes a synergy system and discusses its physical compatibility in details.

In order to make the joint venture of SC and EC a synergy, their *M* value must be positive in (4.1). This generally happens if joint benefits increase and/or joint costs decrease. One of the main costs of control systems is the computational resource. Based on the current state of the system, control force must be calculated that stabilize the system. For a complex system, a large amount of computer power and a sophisticated sensor network may be needed to estimate the current state and calculate the control force in real time before the system's state changes. Since SC and EC are compatible, they could share their computational and sensor network resource to reduce cost. Moreover, the joint and more powerful resource maybe able to analyze the control systems faster/better and therefore give better control input to increase the overall efficiency/benefits of the structural and environmental control synergy system.

4.1.2.1 Compatibilities between Mass Damper and Shading Fin

Although tuned mass dampers (TMDs) and active shading fins (ASFs) have generally different objectives, they are indeed compatible. As discussed in the previous section, structural control (SC) and environmental control (EC) systems are generally compatible with each other but further examinations of the physical compatibility are needed for individual cases. In the SFMD system, the movements of mass dampers require shading fins to be movable whereas typical exterior shading fins are fixed. Movable fins can adjust the amount of direct sunlight coming into the building according to the lighting condition and temperature inside the building. On the other hand, by using movable shading fins, the cost of the shading-fin-mass-damper (SFMD) system can be more easily justified since the mass dampers are not often used (only during strong building vibration). Moreover, the increased number of mass dampers makes the SFMD system more flexible to a wider range of excitations than conventional single TMD systems. Therefore, although the physically compatibility of TMD and shading fins may not be obvious, special and careful design considerations can effectively integrate the SC and EC systems.

4.1.3 Synergy Diagram

A list of SC systems and a list of EC systems are given below. Structural and environmental control synergy can be created by picking one system from each list and checking if the selected systems can complement each other.

Structural Control

Base isolation system
- Elastomeric bearings
- Lead rubber bearings
- Sliding friction pendulum

Passive Energy dissipation
- Metallic dampers
- Friction dampers
- VE dampers
- Viscous fluid dampers
- Tuned mass dampers
- Tuned liquid dampers

Semiactive and active control
- Active bracing systems
- Active mass dampers
- Variable stiffness or damping systems
- Smart materials
- Magnetorheological (MR) dampers are new semiactive control devices that use MR fluids to form a controllable damper

Environmental Control

Passive Systems
- Natural ventilation
- Thermal mass
- Sunspace
- Shading devices (overhangs, fins)
- Ventilation cooling
- Radiant cooling and heating
- Evaporation cooling
- Insulation
- Daylighting

Semiactive and active systems
- Roof radiation trap
- Movable shading devices (overhangs, fins)
- Convective cooling
- Heating units
- Cooling tower
- A/C units
- Air supply (fans)
- Artificial lighting

The list can be used to identify the following structural and environmental control synergy cases. The Shading Fin Mass Damper (SFMD) example is identified by realizing the dual use of the shading fins as mass dampers. The combined control system is designed and analyzed from both structural and environmental aspects in the next chapters. Improvement of structural safety and energy saving is also mentioned.

4.1.4 Case studies

There are few built examples of structural and environmental control synergy. In fact, the following examples were built by the same firm around the same time. Nonetheless, the combined systems illustrate synergy in the integrated SC and EC systems.

4.1.4.1 Sendagaya INTES Building in Tokyo (1991)

An example application of a synergy system is the Sendagaya INTES Building (Figure 4.4) in Tokyo designed by Takenaka Corporation in 1991. The building is 11 stories tall and contains 10,602m^2 in floor area. On the top floor, there are two ice thermal storage tanks serving as Hybrid Mass Dampers (HMDs) to control transverse and torsional motions of the structure (Figure 4.5). Hydraulic actuators are also placed to provide the active control capabilities. Using the ice thermal storage tanks as mass dampers avoids introducing extra weight to the structure, as typically required for mass dampers.

Figure 4.4: Sendagaya INTES Building (Sendagaya, 2003)

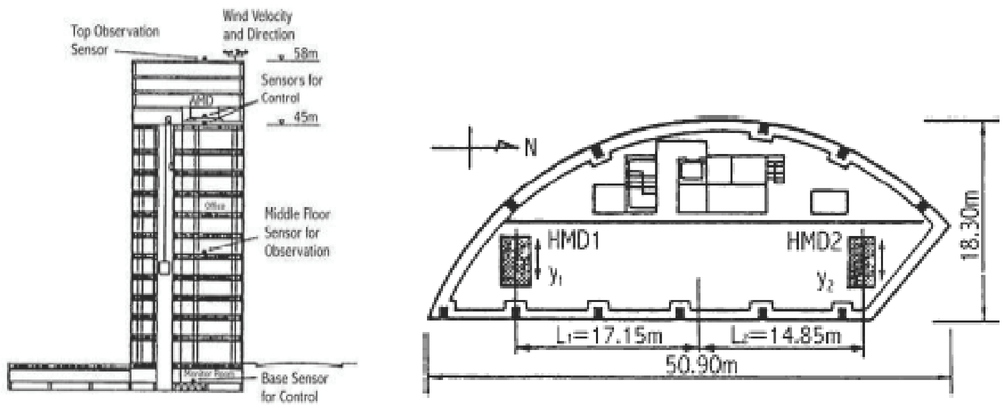

Figure 4.5: Sendagaya INTES building with hybrid mass dampers (Higashino and Aizawa 1993)

4.1.4.2 Crystal Tower in Osaka (1990)

The Takenaka Corporation also designed the Crystal Tower (Figure 4.6) in Osaka in 1990 (Nagase and Hisatoku 1992). It is a 157m tall building weighing 44,000 metric tons. Instead of using the ice thermal storage tanks as HMDs, the tanks were used as pendulum weights. The six 90-ton pendulum dampers hang from the roof girders with lengths of 4m and 3m. Oil dampers are connected to the pendulums to dissipate energy caused by building movements. Under wind excitation, the pendulum mass swings in sync with the sway of the building, reducing the movement of the building.

Figure 4.6: Crystal Tower (Crystal Tower, 2003)

4.2 Structural Control: Mass Damper System

This section discusses the structural control aspect of the Shading Fin Mass Damper system. Due to the integration with the shading fins, the mass damper system adopts a special configuration — called the distributed mass damper (DMD) system — that will be studied in this chapter. The performance of the DMD system is examined and compared with the traditional tuned mass damper system. Although some characteristics of the DMD system can be tuned to optimize performance, they may also be difficult to implement from the point of views of building design and construction. A simpler DMD system configuration is proposed that be more practical for the Shading Fin Mass Damper system while sacrificing only a small degree of performance.

4.2.1 Distributed Mass Damper (DMD)

Since shading fins are placed along the height of the building, the proposed SFMD system behaves differently than traditional TMD or multiple tuned mass damper (MTMD) systems (Figure 4.7). The mass dampers are distributed throughout the height of the building, instead of attaching only the top floors for tuned mass damper(s).

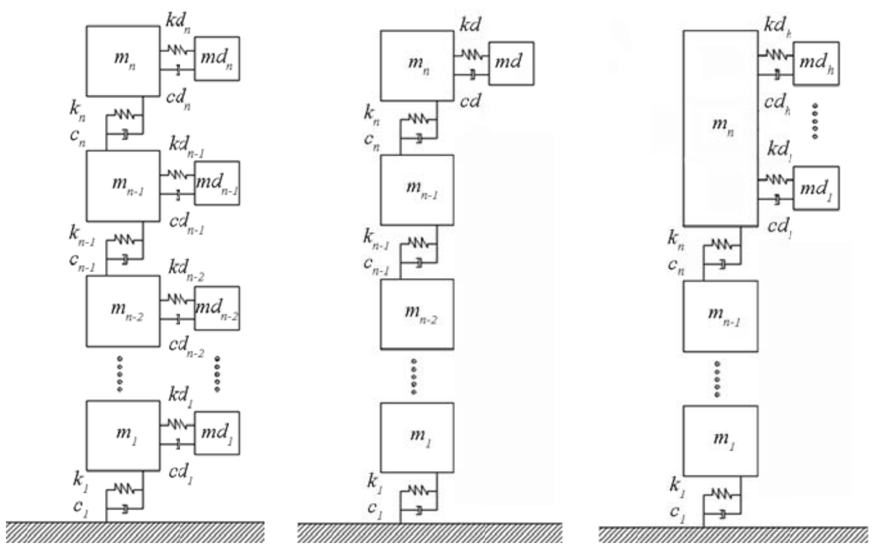

Figure 4.7: DMD, TMD, MTMD diagrams.

The equations of motions for the *n*-story structure with a DMD system can be expressed as

$$\mathbf{M}\ddot{\mathbf{x}} + \mathbf{C}\dot{\mathbf{x}} + \mathbf{K}\mathbf{x} = -\mathbf{M}\mathbf{1}\ddot{x}_{\mathrm{g}} + \mathbf{f} \tag{4.2}$$

where

$$\mathbf{M}=\begin{bmatrix} m_1 & 0 & 0 & 0 & \cdots & & 0 \\ -m_1^{\mathrm{d}} & m_1^{\mathrm{d}} & 0 & 0 & & & 0 \\ 0 & 0 & m_2 & 0 & & & 0 \\ 0 & 0 & -m_2^{\mathrm{d}} & m_2^{\mathrm{d}} & & & 0 \\ \vdots & & & & \ddots & & \vdots \\ & & & & & m_n & 0 \\ 0 & 0 & 0 & 0 & \cdots & -m_n^{\mathrm{d}} & m_n^{\mathrm{d}} \end{bmatrix},$$

$$\mathbf{K}=\begin{bmatrix} k_1+k_2 & -k_1^{\mathrm{d}} & -k_2 & 0 & 0 & \cdots & 0 \\ 0 & k_1^{\mathrm{d}} & 0 & 0 & 0 & & 0 \\ -k_2 & 0 & k_2+k_3 & -k_2^{\mathrm{d}} & -k_3 & & 0 \\ 0 & 0 & 0 & k_2^{\mathrm{d}} & 0 & & 0 \\ \vdots & & & & \ddots & & \vdots \\ 0 & \dots & 0 & -k_{n-1} & 0 & k_n & -k_n^{\mathrm{d}} \\ 0 & & 0 & 0 & 0 & 0 & k_n^{\mathrm{d}} \end{bmatrix},$$

$\mathbf{C}$ takes a similar form as $\mathbf{K}, \mathbf{x}=\begin{bmatrix} x_1 & x_1^{\mathrm{d}} & x_2 & x_2^{\mathrm{d}} & \cdots & x_n & x_n^{\mathrm{d}} \end{bmatrix}^{\mathrm{T}}$, x_{g} is the ground displacement, $\mathbf{f}$ is the external force vector of the system (*e.g.*, wind) and $\mathbf{1}$ is a column vector of ones. Here, m_i and m_i^{d} are the masses of the i^{th} floor and of the damper attached to the i^{th} floor, respectively, k_i and k_i^{d} are the stiffness coefficients of the i^{th} floor and between the i^{th} floor and the i^{th} damper, respectively, and x_i and x_i^{d} are the i^{th} floor displacement relative to the ground and the damper displacement relative to the i^{th} floor, respectively. The following basic structural terms are useful in describing dynamic structural systems:

- i^{th} floor frequency (for standalone floor): $w_i=\sqrt{k_i/m_i}$

- i^{th} floor damping ratio (for standalone floor): $\varsigma_i = c_i / (2 w_i m_i)$

- i^{th} floor damper frequency (for rigid structure): $w_i^{\mathrm{d}} = \sqrt{k_i^{\mathrm{d}} / m_i^{\mathrm{d}}}$

- i^{th} floor damper damping ratio (for rigid structure): $\varsigma_i^{\mathrm{d}} = c_i^{\mathrm{d}} / (2 w_i^{\mathrm{d}} m_i^{\mathrm{d}})$

4.2.2 Formulation / Simulation Model

The state space representation of (4.2) is

$$\begin{bmatrix} \dot{\mathbf{x}} \\ \ddot{\mathbf{x}} \end{bmatrix} = \begin{bmatrix} \mathbf{0} & \mathbf{I} \\ -\mathbf{M}^{-1}\mathbf{K} & -\mathbf{M}^{-1}\mathbf{C} \end{bmatrix} \begin{bmatrix} \mathbf{x} \\ \dot{\mathbf{x}} \end{bmatrix} + \begin{bmatrix} 0 & 0 \\ -\mathbf{1} & \mathbf{M}^{-1} \end{bmatrix} \begin{bmatrix} \ddot{x}_g \\ \mathbf{f} \end{bmatrix} \tag{4.3}$$

or $\dot{\mathbf{z}} = \mathbf{A}\mathbf{z} + \mathbf{B}\mathbf{u}$, where $\mathbf{u}$ is the input of the system. For earthquake loads, $\mathbf{f}$ is assumed to be zeros and $\mathbf{u}$ only depends on the ground acceleration. Four earthquake records are used for this analysis (Figure 4.8) (Ramallo *et al.,* 2002):

- *El Centro* — north-south component of the 1940 Imperial Valley, California earthquake (magnitude 7.1) recorded at the Imperial Valley Irrigation District substation in El Centro, CA;
- *Hachinohe* — north-south component of the 1968 Takochi-oki (Hachinohe) earthquake (magnitude 7.9) signal recorded at Hachinohe City, Japan;
- *Kobe* — north-south component of the 1995 Hyogo-ken Nanbu (Kobe) earthquake (magnitude 7.2) recorded at the Kobe Japanese Meteorological Agency (JMA), Kobe, Japan;

• *Northridge* — north-south component of the 1994 Northridge earthquake (magnitude 6.8) recorded at the Sylmar County Hospital parking lot in Sylmar, CA.

A Kanai-Tajimi shaping filter (Soong and Grigoriu, 1993) is then used to approximate the design earthquakes to allow for stochastic simulations with representative ground site frequency characteristics (Figure 4.9).

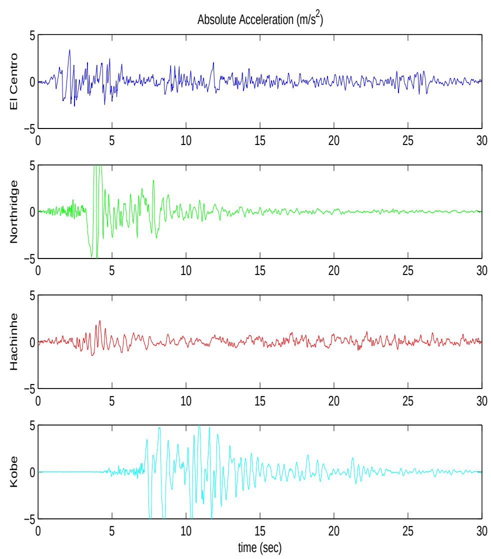

Figure 4.8: Design earthquakes

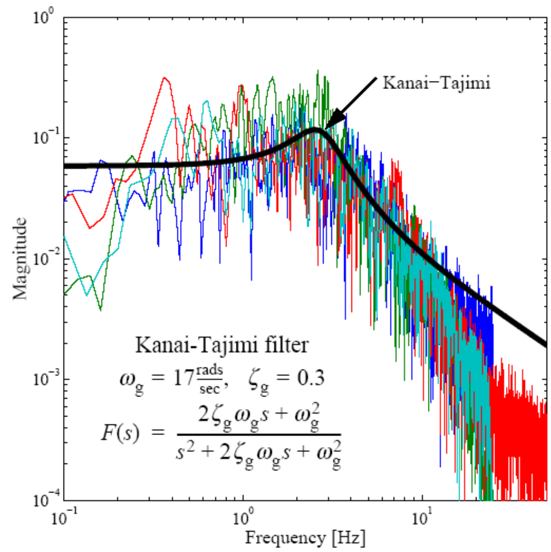

Figure 4.9: Frequency content of design earthquakes and Kanai-Tajimi filter (Ramallo *et al.*, 2002)

A 20-story simulation structure is modeled after an office building with floor dimensions of 150ft (length), 60ft (width) and 13ft (height), and at 90lb/ft^2. The story stiffness is determined according to the 1997 Uniform Building Code (International Code Council , 1997) with a story period of 0.1609sec for a 13ft high story. Table 4.1 lists the properties of the primary systems along with its modal characteristics.

20DOF ($i = i^{th}$ floor, i =1,2,…,20)					
		m_i (lbf)	25155		
		k_i (lbf/ft)	38359841		
		damping ratio	5%		
mode	frequency (rad/sec)	period (sec)	mode	frequency (rad/sec)	period (sec)
1	2.99	2.10	10	51.96	0.12
2	8.96	0.70	11	56.27	0.11
3	14.87	0.42	12	60.25	0.10
4	20.70	0.30	13	63.88	0.10
5	26.40	0.24	14	67.13	0.09
6	31.95	0.20	15	69.99	0.09
7	37.31	0.17	16	72.44	0.09
8	42.45	0.15	17	74.46	0.08
9	47.35	0.13	18	76.05	0.08
10	51.96	0.12	19	77.19	0.08
11	56.27	0.11	20	77.87	0.08

Table 4.1: Properties of the primary systems

4.2.3 Passive Control

The passive control of the DMD system is first studied in this section. The biggest challenge for the passive DMD system is designing the characteristics of the dampers in different floors. Each damper affects the overall structural behavior differently and must be designed appropriately to minimize vibration. In the following sections, a simplified DMD system is analyzed and optimization of the DMD system is also studied.

4.2.3.1 Simple Case: Equally Distributed Mass Dampers

To understand the behavior of the DMD, consider an equally-distributed mass damper (EDMD) system that has equal damper parameters ($m_i^{\mathrm{d}}, k_i^{\mathrm{d}}$ and ς_i^{d}) for each floor. For a given structure with known m_i, k_i, c_i and a fixed mass ratio, $\overline{m} = \sum_{i=1}^{n} m_i^{\mathrm{d}} \Big/ \sum_{i=1}^{n} m_i$, an optimal solution of the two damper parameters (k_i^{d} and ς_i^{d}) can be found for the following objective function:

$$J = \sum_{i=1}^{n} E\left[(x_i - x_{i-1})^2\right] \tag{4.4}$$

where $x_0 = 0$ because x_i's are relative to the ground, and $E\left[(x_i - x_{i-1})^2\right]$ is the expected value of the squared floor-to-floor drift. Figure 4.10a shows how objective (4.4) changes for different values of damper parameters (k_i^{d} and ς_i^{d}) of the EDMD system ($\overline{m}$ =5%) for a 20-story building and indicates a minimum value of J in the region. The damper parameters (k_i^{d} / k_i =0.00024 and ς_i^{d}=12.5%, i=1,…,20) associated with the $J_{\min}$ are the optimal parameters illustrated in Figure 4.10(a). Figure 4.10 compares performance of the EDMD system and a single TMD system ($\overline{m}$ =5%) with the damper at the top floor on the 20-story building. The parameters (k_n^{d} / k_n =0.0045 and ς_n^{d} =16%) for the single TMD in Figure 4.10(b) are obtained by finding the parameters associated with the $J_{\min}$.

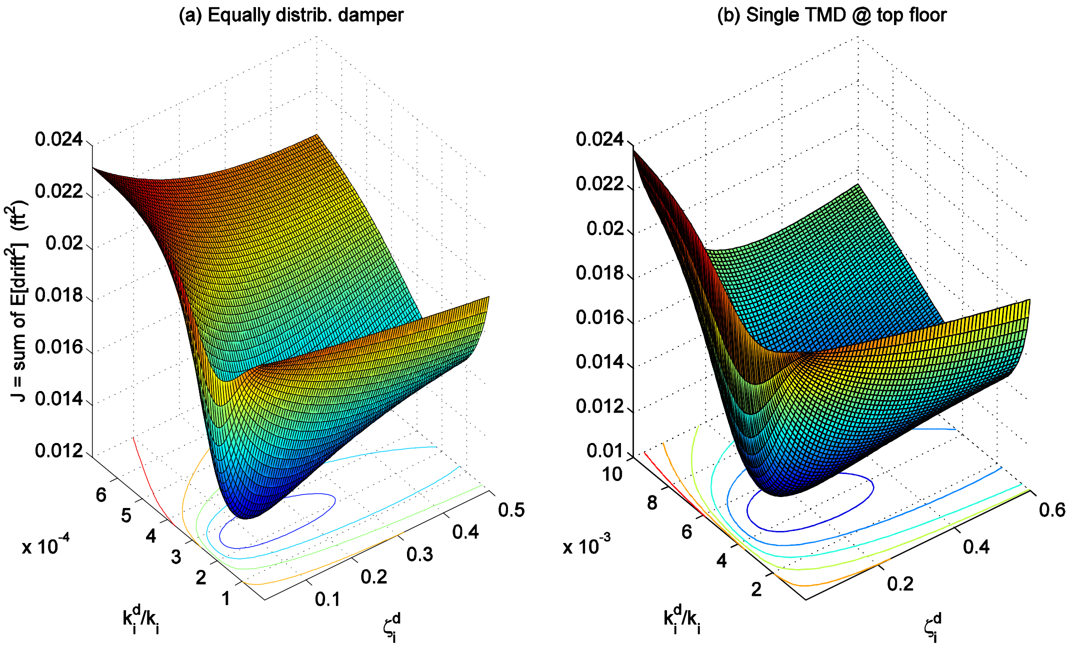

Figure 4.10: Objective function over damper parameters: (a) equally distributed mass damper and (b) single mass damper located at the top floor ($\overline{m}$ =5%)

Figure 4.11(a) shows the story-by-story DMD configuration; the optimal floor stiffness ratio, k_i^d / k_i, is similar to the given floor mass ratio, m_i^d / m_i, while the damping terms of the EDMD are a little different from the damping term of the single TMD. The single damper system in Figure 4.11(b) reduces the objective function, J, by 48.9% compared to the same building without dampers whereas the EDMD system reduces J by 40.9%. Although the single damper system performs better in reducing drifts, the damper at the top floor weighs as much as the floor itself, significantly affecting the structural and architectural design of that floor. On the other hand, the EDMD weighs as little as 5% of each floor and, therefore, allows more flexible integration with the building. However, the DMD damper system affects the design of all floors while the single damper system affects only one floor. Figure 4.12 demonstrates the performance of the two damper systems for the four design earthquake records compared to the building without dampers. The single damper system marginally outperforms the EDMD system for all four earthquake records.

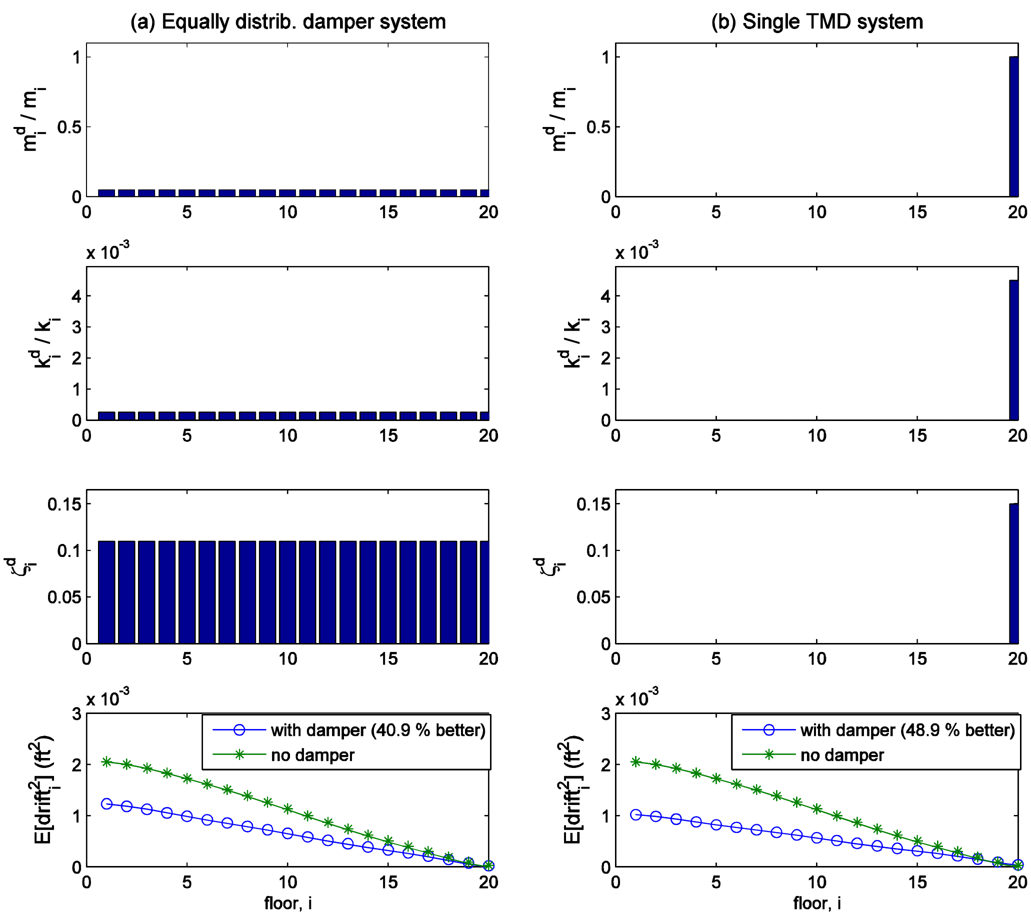

Figure 4.11: Comparison between the (a) equally distributed and (b) single damper systems

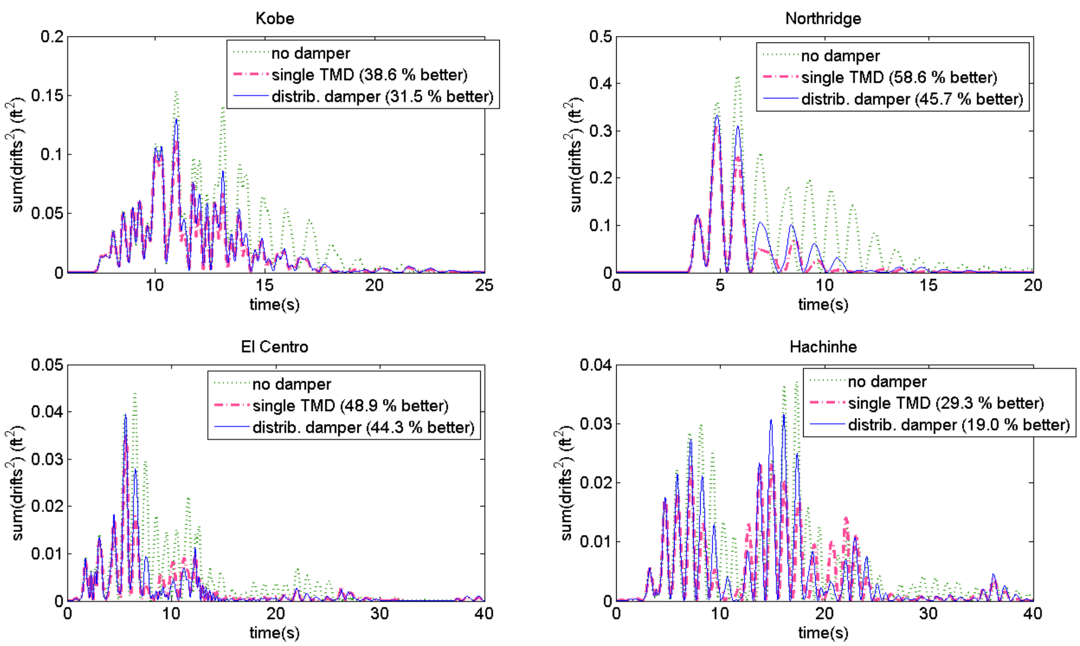

Figure 4.12: Performance of the EDMD and single TMD on different historical earthquake records

4.2.3.1.1 Fine Tuning the Parameters

To improve the performance of the DMD system, the parameters can be fine tuned according to the single TMD and EDMD systems. To understand the effect of dampers on different floors, single TMDs ($\overline{m}$ =5%) on different floors are simulated to determine their corresponding optimal damper parameters using a parametric study similar to Figure 4.10(a). Table 4.2 presents the performance of TMDs located at different floors. A TMD on the upper floors yields the best performance in reducing J up to 48.9%. A TMD on one of the lower floors reduces drifts significantly less than on other floors.

Floor, i	1	2	3	4	5	6	7	8	9	10
$m_i^d / \sum m_i$ (%)	5.00	5.00	5.00	5.00	5.00	5.00	5.00	5.00	5.00	5.00
k_i^d / k_i (%)	0.53	0.53	0.53	0.53	0.52	0.52	0.51	0.50	0.50	0.49
ζ_i^d (%)	2.00	3.00	4.00	5.00	6.00	7.00	8.00	9.00	10.0	11.0
Reduction in J (%)	4.46	9.88	15.3	20.4	24.8	28.7	32.0	34.9	37.4	39.6
Floor, i	11	12	13	14	15	16	17	18	19	20
$m_i^d / \sum m_i$ (%)	5.00	5.00	5.00	5.00	5.00	5.00	5.00	5.00	5.00	5.00
k_i^d / k_i (%)	0.48	0.47	0.47	0.46	0.46	0.45	0.45	0.45	0.45	0.45
ζ_i^d (%)	12.0	13.0	13.0	14.0	14.0	15.0	15.0	16.0	16.0	16.0
Reduction in J (%)	41.4	42.9	44.3	45.4	46.3	47.1	47.8	48.4	48.8	48.9

Table 4.2: Performances and optimal parameters for single TMDs on different floors

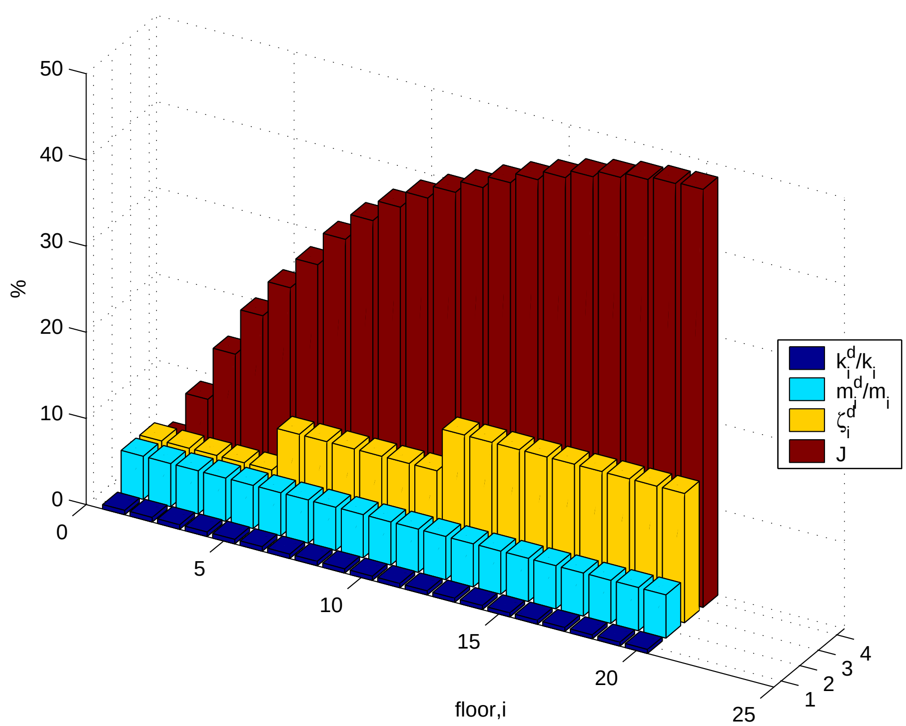

Figure 4.13: Performance and parameters for single TMDs on different floors (Table 4.2)

Table 4.2 and Figure 4.13 clearly show that the TMDs on the upper floors reduce the better drifts compared to those on the lower floors. In the DMD system, the damper masses can be divided according to the "importance" of the floor location from Table 4.2 and Figure 4.13. For example, the top floor should have the heaviest damper since it would better reduce the drifts while the first floor should have the lightest damper. Following such logic, the damper masses ratio perhaps should be given as

$$m_i^d \Big/ m_i = 0.05n \frac{\left(\tilde{J}_i\right)_s}{\sum_{i=1}^{n} \left(\tilde{J}_i\right)_s}, \qquad \text{for } i = 1, 2, \ldots, n. \tag{4.4}$$

where n is the number of floors, 0.05 to make the sum of all damper masses 5% of the structure mass, and $\left(\tilde{J}_i\right)_s$ is the reduction in J from the single TMD in i^{th} floor as in Table 4.2. From Figure 4.11, the stiffness ratios are seen to be proportional to the damper mass when comparing the stiffness ratios between the single TMD and EDMD systems. Therefore, the stiffness parameters in Figure 4.15 are calculated using

$$k_i^d \Big/ k_i = \left(k_i^d \Big/ k_i \right)_s \frac{m_i^d / m_i}{0.05}, \qquad \text{for } i = 1, 2, \ldots, n. \tag{4.5}$$

where $\left(k_i^d \Big/ k_i \right)_s$ is the stiffness ratios of the single damper systems from Table 4.2. Lastly, the damping ratios are set to the values from Table 4.2 since Figure 4.11

suggests little changes in damping ratios between the single TMD and EDMD systems.

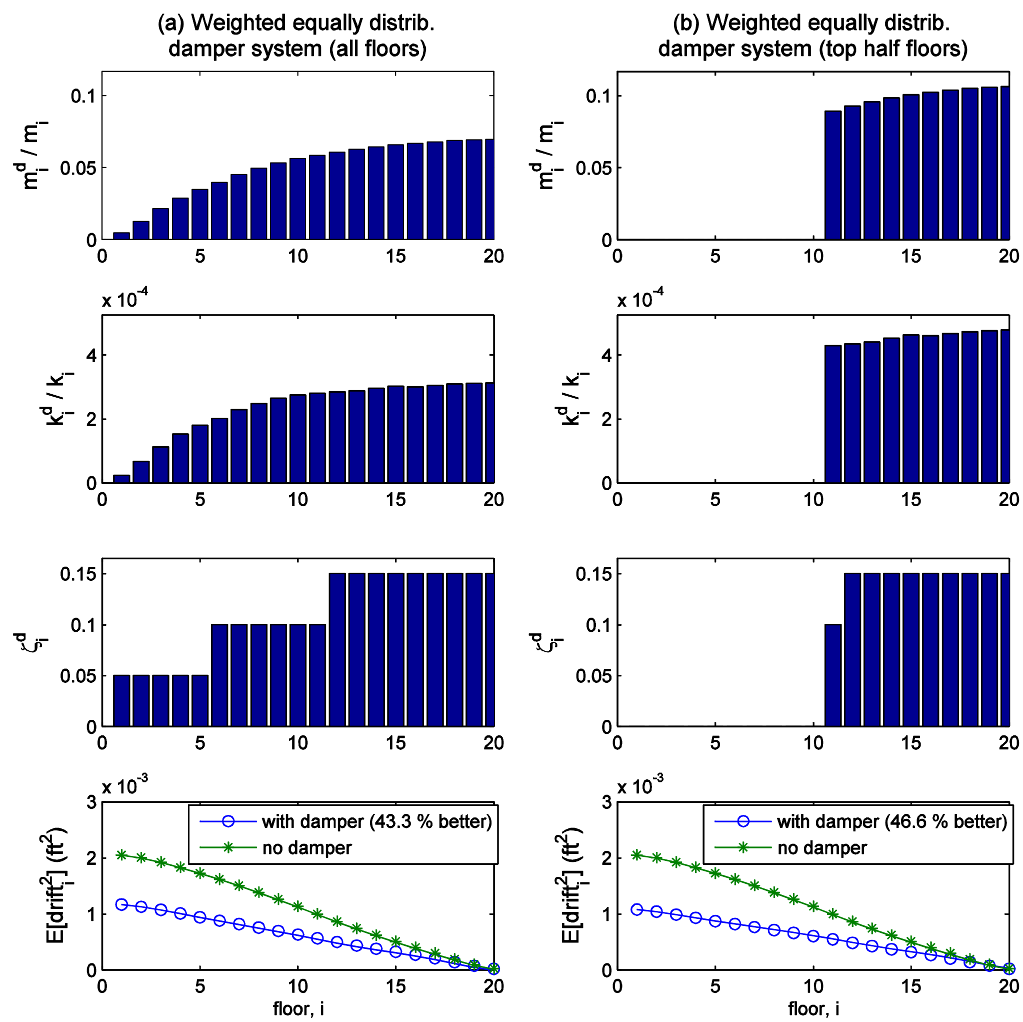

Figure 4.14: Comparison between weighted EDMD systems of (a) all floors and (b) top half floors only

Figure 4.14 shows the improvement over the EDMD system using (4.4) and (4.5). In fact, the DMD system described (Figure 4.14(a)) only suffers a small drop performance compared to the single TMD in Figure 4.11(b) (43.3% compared to 48.9% respectively). The advantage of the DMD system shown is that the dampers can be fairly distributed throughout the floors instead of being concentrated in one floor. Figure 4.14(b) also shows a variation where only the top half of the floors is equipped with dampers. The performance is very much in line with the single TMD in Figure 4.11(b) with only 2.3% drop off. This shows how little structural performance is sacrificed to incorporate the DMD system for shading fins. Since the DMD system with dampers in all floors in Figure 4.14(a) is obtained by weighting the damper masses and stiffness according to (4.4) and (4.5), it will be referred as the "weighted EDMD" system; Figure 4.15 illustrates the performance of this system subject to the four design earthquake records. Figure 4.16 indicates that the performance of the weighted EDMD system is also good for excitations other than the design records; the results show that the weighted EDMD system performs close to the single TMD system.

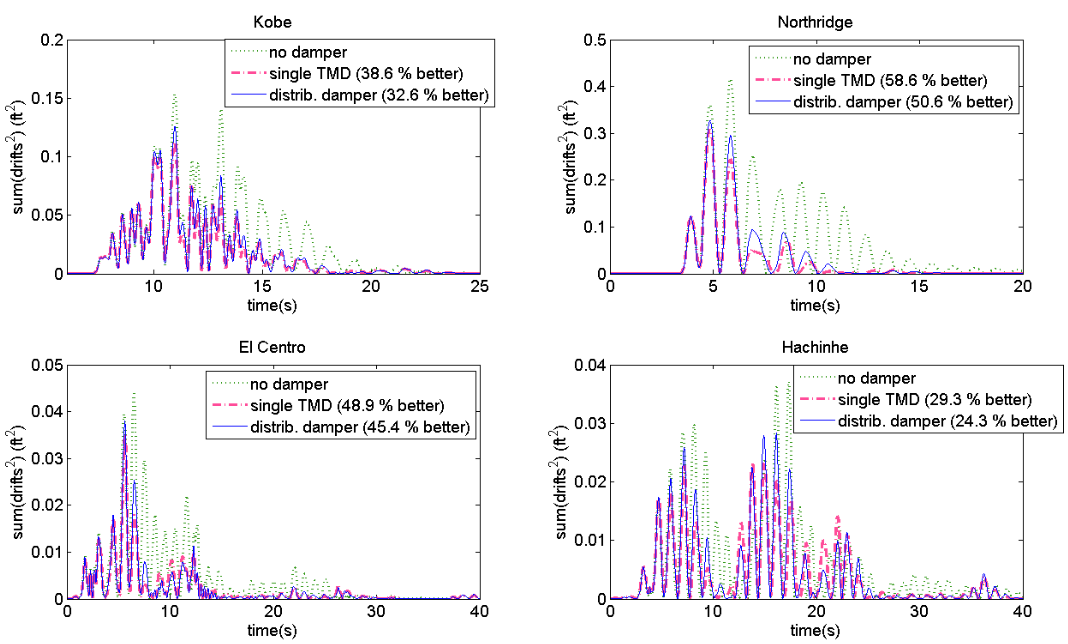

Figure 4.15: Performance of the weighted DMD system on the four designed earthquake records

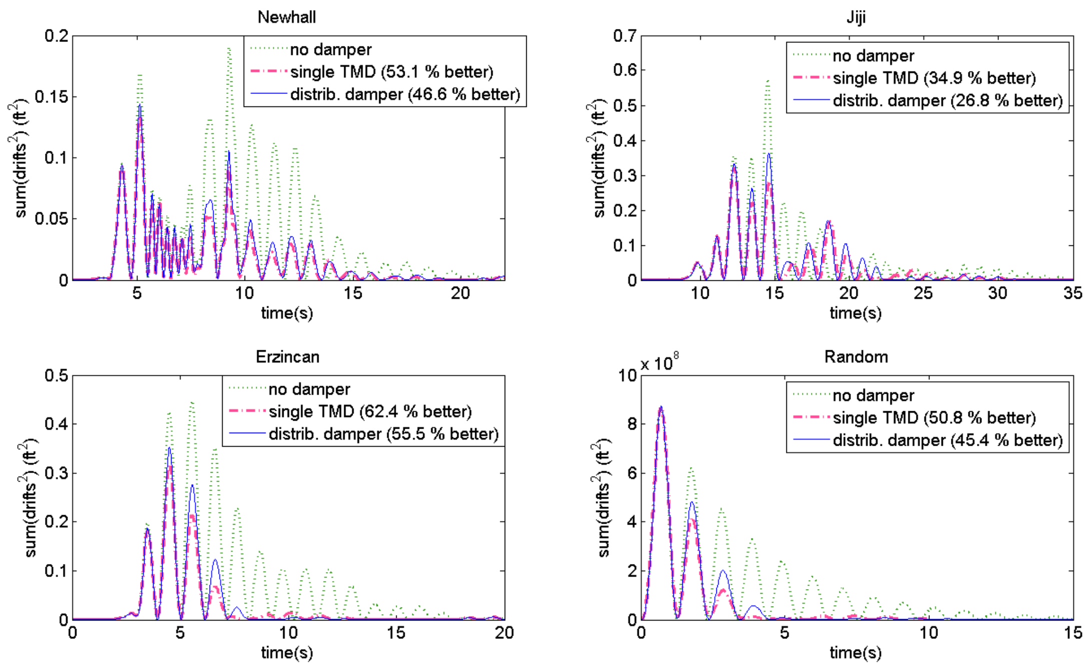

Figure 4.16: Performance of the weighted EDMD system on the other earthquake records and random excitation

4.2.3.2 Optimization of Damper Parameters

In order to design an effective DMD system, the damper parameters must be optimized for vibration reduction. The weighted EDMD system from the previous section shows that the DMD system can significantly reduce strcutural motion, though not quite as well compared with the conventional single TMD system. This section will outline a method to improve the DMD system by finding an optimal set of damper parameters that minimizes the damage caused by the input excitation. The parameters are

- m_i^d , $i = 1,2, \ldots, n$ (masses of the n dampers)

- ζ_i^d , i = 1,2, …, n (damping ratios of the n dampers: $\zeta_i^d = c_i^d \Big/ \left(2\sqrt{k_i^d m_i^d}\right)$)
- k_i^d , i = 1,2, …, n (stiffness between the n dampers and the corresponding floors).

The ranges of these parameters are defined as the following:

Mass: $0 \leq m_i^d \leq 15\% \text{ x } m_i$ (each damper mass must be less than 15% of the corresponding floor mass)

$\sum m_i^d \leq 5\% \text{ x } \sum m_i$ (sum of the damper masses must be less than 5% of the total structural mass)

Damping: $0 \leq \zeta_i^d \leq 200\%$ (each mass damper ratio must be less than 200%)

Stiffness: $0 \leq k_i^d \leq k_i$ (each damper stiffness must be less than floor stiffness).

For an n-story building, there are 3n variables to optimize (damper mass, stiffness and damping of each damper). With tall buildings being most suitable for the SFMD system, a large number of design variables are included in the optimization. For example, the 20-story building discussed in the last section has 60 variables to optimize. Such a large number of variables is difficult to optimize due to the many possible combinations of the variables. The following section details an optimization method suitable for this type of optimization.

4.2.3.2.1 Pattern Search Optimization

A pattern search is a particular set of direct search optimization methods first proposed by Hooke and Jeeves (1961). Recent developments by Dennis and Torzcon (1991) and Torzcon (1989, 1997) have generalized the method. One major reason that the pattern search method is used for the damper optimization is that the method can handle many variables without requiring enormous computational resources. However, like many other optimization methods, a pattern search is subject to getting stuck at local minima and, generally, produces different optimization results with different initial values for the damper parameter problem. MATLAB® includes a number of routines for pattern search methods in its Genetic Algorithm Toolbox; the damper parameters are optimized using these routines. The following briefly explains how a pattern search works.

Consider a problem minimizing an object function $f : \mathbf{R}^n \rightarrow \mathbf{R}$. Let $\mathbf{x}$ be the vector of n variables to be optimized and $\mathbf{x}_0$ and $\mathbf{x}_k$ be the initial values and the values at the k^{th} iteration, respectively. At iteration k, $\mathbf{x}_+ = \mathbf{x}_k + \Delta_k\mathbf{d}$, where Δ_k is the weight and $\mathbf{d}$ is the directions applied to $\mathbf{x}$. There are two potential directions for each variable x_i (i = 1,2, …, n): positive and negative (increasing and decreasing the value of x_i respectively). Thus, there are $2n$ directions of $\mathbf{x}$ if each x_i is regarded independently; collectively, there are 2^n possible combinations of $\mathbf{x}_+$. After exhausting all combination of $\mathbf{x}_+$ ($2n$, 2^n or any other number of $\mathbf{x}_+$ depending on the method applied), if $\min_{\mathbf{x}_+} f(\mathbf{x}_+) < f(\mathbf{x}_k)$ then iteration k is a success and the algorithm moves to iteration k+1 with $\mathbf{x}_{k+1} = \mathbf{x}_{+}$ and an increased Δ_{k+1} (typically $\Delta_{k+1} = 2\Delta_k$). Otherwise, an unsuccessful iteration k would lead to $\mathbf{x}_{k+1} = \mathbf{x}_k$ and a decreased Δ_{k+1} (typically $\Delta_{k+1} = \Delta_k/2$) for the next iteration. The process is repeated until preset stopping criteria are met.

4.2.3.2.2 Optimization Results

The optimization problem is expected to have local minima. Therefore, the optimized result of the pattern search is heavily dependent on the initial set of parameters. Figures 4.17 and 4.18 show two pattern search results from two initial sets of randomly chosen parameters. The initial DMD systems perform worse (larger drifts) than the base system (no damper), and the optimized DMD systems outperform the baseline by 32.1% and 27.8%, respectively. In both cases, many of the damper masses of the DMD systems are reduced to zeros and the optimized DMD systems only have a few dampers (4 dampers and 3 dampers, respectively). Since pattern search optimization looks for the largest improvement of the overall system at each iteration, pattern search can select either improvement through correctly tuning the damper stiffness and damping ratios or improvement through reducing damper masses. In the two cases from Figure 4.17 and 4.18, the pattern search favors improvement by reducing damper mass except for a few floors. This implies that, most of time, a reduction in damper masses shows greater improvements than tuning damper stiffness and damping ratios for the initial DMD systems in Figures 4.17 and 4.18.

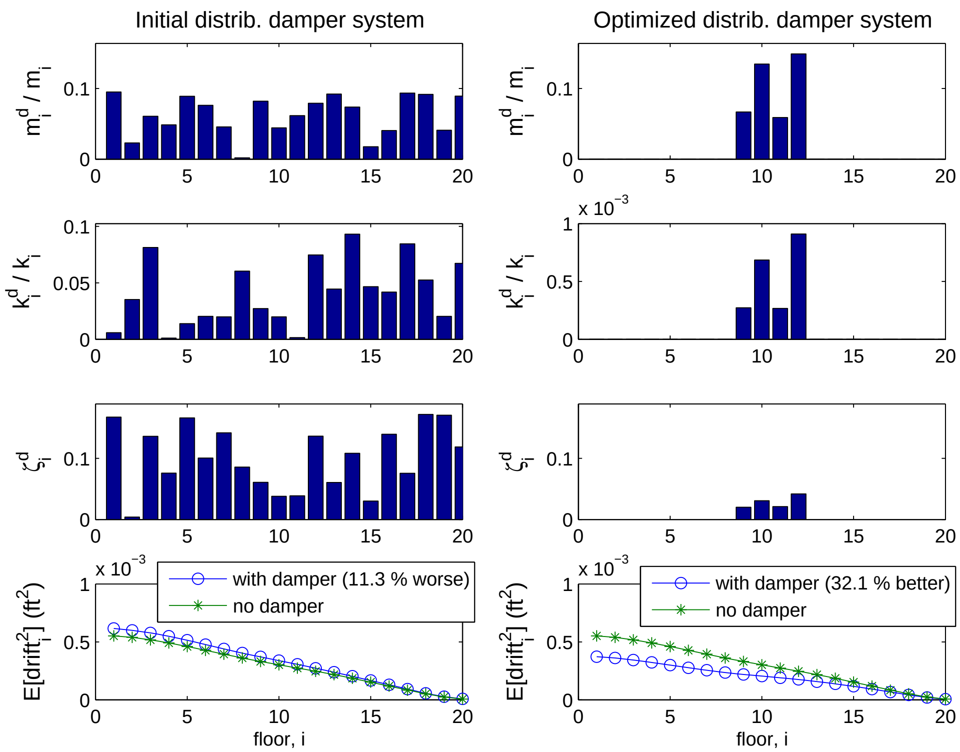

Figure 4.17: Pattern search optimization with randomly chosen initial parameters (1)

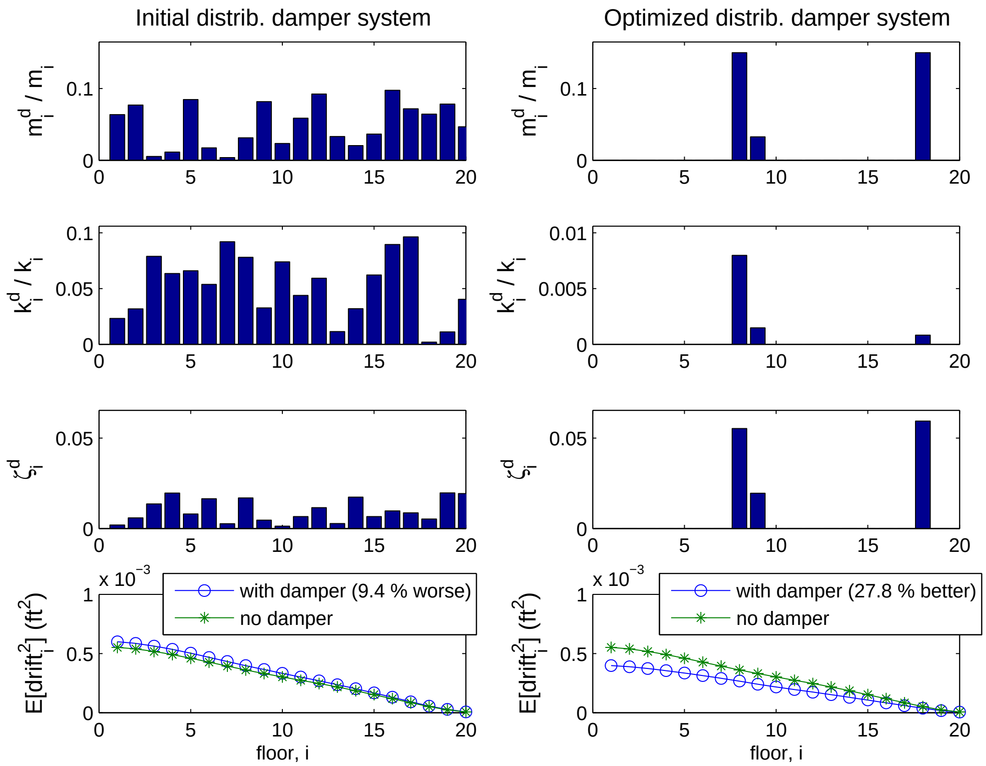

Figure 4.18: Pattern search optimization with randomly chosen initial parameters (2)

Figures 4.19 and 4.20 show two initial DMD systems from Figures 4.11(a) (the EDMD system) and 4.14(a) (the weighted EDMD system), respectively. Before optimizing, they already outperform the uncontrolled system by 40.9% and 43.3%, respectively. The optimized results of the pattern search shows improvements of 45.7% and 48.6%, respectively; 48.6% is very close to the 48.9% improvement from the best single TMD system (damper on the top floor). The two optimized DMD systems place small or no dampers at the lower floors, agreeing with Table 4.2 that shows smaller effects from dampers at lower floors. The optimized DMD systems have small damping ratios for all floor compared to the initial DMD systems, while damper stiffness remains similar to the ones of the initial systems except some increases for a few floors. Interestingly, the lowest floor with a significant damper mass (floor 4 in Figure 4.19 and floor 6 in Figure 4.20) shows the large increases in damper stiffness. The stiffness jumps could be caused by tuning to the 2nd natural frequency, that equals to 8.96 rad/s, of the uncontrolled structure. In Figure 4.19, $\sqrt{k_4^d / m_4^d}$ = 8.71 rad/s whereas $\sqrt{k_6^d / m_6^d}$ = 8.74 rad/s in Figure 4.20.

Figures 4.21 and 4.22 show how the optimized DMD system in Figure 4.20 performs with various types of ground excitations. Of the eight excitations simulated, the optimized DMD system outperforms the single TMD system five times. In fact, in these five excitations, the DMD system surpasses the TMD system on average by 4.72% compared to the average 1.33% of the TMD system over the DMD system in the remaining three excitations. The largest performance improvements by both control systems show over each other occur in the Erincan (the DMD system outperforms by 12.6%) and Northridge (the TMD system outperforms by 2.1%) earthquake records. Although, Figure 4.20 shows that the optimized DMD system performs very similar to the single TMD system, simulations of individual excitations indicate that the optimized DMD system performs better in most cases.

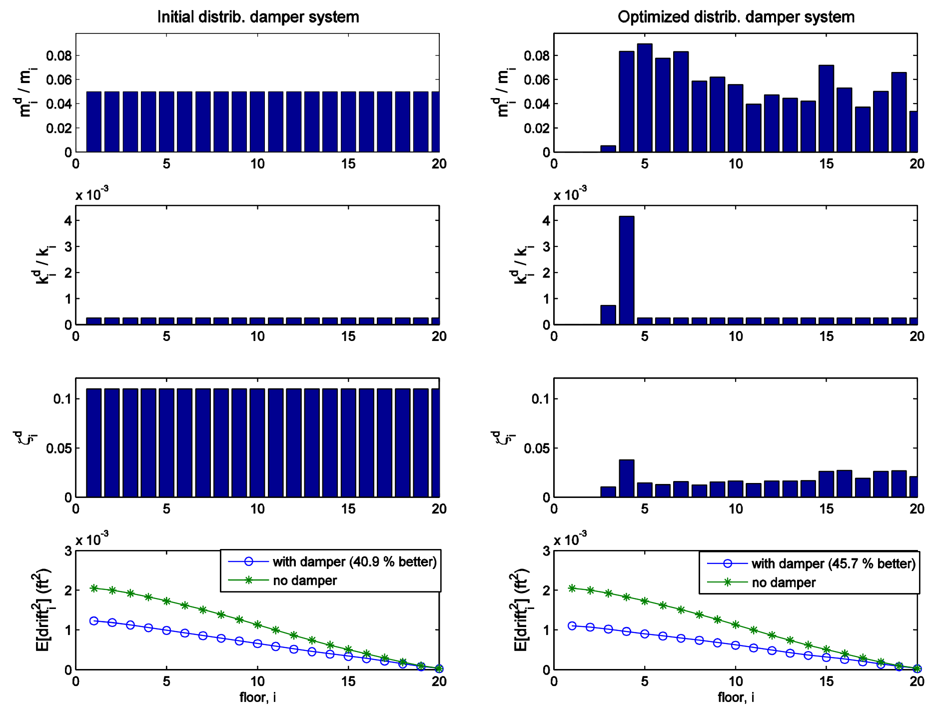

Figure 4.19: Pattern search optimization with the EDMD system as the initial guess

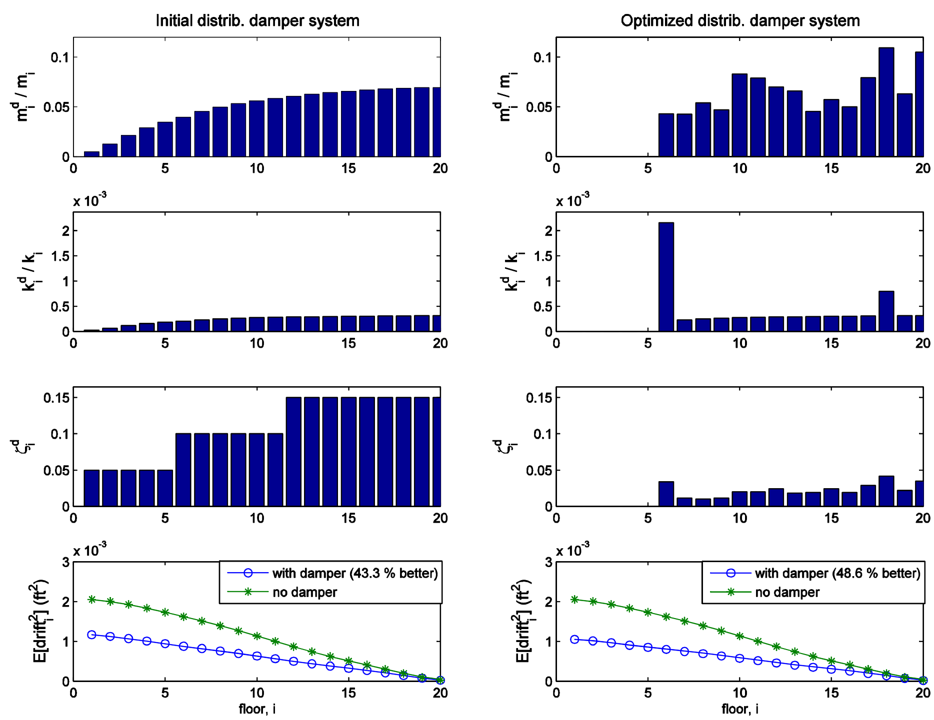

Figure 4.20: Pattern search optimization with the weighted EDMD system as the initial guess

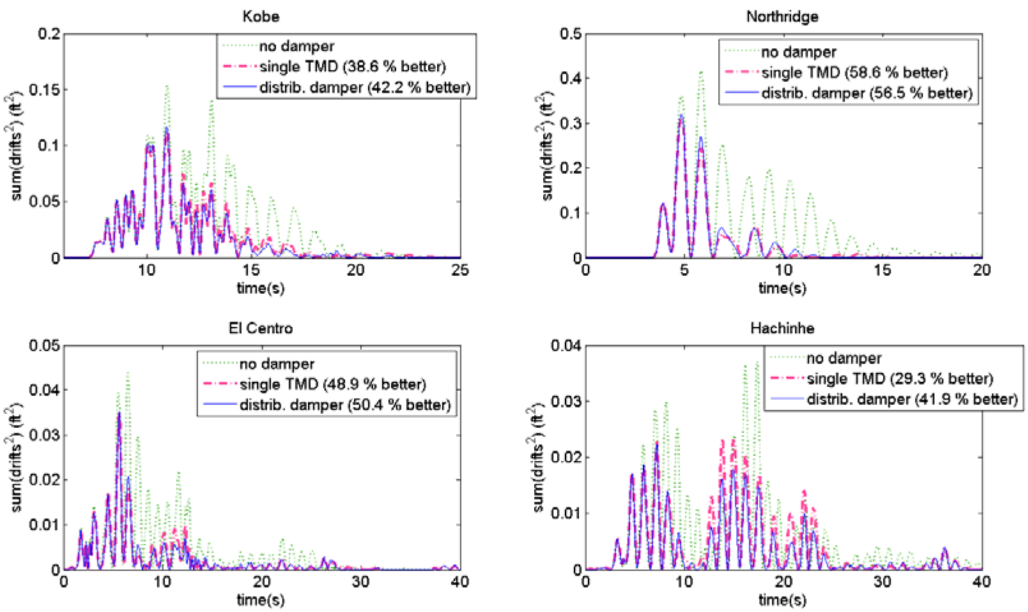

Figure 4.21: Performance of the optimized DMD system (from Figure 4.20) subject to the four designed earthquake records

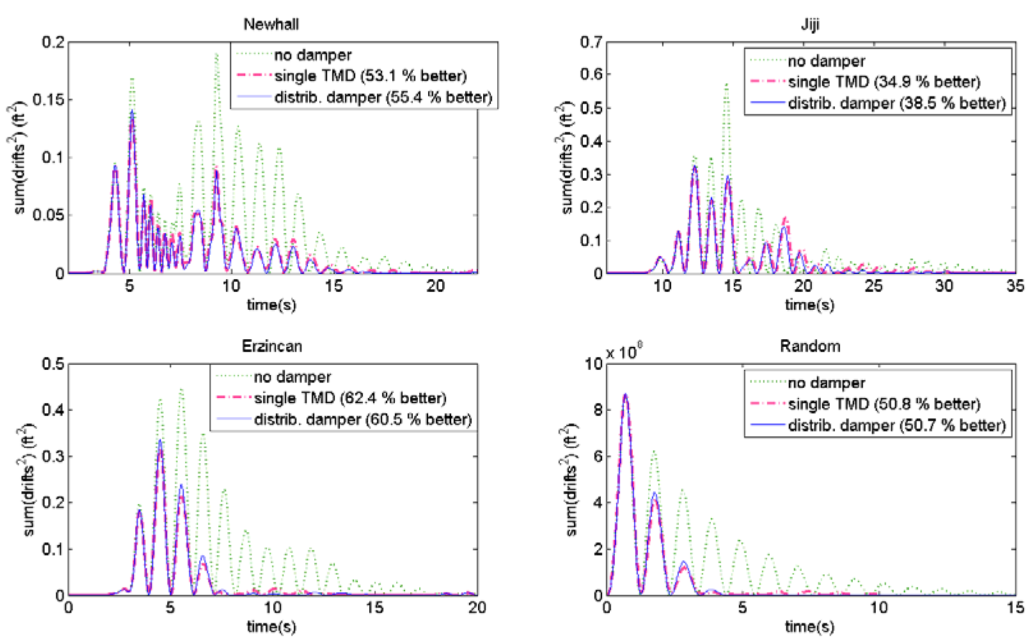

Figure 4.22: Performance of the optimized DMD system (from Figure 4.20) subject to the other earthquake records and random excitation

4.2.3.3 Discussion on Performance and Practicality

From the optimization results, the DMD system can be optimized to perform on par with (or better than) the traditional single damper system. However, the optimized DMD systems may not be ideal for building design and construction with the damper masses being significantly different from floor to floor. On the other hand, the EDMD and the weighted EDMD systems in Section 4.2.3.1 have rather simple damper mass distributions (uniform or gradually increasing, respectively) and, thus, are probably more practical for building designers and builders. The downside of the EDMD systems is the drop in performance compared the optimized DMD systems (see Figures 4.19 and 4.20).

	Drift reduction relative to structure with no dampers		
Excitation	**Weighted EDMD system**	**Optimized DMD system**	**Single TMD system (top floor)**
Kobe	38.6%	42.2%	38.6%
Northridge	50.6%	56.5%	58.6%
El Centro	45.4%	50.4%	48.9%
Hachinhe	24.3%	41.9%	29.3%
Newhall	46.6%	55.4%	53.1%
Jiji	26.8%	38.5%	34.9%
Erzincan	55.5%	60.6%	62.4%
Random (KT-filter white noise)	45.5%	50.7%	50.8%

Table 4.3: Performance of the weighted EDMD and optimized DMD system on different excitations

From Table 4.3, there is a clear performance gap between the weighted EDMD and optimized DMD systems on the simulated excitations with an average difference at about 8%. Since future earthquakes will behave differently than the historical records, simplicity in the actual implementation of the DMD systems is as practical as an increase in performance. Therefore, DMD systems with a simple damper mass distribution (such as the EDMD system) are more suitable for the proposed Shading Fin Mass Damper system.

4.2.3.3.1 Sub-optimization of Damper Stiffness and Damping Only

Sub-optimizing the damper stiffness and damping ratios while leaving the damper masses unchanged can improve the performance of the DMD system as well as keeping the whole system more constructible. Figures 4.23, 4.24 and 4.25 show improvements with the sub-optimization with initial guesses as the EDMD, weighted EDMD and stepped EDMD systems, respectively. For the stepped EDMD system, the floors are divided into groups (*i.e.*, 1^{st} to 5^{th} floors as a group, 6^{th} to 10^{th} as another group, etc.) in a fashion similar to how high-rise buildings are designed and built by grouping together adjacent floors. Figure 4.23 shows that the sub-optimized EDMD system reduces 42.5% structural responses. This is the worst performance of the three systems, though the EDMD system would be the easiest to build due to the uniform damper masses. The weighted EDMD (Figure 4.24) performs the best (47% reduction) but is the hardest to build because of different damper masses on each floor. The stepping system in Figure 4.25 performs close to the weighted EDMD system with a response reduction of 46.3%; this is also very close the 48.6% improvement from the best performer — the single TMD. The fine performance of the stepped EDMD suggests that only a little sacrifice is needed for greater practicality.

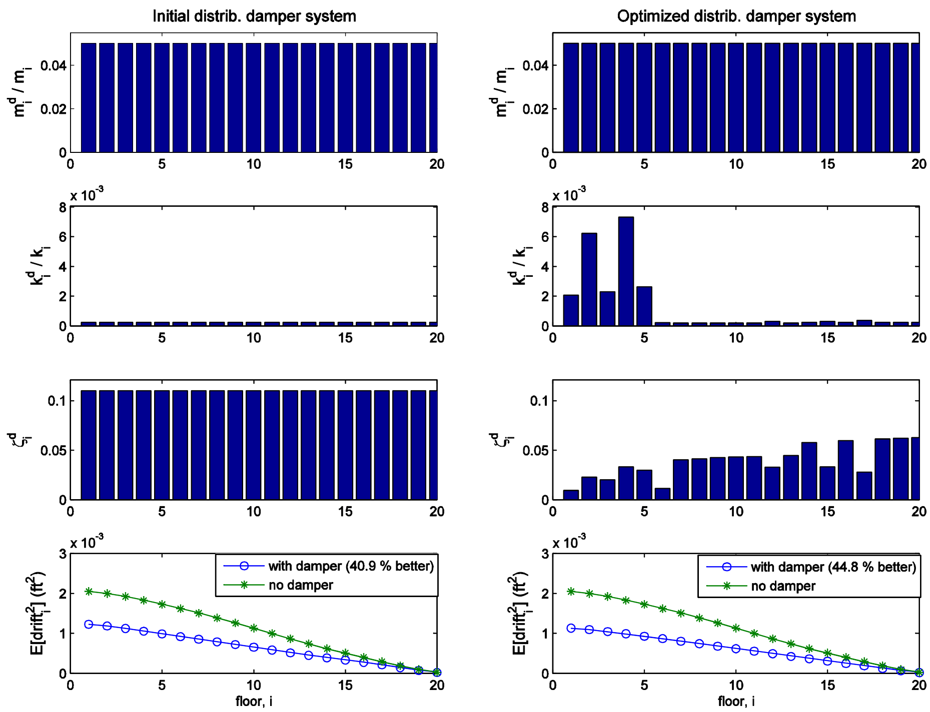

Figure 4.23: Pattern search sub-optimization with the EDMD as the initial guess

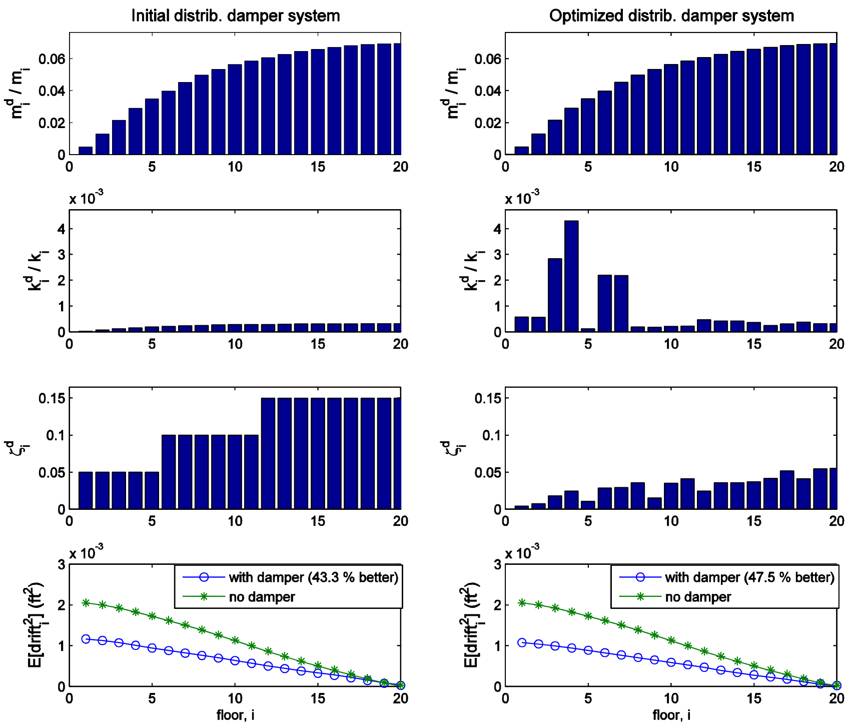

Figure 4.24: Pattern search sub-optimization with the weighted EDMD as the initial guess

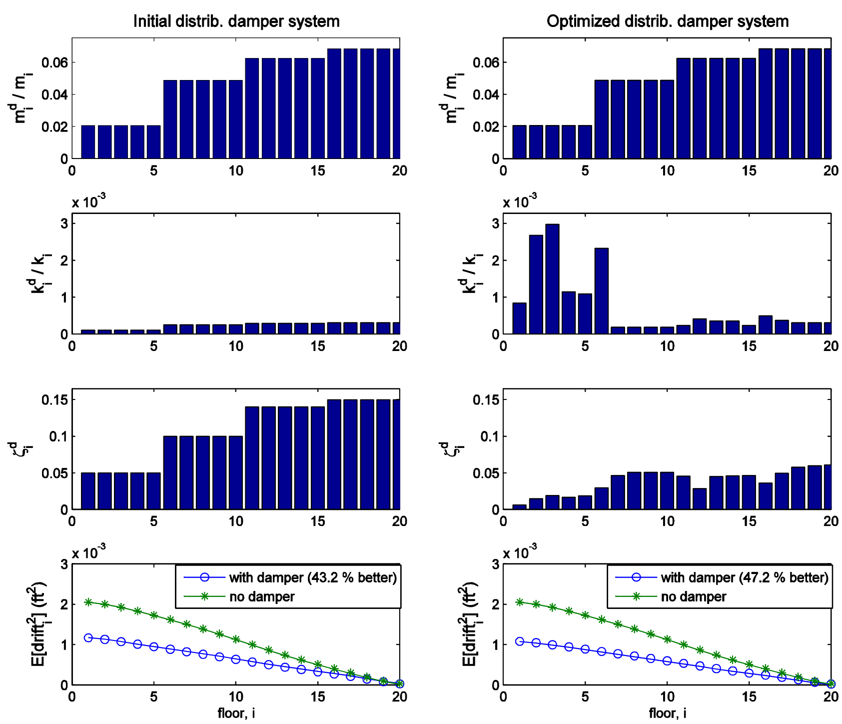

Figure 4.25: Pattern search sub-optimization with the stepped EDMD as the initial guess

Another important aspect of the sub-optimization of the damper stiffness and damping ratios is the inclusion of a non-passive control system. Passive control systems have the control parameters tuned and fixed while non-passive systems vary the parameters according the condition of the system. For the DMD system, stiffness and damping varying devices can be installed with the dampers to become an active or semiactive control system. Such a non-passive system can be easy to build while achieving excellent performance.

4.2.4 Active/Semiactive Control

Since there are actuators for adjusting the position of the shading fins, an active control scheme is studied to further utilize these actuators. However, these actuators may be less powerful than desired because their main purpose is to gradually adjust the fin positions as weather and building conditions change. Semiactive control is considered with semiactive dampers to compensate for the weak actuators. The following diagrams illustrate the schemes of passive, active and semiactive control systems.

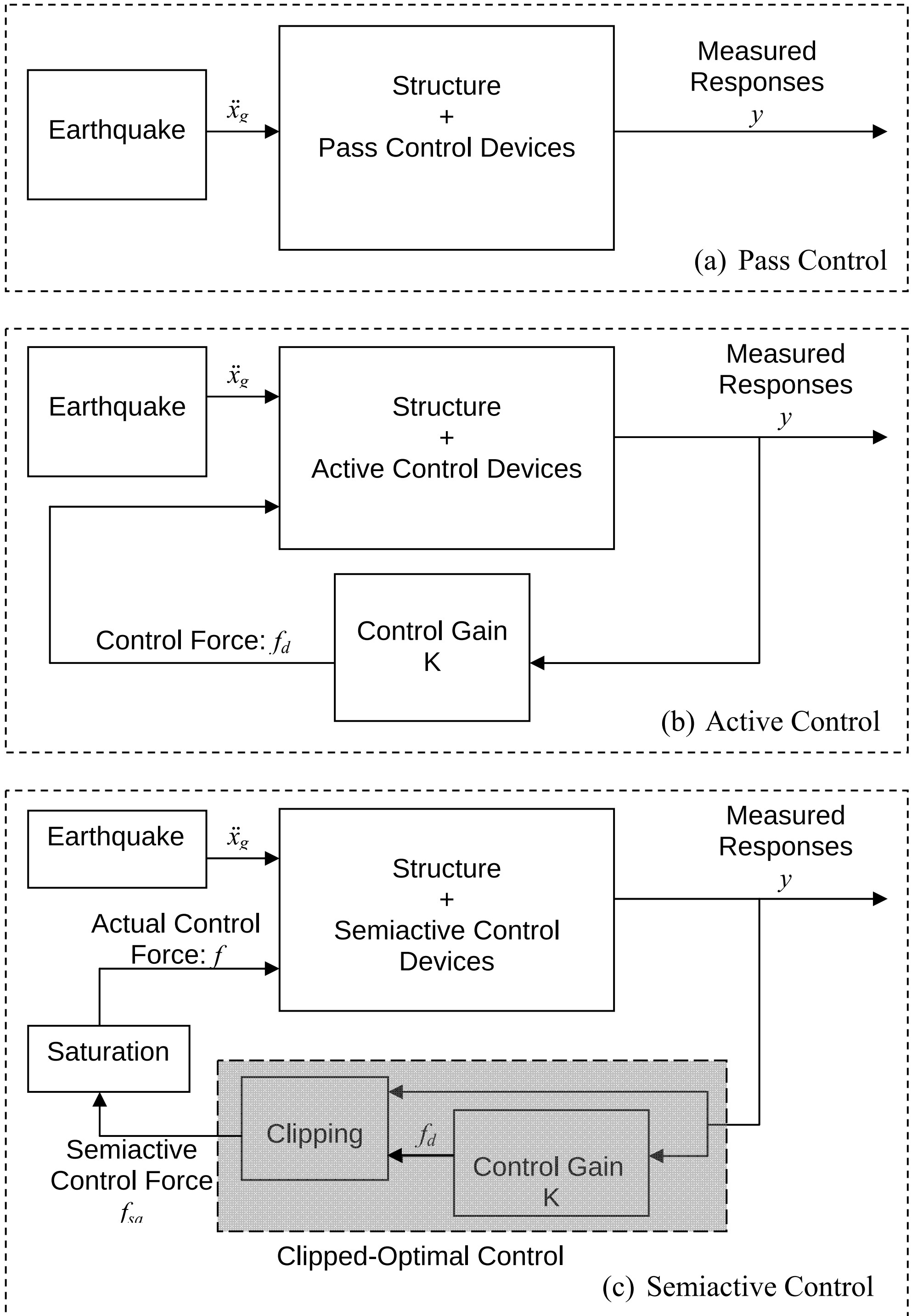

Figure 4.26: Passive, active and semiactive control

4.2.4.1 Active Control

Three active control strategies are studied here as a comparison with the passive DMD system:

- active control (ACT): n actuators, one attached in each story of the structure;
- active mass driver (AMD): one actuator attached between the roof and the roof-mounted mass damper;
- active distributed mass dampers (ADMD): n actuators, one attached between each floor and its corresponding mass damper.

The equation of motion remains similar to (4.2)

$$\mathbf{M}\ddot{\mathbf{x}} + \mathbf{C}\dot{\mathbf{x}} + \mathbf{K}\mathbf{x} = -\mathbf{M}\mathbf{1}\ddot{x}_{\mathrm{g}} + \mathbf{f}_{\mathrm{c}} \tag{4.6}$$

with $\mathbf{f}_{\mathrm{c}}$ being the control force of the form of $\mathbf{f}_{\mathrm{c}} = \mathbf{B}_{\mathrm{c}}\mathbf{f}$,

$$\mathbf{f}_{\mathrm{ACT}} = \begin{bmatrix} -1 & 1 & 0 & & & & \\ 0 & -1 & 1 & & & & \\ & & & \ddots & & & \\ & & & & 0 & -1 & 1 \\ & & & & 0 & 0 & -1 \end{bmatrix} \begin{bmatrix} f_1 \\ f_2 \\ \vdots \\ f_{n-1} \\ f_n \end{bmatrix} = \mathbf{B}_{\mathrm{ACT}}\mathbf{f} \ ,$$

$$\mathbf{f}_{\mathrm{AMD}} = \begin{bmatrix} 0 \\ \vdots \\ 0 \\ -1 \\ 1 \end{bmatrix} f = \mathbf{B}_{\mathrm{AMD}} f \ ,$$

and $$\mathbf{f}_{\mathrm{ADMD}} = \begin{bmatrix} -1 & 0 & 0 & & & & \\ 1 & 0 & 0 & & & & \\ 0 & -1 & 0 & & & & \\ 0 & 1 & 0 & & & & \\ & & & \ddots & & & \\ & & & & 0 & -1 & 0 \\ & & & & 0 & 1 & 0 \\ & & & & 0 & 0 & -1 \\ & & & & 0 & 0 & 1 \end{bmatrix}_{2n\times n} \begin{bmatrix} f_1 \\ f_2 \\ f_3 \\ f_4 \\ \vdots \\ f_{n-3} \\ f_{n-2} \\ f_{n-1} \\ f_n \end{bmatrix}_{n\times 1} = \mathbf{B}_{\mathrm{ADMD}}\mathbf{f}$$

for active control, active mass driver, and active DMD systems, respectively. (4.6) can be represented in state space form

$$\begin{bmatrix} \dot{\mathbf{x}} \\ \ddot{\mathbf{x}} \end{bmatrix} = \begin{bmatrix} \mathbf{0}_{n\times n} & \mathbf{I}_{n\times n} \\ -\mathbf{M}^{-1}\mathbf{K} & -\mathbf{M}^{-1}\mathbf{C} \end{bmatrix} \begin{bmatrix} \mathbf{x} \\ \dot{\mathbf{x}} \end{bmatrix} + \begin{bmatrix} \mathbf{0}_{n\times 1} \\ -\mathbf{1}_{n\times 1} \end{bmatrix} \ddot{x}_{\mathrm{g}} + \begin{bmatrix} \mathbf{0}_{n\times n} \\ \mathbf{M}^{-1}\mathbf{B}_{\mathrm{c}} \end{bmatrix} \mathbf{f}$$

$$\mathbf{y} = \mathbf{C}_1 \begin{bmatrix} \mathbf{x} \\ \dot{\mathbf{x}} \end{bmatrix} + \mathbf{D}_1 \ddot{x}_{\mathrm{g}} + \mathbf{D}_2 \mathbf{f} \tag{4.7}$$

where $\mathbf{y}$ is the output vector that can observe floor drifts, accelerations and/or damper displacements depending on $\mathbf{C}_1$, $\mathbf{D}_1$ and $\mathbf{D}_2$.

4.2.4.1.1 Linear Quadratic Regulator (LQR)

The linear quadratic regulator (LQR) is used to determinate the appropriate control force for the active systems, minimizing the cost function

$$J = E[\mathbf{y}^{\mathrm{T}}\mathbf{Q}\mathbf{y} + \mathbf{f}_{\mathrm{c}}^{\mathrm{T}}\mathbf{R}\mathbf{f}_{\mathrm{c}}] \tag{4.8}$$

where **Q** and **R** are response and control weighting matrices respectively. Consider the case that **y** in (4.8) measures floor drifts, floor accelerations and damper displacements, or $\mathbf{y} = [\mathbf{y}_{\text{drift}}, \mathbf{y}_{\text{accel}}, \mathbf{y}_{\text{damper}}]^T$, **Q** can take the following form:

$$\mathbf{Q} = \begin{bmatrix} \mathbf{Q}_{\text{drift}} & \mathbf{0} & \mathbf{0} \\ \mathbf{0} & \mathbf{Q}_{\text{accel}} & \mathbf{0} \\ \mathbf{0} & \mathbf{0} & \mathbf{Q}_{\text{damper}} \end{bmatrix} = \begin{bmatrix} \frac{1-10^{\alpha}-10^{\beta}}{\bar{y}^2_{\text{drift}}}\mathbf{I} & \mathbf{0} & \mathbf{0} \\ \mathbf{0} & \frac{10^{\alpha}}{\bar{y}^2_{\text{accel}}}\mathbf{I} & \mathbf{0} \\ \mathbf{0} & \mathbf{0} & \frac{10^{\beta}}{\bar{y}^2_{\text{damper}}}\mathbf{I} \end{bmatrix} \quad (4.9)$$

where α and β are constants. $\bar{y}_{\text{drift}}$, $\bar{y}_{\text{accel}}$ and $\bar{y}_{\text{damper}}$ are means of mean squares of $\mathbf{y}_{\text{drift}}$, $\mathbf{y}_{\text{accel}}$ and $\mathbf{y}_{\text{damper}}$ of the corresponding passive system of the active system respectively (*i.e.*, the passive systems of AMD and ADMD systems are the TMD and DMD systems, respectively), given by

$$\bar{y}_{\text{drift}} = \frac{1}{n}\sum_{i=1}^{n} \mathrm{E}\left[(y_{\text{drift}}(t))_i^2\right] \quad (4.10)$$

where $(y_{\text{drift}}(t))_i$ is the drift response for i^{th} story, and $\bar{y}_{\text{accel}}$ and $\bar{y}_{\text{damper}}$ have similar forms. In the case of the ACT system, since there are no damper involved, $\mathbf{Q}_{\text{damper}}$ does not exist and $\beta = -\infty$. Adjusting α and β can change the importance of $\mathbf{y}_{\text{drift}}$, $\mathbf{y}_{\text{accel}}$, and $\mathbf{y}_{\text{damper}}$ relative to each other in minimizing (4.8). Meanwhile, **R** is only concerned with the control forces and thus has a simpler form of $\mathbf{R} = r\,\mathbf{I}$ (assuming the control force in each floor is equally important), where a large value of the constant r calls for small control forces and vice versa. By varying r, α and β, the control forces can be designed for different types of active systems and for different levels of performance.

4.2.4.1.2 Result

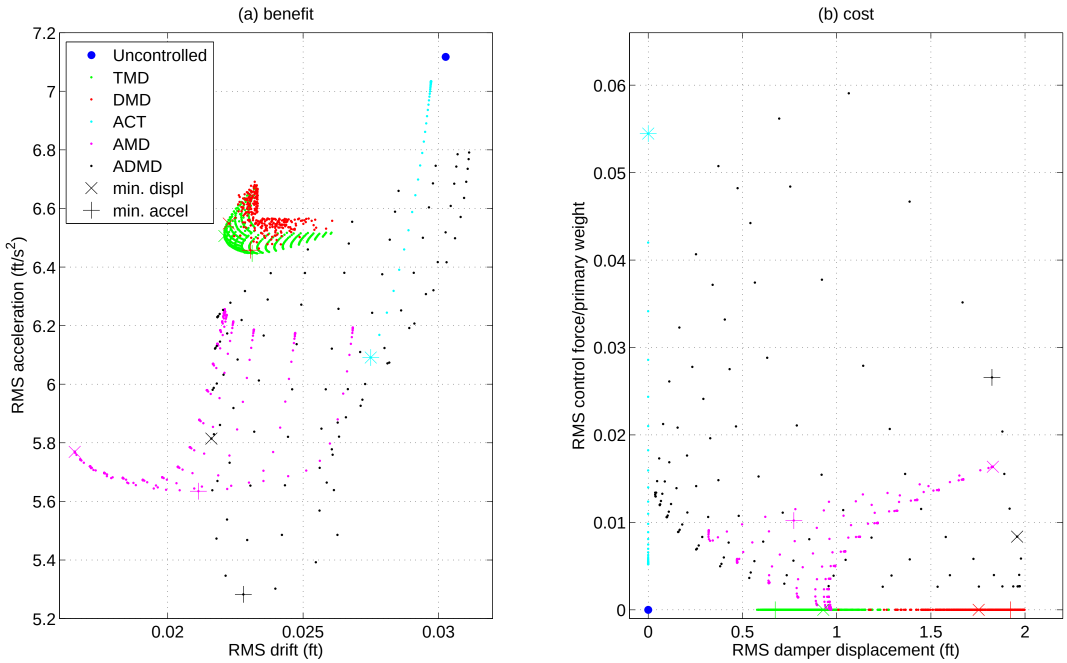

Figure 4.27: Benefit and cost of different control systems

Figure 4.27 shows the cost and benefit of the active systems (ACT, AMD and ADMD) along with the passive systems (TMD and DMD). The different active systems are obtained by varying the weighting matrices **Q** and **R** for each type of active control, whereas the passive systems are from varying damper stiffness, damping terms and/or masses (for the DMD system only). Among all of these control strategies, the AMD and ADMD systems best reduce the structural motions. The AMD systems can reduce the greatest amount of drifts while the ADMD systems can reduce the greatest amount of acceleration but generally at larger cost (larger damper displacements and control force) than the AMD systems.

4.2.4.2 Semiactive Control

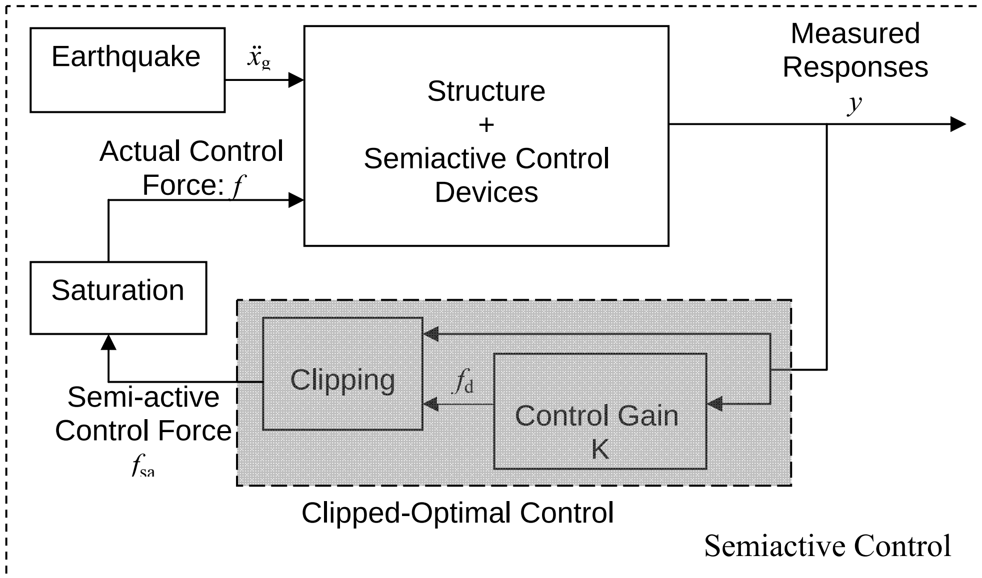

Figure 4.28: Semiactive control

Figure 4.28 illustrates the scheme of a semiactive control system for structure experiencing external excitation such as earthquakes. The rest of this section further discusses different aspects of semiactive control and applying such control system on the DMD system.

4.2.4.2.1 Clip Optimal Control

In the case of SFMD system, the primary (or most frequent) purpose of the actuators is to control the fins for shading. The adjusting movement for shading is not as demanding as structural control since the sun moves gradually. To compensate for the loss of power in the small actuators, semiactive dampers are also connected to the SFMDs (Figure 4.29).

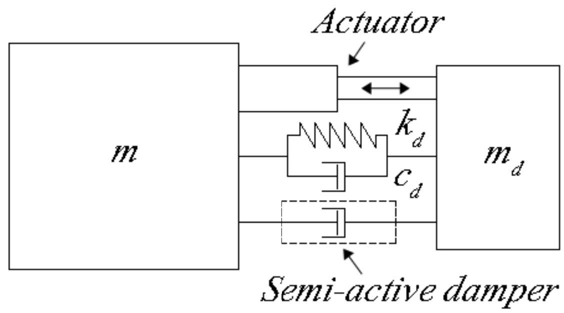

Figure 4.29: Active + semiactive mass damper

Smart dampers or semiactive dampers can effectively reduce vibration by altering the characteristics of the dampers depending on the responses of the structure. Controllable fluid dampers, such as magnetorheological (MR) fluid dampers, use less energy compared to fully active devices such as hydraulic actuators. Various studies (*e.g.*, Dyke *et al.* 1996a,b; Ramallo, *et al.* 2002; Johnson *et al.*, 2007; Jansen and Dyke, 2000) showed the effectiveness of semiactive control for vibration reduction.

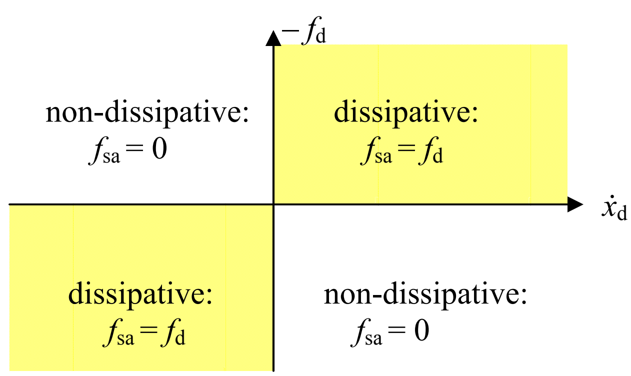

Figure 4.30: Semiactive damper dissipative forces (clipped control)

Unlike the active control that can inject energy into and dissipate energy from the system, semiactive dampers can only dissipate energy (Figure 4.30). A clipped-optimal strategy has been used to derive a suitable control scheme for semiactive DMD system (Dyke *et al.* 1996a,b). In the clipped-optimal strategy, assuming f_d is the desired control force, the semiactive force can be expressed as

$$f_{\mathrm{sa}} = \begin{cases} f_{\mathrm{d}}, & f_{\mathrm{d}}\dot{x}_{\mathrm{d}} < 0 \quad (f_{\mathrm{d}} \text{ would dissipate energy}) \\ 0, & \text{otherwise} \quad (f_{\mathrm{d}} \text{ would inject energy}) \end{cases} \tag{4.11}$$

where $\dot{x}_d$ is the velocity of the damper. Using this clipping strategy, the semiactive force can be caused to act on the system; often, low pass filters will also be applied to the control force to mimic the delays (*i.e.*, rise-times, etc.) of the actual dampers.

4.2.4.2..2 Model

Semiactive dampers require simulation for nonlinear behavior that typically requires larger computing power. Thus, a simplified 5DOF primary system is studied instead of the 20DOF primary system to analyze the performance of the semiactive dampers on the DMD system. The 5DOF primary system shares the total structural mass, damping ratios and similar natural frequencies with the 20DOF primary system. Table 4.4 lists the properties of the primary systems.

20DOF ($i = i^{th}$ floor, i =1,2,…,20)			5DOF ($i = i^{th}$ floor, i =1,2,…,5)		
m_i (lbf)		25155	m_i (lbf)		100621
k_i (lbf/ft)		38359841	k_i (lbf/ft)		11507952
damping ratio		5%	damping ratio		5%
frequency (rad/s)	1st mode	2.99	frequency (rad/s)	1st mode	3.04
	2nd mode	8.96		2nd mode	8.89
	3rd mode	14.87		3rd mode	14.01
	4th mode	20.70		4th mode	17.99
	5th mode	26.40		5th mode	20.52

Table 4.4: Properties of the 20DOF and 5DOF primary systems

(4.6) remains the equation of motions for the 5DOF primary systems with 5 semiactive dampers attached at each floor with the following parameters — damper mass ratio of 5%, stiffness of 210836 lbf/ft, and damping coefficient of 22019 lbf/(ft/s) for each damper. The desired control force is determined by a LQR controller that minimizes the cost function in (4.8) and is clipped using (4.11) to apply only the dissipative forces applicable by the semiactive dampers. A low pass filter (Yang, *et al.*, 2004),

$$\frac{31.4}{s+31.4}\ , \qquad (4.12)$$

is applied to represent the delaying effect of the dampers observed in real world practices.

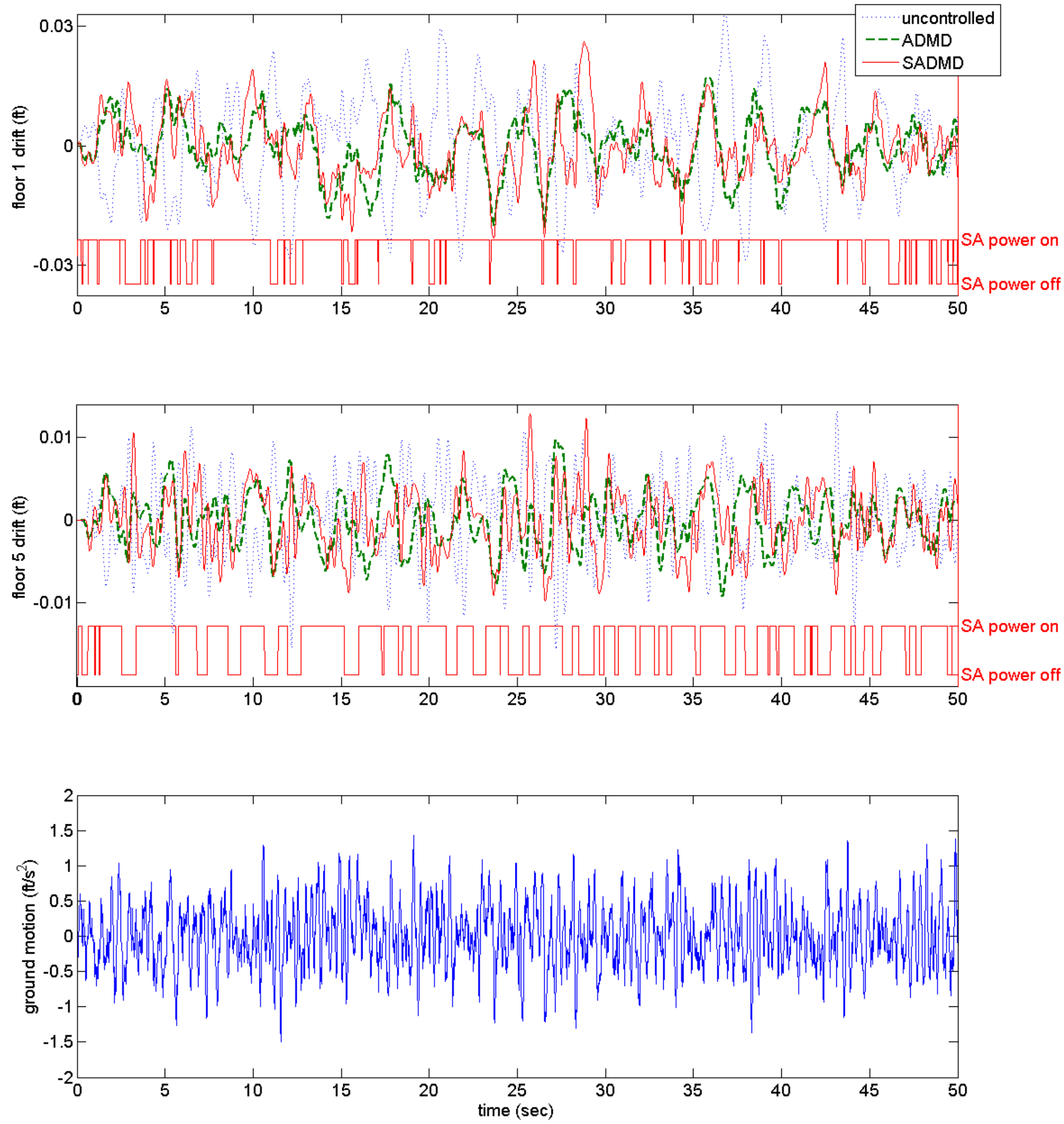

Figure 4.31: Responses of uncontrolled, ADMD and SADMD systems

Under the excitation generated by white noise and the KT filter, Figure 4.31 shows the responses of the 5DOF primary structure without control, with an ADMD and with a SADMD. The two controlled cases significantly reduce the structural motions from the uncontrolled system. Given that the SADMD can only apply dissipative forces, the semiactive system underperforms compared to the active system in reducing responses. Figure 4.32 compares the performance of the uncontrolled and controlled systems in terms of floor and damper displacements; the floor displacements are significantly reduced by the control systems with the active and semiactive further reducing the floor motions at the increase of the damper motions. Between the active systems, the ADMD system reduces more motions (drifts and accelerations) compared to the SADMD system.

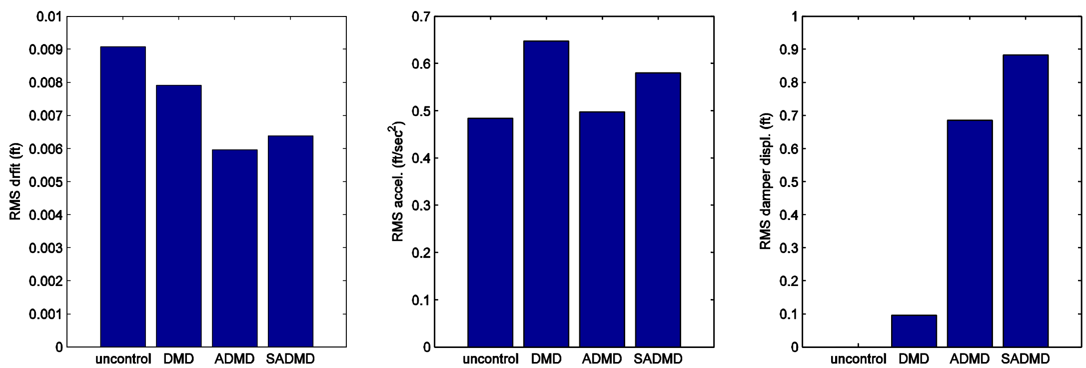

Figure 4.32: Comparison of control systems

4.2.4.2.3 Nonlinear Control: Gain Scheduling

In semiactive control, the dampers are only active when dissipative forces (or $f_d \dot{x}_d < 0$ in (4.11)) are needed to reduce the structural motions. On the other hand, in active control, the dampers are continuously active, thus making active dampers generally more effective than the semiactive dampers. In a multiple damper system like the DMD system, the effectiveness of the semiactive dampers can be improved via gain scheduling.

Gain scheduling is one of the most popular approaches for nonlinear control designs (Leith and Leithead, 2000). The nonlinear system is first divided into different points where the system behaves more linearly, and multiple linear controllers are designed to work best for different points of the nonlinear system. By "scheduling" these controllers at appropriate points of the nonlinear system, the system can be controlled effectively. The following paragraphs describe how gain scheduling can be applied to the semiactive DMD system.

Consider an n semiactive damper system; there are n dampers that can be either active or inactive depending on the directions of the control force and the velocities of the dampers. In other words, there are 2^n configurations of active and inactive dampers. Table 4.5 illustrates all 32 configurations for the 5DOF primary system with the DMD system.

configuration	damper at (1=active, 0=inactive)					# of damper active
	1st floor	2nd floor	3rd floor	4th floor	5th floor	
1	1	1	1	1	1	5
2	0	1	1	1	1	4
3	1	0	1	1	1	4
4	1	1	0	1	1	4
5	1	1	1	0	1	4
6	1	1	1	1	0	4
7	0	0	1	1	1	3
8	0	1	0	1	1	3
9	0	1	1	0	1	3
10	0	1	1	1	0	3
11	1	0	0	1	1	3
12	1	0	1	0	1	3
13	1	0	1	1	0	3
14	1	1	0	0	1	3
15	1	1	0	1	0	3
16	1	1	1	0	0	3
17	0	0	0	1	1	2
18	0	0	1	0	1	2
19	0	0	1	1	0	2
20	0	1	0	0	1	2
21	0	1	0	1	0	2
22	0	1	1	0	0	2
23	1	0	0	0	1	2
24	1	0	0	1	0	2
25	1	0	1	0	0	2
26	1	1	0	0	0	2
27	0	0	0	0	1	1
28	0	0	0	1	0	1
29	0	0	1	0	0	1
30	0	1	0	0	0	1
31	1	0	0	0	0	1
32	0	0	0	0	0	0

Table 4.5: All possible damper configurations of the 5DOF DMD system

For each configuration, the inactive dampers can be treated as the active dampers applying infinitively small control forces. Recall the LQR cost function (4.8):

$$J = E[\mathbf{y}^{\mathrm{T}}\mathbf{Q}\mathbf{y} + \mathbf{f}_{\mathrm{c}}^{\mathrm{T}}\mathbf{R}\mathbf{f}_{\mathrm{c}}]$$

where **R** is the weighting matrix for control forces. With an appropriate **R**, a set of the damper control forces can be limited to relatively small by the LQR control gain that minimizes J in (4.8). More specifically, the control force of the j^{th} damper would be relatively small by using a diagonal matrix, **R**, with the diagonal elements as

$$\mathbf{R}(i,i) = \begin{cases} r & i \neq j \\ r' & i = j \end{cases} \qquad i = 1,2,3\ldots, n \quad \text{and} \quad r' >> r \tag{4.13}$$

where r and r' are constants that determine the amount of control forces applied by the i^{th} damper. A large value of r (or r') indicates small control forces and, by setting $r' >> r$, the control force applied by the j^{th} damper would be relatively small compared to the forces by other dampers. For configurations with multiple inactive dampers, the weighting matrix **R** would have the corresponding diagonal elements equal to r'. Using (4.13), the control gains can be computed for different configurations of active and inactive dampers. These control gains then can be used to compute the appropriate control forces in each time step during the excitation. To determine which control gain is most effective in reducing vibration in each time step, two assumptions are made: 1) more active dampers are more effective and 2) dampers at higher floors are more effective than dampers at lower floors. The first assumption is based on that more active dampers are more likely to produce larger control forces though it is possible that fewer active dampers can produce larger control forces (thus possibly more effective) for certain structural and damper motions. The second assumption is based on the observation in the previous section that TMDs are more effective when placed at higher floors. With these two assumptions, the control gains computed from different **R** or different configurations of active and inactive dampers can be ranked in the following manner:

Rank	# of active dampers	active damper locations
most effective	n	all floors
2nd most effective	$n-1$	all floors except floor 1
3rd most effective	$n-1$	all floors except floor 2
$\vdots$	$\vdots$	$\vdots$
3rd least effective	1	none except floor 2
2nd least effective	1	none except floor 1
least effective	0	none

Table 4.6: Rank among configurations of active and inactive dampers

Table 4.5 presents all configurations of active and inactive dampers for the 5DOF primary system in the rank order described by Table 4.6 (*e.g.*, first configuration is most effective while 32nd configuration is the least effective). Knowing which control gain (or configuration of active and inactive dampers) is most effective in each time step, a new semiactive control strategy of the DMD system can be explained in the following flow chart.

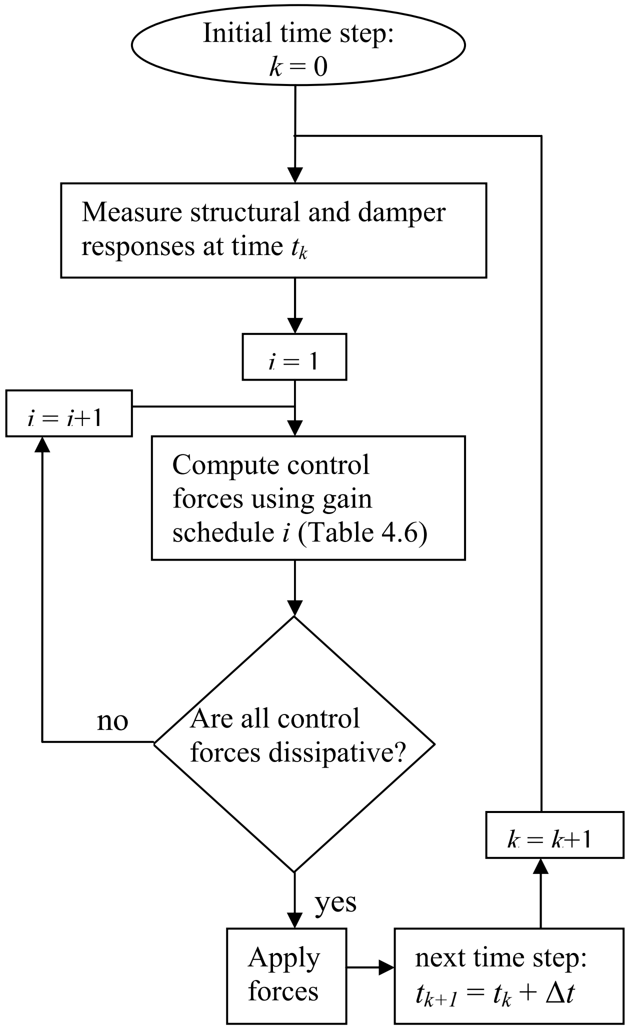

Figure 4.33: Flow chart for improved semiactive control

4.2.4.2.4 Result

Using the configurations from Table 4.4 and the flow chart in Figure 4.33, the behavior of the 5DOF primary system with the semiactive DMD system is simulated. Figure 4.34 shows the comparison between the responses of the uncontrolled and controlled systems. Although the semiactive system reduces the larger story drifts, the fully active control system is the best performer considering both story drifts and accelerations (the semiactive system has a much larger acceleration compared to the active system). Overall, the semiactive system with gain scheduling outperforms the semiactive system in both story drifts and accelerations, but at the expense of larger damper motions. Although the improvement is not substantial in this specific example, larger improvements are expected when there are large gaps between the active and semiactive control systems. In other words, the gain scheduling is more effective for systems in which active control is far superior than semiactive control.

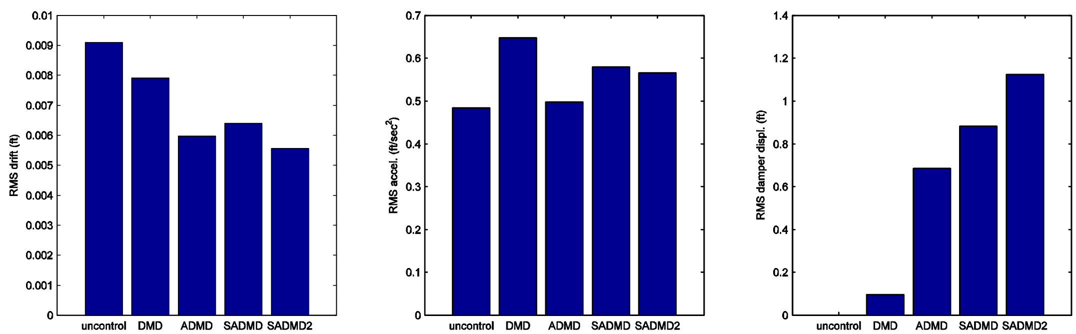

Figure 4.34: Comparison of control systems (SADMD2 is the SADMD system with gain scheduling)

4.3 Environmental Control: Shading Fin

Similar to a TMD, shading fins are typically passive devices that are fixed on building façades. However, by allowing shading fins to be movable (through mechanical means), the system can adjust to the weather and to sun orientation. Moreover, movable fins can integrate with a mass damper system to achieve synergy between structural and environmental control systems. This section discusses the energy effectiveness of movable shading fins from the Shading Fin Mass Damper (SFMD) system.

Due to the motion requirement of the mass dampers, the shading fins must be movable. There are typically two types of shading fin movements — protracting/retracting and rotating (Figure 4.35). Movable fins can track sun paths for different hours in a day and for different seasons in a year (Figure 4.36).

There are several buildings that adopt movable shading devices. One of the oldest examples is the Hall of Records Building (Figure 4.37) in Los Angeles designed by Richard Neutra in 1962; a more recent example is the Caltrans District 7 Headquarters Building (Figure 4.38) in Los Angeles by Thom Mayne in 2004. The tall vertical shading fins on the south side of Hall of Records Building rotate throughout the day to block direct sunlight, trying to decrease heat gain in the warm southern California climate. The "flappable" shading devices (so called due to the slapping motion of the devices) on the Caltrans Building are placed in the east and west sides of the building. The shades flap open and close to control heat gain from direct sunlight in mornings and afternoons, and in winters and summers.

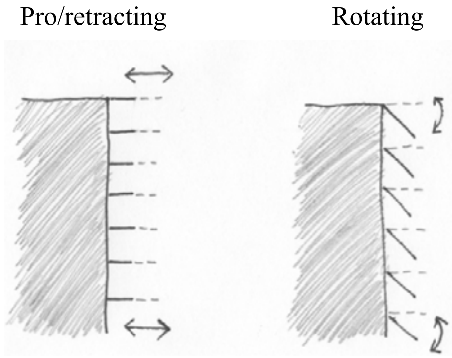

Figure 4.35: Movements of shading fins (plan view)

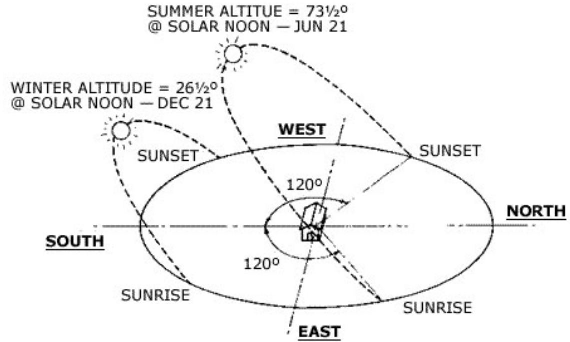

Figure 4.36: Sun paths for summer and winter (Alward and Shapiro, 1981)

Figure 4.37: Hall of Records, Los Angeles (1962) by Richard Neutra (photo: Martin, 1995)

Figure 4.38: Caltrans District 7 Headquarter, Los Angeles (2004) by Thom Mayne (photo: Halbe, 2004)

4.3.1 Simulation Model

A 3-story office building model (Figure 4.39) is used to analyze the effect of different shading movements using eQuest (version 3.5) — the QUick Energy Simulation Tool for building. The building is 150ft by 60ft located in Los Angeles (warm climate region), with the longer dimension in the north-south direction. The windows and fins are located only on the east and west façades of the building. The HVAC system of the building is automatically chosen by eQuest to satisfy the energy consumption profile of the building. Figure 4.40 compares office buildings with and without shading fins (5ft long and perpendicular to the building façades). As shown, the building with fins has improved energy efficiency in most months. For more discussion on the economy of shading devices, the reader is referred to *Solar Control and Shading Devices* by Olgyay and Olgyay (1957).

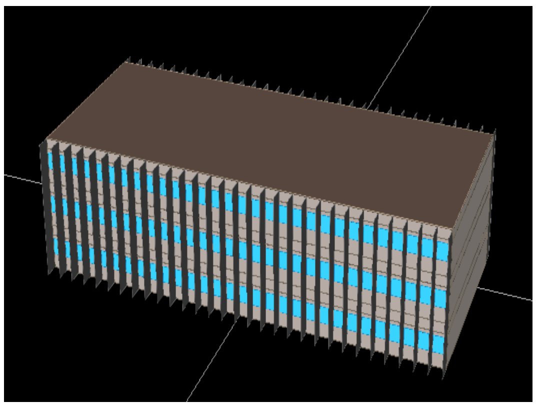

Figure 4.39: eQUEST building model

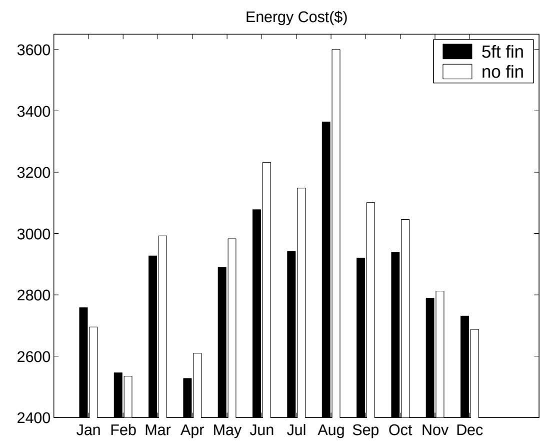

Figure 4.40: Effect of 5ft shading fins

4.3.2 Stationary Shading Fins

Most shading devices on buildings are stationary. This section studies the typical stationary shading fins that offer insight on more complex movable shading fins.

4.3.2.1 Effect of Fin Length

The length of shading fins has simple effects on sunlight (Figure 4.41). Retracted fins allow more sunlight to enter the building while protracted fins allow less. Figure 4.42 shows the monthly energy consumption profiles for shading fins at different lengths. Since cooling is the largest portion of the electric consumption, longer fins outperform shorter ones in electricity consumption because longer fins allow less sunlight (solar heat gain) into the building. On the contrary, buildings with longer fins use more gas for heating due to the reduction of sunlight. In most months, the energy cost is lower for longer fins because electricity currently costs more than gas (*i.e.*, it is usually cheaper to heat a space using gas than cooling it using electricity for the same magnitude of temperature changes). However, the energy cost is higher in winter months for longer fins because the building is using more heating than cooling. This study of long and short fins shows that buildings should, generally, protract shading fins during summer and retract them during winter to minimize energy. The daylighting effect is also included in the study, but the lighting loads do not differ significantly between different fin lengths.

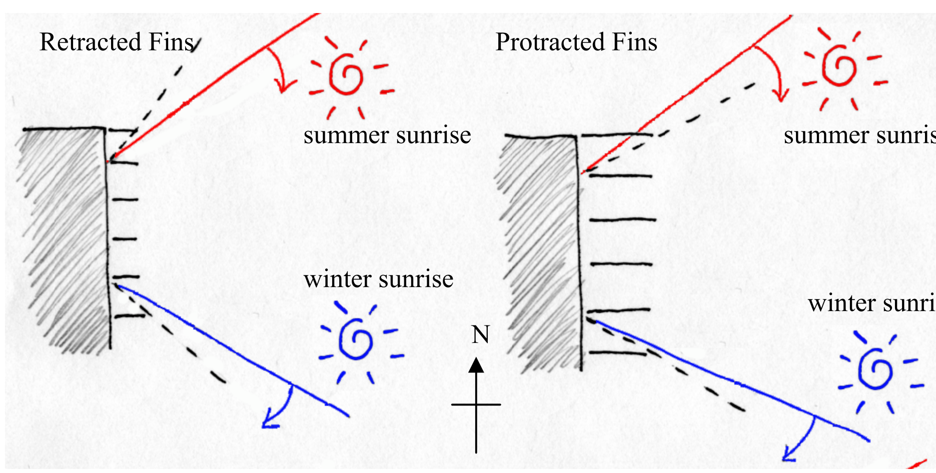

Figure 4.41: Sunlight effect for short and long vertical shading fins in plan view

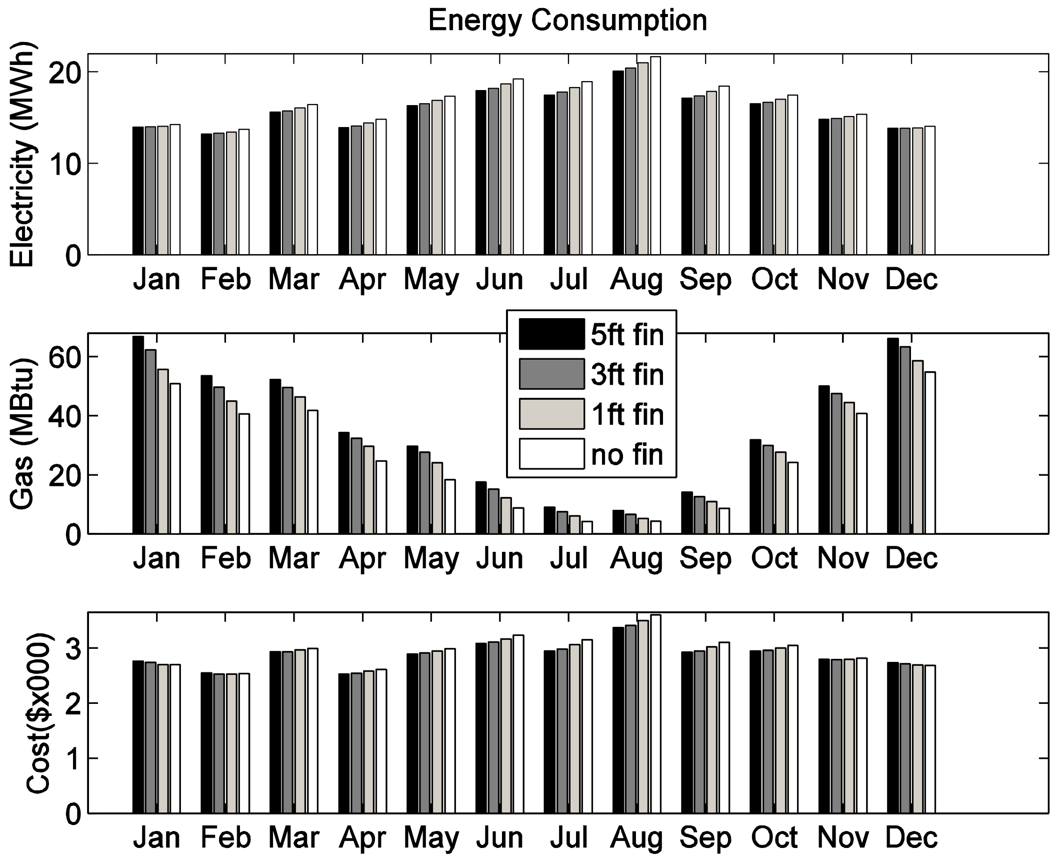

Figure 4.42: Effect of protracting shading fins

4.3.2.2 Effect of Fin Orientation

Rotating shading fins have more complicated effects on sunlight (Figure 4.43). Fins that are rotated toward the North let in summer early morning and late afternoon sun while blocking off all winter sun into the building. On the other hand, fins that are rotated toward the South let in summer late morning sun and early afternoon sun while letting in some winter early morning and late afternoon sun.

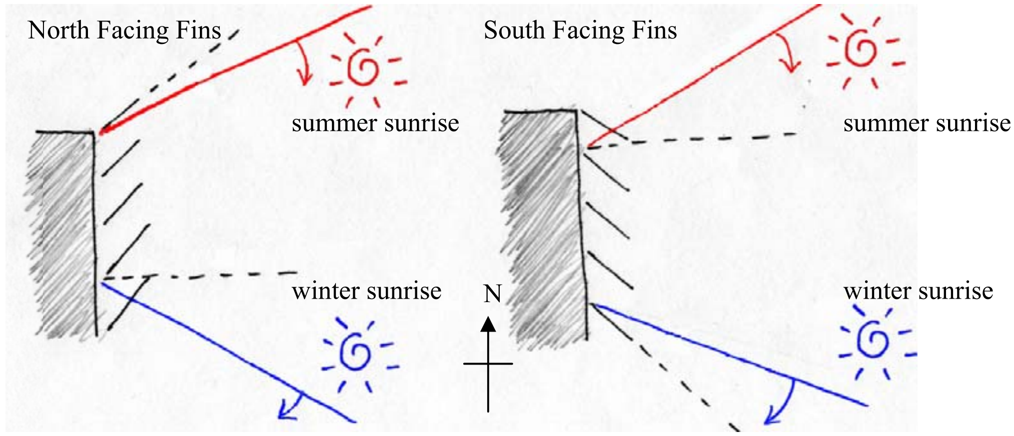

Figure 4.43: Sunlight effect for rotated vertical shading fins in plan view

Figure 4.44 shows the monthly energy consumption profiles for stationary shading fins at different angles and directions. Fins rotated 45^{o} toward the North are associated with the least electricity usage. In this scenario, less cooling is needed because the sun is blocked in late morning to early afternoon when the day is hottest. For gas consumption, North facing fins typically perform at similar levels as 90^{o} fins and no fins because all these cases let in sunlight in the early mornings when the building needs to heat up for the beginning of office hours. In contrast, South facing fins cause higher gas demand during the summer months because they block sunlight in the early mornings. Nevertheless, South facing fins outperform other configurations in gas consumption for winter months. Cold weather requires heating throughout the day and South facing fins let in sunlight during late mornings and early afternoons when the sun is producing the most solar heat. This study of fin orientations shows that buildings should rotate shading fins toward the North for most of the year, but should also rotate them to track the sun in cold weather to minimize energy cost. Here the energy saving (28.6% per year) is substantially larger than the pro/retracting fins, though the rotating motion may be harder to incorporate with the mass damper motion.

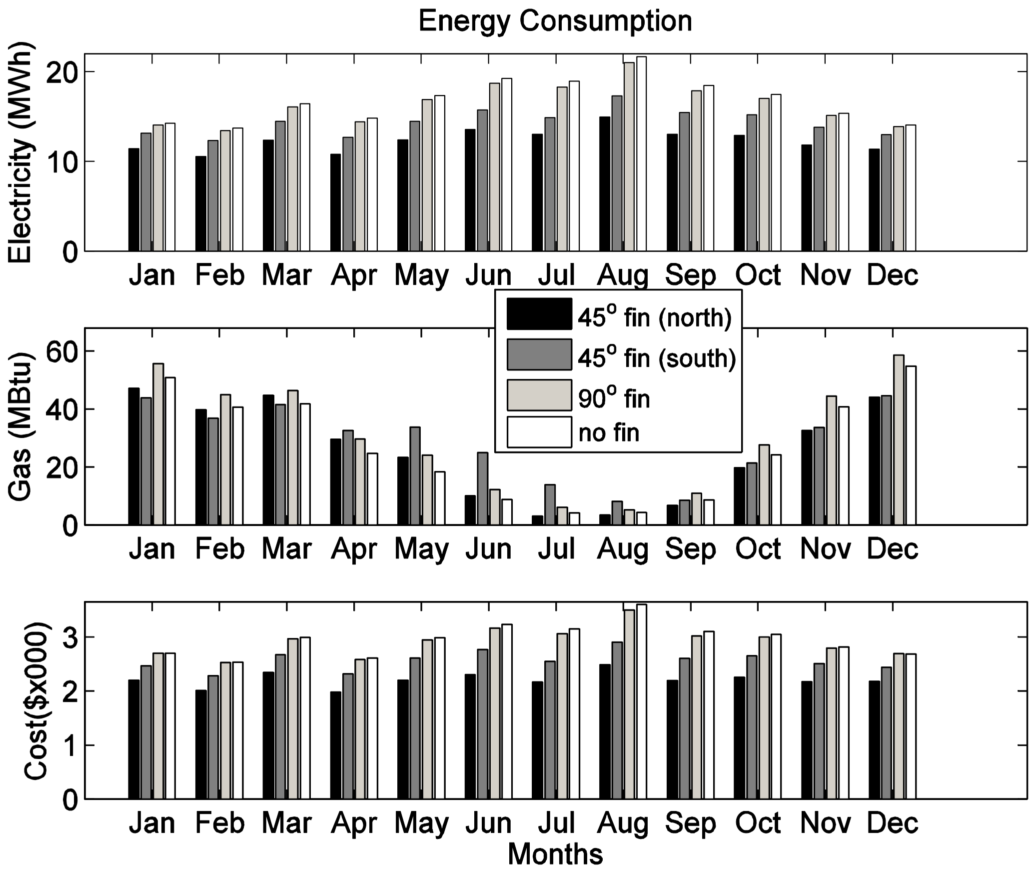

Figure 4.44: Effect of rotating shading fins

Both studies of pro/retracting and rotating fins demonstrate the benefits of movable fins. The next phase of research will focus on simulating energy consumption profiles for shading fins that actively adjust throughout the day and year. The rest of this paper focuses on movable fins that rotate and not those that protract/retract. Simulations show that different fin orientations have a larger impact on energy consumption compared to different fin lengths.

4.3.3 Movable Shading Fins

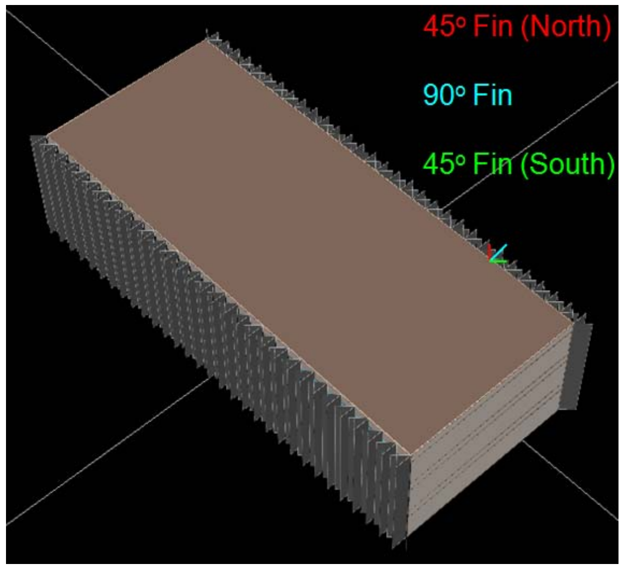

Figure 4.45: eQuest model for active rotating shading fins.

To simulate the effect of active shading fins on building energy consumption, the eQuest simulation model is used with some modification. Since eQuest treats the shading elements as physically fixed, shading schedules are applied on the fins to "move" them throughout the year. Shading schedules in eQuest deal with shading elements that behave differently throughout the year, such as leaves falling off trees (a shading element) in winter. To mimic the movements of active shading fins, a building model is equipped with multiple fins at each location and each fin is turned "transparent" or "solid" by the shading schedule. For example, an active rotating fin model would have multiple shading fins at various angles (45^o North, 90^o and 45^o South) at each location (Figure 4.45). If sunlight is desirable throughout the day, such as on a cold day, the following fin arrangement would be placed (assuming it is summer time where the sun rises and sets at Northeast and Southwest):

	45^o North Fins	90^o Fins	45^o South Fins
Early morning	S	T	T
Mid morning	T	S	T
Late morning	T	T	S
Noon	T	T	S
Early afternoon	T	T	S
Mid afternoon	T	S	T
Late afternoon	S	T	T
		S = Solid	T = Transparent

Table 4.7: Shading schedule arrangement

The shading schedule arrangement only has one fin solid at a time and, thus, mimics rotating fins that track the sun path, allowing the maximum amount of direct sunlight into the building.

4.3.3.1 Shading Schedule in eQuest

The limitation of the shading schedule is that it only adjusts the solar-transmittance of the fins and leaves the visibility-transmittance constant. In other words, the shading schedule adjusts heat-gain due to sunlight but not the lighting effect. This makes daylight calculation unreliable. Daylight calculation assumes that there are light sensors in the building tracking natural lighting throughout the day. The amount of required electric lighting can be decreased in daytime with the presence of both direct and indirect sunlight (indirect or ambient sunlight is more useful for daylighting because direct sunlight causes a glaring problem and, therefore, is diffused or reflected for daylighting).

a) No daylight calculation	No Fin	90° Fins	45° South Fins	45° North Fins
Space Cooling / Heating ($)	22,064	19,176 (6.4%)	15,922 (13.6%)	12,378 (21.5%)
Electric Lighting ($)	14,848	14,579 (0.6%)	14,498 (0.8%)	14,522 (0.7%)
Misc. Equip. ($)	8,227	8,077 (0.3%)	8,032 (0.4%)	8,046 (0.4%)
b) With daylight calculation	No Fin	90° Fins	45° South Fins	45° North Fins
Space Cooling / Heating ($)	21,043	18,649 (6.5%)	14919 (16.7%)	11,466 (26.1%)
Electric Lighting ($)	7,354	6,822 (1.5%)	7,375 (-0.1%)	6,684 (1.8%)
Misc. Equip. ($)	8,294	8,166 (0.4%)	8,066 (0.6%)	8,090 (0.6%)
	numbers in ( ) are savings in % of the total energy cost from No-Fin case			
c) Daylight difference (%)	No Fin	90° Fins	45° South Fins	45° North Fins
Space Cooling / Heating	4.63%	2.75%	6.30%	7.36%
Electric Lighting	50.47%	53.20%	49.13%	53.97%
Misc. Equip.	0.82%	1.11%	0.43%	0.55%

Table 4.8: Daylight calculation effects

Table 4.8 shows the effects of daylight calculations without shading schedules, combining space cooling and heating in terms of monetary cost. However, it should be noted that space cooling uses electricity while space heating burns natural gas as energy sources. Electricity and natural gas differ in more than their cost, but also in site and source energy consumption. Site energy is the energy consumed on site, at the building location as an end-user. Source energy is the energy cost to natural resources. Natural gas uses equal amounts of site and source energy, meaning that there is no energy loss in converting from source to site energy. In contrast, electricity uses significantly more source energy than site energy, or there is a considerable amount of energy exhausted in producing the electricity to provide to end-users from natural resources. This remains true as long as fossil fuels are used to generate most electricity.

Changes in miscellaneous equipment can be neglected because such changes are due to the difference in energy rates for peak and off-peak hours; the amount of energy consumption by miscellaneous equipment remains the same for all cases. As shown in Table 4.8(c), daylight calculations clearly have profound effects on electric lighting. In contrast, the effect of on space cooling and heating daylighting is smaller and less obvious because the effect occurs indirectly when electric lighting gives off heat while lighting the space.

Since the shading schedules make daylight calculation unreliable, eQuest can only calculate accurately the energy effect of active shading fins without daylight calculation. In other words, electric lighting will be kept fairly constant throughout all cases (similar to Table 4.8(a)) and eQuest is primarily computing the effect on cooling and heating energy cost. Although the daylighting effect of active shading fins on electric lighting savings cannot be computed, it should remain moderately small (within 2% of the total energy cost) as suggested by Table 4.8(b). Meanwhile, savings in cooling and heating can be significantly larger (more than 25% in one case). Moreover, Table 4.8(a) shows similar trends of energy saving in cooling and heating for the different fin cases when compared to Table 4.8(b). The difference in percentage is largely due to the difference in total energy costs between the cases;

the actual cost savings are quite consistent between Table 4.8(a) and 4.8(b). Therefore, despite the lack of daylight calculation, the simulation of the active shading fins by eQuest using shading schedules can be treated confidently while being aware of its limitations.

4.3.3.2 Comparing Simulations with and without Shading Schedule

Since shading schedule in eQuest cannot accurately compute the daylighting effects, the following comparison cases turn off daylight control such that all cases, despite having different shading fin configuration, use the same amount of energy on lighting. Thus the difference in energy consumption profiles is caused by the difference in heat gain affected by the fins with or without the shading schedules. Figure 4.46 shows that the energy costs of unshaded and shaded buildings with or without using the shading schedule. For the shaded case using shading schedule, the transmittance of the fin is set to be 0% such that the fin should be "opaque" like a regular fin. On the other hand, the unshaded case has the transmittance is set to be 100% for the fin to be "transparent." The shaded cases (with and without shading schedule) yield identical electricity and gas costs, suggesting that the shading schedule is working accurately for these cases. Nonetheless, the unshaded cases do not match, casting doubts about how accurately the shading schedule calculates "transparent" fins.

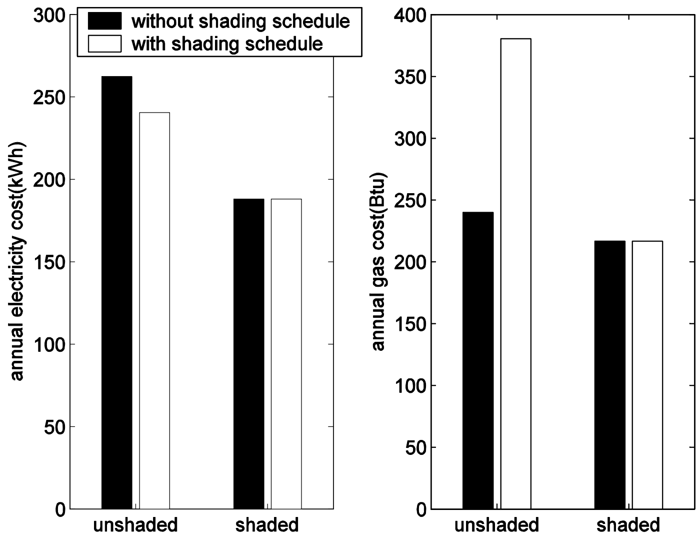

Figure 4.46: Comparison of shading fins using shading schedule

Figure 4.47 compares the effects of shading schedules on different fixed (non-movable) shading fin orientations on east and west windows (45^o from north, 90^o and 45^o from south). For the cases that using shading schedules, all of the three oriented fins are presented in the building model similar to Figure 4.45. The fins are then turned "solid" or "transparent" using the shading schedules to mimic the cases without shading schedules. From Figure 4.47, the cases with shading schedule follow both the electricity and gas consumption pattern of the cases without schedules. However, it is clear that the no fin cases are the least accurate, which agrees with the observation from Figure 4.44. And for the cases with fins, although the absolute energy cost is off, the errors are more consistent throughout different orientations. In other words, the finned cases with shading schedules are able to capture the changes on energy consumption due to different fin orientations. This suggests that any further comparison study using shading schedules should have a base case that has some "solid" fins using shading schedules. In fact, the cases with fixed fins using shading schedules (Figure 4.47) are shown for the following comparison study of actively rotating fins.

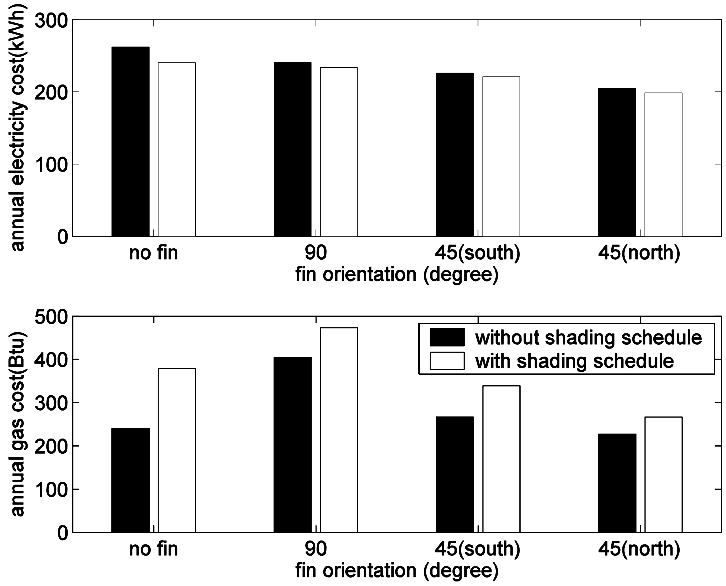

Figure 4.47: Comparison of rotating fins using shading schedule

4.3.3.3 Actively Rotating Fin using Shading Schedules

To simulate the effect of actively rotating fins, a year-long shading schedule is determined by trying to decrease the energy cost from the case of 45^{o} North oriented fins (the least energy consuming case). More specifically, in every month, the 45^{o} North case is substituted with different shading schedules to determine one that uses the minimum energy cost. A monthly interval is chosen instead of a shorter (daily) or longer (seasonal) interval because weather changes too little over shorter intervals to justify computational cost for the increased cases (*i.e.*, 365 cases in daily intervals instead of 12 in monthly intervals), and weather changes too much over longer intervals for the determined shading schedule to be fully representative of the current weather. There is another reason why a longer interval such as a seasonal interval (3-month period) is not suitable for eQuest. Depending on the annual peak demand of the energy profile on the simulated building model, eQuest automatically chooses an appropriate HVAC system that satisfies the demand. And longer intervals can cause too great of an effect in the energy profile of the overall system that changes the size of the HVAC system in the simulation, which outweighs the effects of the rotating fins in energy consumption.

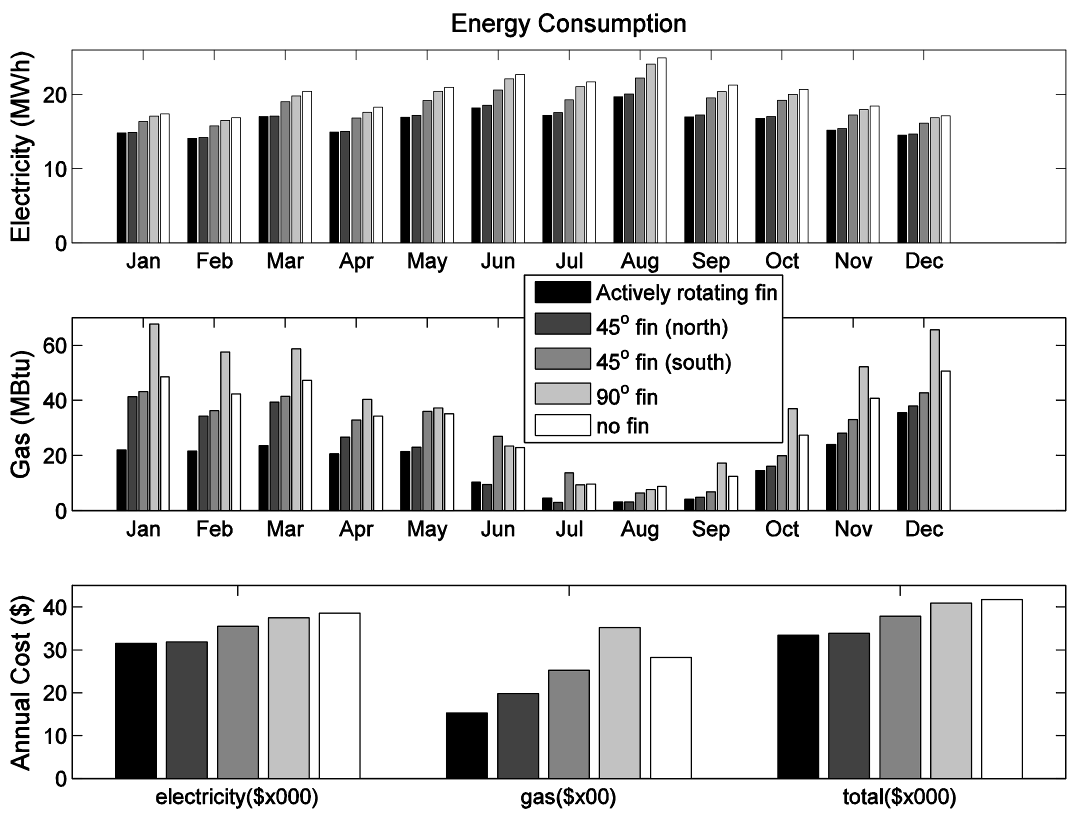

Figure 4.48: Comparison of actively rotating and fixed fins using shading schedules

Table 4.9 details the shading schedule chosen for the entire year. In winter months, since heat-gain is more desirable, the fins are more likely to orient toward 45^{o} South where the sun is. In summer, when the sun is avoided to prevent overheating, the fins are mostly oriented toward South in the morning/evening and North for mid-days to counter the sun path in summer. In spring and fall, a combination of embracing and avoiding direct sunlight is useful to minimize both cooling and heating costs. Figure 4.48 compares the effectiveness of the actively rotating fin to other fixed fin orientations with the shading schedule. The actively rotating fin case is the most energy efficient system with a very significant advantage in gas consumption. The advantage of the electricity consumption is less obvious since it includes more than cooling loads, such as lighting and equipment that are constant throughout different shading configurations.

The lighting loads are not affected by the active shading fins because the daylighting effect is not considered in the shading schedule in Table 4.9 and Figure 4.48. As discussed earlier in this chapter, eQuest cannot accurately simulate the daylighting effect with the solid fin shading schedule. If daylighting could be included in the analysis, electricity consumption could be further optimized by exploiting natural light and lessening the lighting loads. The changes would depend on individual requirements for light, heat gain and the compromises between them.

Table 4.9 and Figure 4.48 illustrate the effect of active shading fins for a warm climate (Los Angeles). If the study was to be performed for colder climates, the shading fins are expected to welcome more direct sunlight compared to the schedule in Table 4.9. Gas consumption would be a larger portion of the overall energy consumption with increased heating loads.

	Time	Fin Orientation				Time	Fin Orientation		
		$45^{o}N$	90^{o}	$45^{o}S$			$45^{o}N$	90^{o}	$45^{o}S$
Jan	5 ~ 8am			x	Jul	5 ~ 8am			x
	8 ~ 10am			x		8 ~ 10am			x
	10 ~12pm			x		10 ~12pm	x		
	12 ~ 2pm			x		12 ~ 2pm	x		
	2 ~ 4pm			x		2 ~ 4pm	x		
	4 ~ 8pm			x		4 ~ 8pm			x
Feb	5 ~ 8am			x	Aug	5 ~ 8am			x
	8 ~ 10am			x		8 ~ 10am	x		
	10 ~12pm			x		10 ~12pm	x		
	12 ~ 2pm		x			12 ~ 2pm	x		
	2 ~ 4pm		x			2 ~ 4pm	x		
	4 ~ 8pm		x			4 ~ 8pm	x		
Mar	5 ~ 8am			x	Sept	5 ~ 8am	x		
	8 ~ 10am			x		8 ~ 10am	x		
	10 ~12pm			x		10 ~12pm	x		
	12 ~ 2pm		x			12 ~ 2pm	x		
	2 ~ 4pm		x			2 ~ 4pm	x		
	4 ~ 8pm		x			4 ~ 8pm	x		
Apr	5 ~ 8am			x	Oct	5 ~ 8am	x		
	8 ~ 10am		x			8 ~ 10am	x		
	10 ~12pm		x			10 ~12pm	x		
	12 ~ 2pm	x				12 ~ 2pm	x		
	2 ~ 4pm	x				2 ~ 4pm	x		
	4 ~ 8pm	x				4 ~ 8pm	x		
May	5 ~ 8am			x	Nov	5 ~ 8am		x	
	8 ~ 10am	x				8 ~ 10am		x	
	10 ~12pm	x				10 ~12pm	x		
	12 ~ 2pm	x				12 ~ 2pm	x		
	2 ~ 4pm	x				2 ~ 4pm	x		
	4 ~ 8pm	x				4 ~ 8pm	x		
Jun	5 ~ 8am			x	Dec	5 ~ 8am			x
	8 ~ 10am			x		8 ~ 10am			x
	10 ~12pm	x				10 ~12pm			x
	12 ~ 2pm	x				12 ~ 2pm			x
	2 ~ 4pm	x				2 ~ 4pm		x	
	4 ~ 8pm			x		4 ~ 8pm		x	

Table 4.9: Shading schedule for the actively rotating fins throughout a year (x = oriented direction).

4.4 SHM: Distributed Actuators

In the previous sections, the shading fin mass dampers are shown to be synergistic in vibration migration and energy reduction in buildings. This section introduces another useful aspect of the SFMDs — structural health monitoring (SHM). SHM automatically assesses the current state of the structure and identifies possible damage such that the building safety is constantly monitored. The SFMD system has the potential for use in SHM by providing low-level excitation within the structure so that structural parameters may be estimated from the dynamic response to the excitation. One of the difficulties in global vibration based SHM for civil structures is that small excitations, such as micro-tremors, wind, traffic, people or equipment in the structure and so forth, are of unknown characteristics and are often not measureable. With the SFMD placed on all floors of the structure, there are many small actuators installed to adjust the position of the fins and provide low-level active structural control. Using these actuators to excite the structure and measure the resulting responses, structural damage can be detected with excitation-based SHM techniques.

Other than local excitations, combinations of excitations can also be helpful in SHM to excite certain modes of the structure. Different modes can amplify responses at different locations of the structure and can improve the noise-to-signal ratio of sensor measurements in these locations. Moreover, exciting different modes of the structure can yield more information about the structure, helping assessing the state of the structure. In this section, it is shown how to excite multiple locations of the structure to improve SHM using the same 20-story computer model from prior structural simulations.

4.4.1 Model

The actuators used to excite the structure are installed connecting the mass dampers and the floors. The actuators apply forces on the structure by pushing or pulling the mass dampers, creating reaction forces on the structure. Since the actuators are designed for low-level forces, they are most effective exciting the structure by oscillating the dampers at frequencies close to the fundamental modal frequencies of the structure. At these frequencies, the structural responses are amplified and, thus, most observable by sensors in spite of noises in measurements. From the DMD system in (4.2), eliminating the ground motions, the equation of motions used for the SHM study can be represented as

$$\mathbf{M}\ddot{\mathbf{x}} + \mathbf{C}\dot{\mathbf{x}} + \mathbf{K}\mathbf{x} = \mathbf{B}_c\mathbf{f} = \begin{bmatrix} -1 & 0 & & & \\ 1 & 0 & & & \\ 0 & -1 & & & \\ 0 & 1 & & & \\ & & \ddots & & \\ & & & -1 & 0 \\ & & & 1 & 0 \\ & & & 0 & -1 \\ & & & 0 & 1 \end{bmatrix}_{2n\times n} \begin{bmatrix} f_1 \\ f_2 \\ f_3 \\ f_4 \\ \vdots \\ f_{n-3} \\ f_{n-2} \\ f_{n-1} \\ f_n \end{bmatrix}_{n\times 1} \tag{4.14}$$

where f_i is the excitation in the i^{th} story. Since the excitations are oscillating forces, they have the forms of

$$f_i = A\,\alpha_i \sin(\omega\, t), \qquad i = 1, 2, \ldots, n \tag{4.15}$$

where A is the amplitude (which is set to be 5% of the floor mass), α_i is th adjustable scalar (more explanation in Section 4.4.4) and ω is the harmonic frequency of excitation. By simulating (4.14), the structural responses due to different excitation (4.15) at various frequencies can be measured for SHM.

4.4.2 Modal Estimation of Steady State Response

Although it is effective to excite the mass dampers at the structure's fundamental frequencies for SHM, not all frequencies are suitable, especially on the DMD system. For any n-DOF system, there are n modes or fundamental frequencies (more explanations about modal characteristics of structures are detailed in Section 3.2). Sometimes, two or more of these frequencies are very close to each other, causing their modal characteristics to overlap. Extracting these modal parameters is known to be very difficult. When m dampers are introduced into an n-DOF primary system, not only do the dampers shift the n original modes, they also add m modes to create a new $(n + m)$-DOF system with $(n + m)$ modes. Often, the $(n + m)$ modes of the damper system have frequencies closely spaced.

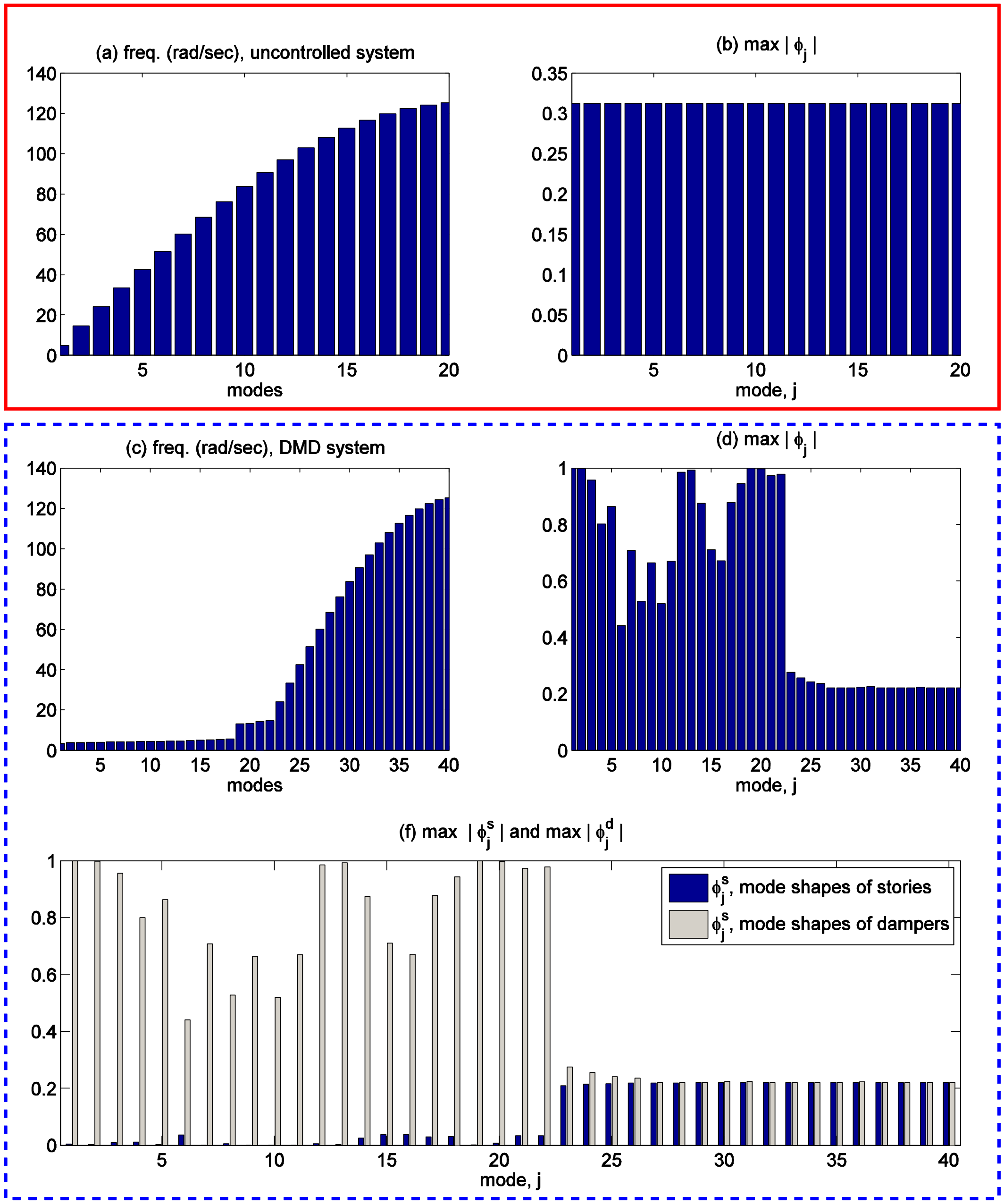

Figure 4.49: Comparison of modal characteristics of the uncontrolled (floors only) and DMD (floors and dampers) systems

Figure 4.49 illustrates some of the modal parameters of the 20-DOF primary structure and the same structure with the DMD system (see Figure 4.25 for the details on the structural and damper parameters of the sub-optimized weighted EDMD system). Figures 4.49(a) and 4.49(c) show the modal frequencies of the two systems (20 modes and 40 modes for the uncontrolled system and the DMD system, respectively). In the system without dampers, there are 20 clearly distinguishable frequencies. The lower frequencies of the DMD system are hard to distinguish from one another. In the DMD system, there are two groups of closely spaced modes — first to 18th modes and 19th to 22nd modes. One reason that these modes are closely spaced is that they are damper modes (modes that are heavily influenced by the mass dampers) with similar characteristics. Multiple dampers of the DMD system (in Figure 4.25) are tuned to have similar parameters to reduce large motions. Although this tuning method is effective for vibration reduction, it causes many overlapping modes that are troublesome for modal parameter estimation.

Figures 4.49(b) and 4.49(d) show the maximum magnitudes of (normalized) mode shapes of the uncontrolled and DMD systems, defined by

$$\max_i \left|\varphi_{i,j}\right| \tag{4.16}$$

where $\varphi_{i,j}$ is the i^{th} element of mode shape $\boldsymbol{\varphi}_j$ for the j^{th} mode. For the DMD system, the mode shapes can be expressed as $\boldsymbol{\varphi}_j = [\boldsymbol{\varphi}_j^{\text{s}} \quad \boldsymbol{\varphi}_j^{\text{d}}]^{\text{T}}$, with $\boldsymbol{\varphi}_j^{\text{s}}$ and $\boldsymbol{\varphi}_j^{\text{d}}$ being the portions of mode shapes for the structural floors and mass dampers, respectively, and Figure 4.49(f) shows both

$$\max_i \left|\varphi^{s}_{i,j}\right| \qquad \text{and} \qquad \max_i \left|\varphi^{d}_{i,j}\right| . \tag{4.17}$$

Since $\boldsymbol{\varphi}_j$ is normalized, or $|\boldsymbol{\varphi}_j^{\mathrm{T}}\boldsymbol{\varphi}_j| = 1$, $|\varphi_{i,j}|$ has values between 1 and 0. A large magnitude values of $\varphi_{i,j}$ (*i.e.*, close to 1) implies that the i^{th} element (location) dominates all other elements for this particular mode. In other words, a large value in (4.16) signifies that the j^{th} mode ($j = 1,2,3,\ldots,n+m$) is dominated by, or heavily skewed toward, one of the $(n+m)$-DOF. Figure 4.49(d) shows many skewed modes (the lower modes) for the DMD system while there is no skewed mode for the system without dampers in Figure 4.49(b). By separating the mode shapes for the primary structure and damper, Figure 4.49(d) shows that all the skewed modes are dominated by the dampers in the system because $\max_i |\varphi^d_{i,j}| >> \max_i |\varphi^s_{i,j}|$ for these modes. This further evidences that the lower modes (first 22 modes) are damper modes where their associated mode shapes are dominated by the dampers. Since the first 22 modes are closely spaced and, thus, difficult for system identification via modal estimation, the DMD system is only excited from 23rd to 40th modes for the rest of the SHM study.

When the system is excited at a natural frequency, the steady state responses are related to the mode shape. Figure 4.50 shows the responses of the floor and damper displacements at first to fifth floors when the DMD system is excited for the 23rd mode (at the frequency of 23.95 rad/sec). Figure 4.50(c) presents the steady state responses of the floors (shown in Figure 4.50(a)) after the transient responses settle; Figure 4.50(d) shows the steady state response of the dampers. In the steady state responses, there are clear amplitude levels each of the floor and damper responses oscillate to. These amplitude levels are related to the mode shapes of the system.

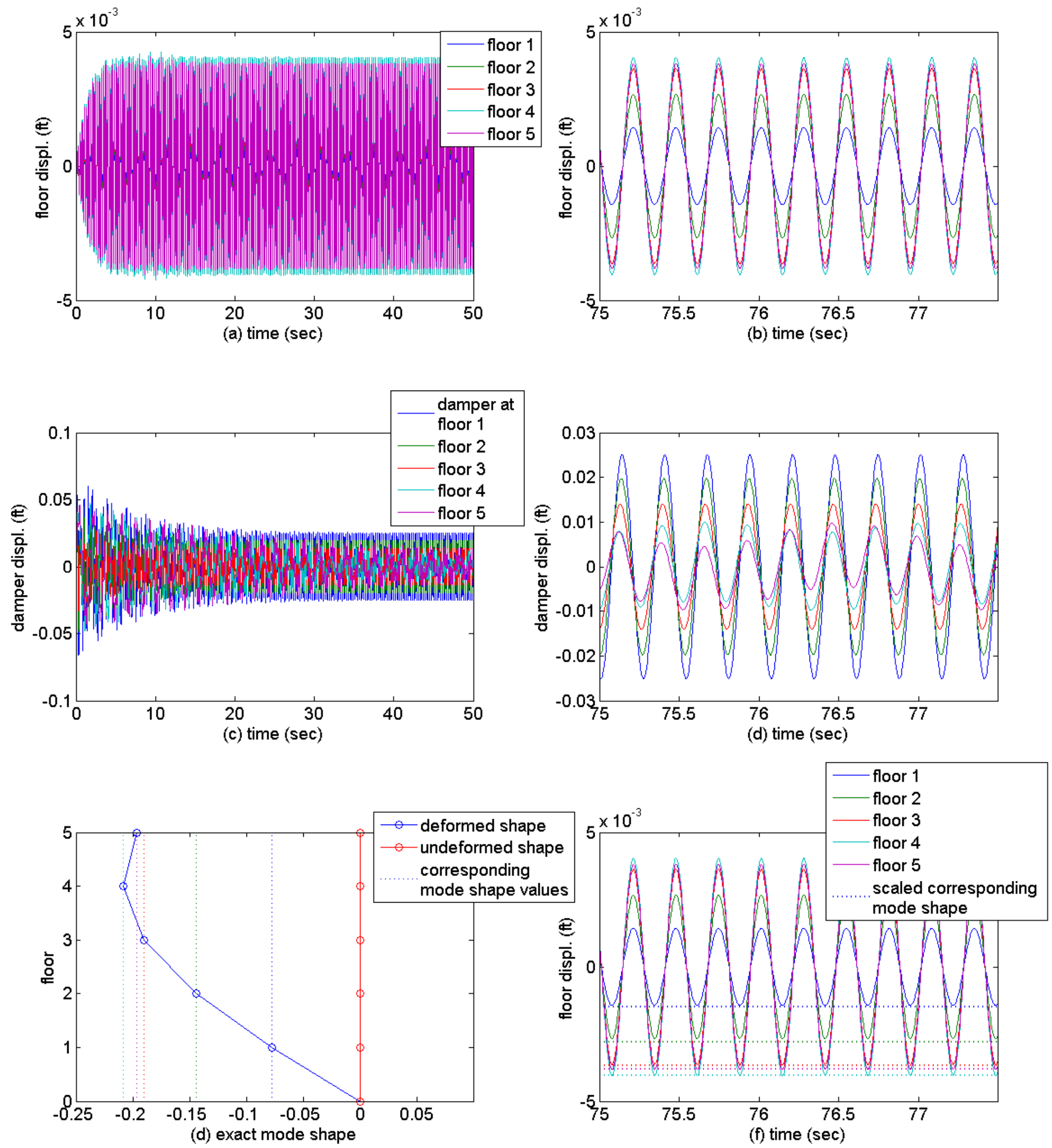

Figure 4.50: Relationship between harmonic response and mode shapes

Figure 4.50(e) and 4.50(f) demonstrate the relationship between the amplitudes of the steady state responses and the corresponding mode shape. Figure 4.50(e) shows a subset of the mode shape (floors 1 t o 5) of the 23rd mode (the mode excited in the responses in Figure 4.50) of the structure. The mode shape values shown in Figure 4.50(e) indicate how floors 1 to 5 deform relative to one another in steady state for this particular mode. For example, when floor 5 deforms 0.2ft (the unit here is arbitrary; it can be inch, meter, etc.), floor 1 would deform 0.08ft and floor 4 would deform 0.22ft when the responses are in steady state. The mode shape values are linearly scalable; floors 1 to 5 would deform proportionally to one another according the mode shape values (*i.e.*, floor 4 would always deform 20% more than floor 5 does) as long as the structural behavior remains linear. Figure 4.50(f) is a redraw of Figure 4.50(b) with the scaled corresponding mode shape of floors 1 to 5 shown. The mode shape is scaled by fitting the largest amplitude of responses to the larger mode shape values (floor 4). The steady state responses in Figure 5.40(f) fit exactly with the corresponding mode shape. This relationship can be used to estimate mode shapes of the system by measuring its steady state responses for specific modes.

4.4.3 Stiffness Estimation of the DMD System

After finding the modal parameters of the structure, the structural stiffness can be estimated using a least square estimate (details in Section 3.2.2). From (4.2), the n-story DMD system has mass and stiffness matrices,

$$\mathbf{M} = \begin{bmatrix} m_1 & 0 & 0 & 0 & \cdots & & 0 \\ -m_1^{\mathrm{d}} & m_1^{\mathrm{d}} & 0 & 0 & & & 0 \\ 0 & 0 & m_2 & 0 & & & 0 \\ 0 & 0 & -m_2^{\mathrm{d}} & m_2^{\mathrm{d}} & & & 0 \\ \vdots & & & & \ddots & & \vdots \\ & & & & & m_n & 0 \\ 0 & 0 & 0 & 0 & \cdots & -m_n^{\mathrm{d}} & m_n^{\mathrm{d}} \end{bmatrix},$$

$$\mathbf{K} = \begin{bmatrix} k_1 + k_2 & -k_1^{\mathrm{d}} & -k_2 & 0 & 0 & \cdots & 0 \\ 0 & k_1^{\mathrm{d}} & 0 & 0 & 0 & & 0 \\ -k_2 & 0 & k_2 + k_3 & -k_2^{\mathrm{d}} & -k_3 & & 0 \\ 0 & 0 & 0 & k_2^{\mathrm{d}} & 0 & & 0 \\ \vdots & & & & \ddots & & \vdots \\ 0 & \ldots & 0 & -k_{n-1} & 0 & k_n & -k_n^{\mathrm{d}} \\ 0 & & 0 & 0 & 0 & 0 & k_n^{\mathrm{d}} \end{bmatrix},$$

with a displacement vector of $\mathbf{x} = \begin{bmatrix} x_1 & x_1^{\mathrm{d}} & x_2 & x_2^{\mathrm{d}} & \cdots & x_n & x_n^{\mathrm{d}} \end{bmatrix}^{\mathrm{T}}$. Here, m_i and m_i^{d} are the masses of the i^{th} floor and of the damper attached to the i^{th} floor, respectively, k_i and k_i^{d} are the stiffness coefficients of the i^{th} floor and between the i^{th} floor and the i^{th} damper, respectively, and x_i and x_i^{d} are the i^{th} floor displacements relative to the ground and the damper displacement relative to the i^{th} floor respectively. By rearranging the elements, the displacement vector becomes

$\mathbf{x} = \begin{bmatrix} x_1 & x_2 & \cdots & x_n & x_1^{\mathrm{d}} & x_2^{\mathrm{d}} & \cdots & x_n^{\mathrm{d}} \end{bmatrix}^{\mathrm{T}}$ while the mass and stiffness matrices become

$$\mathbf{M} = \left[\begin{array}{cccc:cccc} m_1 & 0 & \cdots & 0 & & & & \\ 0 & m_2 & & \vdots & & & & \\ \vdots & & \ddots & 0 & & \mathbf{0} & & \\ 0 & \cdots & 0 & m_n & & & & \\ \hdashline -m_1^{\mathrm{d}} & 0 & \cdots & 0 & m_1^{\mathrm{d}} & 0 & \cdots & 0 \\ 0 & -m_2^{\mathrm{d}} & & \vdots & 0 & m_2^{\mathrm{d}} & & \vdots \\ \vdots & & \ddots & 0 & \vdots & & \ddots & 0 \\ 0 & \cdots & 0 & -m_n^{\mathrm{d}} & 0 & \cdots & 0 & m_n^{\mathrm{d}} \end{array}\right] = \begin{bmatrix} \mathbf{M}_{\mathrm{s}} & \mathbf{0} \\ -\mathbf{M}_{\mathrm{d}} & \mathbf{M}_{\mathrm{d}} \end{bmatrix}$$

$$\mathbf{K} = \left[\begin{array}{ccccc:ccccc} k_1+k_2 & -k_2 & 0 & \cdots & 0 & -k_1^{\mathrm{d}} & 0 & \cdots & 0 & 0 \\ -k_2 & k_2+k_3 & -k_3 & & & 0 & -k_2^{\mathrm{d}} & & 0 & 0 \\ \vdots & \ddots & \ddots & \ddots & \vdots & \vdots & & \ddots & & \vdots \\ & & -k_{n-1} & k_{n-1}+k_n & -k_n & 0 & 0 & & -k_{n-1}^{\mathrm{d}} & 0 \\ 0 & \cdots & 0 & -k_n & k_n & 0 & 0 & \cdots & 0 & -k_n^{\mathrm{d}} \\ \hdashline & & & & & k_1^{\mathrm{d}} & 0 & \cdots & 0 & 0 \\ & & & & & 0 & k_2^{\mathrm{d}} & & 0 & 0 \\ & & \mathbf{0} & & & \vdots & & \ddots & & \vdots \\ & & & & & 0 & 0 & & k_{n-1}^{\mathrm{d}} & 0 \\ & & & & & 0 & 0 & \cdots & 0 & k_n^{\mathrm{d}} \end{array}\right]$$

$$= \begin{bmatrix} \mathbf{K}_{\mathrm{s}} & -\mathbf{K}_{\mathrm{d}} \\ \mathbf{0} & \mathbf{K}_{\mathrm{d}} \end{bmatrix}$$

where $\mathbf{M}_{\mathrm{s}}$ and $\mathbf{M}_{\mathrm{d}}$ are mass sub-matrices related to structural floor masses and damper masses, respectively, and $\mathbf{K}_{\mathrm{s}}$ and $\mathbf{K}_{\mathrm{d}}$ are stiffness sub-matrices related to story stiffness and mass damper stiffness terms, respectively. The eigenvalue problem of

$$(\mathbf{K}-\lambda_j\mathbf{M})\boldsymbol{\varphi}_j = 0 \qquad \text{or} \qquad \mathbf{K}\boldsymbol{\varphi}_j = \lambda_j\mathbf{M}\boldsymbol{\varphi}_j$$

becomes

$$\begin{bmatrix} \mathbf{K}_\mathrm{s} & -\mathbf{K}_\mathrm{d} \\ \mathbf{0} & \mathbf{K}_\mathrm{d} \end{bmatrix}\begin{bmatrix} \boldsymbol{\varphi}_j^\mathrm{s} \\ \boldsymbol{\varphi}_j^\mathrm{d} \end{bmatrix} = \lambda_j \begin{bmatrix} \mathbf{M}_\mathrm{s} & \mathbf{0} \\ -\mathbf{M}_\mathrm{d} & \mathbf{M}_\mathrm{d} \end{bmatrix}\begin{bmatrix} \boldsymbol{\varphi}_j^\mathrm{s} \\ \boldsymbol{\varphi}_j^\mathrm{d} \end{bmatrix} \tag{4.18}$$

where λ_j and $\boldsymbol{\varphi}_j = [\boldsymbol{\varphi}_j^\mathrm{s} \quad \boldsymbol{\varphi}_j^\mathrm{d}]^\mathrm{T}$ are the j^{th} eigenvalue and eigenvector of the structure, respectively, with $\boldsymbol{\varphi}_j^\mathrm{s}$ and $\boldsymbol{\varphi}_j^\mathrm{d}$ being the portions of eigenvectors or mode shapes for the structural floors and mass dampers respectively. (4.18) can be expanded to

$$\mathbf{K}_\mathrm{s}\boldsymbol{\varphi}_j^\mathrm{s} - \mathbf{K}_\mathrm{d}\boldsymbol{\varphi}_j^\mathrm{d} = \lambda_j\mathbf{M}_\mathrm{s}\boldsymbol{\varphi}_j^\mathrm{s} \qquad \text{or} \qquad \mathbf{K}_\mathrm{s}\boldsymbol{\varphi}_j^\mathrm{s} = \lambda_j\mathbf{M}_\mathrm{s}\boldsymbol{\varphi}_j^\mathrm{s} + \mathbf{K}_\mathrm{d}\boldsymbol{\varphi}_j^\mathrm{d} \tag{4.19}$$

and

$$\mathbf{K}_\mathrm{d}\boldsymbol{\varphi}_j^\mathrm{d} = \lambda_j\left(-\mathbf{M}_\mathrm{d}\boldsymbol{\varphi}_j^\mathrm{s} + \mathbf{M}_\mathrm{d}\boldsymbol{\varphi}_j^\mathrm{d}\right) \tag{4.20}$$

Assuming the mass matrices, $\mathbf{M}_\mathrm{s}$ and $\mathbf{M}_\mathrm{d}$, are known and the modal parameters, λ_j and $\boldsymbol{\varphi}_j = [\boldsymbol{\varphi}_j^\mathrm{s} \quad \boldsymbol{\varphi}_j^\mathrm{d}]^\mathrm{T}$, can be estimated from the steady state responses of an excited system (the description of estimating mode shapes from steady state responses is detailed in Section 4.4.2), the stiffness matrix of the dampers, $\mathbf{K}_\mathrm{d}$, can be found from (4.20). Using (4.19) and the estimated $\mathbf{K}_\mathrm{d}$, $\mathbf{K}_\mathrm{s}$ can be also found. The actual stiffness terms of $\mathbf{K}_\mathrm{s}$ and $\mathbf{K}_\mathrm{d}$ can obtained using a least square approach described in (3.8). Any significant loss in the stiffness values can be treated as damage in the structure.

4.4.3.1 Damper Mode Shapes

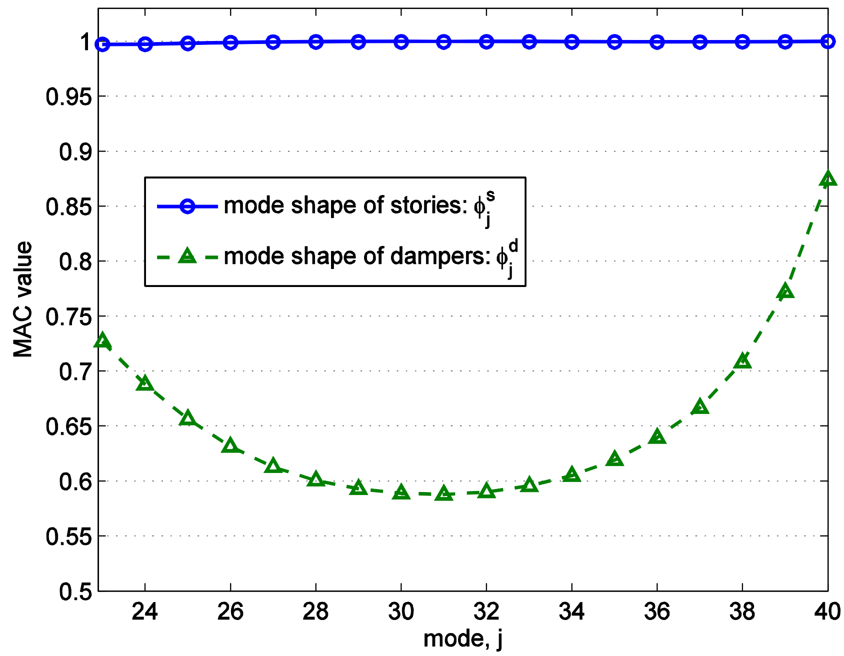

Figure 4.51: Estimation error comparison between the mode shapes of stories and of dampers

Observed in Figure 4.51, the estimation of the floor mode shapes, $\boldsymbol{\varphi}_j^s$, is much more accurate compared to the damper mode shapes, $\boldsymbol{\varphi}_j^d$, from steady state responses. Using steady responses of the DMD system excited at the 20 modal frequencies, the mode shapes are estimated and compared with the actual mode shapes for stories and dampers separately. The MAC values (from (3.24)) shown in Figure 4.51 illustrates the accuracy of the mode shape estimations with the value of 1 being the most accurate. The MAC values are always higher, and, thus, more accurate mode shape estimation for the stories than for the dampers. The inaccuracy of damper mode shape estimations can be caused by the closely spaced frequencies of the dampers, thus creating the overlapping of the modal characteristics that gives great difficulties to estimate individual mode shapes. To compensate for the inaccurate estimates of $\boldsymbol{\varphi}_j^{\mathrm{d}}$, another method of obtaining $\boldsymbol{\varphi}_j^{\mathrm{d}}$ is studied by rearranging (4.20) in

$$\boldsymbol{\varphi}_j^{\mathrm{d}} = -\left(\mathbf{K}_{\mathrm{d}} - \lambda_j \mathbf{M}_{\mathrm{d}}\right)^{-1} \lambda_j \mathbf{M}_{\mathrm{d}} \boldsymbol{\varphi}_j^{\mathrm{s}} \ . \tag{4.21}$$

By assuming $\mathbf{K}_{\mathrm{d}}$ is now also known, $\boldsymbol{\varphi}_j^{\mathrm{d}}$ can be found from (4.21). The assumption of a known $\mathbf{K}_{\mathrm{d}}$ effectively reduces the size of the system identification by half since now only $\mathbf{K}_{\mathrm{s}}$ is unknown. Nonetheless, this is a realistic assumption because the damper system has to be carefully constructed to fit design specifications, making the parameters of the dampers, $\mathbf{M}_{\mathrm{d}}$ and $\mathbf{K}_{\mathrm{d}}$, known with certainty. In the case that the mass dampers are damaged (and, thus, $\mathbf{M}_{\mathrm{d}}$ and $\mathbf{K}_{\mathrm{d}}$ become unreliable), the following approach eliminates the need of f $\mathbf{M}_{\mathrm{d}}$ and $\mathbf{K}_{\mathrm{d}}$ for modal identification.

Another approach to compensate the inaccurate estimates of $\boldsymbol{\varphi}_j^{\mathrm{d}}$ from steady state responses is to neglect $\boldsymbol{\varphi}_j^{\mathrm{d}}$ altogether. From the studied DMD system, the elements of $\mathbf{K}_{\mathrm{d}}$ are about three orders of magnitude smaller than the elements in $\mathbf{K}_{\mathrm{s}}$. As long as $\boldsymbol{\varphi}_j^{\mathrm{d}}$ is not orders of magnitude larger than $\boldsymbol{\varphi}_j^{\mathrm{s}}$, the effect of $\mathbf{K}_{\mathrm{d}}\boldsymbol{\varphi}_j^{\mathrm{d}}$ can be neglected in (4.19), reducing the equation into

$$\mathbf{K}_{\mathrm{s}} \boldsymbol{\varphi}_j^{\mathrm{s}} = \lambda_j \mathbf{M}_{\mathrm{s}} \boldsymbol{\varphi}_j^{\mathrm{s}} \ . \tag{4.22}$$

$\mathbf{K}_{\mathrm{s}}$ can then be estimated without knowing the damper parameters: $\mathbf{M}_{\mathrm{d}}$, $\mathbf{K}_{\mathrm{d}}$ and $\boldsymbol{\varphi}_j^{\mathrm{d}}$.

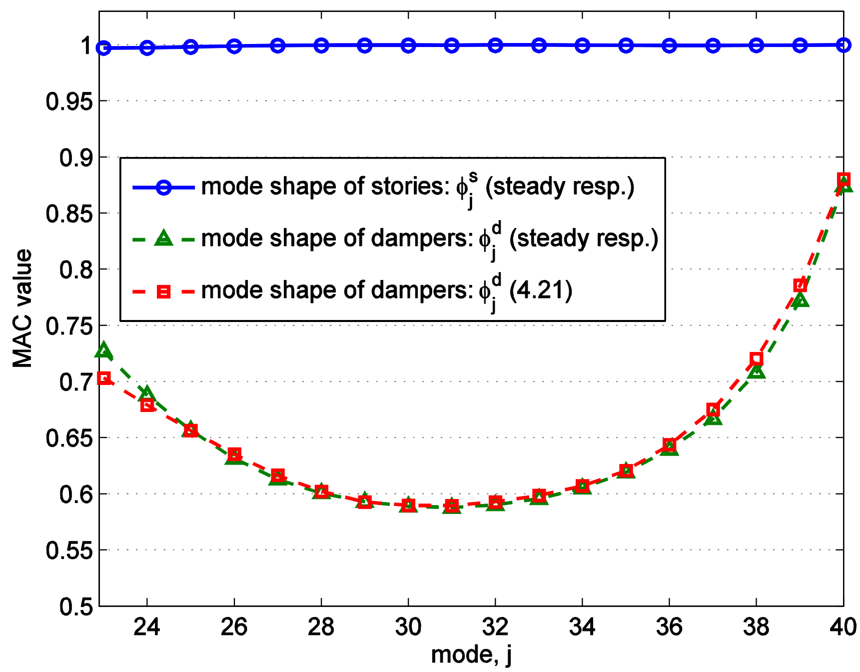

Figure 4.52: Estimation error comparison between the mode shapes of stories and of dampers estimated from steady responses and from (4.21)

Figure 4.52 shows the performance of estimating mode shapes using (4.21). The estimations from (4.21) are not more accurate than estimating from steady responses, and, thus, cannot be relied on to estimate stiffness of the structure. For the rest of this section, (4.22) will be used to estimate stiffness.

4.4.4 Excitations by the Dampers

One of the key objectives of the SHM study is determine a way to utilize the DMDs to improve SHM. The previous sections detail system identification with the

DMD system. This section studies the effect on SHM by different excitations generated using the DMDs. Recall the excitation forces in (4.15) have forms of

$$f_i = A\,\alpha_i \sin(\omega\, t), \qquad i = 1, 2, \ldots, n$$

where A is the amplitude, α_i is the adjustable scalar and ω is the harmonic frequency of excitation. Six sets of excitation by the DMDs are presented in Table 4.10 for the 20 story DMD system, where $\phi_{i,j}$ is the i^{th} element of the j^{th} mode shape of the structure for the excitation frequency at j^{th} mode.

Cases	excitation factor (α_i)					
	floor 1	floor 2	floor 3	…	floor 19	floor 20
1 top	0	0	0	…	0	20
2 equal	1	1	1	…	1	1
3 random	1	1	-1	…	-1	1
4 alternating	1	-1	1	…	1	-1
5 direc. corresp. to mode shape	$\mathrm{sgn}(\phi_{1,j})$	$\mathrm{sgn}(\phi_{2,j})$	$\mathrm{sgn}(\phi_{3,j})$	…	$\mathrm{sgn}(\phi_{19,j})$	$\mathrm{sgn}(\phi_{20,j})$
6 shaped corresp. to mode shape	$\frac{20\phi_{1,j}}{\sum_i \phi_{i,j}}$	$\frac{20\phi_{1,j}}{\sum_i \phi_{i,j}}$	$\frac{20\phi_{3,j}}{\sum_i \phi_{i,j}}$	…	$\frac{20\phi_{19,j}}{\sum_i \phi_{i,j}}$	$\frac{20\phi_{20,j}}{\sum_i \phi_{i,j}}$

Table 4.10: Excitation cases

- Case 1 (top) has excitation force only at the top floor with the force magnitude equivalent of other excitation cases. This case behaves similar to an AMD system.
- Case 2 (equal) has identical forces for all floors, both in direction and magnitude.
- Case 3 (random) has forces of the same magnitudes at random directions in each floor.

- Case 4 (alternating) has forces of the same magnitudes in alternating directions in each floor.
- Case 5 (directions corresponding to mode shape) has forces of the same magnitudes in directions in each floor equal to the corresponding direction in the mode shape of the j^{th} mode.
- Case 6 (shaped corresponding to mode shape) has forces in each floor with directions and magnitudes scaled to the mode shape of the j^{th} mode.

To test the six cases of excitations, the DMD system is excited using all six cases at frequencies of 23rd to 40th modes of the system. Mode shapes and stiffness terms are then estimated from the measured steady state responses of floor accelerations. Figure 4.53(a) shows that Cases 5 and 6 have the least error in stiffness estimations. The two cases also have the most accurate estimates of the mode shapes in the excited modes, shown in Figure 4.53(b) (MAC values of 1 represent 100% accuracy in mode shape estimation). Figure 4.53(c) shows that the magnitudes of the steady state responses are fairly consistent for different modes for Cases 5 and 6. Cases 1 and 2 show significant smaller response magnitudes in higher modes while Cases 3 and 4 show the opposite. In measuring responses, sensors are designed to achieve certain accuracy level depending on the application. This accuracy level is heavily influenced by the magnitude levels of the responses; a small response magnitude requires more capable (more costly) sensors than a large responses magnitude does. If the response magnitudes vary greatly between modes, such as in Cases 1 to 4, either expensive sensors are needed for modes with lower magnitudes nor these modes are measured inaccurately using less capable sensors.

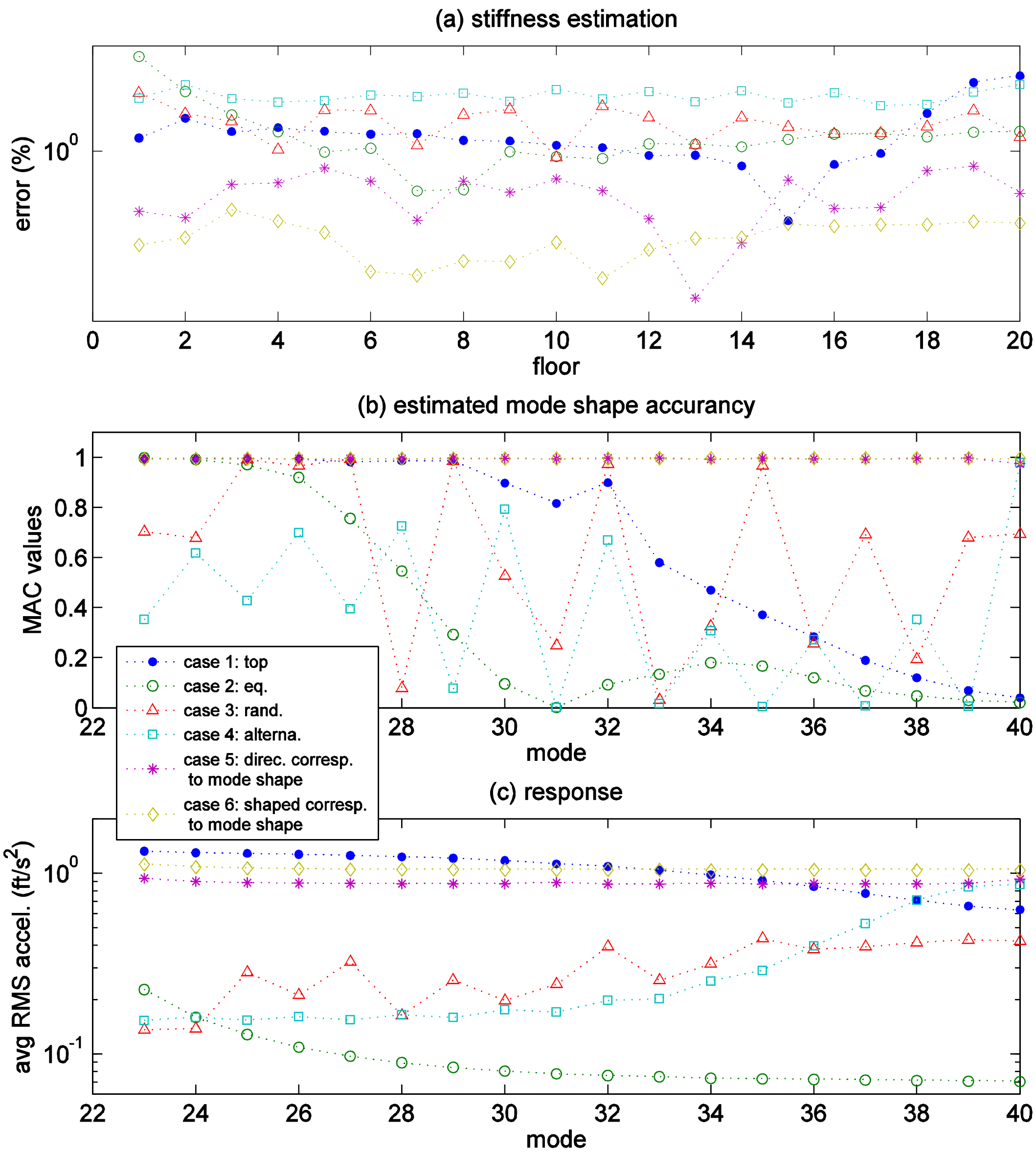

Figure 4.53: Comparison of stiffness estimation errors, MAC values of mode shape estimation and acceleration response

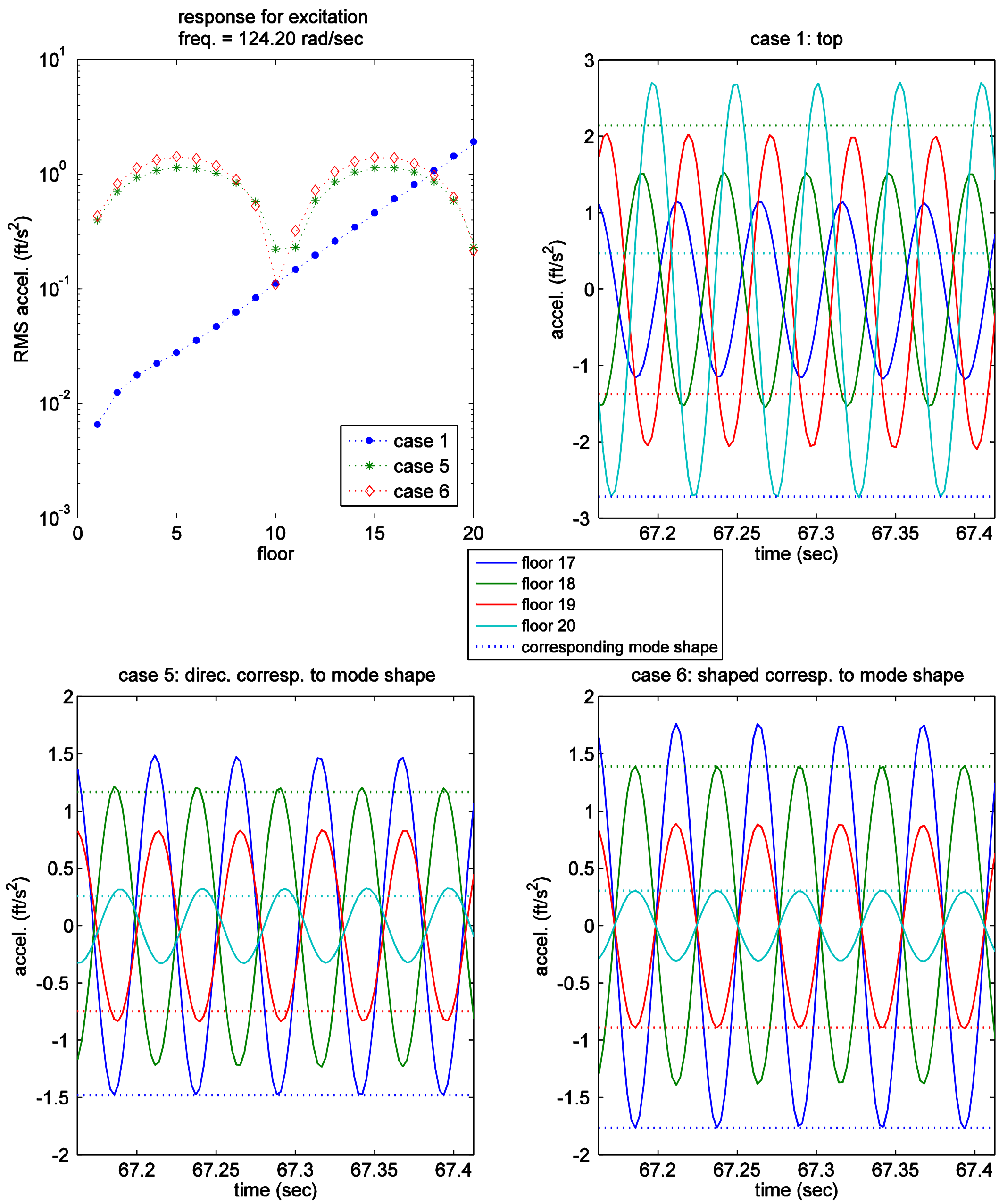

Figure 4.54: Response and mode shapes of Cases 1, 5 and 6

Figure 4.54 helps illustrate why Cases 5 and 6 perform better than the other cases. There is a shifting effect in the steady state responses of the excited system such that the peaks of the periodic responses are not in phase. Figures 4.54(b), 4.54(c) and 4.54(d) shows the steady state responses of the structure under excitation Cases 1, 5 and 6, respectively. When the steady state responses are in phase, as shown in Figure 4.54(d), the mode shape is proportional to the amplitudes of the response (see Section 4.4.2 and Figure 4.50 for more explanation). With this proportionality relationship, mode shapes can be accurately estimated from the steady states responses. Figure 4.54(c) (Case 5) demonstrates the effect on the proportionality relationship when the responses are slightly out of phase. The responses are not longer exactly proportional to the corresponding mode shape. Since the responses are only slightly out of phase and, thus, cause a small amount of errors in mode shape estimation. On the other hand, the steady state responses excited by Case 1 (Figure 4.54(b)) are significantly out of phase that results a strong mismatch between the mode shape and the response.

The cases shown in Figure 4.54 demonstrate that out of phase responses leads to inaccurate mode shape estimations and that exciting the structure using information from the mode shape (Cases 5 and 6) decreases the extent of phase shifts. This is why Cases 5 and 6 outperform the other cases in Figure 4.54 on stiffness estimations.

There is another reason why Cases 5 and 6 are better excitation choices for stiffness and modal identification. Figure 4.54(a) illustrates the responses for all floors under excitation Cases 1, 5 and 6. Unlike in Case 1, the magnitudes of response for Cases 5 and 6 are fair constantly across the floors. As discussed in the previous section, sensors are easily to implement for similar level of response magnitudes.

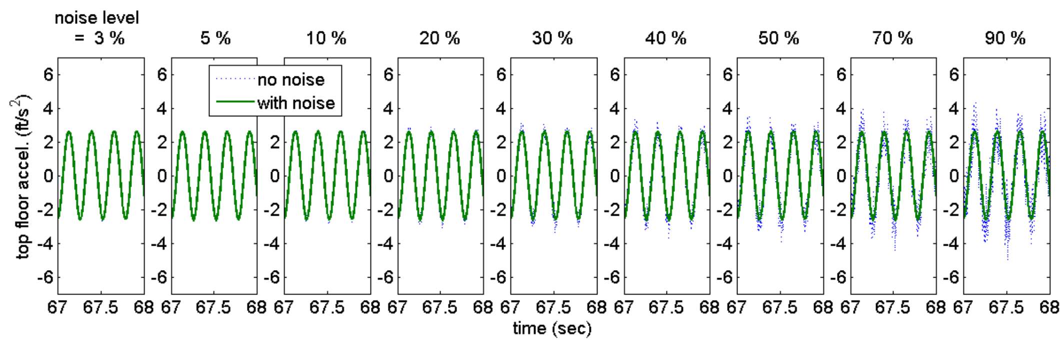

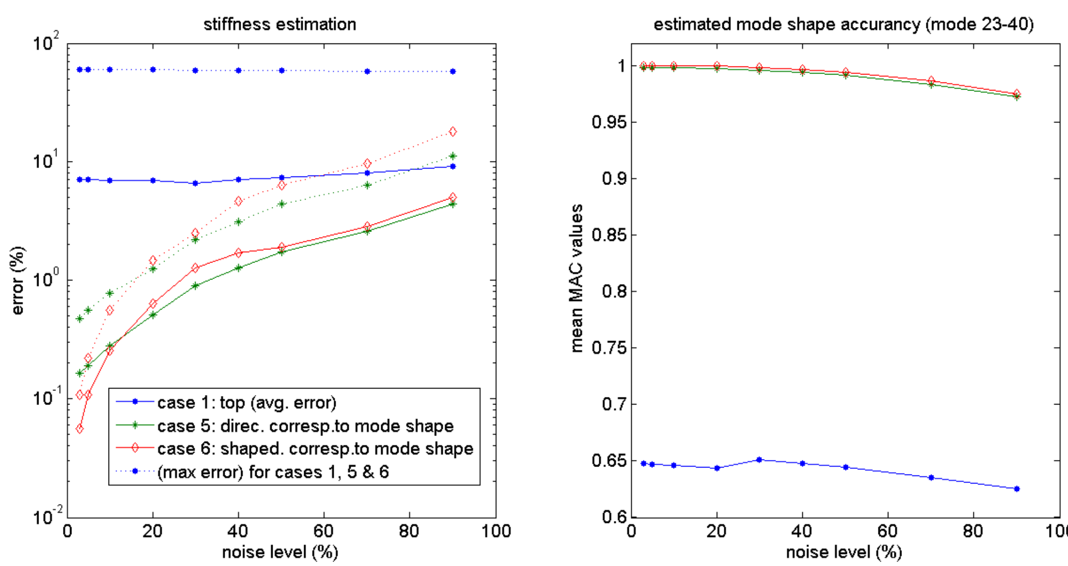

Figure 4.55: Effect of noise in stiffness and mode shape estimation

Figure 4.55 illustrates the effect of measurement noise on stiffness and mode shape estimations for Cases 1, 5 and 6. The measurement noise is induced into the response, $y(t)$, by using the root mean squares (RMS) responses, y_{RMS}, in the following way:

$$\hat{y}(\text{t}) = y(\text{t}) + \beta_n \, y_{\text{RMS}} \, N(\text{t}) \qquad (4.23)$$

where $\hat{y}$(t) is the measured response with noise, β_n is the noise level, and N(t) is a random variable with normal distribution (mean = 0, variance = 1). The noise levels (or β_n) in Figure 4.55 range from 3% to 90%. Similar to what was seen in Figure 4.53, Case 1 underperforms compared to Cases 5 and 6 and the noise has surprisingly little effect on the performance of Case 1. Meanwhile, the estimation errors from Cases 5 and 6 noticeably increase at larger levels of measurement noise.

4.4.5 Damage Detection Result

Figure 4.56 presents the estimated stiffness losses for four damage patterns using three excitation cases (Cases 1, 5 and 6) with 40% measurement noise. The stiffness is first estimated for the undamaged system under the three excitation cases. Since the excitation cases require prior knowledge of the modal frequencies and mode shapes, it is assumed that the modal characteristics can be computed from design values. Using the modal characteristics of the undamaged system, the four damaged systems are also excited according to Cases 1, 5 and 6. The stiffness is then estimated for the damaged systems and compared with the estimated undamaged system to detect damage (*i.e.*, stiffness losses). All damaged stories (indicated by "exact damage" in Figure 4.56) in the four patterns are successfully detected by the stiffness estimation except for Case 1 in the 4^{th} damage pattern at the 19^{th} floor. Overall, Case 1 performs the worst with the most false positives, a false negative and generally more errors in the stiffness estimations. Cases 5 and 6 have similar good performance despite some false positives. They identify the damaged stories with fairly accurate estimates of the stiffness losses. Between the two excitation cases, Case 6 performs slightly better with more accurate stiffness estimations. The excellent performance of Case 6, however, comes at the price of detailed knowledge of the modal characteristics of the system. In the simulations of Figure 4.56, prior knowledge of modal frequencies is required in Case 1; in Case 5, knowledge of modal frequencies and the directions of the corresponding mode shapes is needed; modal frequencies and the exact mode shapes are required for Case 6.

Accurate prior knowledge of the modal characteristics is not realistic in real world structures. There is modeling error that prevents engineers from exactly computing the modal characteristics from design values. Moreover, the difference between the constructed and designed structures also impacts the accuracy in modal estimations. The following sections address the uncertainty in modal characteristics for damage detection for the DMD system.

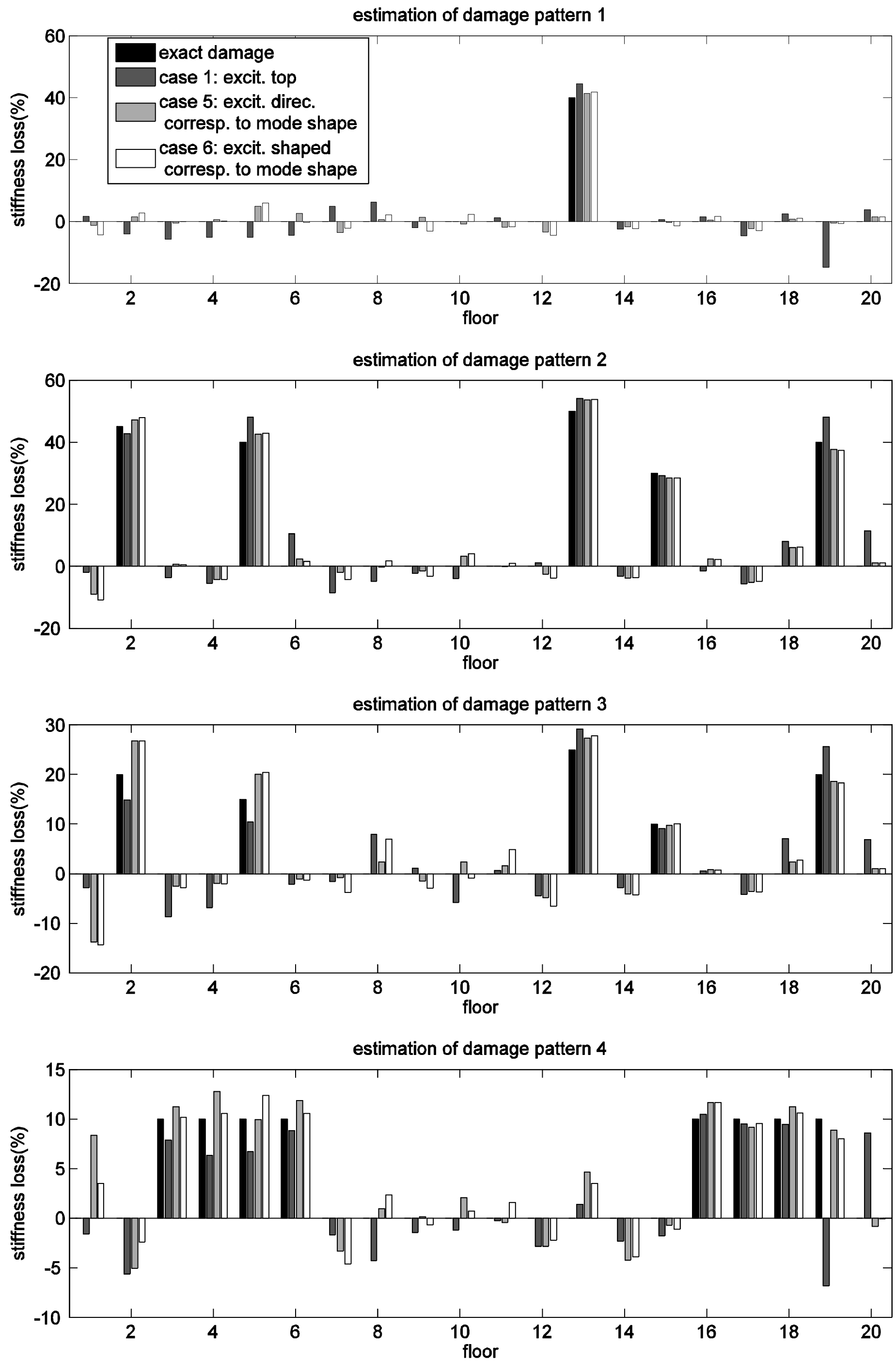

Figure 4.56: Comparison of excitation cases on damage detections

4.4.6 Uncertain Modal Characteristics

This section analyzes stiffness estimations and damage detections with uncertain modal characteristics. Only excitation Case 5 (excitations correspond to the directions of the mode shapes) is considered in this section because Cases 1, 2, 3 and 4 are not as accurate as Case 5, and Case 6 requires greater details of modal characteristics that can be difficult to estimate. Case 5 is a reasonable compromise between performance and knowledge of the uncertain modal characteristics. The flow chart in Figure 4.57 describes how modal frequencies, $\sqrt{\lambda}$ (λ is the eigenvalue), and mode shapes, ϕ, can be updated from uncertain modal characteristics during stiffness estimations:

1. Initial λ_0 and ϕ_0 are estimated from design characteristics of the undamaged structure.
2. **Modal estimation:** the estimation of λ and ϕ will be updated using the last estimated values (denoted λ^* and ϕ^*) if the updated modal estimation was not recently updated.
    a. Design excitation according to λ^* and ϕ^* (using Case 5 in Table 4.10).
    b. Apply the designed excitation to the structure at a range of frequencies close to $\sqrt{\lambda^*}$ and measure the responses.
    c. Since responses are larger when the structure is excited at its natural frequencies, λ can be estimated by comparing the responses measured from step b.

d. Once λ is estimated, ϕ is estimated from the responses (from step b) excited at $\sqrt{\lambda}$ (see Section 4.4.2 for mode shape estimation using steady state responses).

3. **<u>Stiffness estimation:</u>** when the modal estimation, λ^* and ϕ^*, are up-to-dated, the stiffness of the structure will be estimated using λ^* and ϕ^*.

    a. Design excitation according to λ^* and ϕ^* (using Case 5 in Table 4.10).

    b. Apply the designed excitation to the structure at frequencies of $\sqrt{\lambda^*}$ and measure the responses.

    c. ϕ is estimated from the responses from step b (see Section 4.4.2 for mode shape estimation using steady state responses).

    d. Stiffness of the structure is estimated using λ^* and ϕ (see Section 4.4.3 for details).

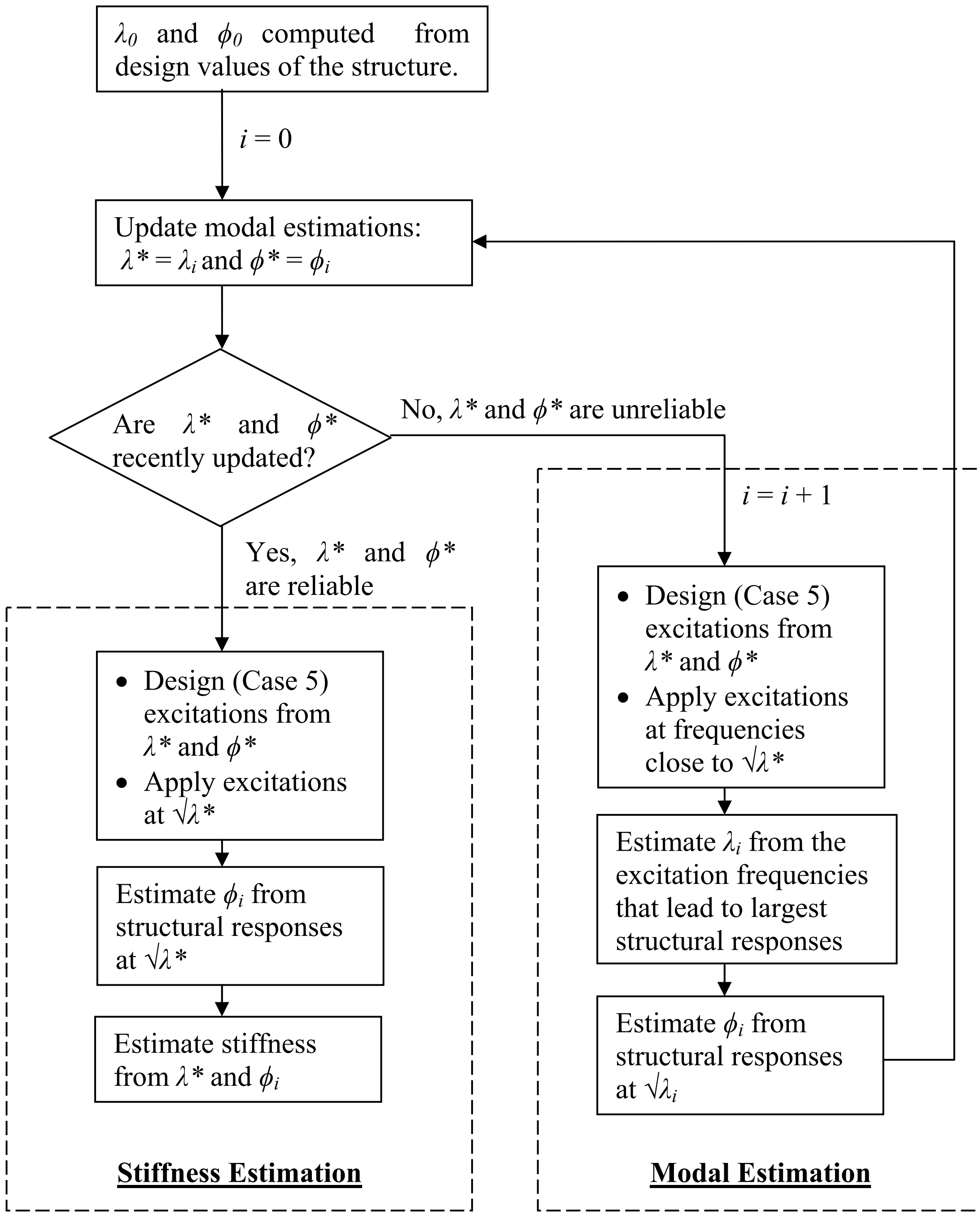

Figure 4.57: Flow chart of modal and stiffness estimation with uncertain modal characteristics

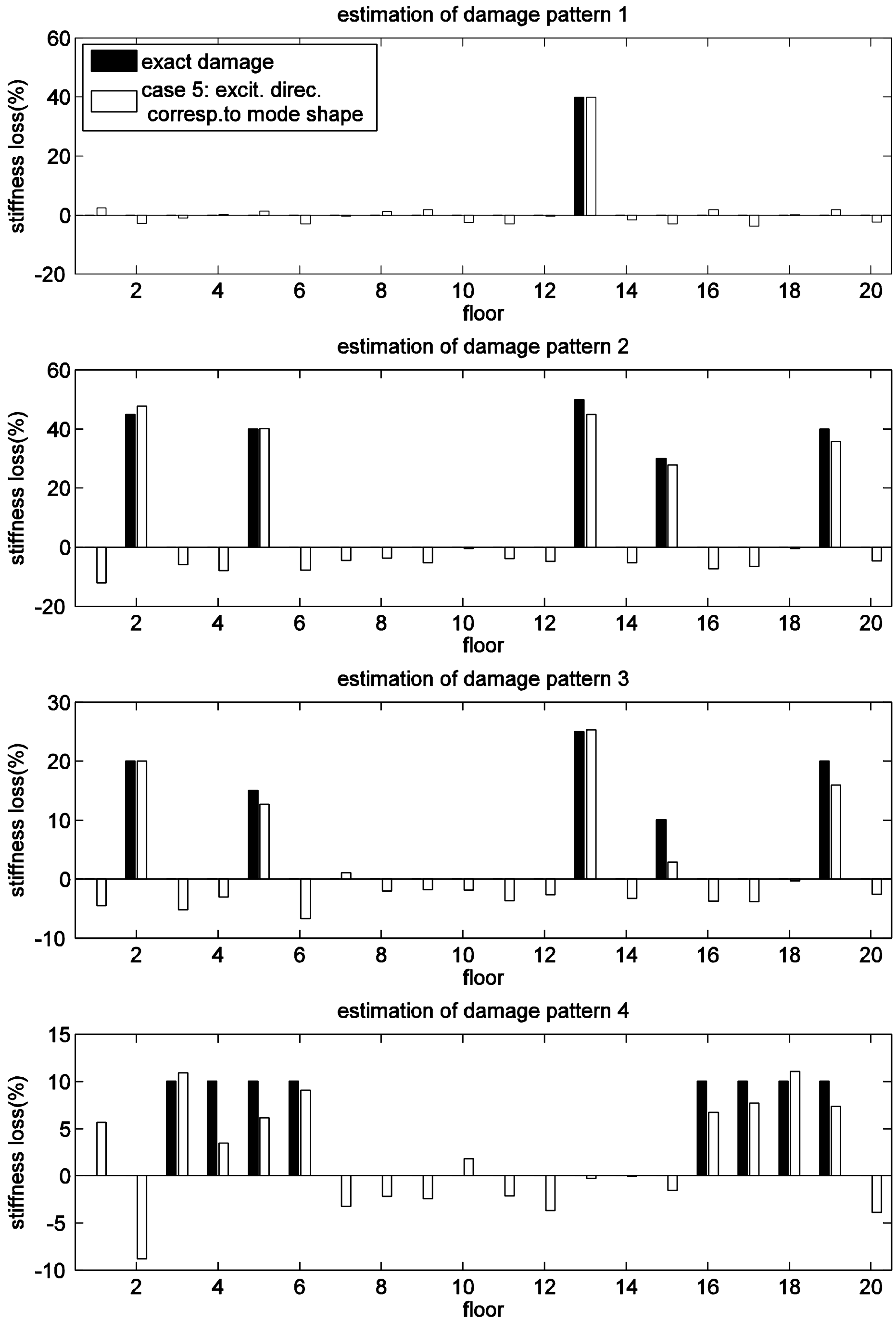

Figure 4.58: Damage detection of four damage patterns with uncertain modal characteristics

Figure 4.58 shows the performance of damage detection using the stiffness and modal estimations from the flow chart (Figure 4.57) for the same four damage patterns in Figure 4.56. Despite the increased uncertainty in the modal characteristics of the structure, all damaged stories are successfully detected. The damage detection method performs the best in damage patterns 1 and 2, where the estimated stiffness losses are very close to the actual amounts. In damage patterns 3 and 4, some of the estimated stiffness losses underreports significantly compared to the actual damage (floor 15 in damage pattern 3 and floors 4 and 5 in damage pattern 4). This is worrisome because underreporting stiffness loss can cause failures in detecting damage. Moreover, a noticeable stiffness loss is estimated in story 1 for damage pattern 4 when there is no actual damage in this floor. The estimated stiffness loss at this undamaged story is larger than or as large as some of estimated stiffness losses in the damaged locations, implying that the undamaged story 1 would be diagnosed as damaged before some of the actual damaged stories. More about how to define and diagnose damage given stiffness estimations will be discussed in Section 4.4.6.1.

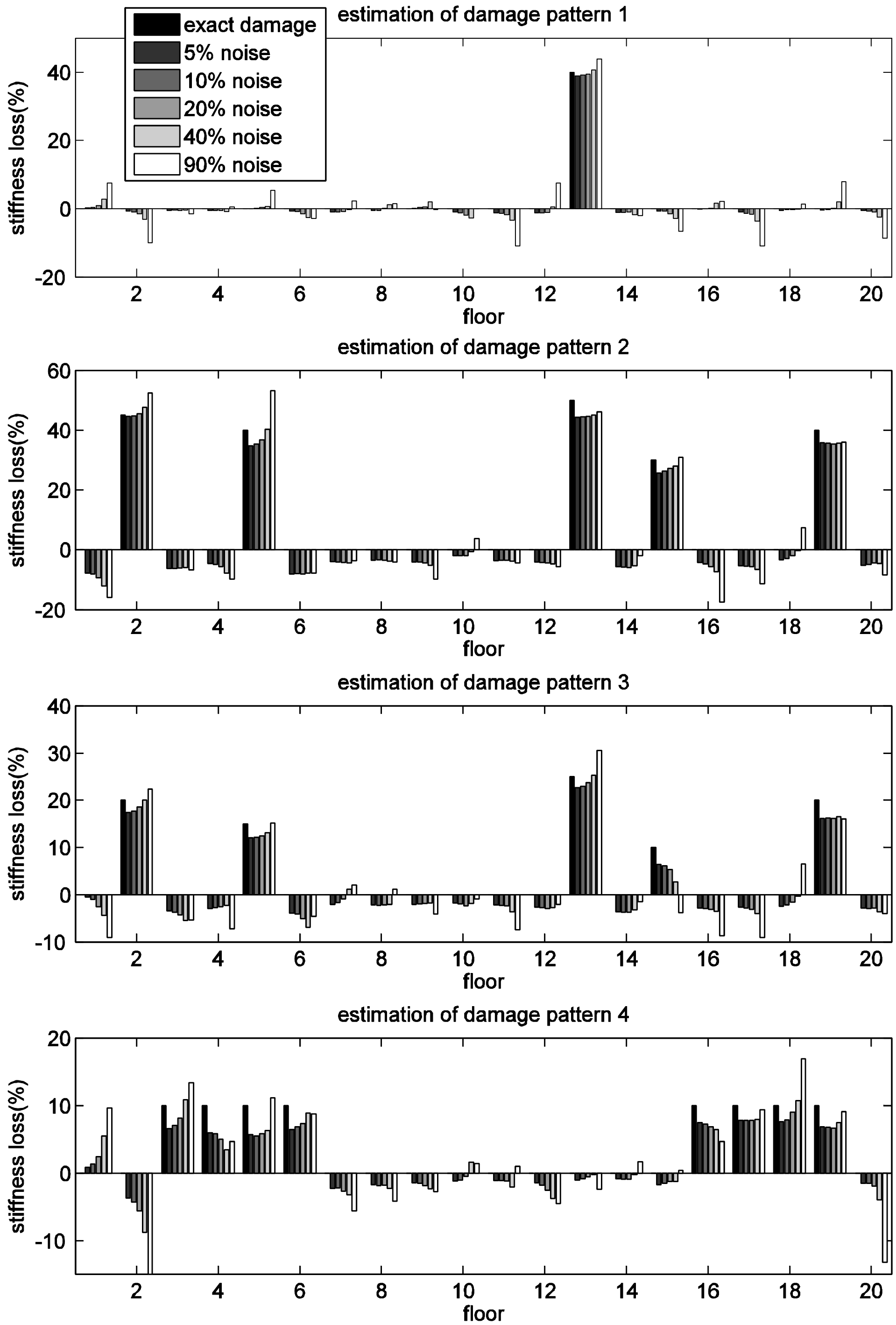

Figure 4.59: Effect of noise on damage detection

Figure 4.59 is a redraw of Figure 4.58 with different levels of measurement noise (the effect of noise levels on responses is presented in Figure 4.55). All damaged stories are successfully detected and, as expected, the quality of the damage estimates decreases with larger noise levels. Interestingly, most of the errors occur in the direction of negative stiffness loss, implying increases in stiffness for these stories. Since only damage is expected and increases of story stiffness are impossible, the negative stiffness loss is easily concluded to be in error. Excluding the largest noise level (90% noise), there is no significant stiffness estimate errors for false positives except in the first floor in the 4th damage pattern. In this particular case, the 40% noise level test shows significant stiffness loss though no damage occurs in the first floor.

4.4.6.1 Statistical Stiffness Loss Threshold for Damage

The previous subsections demonstrate that damage can be detected for the DMD system. However, the stiffness estimates are not error-free, and the success of damage detection depends on how to determine if damage has occurred based on the stiffness estimates. In other words, what should the damage (stiffness loss) threshold be to signal an occurrence of damage in a floor? Threshold of damage is chosen ideally to detect all damage while avoiding any false positives. Too high of a stiffness loss threshold would fail to detect actual damage; too low of threshold increases the chance of false positives when errors make the stiffness loss estimates larger than this low threshold. To choose a threshold, this subsection examines the inherent variation (*i.e.*, errors) of the stiffness estimations in the previous undamaged and damaged DMD systems. The systems are simulated for 200 random realizations with two noise levels of 20% and 90%. Figures 4.60 and 4.61 show how the stiffness estimates of the samples are distributed for 20% and 90% noise levels respectively.

In Figure 4.60 (20% noise level), the estimate samples are mostly within 2% of the estimate sample means and the stiffness estimation errors vary as little as [–2.5%, 2.5%] in the undamaged system to as much as [0%, 17%] in the 2^{nd} damage pattern. This suggests two observations: 1) estimates vary reasonably little (about ±2%) for the 20% noise level, and 2) there are factors other than measurement noises contribute to the stiffness estimation error (such as the uncertainty of modal characteristics), hence the larger range of stiffness estimation errors compared to the sample variations. With a larger noise level (Figure 4.61), the samples are mostly within 20% of the sample means and the stiffness estimation errors vary between [–25%, 25%]. The sample variation in this noise level is the dominating factor in the stiffness estimation errors. Due to the large variations/errors, only large damage (*e.g.*, the first damage pattern) can be reliably detected in the 90% noise level.

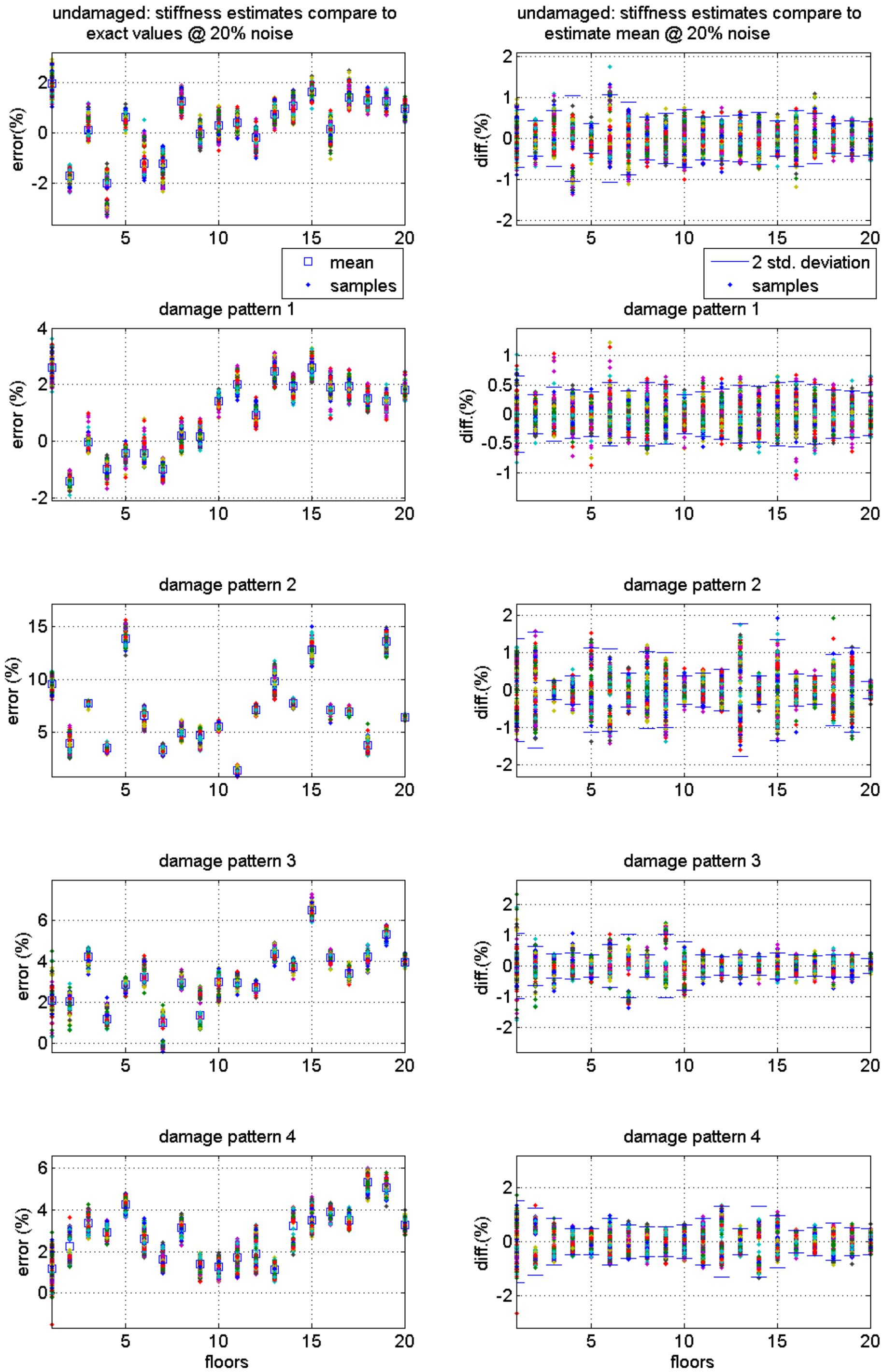

Figure 4.60: Sampling of stiffness estimates with 20% noise level (first column: the difference between the absolute stiffness estimate error; second column: the stiffness estimate error relative to the mean error)

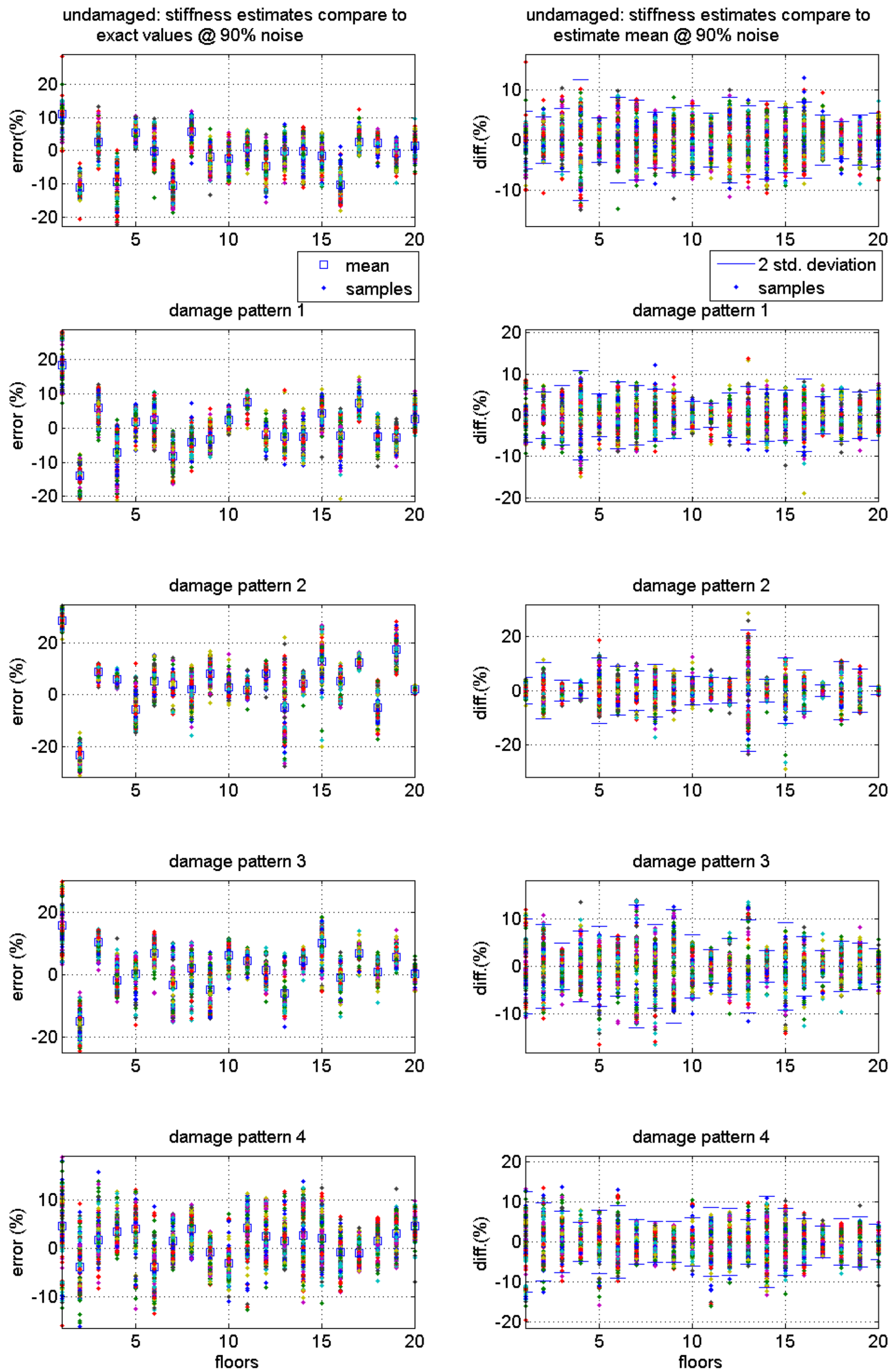

Figure 4.61: Sampling of stiffness estimates with 90% noise level (first column: the difference between the absolute stiffness estimate error; second column: the stiffness estimate error relative to the mean error)

Standard deviations, σ, of the samples, can be used to measure the variations among individual floor stiffness estimates and determine a suitable threshold value for damage detection. For example, within $\pm 2\sigma$ of the means contains roughly 95% of the samples for Gaussian distributions. Although the stiffness estimate samples in Figures 4.60 and 4.61 are not necessarily Gaussian, Figures 4.60(b) and 4.61(b) show that most samples are contained within $\pm 2\sigma$ of the means. Damage is detected by estimating stiffness loss in the structure, given by

$$[\text{stiffness loss (ratio)}] = \frac{(\text{undamaged stiffness est.}) - (\text{damaged stiffness est.})}{(\text{undamaged stiffness est.})}$$

$$= 1 - \frac{(\text{damaged stiffness est.})}{(\text{undamaged stiffness est.})}$$

or
$$Z = 1 - \frac{X}{Y} \tag{4.24}$$

where Z, X and Y are random variables of the stiffness loss, stiffness estimations of the undamaged system and of the damaged system, respectively. The variance of Z, σ_Z^2, can be approximated using the first-order Taylor expansion of Z:

$$\sigma_Z^2 = \sigma_X^2 \left(\frac{\partial Z}{\partial X}\right)^2 \Bigg|_{X=\mu_X, Y=\mu_Y} + \sigma_Y^2 \left(\frac{\partial Z}{\partial Y}\right)^2 \Bigg|_{X=\mu_X, Y=\mu_Y} + 2\mathrm{Cov}(X,Y) \frac{\partial Z}{\partial X \partial Y}\Bigg|_{X=\mu_X, Y=\mu_Y} \tag{4.25}$$

where μ_X and μ_Y are the means of X and Y, respectively; σ_X^2 and σ_Y^2 are their respective variances, and Cov(X,Y) is the covariance of X and Y. (4.25) can be expressed as

$$\sigma_Z^2 = \sigma_X^2 \left(\frac{1}{Y} \right)^2 \Bigg|_{X=\mu_X, Y=\mu_Y} + \sigma_Y^2 \left(\frac{X}{Y^2} \right)^2 \Bigg|_{X=\mu_X, Y=\mu_Y} + 2\rho_{XY}\sigma_X\sigma_Y \left(-\frac{1}{Y}\frac{X}{Y^2} \right) \Bigg|_{X=\mu_X, Y=\mu_Y}$$

$$= \sigma_X^2 \frac{1}{\mu_Y^2} - 2\rho_{XY}\sigma_X\sigma_Y \frac{\mu_X}{\mu_Y^3} + \sigma_Y^2 \frac{\mu_X^2}{\mu_Y^4} = \left(\frac{\mu_X}{\mu_Y} \right)^2 \left(\frac{\sigma_X^2}{\mu_X^2} - 2\rho_{XY} \frac{\sigma_X}{\mu_X} \frac{\sigma_Y}{\mu_Y} + \frac{\sigma_Y^2}{\mu_Y^2} \right)$$

(4.26)

where $\rho_{XY} = \mathrm{Cov}(X,Y)$. Thus, the standard deviation of Z can be computed as

$$\sigma_Z = \left| \frac{\mu_X}{\mu_Y} \right| \sqrt{\frac{\sigma_X^2}{\mu_X^2} - 2\rho_{XY} \frac{\sigma_X}{\mu_X} \frac{\sigma_Y}{\mu_Y} + \frac{\sigma_Y^2}{\mu_Y^2}} . \tag{4.27}$$

Assuming the errors in the (undamaged and damaged) stiffness estimates are due only to measurement noise, which is generally independent from one test to another, X and Y are uncorrelated or $\rho_{XY} = 0$ in (4.27). (If the errors are due to other sources, such as modeling error, then some correlation in the stiffness estimates from test to test may exist.)

When Z in (4.24) is non-zeros, there is a change in the structural stiffness with positive Z values indicate damage (stiffness loss) whereas negative values (stiffness increase) are considered erroneous. However, since Z is a random variable, it varies from estimation to estimation (see Figure 4.59 for the effect of noise on Z). A threshold value can be used to denote significant changes in (4.24) that are more likely to be caused by actual damage than by variations in estimation. Following (4.27) and, the threshold is computed by

$$T_{i,j} = \alpha\left[\left|\frac{\mu_{i,j}}{\mu_{0,j}}\right|\sqrt{\frac{\sigma_{i,j}^2}{\mu_{i,j}^2}+\frac{\sigma_{0,j}^2}{\mu_{0,j}^2}}\right] \qquad i = 1, 2, 3, 4;\ j = 1, 2, \ldots, n \qquad (4.28)$$

where α is a scaling factor, $\mu_{0,j}$, and $\mu_{i,j}$ are means of the j^{th} story stiffness estimate samples in the undamaged system and i^{th} damaged system, respectively, and $\sigma_{0,j}$ and $\sigma_{i,j}$ are the respective standard deviations. Any estimated stiffness loss above $T_{i,j}$ would be considered damage.

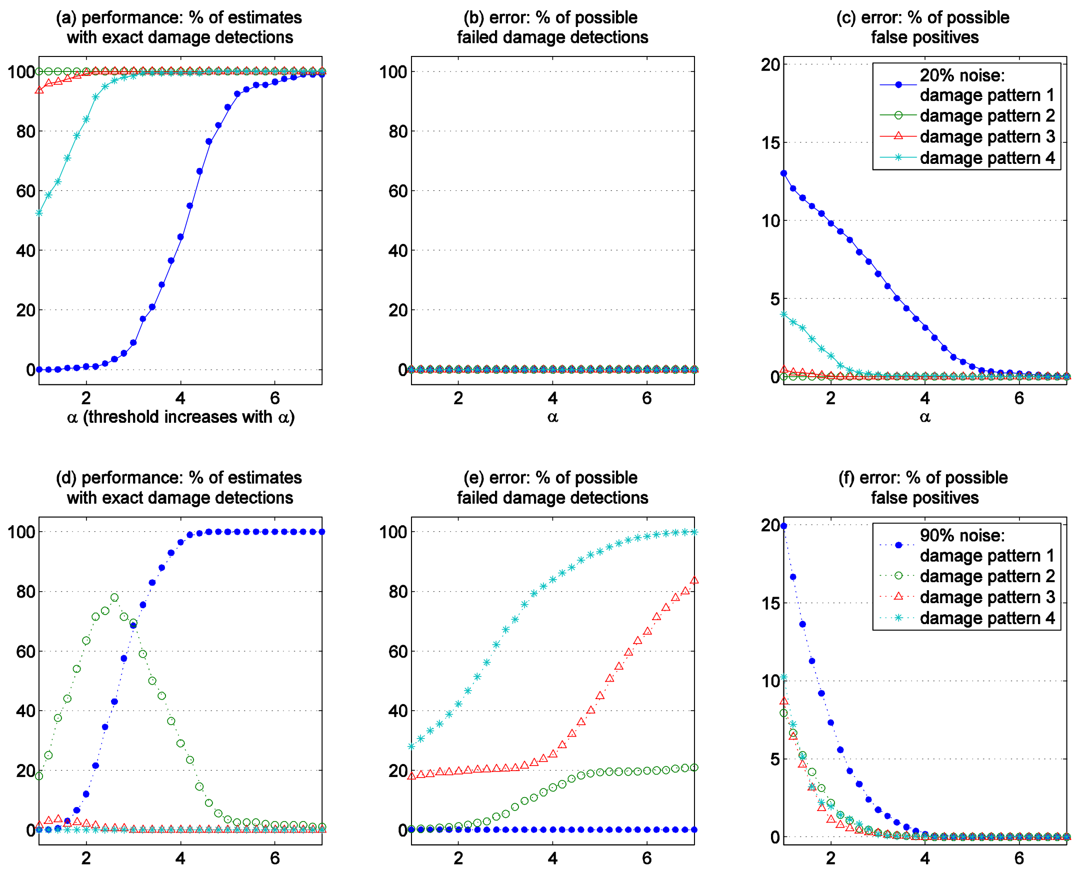

Figure 4.62: Effect of thresholds on damage detection

Figure 4.62 illustrates the effect of the threshold values on the damage detection of the 200 random samples with 20% (Figures 4.60(a)-(c)) and 90%

(Figures 4.62(d)-(f)) noise levels. Figures 4.62(a) and 4.60(d) show the percentage of estimates with exact damage detection or estimations that all damaged locations are successfully identified without any false positive. Meanwhile, the damage detection errors are presented in Figure 4.62(b) and 4.62(c) for the percentages of possible failed damage detection (damage undetected in damaged floors; *i.e.*, false negatives) and possible false positive (damage detected in undamaged floors), respectively, for the 20% noise level (Figures 4.62(e) and 4.62(f) for the 90% noise level). The threshold values have opposite effects on the failed damage detection and false positives; larger threshold values (larger α) increase the number of failed damage detections (at least in Figure 4.62(e)) while decreasing the number of false positive. This is because a large threshold value requires a large stiffness loss to register as damage, effectively encouraging failed damage detections while discouraging false positives. Figure 4.62(d) also shows that exact damage detection peaks at $\alpha = 2.6$ for the 2nd damage pattern. This is because, at such a value of α, the number of failed damage detections have not increased too much (Figure 4.62(e)) and the number of false positives have not yet decreased substantially (Figure 4.62(f)).

Since failed damage detections are more important than false positives (failing to identify real damage instead of labeling undamaged floors damaged), the threshold value should be large to decrease the amount of fail damage detections. A smaller α is more desirable when considering the 90% noise level for damage patterns 3 and 4 where the number of the failed damage detections are at the lowest. For the 1st damage pattern, a large α is desirable since the number of failed damage detections remains zeros for all α; the damage detections on the 2nd pattern performs the best at α = 2.6. Meanwhile, the damage detections in the 20% noise level are significantly more reliable and α has no effect on the number of failed damage detections (which remains zeros for all α in Figure 4.62(b)). Therefore, a large α is more suitable for this noise level to decrease the number of false positives.

4.5 Summary

The shading fin mass damper (SFMD) system serves three functions — structural control, environmental control and structural health monitoring. To integrate structural and environmental controls, the SFMD system employs a distributed mass damper (DMD) system that doubles as active movable shading fins. Unlike typical tuned mass damper (TMD) systems, the DMD are placed along the height of the building (for shading fin function) rather than concentrated in a few locations. For passive structural control, the DMD system shows vibration control comparable to a single TMD system when the parameters — damper mass, stiffness and damping coefficients of each mass damper — are optimized. Several sub-optimizations are also performed for the DMD systems for constant, gradually increasing and stepped damper masses for simple design and constructability; the results are on par with the performance of the single TMD system.

The DMD system is also studied as an active system (active DMD or ADMD) powered by the actuators attached to the SFMDs to adjust fin movements for shading purposes. The ADMD system can reduce motions significantly, more than the passive DMD system. When compared to the active mass driver (AMD) system (active version of the single TMD system), the ADMD system reduces more story accelerations while reducing less story drifts. Since the actuators in the SFMD systems may not be sufficient for active control, semiactive dampers are studied to improve structural control by creating a semiactive DMD (SADMD) system. Analysis shows that the SADMD system underperforms compared to the ADMD system since the semiactive system cannot apply control forces continuously as do the active systems. Gain scheduling is formulated and applied to the SADMD system to increase the performance.

The external shading fins are placed in the east and west sides of the building and are shown, using the building energy simulation program eQuest, to be more energy efficient compared to the same building without fins. Furthermore, different lengths and orientations of the shading fins are simulated to demonstrate possible benefits of actively movable shading fins that can adjust positions to control direct sunlight and minimize energy cost (mass dampers requires the shading fins to be movable). Though there are some restrictions, active shading fins are simulated in eQuest that can turn 45^o, 90^o and 135^o from North in different time periods to control heat gain from sunlight. This active shading fin system is shown to be more energy efficient than the static counterpart.

The actuators of the SFMD system can also help excite the structure for SHM by vibrating the mass dampers. Since the actuators are not powerful, the structure is excited at its fundamental frequencies for resonance (larger magnitudes of responses). The steady state structural responses are used for mode shape estimation at the excited frequencies. The modal characteristics are then used for stiffness and damage estimations. The advantage of the SFMD system is that there are actuators throughout the structure, making it possible to apply different excitation patterns to improve SHM. Six excitation patterns are studied; the excitation pattern shaped to the corresponding mode shapes is most effective. Four damage patterns are simulated and damage is successfully detected. Statistical analysis of damage patterns is also studied to determine the stiffness loss thresholds to declare damage.

Chapter 5 – Conclusion and Future Work

This dissertation extensively examines two important aspects of smart buildings: monitoring and control. Smart buildings must constantly monitor external and internal building conditions, process the updated information and determine appropriate actions to control building behavior. System integration is crucial to smart buildings for exploring synergy and streamlining building systems for efficiency. The first part of the dissertation studies structural health monitoring (SHM) and the second part focuses on integrating SHM, structural and environmental controls with a shading fin mass damper system.

The slow implementation of SHM into civil structure can be attributed to the quality and limitations of SHM and the installation cost. This dissertation expands and improves an SHM algorithm to conduct multi-directional analysis, providing more information and accuracy on damage detection. Issues with SHM using a wireless sensor network (WSN) are examined because WSNs can help lower installation cost by eliminating wiring. Since energy and bandwidth are critical constraints, a distributed algorithm is tested for SHM to reduce radio communication by locally processing the data in the sensors. Wireless sensor placements are optimized to accurately estimate structural characteristics while keeping energy consumption low. Damage detection with local excitation and wave propagation is investigated to help localize damage in structural elements. Simulating with a finite element model of a structural plate, damage is successfully detected and the effect of sensor placements on damage detection accuracy is analyzed.

The shading fin mass damper (SFMD) system provides the functions of SHM, structural and environmental controls. The movable shading fins are shown to reduce energy consumption on cooling/heating and lighting loads while the mass dampers can reduce structural vibration under strong motions. Additionally, the actuators controlling the movements of the SFMDs can excite the structure for SHM. SHM, structural control (SC) and environmental control (EC) systems individually suffer from a lack of investment from builders. The integrated system will promote interests of these individual systems. The cost of the SHM and SC systems can be partially reduced by the energy saving from the EC component of the synergy system. An EC system integrated with structural safety components will receive serious considerations from builders and, in turn, encourages the use of more advanced EC systems with high energy efficiency. Although the synergy system can be more costly initially than simpler but less capable approaches, the combination of energy saving and safety improvement can be attractive to many builders.

5.1 Future Work

Much work on smart buildings, SHM, SC and EC is needed. Smart buildings can benefit from further integrations of building systems to explore synergy and improve efficency. An extensive and more capable WSN can also be adopted to measure and transmit building measurments other than structural responses for SHM. Advances in sensor processors will pave the way for experimental implemention of the distributed algorithm for wireless SHM. More complex/realistic structures can be modeled for optimal wireless sensor placements to account for SHM and sensor energy usage, including other factors such as radio interference caused by walls. In this document, an overestimation of floor stiffness is observed when there are large differences between neighboring floors' stiffnesses. Stiffness estimation can be improved by a careful examination of this overestimating effect. Damage detections via wave propagation can be further explored with more complicated structural members. By reformulating the DMD system as a continuous beam problem, greater analytical insight can be obtained. This dissertation applies gain scheduling on a 5DOF semiactive DMD system; future study of higher DOF can increase our understanding on this topic. SHM using the SFMD system can be further expanded for more complex structures and using multi-directional analysis.

References

Abe M., and Fujino Y., 1994. "Dynamic characterization of multiple tuned mass dampers and some design formulas," *Earthq Engng Struct Dynam*, **23**, 813–35.

Abdullah, M.M., Richardson, A., and Hanif, J., 2001. "Placement of sensor/actuators on civil structures using genetic algorithms," *Earthq. Eng. Struct. Dyn.,* **30**: 1167–84.

Alward, R., and Shapiro, A., 1981. *Low-Cost Passive Solar Greenhouses*, National Center for Appropriate Technology, Butte, MT. 173.

Bradshaw, V., 2006. *The Building Environment: Active and Passive Control Systems*, John Wiley & Sons, Hoboken, N.J.

Caicedo, J.M., Dyke, S.J., and Johnson, E.A., 2004. "Natural Excitation Technique and Eigensystem Realization Algorithm for Phase I of the IASC-ASCE Benchmark Problem: Simulated Data," *Journal of Engineering Mechanics*, **130**(1), 49–61.

Chen, G., and Wu, J., 2001. "Optimal Placement of Multiple Tune Mass Dampers for Seismic Structures," *J. Structural Engineering*, **127**, 1054-62.

Chen, G., and Wu, J., 2003. "Experimental study on multiple tuned mass dampers to reduce seismic responses of a three-storey building structure," *Earthquake Engng Struct. Dyn*, **32**, 793-810.

Chintalapudi, K.K., 2006. "Design of Wireless Sensor Network Based Structural Health Monitoring Systems," *Ph.D. Dissertation, University of Southern California*, 110-115.

Chopra, A.K., 1995. *Dynamics of Structure,* Prentice-Hall, upper Sadley River, N. J.

Cobb, R.G., and Liebst, B.S., 1997. "Sensor placement and structural damage identification from minimal sensor information," *AIAA J.,* **35**, 369–74.

Crossbow, Inc., 2005. Mica-Z:
http://www.xbow.com/Products/productsdetails.aspx?sid=101.

Crystal Tower, 2003. *Crystal01.jpg and Crystal02.jpg*. Retrieved November 5, 2005 from http://www.takenaka.co.jp/ takenaka_e/t-file_e/d_synthesis/crystal/

Den Hartog, J.P., 1956. *Mechanical Vibrations*, McGraw Hill, NewYork.

Dennis, J.E., Jr., and Torczon, V., 1991. "Direct search methods on parallel machines," *SIAM J. Optim.*, **1**, 448-474.

Doebling, S.W., Farrar, C.R., Prime, M.B., and Shevitz, D.W., 1998a. "Damage Identification and Health Monitoring of Structural and Mechanical Systems from Changes in their Vibration Characteristics: A Literature Review," *Los Alamos National Laboratory Report LA-13070-MS.*

Doebling, S.W., Farrar, C.R., Prime, M.B., and Shevitz, D.W., 1998b. "A Review of Damage Identification Methods that Examine Changes in Dynamic Properties," *Shock and Vibration Digest* **30**(2), 91–105.

Dyke, S.J., Spencer, B.F., Jr., Sain, M.K., and Carlson, J.D., 1996a. "Seismic response reduction using magnetorheological dampers." *Proc., IFAC World Congress*, San Francisco, Vol. L, 145–150.

Dyke, S.J., Spencer, B.F., Jr., Sain, M.K., and Carlson, J.D., 1996b. "Modeling and control of magnetorheological dampers for seismic response reduction." *Smart Mater. Struct.*, **5**(5), 565–575.

Gao, Y., Spencer, B.F., Jr., and Ruiz-Sandoval, M., 2006. "Distributed Computing Strategy for Structural Health Monitoring," *Structural Control and Health Monitoring,* **13**, 488-507.

Guo, H.Y., Zhang, L., Zhang, L.L., and Zhou, J.X., 2004. "Optimal placement of sensors for structural health monitoring using improved genetic algorithms," *Smart Materials and Structures*, **13**, 528-534.

Garibaldi, L., Giorcelli, E., Marchesiello, S., and Ruzzene, M., 1999. "CVA-BR Against ARMAV: Comparison over Real Data from an Ambient Noise Excited Bridge," Damage Assessment of Structures, *Proceedings of the International Conference on Damage Assessment of Structures (DAMAS99)*, Dublin, Ireland, 423-431.

Giurgiutiu, V., Bao, J., and Zhao, W., 2003. "Piezoelectric Wafer Active Sensor Embedded Ultrasonic in Beams and Plates," *Experimental Mechanics,* **43**(4): 428-449.

Giurgiutiu, V., and Cuc, A., 2005. "Embedded Non-destructive Evaluation for Structural Health Monitoring, Damage Detection, and Failure Prevention," *Shock and Vibration Digest*, **37**(2), 83–105.

Graff, K. F., 1975. *Wave Motion in Elastic Solids,* Dover, New York.

Halbe, R, 2004. caltrans.jpg Retrieved April 1, 2007 from http://architettura.supereva.com/architetture /20050325/index.htm

Heredia-Zavoni, E., and Esteva, L., 1998. "Optimal instrumentation of uncertain structural systems subject to earthquake ground motions," *Earthquake Engineering and Structural Dynamics,* **23**, 473-362.

Hemez, F.M., and Farhat, C., 1994. "An energy based optimum sensor placement criterion and its application to structure damage detection," *Proc. 12th Conf. on Int. Modal Analysis* (Honolulu, HI: Society of Experimental Mechanics), 1568–75.

Higashino, M., and Aizawa, S., 1993. "Application of active mass damper system in actual buildings", G.W. Housner and S.F. Masri (eds.), *Proc. Int. Workshop on Struct. Control*, 194-205, Los Angeles, CA.

Hooke, R., and Jeeves, T.A., 1961. "Direct search solution of numerical and statistical problems," *J. Assoc. Comput*., **8**(2), 212-229.

Housner, G.W., Bergman, L.A., Caughey, T.K., Chassiakos, A.G., Claus, R.O., Masri, S.F., Skelton, R.E., Soong, T.T., Spencer, B.F. Jr, Yao, T.P., 1997. "Structural control: past, present, and future," *Journal of Engineering Mechanic, ASCE,* **123**(9), 897–971.

Igusa, T., and Xu, K., 1994. "Vibration Control Using Multiple Tuned Mass Dampers," *J. Sound and Vibration*, **4**, 491-503.

International Code Council, 1997. *Uniform Building Code 1997*, International Conference of Building Official, Washington, DC.

Jansen, L.M., and Dyke, S.J., 2000. "Semiactive Control Strategies for MR Dampers: A Comparative Study," *ASCE Journal of Engineering Mechanics*, **126**(8), 795–803.

Johnson, E.A., Baker, G.A., Spencer, B.F., Jr., and Fujino, Y., 2007. "Semiactive Damping of Stay Cables," *Journal of Engineering Mechanics*, ASCE, **133**(1), 1–11.

Johnson, E.A., Katafygiotis, L.S., Lam, H.F., and Beck, J.L., 2000. ''A benchmark problem for structural health monitoring and damage detection.'' *Proc., 14th ASCE Engineering Mechanics Conf.* (CD-Rom), J.L. Tassoulas, (ed.), Reston, Va.

Juang, J.N., and Pappa, R.S., 1985. “An Eigensystem Realization Algorithm for Modal Parameter Identification and Model Reduction,” *Journal of Guidance*, **8**(5), 620–627.

Kammer, D.C., 1991. “Sensor placement for on orbit modal identification and correlation of large space structures,” *AIAA J. Guid. Control Dyn.,* **14**, 251–9.

Kareem, A., and Kline, S., 1995. “Performance of multiple mass dampers under random loading,” *J Struct. Engng.*, **121**, 348–61.

Leith, D.J., and W.E. Leithead (2000). “Survey of gain-scheduling analysis and design.” *International Journal of Control,* **73**(11), 1001–1025.

Lin, Y.K., 1967. *Probabilistic Theory of Structural Dynamics,* McGraw Hill, NewYork.

Lynch, J.P., and Loh, K.J., 2006. “A Summary Review of Wireless Sensors and Sensor Networks for Structural Health Monitoring,” *The Shock and Vibration Digest,* **38**(2), 91-128.

Lynch, J.P., Sundararajan, A., Law, K.H., Kiremidjian, A.S., Carryer, E., Sohn, H., and Farrar, C.R., 2003. “Field Validation of a Wireless Structural Health Monitoring System on the Alamosa Canyon Bridge,” in Smart Structure and Materials: Smart System and Non-destructive Evaluation for Civil Infrastructures, San Diego, CA, March 3-6, *Proceedings of the SPIE,* 5057, 267-278.

Lynch, J.P., Sundararajan, A., Law, K.H., Kiremidjian, A.S., Kenny, T., and Carryer, E., 2003b. “Embedment of Structural Monitoring Algorithms in a Wireless Sensing Unit,” *Journal of Structural Engineering and Mechanics,* **15**(3), 285-297.

Marin, 2005. hall_of_records.jpg. Retrieved April 6, 2006 from http://you-are-here.com/skyscraper/ 1962_hall_of_records.html

Meeker, T.R., and Meitzler, A.H., 1964. “Guided Wave Propagation in Elongated Cylinders and Plates,” *Physical Acoustics,* (Ed. W. P. Mason) Vol. 1, Part A, Chap. 2. Academic Press, New York.

Min, R., and Chandrakasan, A., 2003. “Top Five Myths About the Energy Consumption of Wireless Communication,” *ACM SIGMOBILE Mobile Computing and Communications Review,* **7**(1), 65–67.

Nagase, T., and Hisatoku, T., 1992. "Tuned pendulum mass damper installed in Crystal Tower," *The Structural Design of Tall Building*, **1**, 35−56.

Olgyay A., and Olgyay, V., 1957. *Solar Control and Shading Devices,* Princeton University Press, Princeton, NJ., 73-74.

Papadimitriou, C., Beck, J.L., and Au, S.K., 2000. "Entropy-Based Optimal Sensor Location for Structural Model Updating," *Journal of Vibration and Control*, **6**, 781−800.

Ramallo, J.C., Johnson, E.A., and Spencer, B.F., Jr., 2002. " 'Smart' Base Isolation Systems," *Journal of Engineering Mechanics,* **128**(10), 1088−1099.

Scruggs, J.T., 2007. "Multi-objective optimization of regenerative damping systems in vibrating structures," *Proceedings of the 2007 American Control Conference*, New York, USA, July 11–13.

Sendagaya INTES building, 2003. *Sendagaya_intes.gif*. Retrieved November 5, 2005 from http://www.japan-photo.de/e-mo-j17.htm

Shi, Z.Y., Law, S.S., and Zhang, L.M., 2000, "Optimum sensor placement for structural damage detection," *J. Eng. Mech.,* **126**, 1173–9.

Sohn, H., and Farrar, C.R., 2001. "Damage Diagnosis Using Time-series Analysis of vibrating Signals," *Smart Materials and Structures,* **10**(3), 446-451.

Sohn, H., Farrar, C.R., Hemez, F.M., Czarnecki, J.J., Shunk, D.D., Stinemates, D.W., and Nadler, B.R., 2003. "A Review of Structural Health Monitoring Literature: 1996-2001," *Los Alamos National Laboratory Report, LA-13976-MS.*

Soong, T.T., and Grigoriu, M., 1993. *Random Vibration of Mechanical and Structural System,* Prentice Hall, Englewood Cliffs, NJ.

Soong, T.T., and Spencer, B.F., Jr., 2002. "Supplemental energy dissipation: state-of-the-art and state-of-the practice," *Engineering Structures,* **12**, 243−259.

Straser, E.G., and Kiremidjian, A.S., 1998. "A Modular Wireless Damage Monitoring System, Technical Report," John A Blume Earthquake Engineering Center, Dept. of Civil and Environmental Engineering, Stanford University, Stanford, CA.

"synergy." *Merriam-Webster Online Dictionary*. 2008. Merriam-Webster Online. 25 December 2008 <http://www.merriam-webster.com/dictionary/synergy>

TakenakaCorporation, 2001. *tatemono.gif*. Retrieved July 18, 2006 from http://www.takenaka.co.jp/takenaka_e/quake_e/menshin/menshin.htm

Texas Instruments, 2006. CC2420 Radios:
http://focus.ti.com/docs/prod/folders/print/cc2420.html

Torczon, V., 1989. *Multi-Directional Search: A Direct Search Algorithm for Parallel Machines*, Thesis (Ph.D), Department of Mathematical Sciences, Rice University, Houston, TX.

Torczon, V., 1997. "On the convergence of pattern search algorithms," *SIAM J. Optim.*, **7**, 1–25.

Wang, A., Cho, S.H., Sodini, C., and Chandrakasan, A., 2001. "Energy Efficient Modulation andMAC for Asymmetric RF Microsensor Systems," *International Symposium on Low Power Electronics and Design,* CA, 106–111.

Wirsching, P.H., and Campbell, G.W., 1974. "Minimal Structural Response Under Random Excitation Using The Vibration Absorber." *Earthquake Engineering and Structural Dynamics*, **2**, 303–312.

Udwadia, F.E., and Sharma, D.K., 1978. "Some Uniqueness Results Related to Building Structural Identification," *SIAM Journal on Applied Mathematics*, **34**(1), 104−118.

Udwadia, F.E., 1994. "Methodology for Optimum Sensor Locations for Parameter Identification in Dynamic Systems," *Journal of Engineering Mechanics,* **120**(2), 368−390.

Yamaguchi H., and Harnpornchai, N., 1993. "Fundamental characteristics of multiple tuned mass dampers for suppressing harmonically forced oscillations," *Earthq Engng Struct Dynam*, **22**, 51–62.

Yang, G., Jung, H.J., Spencer, B.F., Jr., and Carlson, J.D., 2004. "Dynamic Modeling of Large-Scale Magnetorheological Damper Systems for Civil Engineering Applications," *Journal of Engineering Mechanics*, **130**(9), 1107−1114.

Yuan, S., Lai, X., Zhao, X., Xu, X., and Zhang, L., 2006. "Distributed Structural Health Monitoring System Based on Smart Wireless Sensor and Multi-agent Technology," *Smart Materials and Structure*, **15**, 1−8.